New Phases of Two-Dimensional Electrons in Excited Landau Levels

Thesis by

Ken B. Cooper

In Partial Fulfillment of the Requirements

for the Degree of

Doctor of Philosophy

California Institute of Technology

Pasadena, CA

2003

(Defended May 21, 2003)

Acknowledgements

My deep gratitude goes first to Professor Jim Eisenstein, who expertly guided me through my graduate education and who shared the excitement of six years of discovery. His unwavering enthusiasm for physics kept me constantly engaged with my research, and his personal generosity helped make my time at Caltech enjoyable.

My appreciation also extends to my laboratory colleagues. Mike Lilly's mentoring and encouragement have been especially valuable, and his early insights launched the greater part of this dissertation. Thanks also go to Peter Burke and Keith Schwab, who enlivened the subbasement of Sloan with good physics and good humor. Ian Spielman's superluminal mind and Mindy Kellogg's genuine kindness also helped sustain a positive atmosphere in which to do science.

Above ground, I am indebted to my family, whose value to me only grows with age. And finally, I acknowledge my wife, Sarah, who is my champion and who blessed me with a life of joy in the hours when the lab lights were off.

Abstract

The subject of this dissertation is the experimental discovery and investigation of a new class of collective phases in two-dimensional electron systems. The experiments mainly involve magnetotransport measurements in very high quality GaAs/AlGaAs semiconductor heterostructures, where a large perpendicular magnetic field serves to resolve the electrons' energy spectrum into discrete Landau levels. The most dramatic evidence of a new many-body phase is the huge and unprecedented resistance anisotropy observed only below 150 mK and around the half-filling points of the highly excited Landau levels $N \geq 2$. Associated with these anisotropic states are other novel electron phases whose transport signature is a vanishing longitudinal conductivity occurring in the flanks of the same excited Landau levels. Although reminiscent of the well-understood integer quantum Hall states, the insulating phases are exceptional for being driven by electron interactions rather than single-particle localization. A persuasive theoretical picture based on "stripe" and "bubble" charge density wave formation in high Landau levels can account for many of the experimental results. For example, the broken orientational symmetry of the stripe state may underlie the observed transport anisotropy, while disorder-induced pinning of the bubble lattice could give rise to the insulating regions in high Landau levels. Further investigation of the anisotropic transport characteristics has elucidated possible symmetry-breaking mechanisms of the purported stripe phase and has provided evidence that the stripes may be more accurately described as a quantum electronic liquid crystal. In addition, experiments involving the breakdown of the insulating regions at high voltage biases may point to a depinning transition of the bubble phase. These results have spurred intense interest in the field of correlated electron systems in two dimensions and may be an indication of the variety of new phenomena in condensed matter systems still awaiting discovery.

Table of Contents

Introduction and Summary

For over two decades, the two-dimensional electron system (2DES) has been a pillar of condensed matter physics because it provides an unrivaled setting in which to explore highly correlated electrons. The manifestations of interparticle interactions are especially prominent in the quantum Hall regime, where a perpendicular magnetic field quantizes the electrons' kinetic energy into a ladder of massively degenerate Landau levels (LLs) labeled $N = 0, 1, 2\ldots$. This quenching of kinetic energy permits the potential energy to play the dominant role in determining the 2DES ground state, and fascinating collective electronic phases may emerge. The most famous example of correlated electron physics in 2DESs is the fractional quantum Hall effect (FQHE). The discovery of the FQHE and its explanation in terms of a bizarre quantum fluid was the subject of the 1998 Nobel Prize in Physics. FQHE research has also spawned a zoo of new physics concepts ranging from fractionally charged quasiparticles to composite Fermions to nonabelian statistics.

This thesis dissertation describes the discovery of a new class of collective electronic phases in the quantum Hall regime which are distinct from the FQHE. The most dramatic evidence of these new phases is a huge and unprecedented resistance anisotropy that develops around half-filling of highly excited LLs. In very clean systems, the ratio of resistances along two orthogonal axes can exceed 1000. In addition, unusual insulating electronic phases accompany the anisotropies on the flanks of the high LLs. In contrast to the FQHE states, which are restricted to the two lowest $N = 0$ and 1 LLs, the anisotropic and insulating phases are observed only in the $N \geq 2$ LLs.

Both the anisotropic and the insulating electronic phases in high LLs are now widely believed to originate from the same physical principle: charge density wave (CDW) formation. About two years before the experimental detection of these electron phases, Hartree-Fock calculations predicted that electrons in partially filled excited LLs will form CDWs as a way of minimizing the competing direct and exchange energies of the Coulomb interaction. Around half-filling of the valence LLs, these calculations predicted that a “stripe” CDW would form with alternating rows of filled and empty

electron states. Away from half-filling, the theories suggested that a "bubble" CDW would form, consisting of a triangular lattice of charge with two or more electrons at each node. The anisotropic transport can be accounted for in the striped CDW model by assuming that the electrons flow more easily along than across the stripes, provided there is some orientational symmetry-breaking mechanism within the host semiconductor crystal. Likewise, the insulating states would arise naturally from a disorder-induced pinning of the bubble CDW.

The discovery of new physics in high LLs has generated intense interest in the quantum Hall and the wider condensed matter physics community. For example, our measurements of huge resistance anisotropies were singled out as groundbreaking research by *Physics Today* [1] and *Physical Review Focus* [2], and dozens of theoretical research articles have subsequently been devoted to exploring the physics of stripe and bubble formation in 2DESs. The principle of stripe CDW formation has had an impact on other fields as well, including high-temperature superconductivity. Most importantly, the presence of new electronic phases in high LLs has permanently altered the general picture of 2DES physics in the quantum Hall regime. Prior to our experiments, it was generally assumed that any new interaction-driven electron ground states discovered in the quantum Hall regime would be accounted for by the basic principles of the FQHE. Now, however, collective phases of the 2DES in a magnetic field are understood to belong to one of two categories: For $N < 2$, FQHE states prevail, while for $N \geq 2$, CDW physics is the rule.

In addition to describing the basic phenomena of the anisotropic and insulating electronic phases in high LLs, this thesis summarizes our efforts to explore these states in greater depth. Highlights of these experiments include quantitative comparisons to transport models of the stripe CDW; investigations of intrinsic and extrinsic symmetry-breaking mechanisms that orient the stripe CDW; measurements supporting a liquid crystal-based generalization of the stripe CDW model; and a study of the bubble CDW response to high electric fields.

This thesis is long and contains data obtained over several years of research. Therefore, to provide the reader with a "road map" of what lies ahead, the following summary emphasizes the most important results from each chapter. For those interested

in a more concise description of the major results, this summary also contains references to our group's relevant publications on each topic.

Chapter 1 contains an introduction to the physics of electrons in two dimensions and lays the groundwork for concepts discussed in subsequent chapters. First, the Drude theory of magnetotransport is reviewed, and the longitudinal and Hall resistances are defined. These resistances constitute the core measurements used in almost all of our experiments. Then LL formation by a perpendicular magnetic field is introduced and the filling factor $\nu = hn/eB$ is defined as the total number of electrons in the 2DES divided by the number of available electron states in each LL. Next, the integer quantum Hall effect is explained in terms of LL quantization and disorder in the 2DES. Finally, the FQHE and the interaction physics behind it is briefly described

Chapter 2 describes the major experimental materials and methods used in this research. The chapter begins with a description of how bandstructure engineering in GaAs/AlGaAs heterostructures grown by molecular beam epitaxy (MBE) enables the creation of extremely clean 2DESs. Because the orientation of the anisotropic electronic phases in high LLs is strongly affected by the host crystal of the 2DES, the methods we use to determine the crystal axes of the MBE wafers are described. Next, the sample preparation steps, the transport measurement techniques, and the refrigeration apparatus are reviewed. The chapter concludes with a description of the experimental techniques of *in situ* sample rotation and illumination.

Chapter 3 is the most important part of this thesis because it provides an overview of the phenomenon of anisotropic transport in high LLs. The main results of Chapter 3 can be found in ref. [3], and the basic observation of anisotropic transport in high LLs, contained in Fig. 3.4, is reproduced here. In Fig. 3.4, two low-temperature traces of longitudinal resistance versus magnetic field are shown. Each trace was obtained under identical circumstances except for one crucial difference: the current and voltage probes of the 4-terminal resistance measurements were rotated around the square sample by 90°. The two resistances R_{xx} and R_{yy} correspond to current flowing along either the $[1\bar{1}0]$ or the $[110]$ crystal direction within the plane of the 2DES. Normally, these two directions are indistinguishable using transport-based probes, but in this case

R_{xx} and R_{yy} spectacularly diverge from one another for the sequence of filling factors $\nu =$ 9/2, 11/2, 13/2, etc.

After introducing this basic anisotropy effect, the remainder of Chapter 3 fills in many details about where and when it occurs. By presenting data from nine different MBE wafers, the anisotropy is shown to consistently appear in high-quality samples only below 100 to 150 mK and only around half-filling of high LLs. The anisotropy is also robust in non-square 2DES geometries, with its twofold in-plane symmetry preserved. Finally, an intriguing resistance nonlinearity associated with the peak in R_{xx} is revealed.

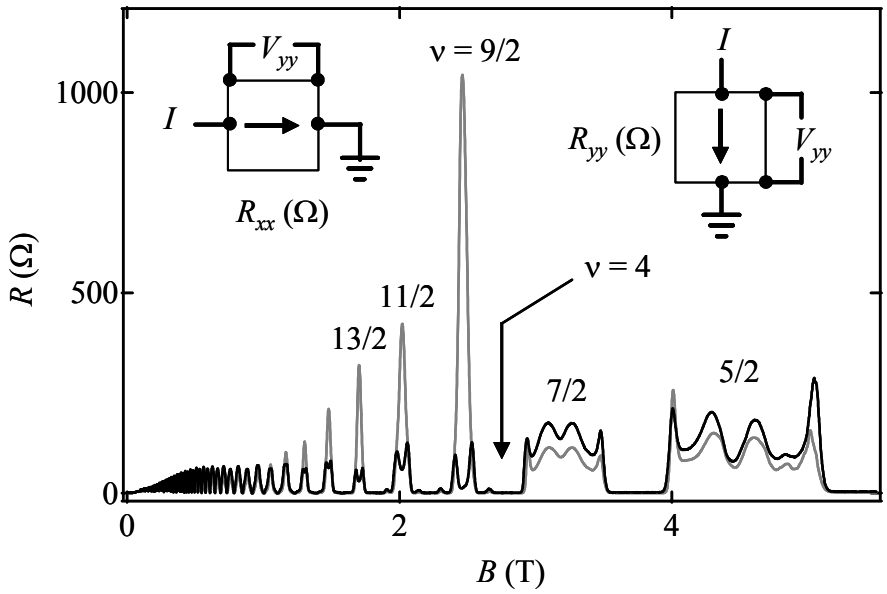

Figure 3.4: Magnetotransport at 25 mK in a square 2DES. R_{xx} (gray) corresponds to current flow along $[1\bar{1}0]$; R_{yy} (black) corresponds to current flow along $[110]$. A dramatic anisotropy in longitudinal resistance develops only around the half-filling points of high LLs: at $\nu =$ 9/2, 11/2, 13/2, etc.

Chapter 4 demonstrates that the resistance anisotropies are not the only unusual feature of low-temperature transport measurements in high LLs. Regions of vanishing R_{xx} and R_{yy} that develop on either side of the anisotropic phases signify the presence of a second class of *insulating* electronic phases unique to high LLs. (Counterintuitively, a vanishing longitudinal resistance is equivalent to a vanishing longitudinal conductance in the presence of a magnetic field—hence the designation "insulating.") Fig. 4.2, reproduced here, shows that these insulating phases actually represent a re-entrant integer quantum Hall effect (RIQHE) because they share the two primary signatures of the

IQHE: vanishing longitudinal resistance and integrally quantized Hall resistance. However, unlike the IQHE, which can be accounted for strictly in terms of single-particle physics, the origin of the RIQHE is inherently a many-body phenomenon. After introducing the RIQHE, it is shown to be a generic feature of high LL transport in several different samples. Also, the temperature dependence of the RIQHE provides quantitative insight into the energetics of the underlying electronic phase. Some basic elements of the RIQHE are described also in ref. [4].

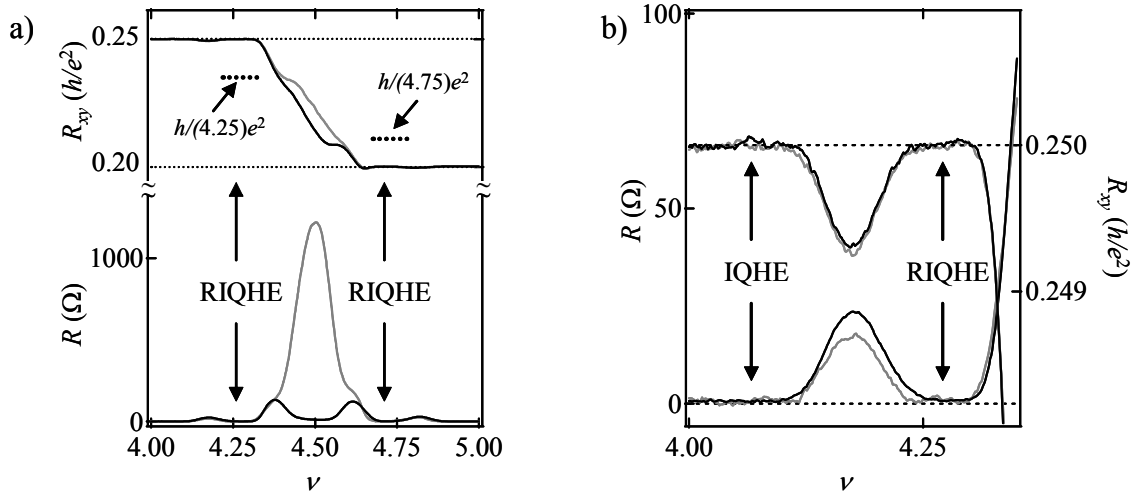

Figure 4.2: a) 50 mK longitudinal and Hall resistance between $4 < \nu < 5$ for current along $[1\,\bar{1}0]$ (gray) and $[110]$ (black). The minima in R_{xx} and R_{yy} near $\nu = 4.25$ and $\nu = 4.75$ do not coincide with a fractionally quantized R_{xy} at the locations expected from the FQHE (short dashed lines). b) Close-up view of the longitudinal and Hall resistances demonstrating that the IQHE is re-entrant around $\nu = 4.25$.

Chapter 5 reviews the Hartree-Fock theory of stripe and bubble CDW formation in high LLs and describes how these results may account for the observation of resistance anisotropies and the RIQHE. The physics behind CDW formation is motivated both mathematically and intuitively as a compromise satisfying the competing repulsive and attractive forces of the direct and exchange Coulomb interactions. Hartree-Fock theory predicts that the valence LL electrons in a half-filled level self-assemble into alternating rows of filled and empty states. To account for the resistance anisotropy, these stripes are presumed to be oriented by a still unknown symmetry-breaking field associated with the host crystal, and electron conductivities along versus across the stripes are presumed to

differ. At smaller partial filling factors, Hartree-Fock theory predicts that the valence LL electrons segregate into a lattice of charged bubbles with two or more electrons per site. If this electron solid is then pinned by disorder, the RIQHE states can be accounted for. Fig. 5.1b is reproduced here, and it shows a cartoon of how the anisotropic and insulating states are attributed to stripe and bubble formation. Chapter 5 concludes by showing how the quantum Hall stripe and bubble phases are just two examples of similar pattern formation phenomena that occur in a wide variety of physical systems.

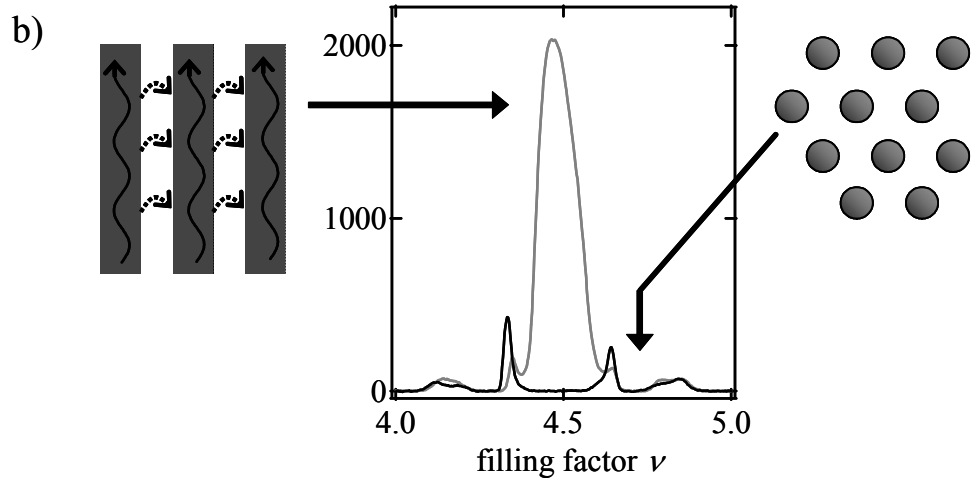

Figure 5.1b: The stripe phase (left) could account for the anisotropy at half-filling if electrons travel more easily along the stripes than between them. If pinned by disorder, the bubble phase (right) would not conduct current, consistent with the RIQHE.

Chapter 6 presents a quantitative analysis of the transport anisotropy and makes contact with two theories of electron transport through the stripe CDW phase. A classical model of current flow through an isotropic medium illustrates how square sample geometries can greatly exaggerate the apparent anisotropy ratio. For example, an underlying resistivity ratio of $\rho_{xx}/\rho_{yy} \approx 10$ results in a resistance ratio $R_{xx}/R_{yy} \approx 150$. By converting the measured resistances to resistivities, the experimental results can be compared to two theories of electron transport through a stripe CDW. Fair agreement between theory and experiment is found.

Chapter 7 summarizes experiments designed to elucidate the symmetry-breaking mechanism responsible for orienting the anisotropic electronic phases. Using crystal symmetry arguments, it is shown that the electronic symmetry between the $[1\,\bar{1}0]$ and

[110] directions in GaAs may be broken at surfaces and interfaces. Indeed, anisotropic surface roughness is a common feature of MBE-grown GaAs crystals, and the possible impact of the sample surface morphology on the anisotropic phases is addressed. Using atomic force microscopy, we find that there is no correlation between the strength or orientation of micron-scale surface roughness and the principal axes of anisotropic transport. A crystal electric field associated with the GaAs/AlGaAs interface symmetry is also ruled out as an orienting mechanism. Other possible symmetry-breaking mechanisms not fully investigated yet include interface roughness at the 2DES layer of the heterostructure and an interesting piezoelectric interaction between the crystal and a stripe CDW. Many of the major conclusions of this chapter can also be found in ref. [5].

Chapter 8 reveals that the principal axes of anisotropy need not be exclusively determined by the host GaAs crystal. Rather, the anisotropy orientation can be extremely sensitive to the direction and magnitude of small in-plane magnetic fields that are generated by tilting the sample *in situ*. In general, the anisotropy orientation is such that the hard transport direction lies along the in-plane field $B_{||}$. As an illustration, Fig. 8.1 is reproduced here and shows how the anisotropy orientation can be rotated by 90° when $B_{||}$ is applied along [110]. Whereas the longitudinal resistances R_{xx} and R_{yy} around $\nu = 9/2$ begin with R_{xx} exhibiting a large peak and R_{yy} a deep minimum for $B_{||} = 0$, they become comparable for a tilt angle of $\theta = 22°$, and finally R_{xx} and R_{yy} reverse for $\theta = 31°$. In addition to reorienting the anisotropy axes in high LLs, $B_{||}$ also induces anisotropic transport in the $N = 1$ LL where the enigmatic $\nu = 5/2$ and $\nu = 7/2$ FQHE states occur.

According to a successful theoretical model, the anisotropy reorientation is probably a consequence of $B_{||}$ playing the role of an orientational symmetry-breaking field of the stripe CDW. By coupling to the finite thickness of the 2DES, $B_{||}$ is able to overcome the native crystal orienting field and reorient the stripe CDW along a different direction. This theoretical model is used to make a quantitative estimate of the native crystal orienting mechanism strength, yielding an energetic advantage of ~1 mK per electron. Many of the results of Chapter 8 are also contained in ref. [6].

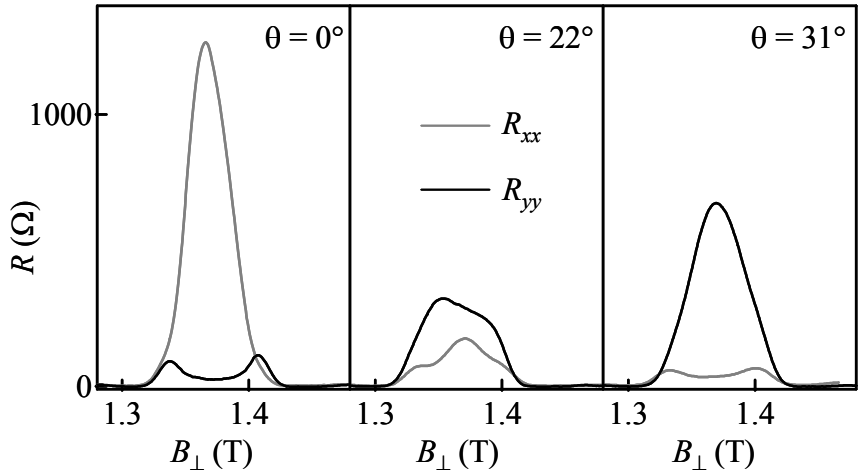

Figure 8.1: R_{xx} (gray) and R_{yy} (black) data through $\nu = 9/2$ for tilt angles of 0°, 22°, and 31°. The in-plane magnetic field lies along $[110]$, and the principal axes of anisotropy reverse by 31°.

Chapter 9 explores the effect of an in-plane field on the low-temperature development of anisotropic transport appears. Normally, the resistance anisotropies in high LLs develop rapidly only once the temperature is lowered below 100 or 150 mK. However, an in-plane field systematically broadens the anisotropic-to-isotropic transition, allowing resistance anisotropies to persist up to several hundred mK. Treating $B_{||}$ as an external orientational symmetry-breaking field, these observations support the proposal that the transition from anisotropic to isotropic transport reflects an electronic liquid crystal phase transition where local stripe order persists even into the isotropic regime. The experiments suggest that rather than melting above ~100 mK, the stripe CDW phase merely becomes orientationally disordered, as shown here in the reproduction of Fig. 9.2.

In one simplified picture, the nematic-to-isotropic phase transition as a function of temperature can be described by a two-dimensional classical XY model with a director order parameter. Motivated by that analogy, original Monte-Carlo calculations are presented which describe how the nematic-to-isotropic transition is affected by the presence of an adjustable external symmetry-breaking field. The calculations provide qualitative support to the electronic liquid crystal model of stripes. The experiments of Chapter 9 are also described in ref. [7].

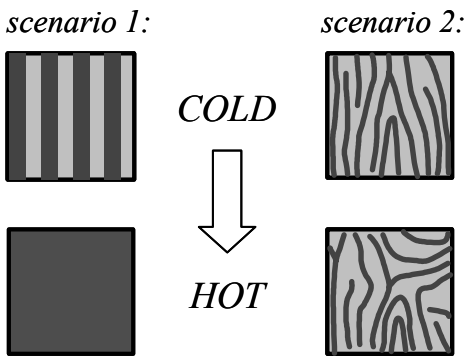

Figure 9.2: Two scenarios for the transition from anisotropic to isotropic transport in the stripe CDW phase as T increases. Left: the stripes melt. Right: the stripes lose their net orientation. Experimental evidence favors scenario 2.

Chapter 10 returns to the subject of the RIQHE phases on the flanks of high LLs, focusing on their response to high electric fields. An electric field in the quantum Hall regime is most easily generated by a dc current, which generates a transverse voltage drop across the sample by virtue of the Hall resistance. Fig. 10.2, reproduced here, shows how the longitudinal voltage in the RIQHE regime responds to a dc current bias in an extremely nonlinear way once the current passes a threshold of ~500 nA. The I-V curve exhibits a discontinuous and hysteretic transition suggestive of the sudden depinning of the insulating bubble CDW phase of the RIQHE. The temperature, filling factor, and sample dependence of this RIQHE breakdown phenomenon are discussed in Chapter 10, and possible models other than a depinning transition are considered.

The second part of the chapter describes how the sharp transitions to conduction of the RIQHE states are often accompanied by narrow- and broad-band voltage noise at kHz scales. These ac signals develop spontaneously within the 2DES in response to the purely dc applied current. The narrow-band oscillations can be extremely periodic in time, and their frequencies are strongly dependent on the magnitude of the applied dc current. The breakdown and noise features of the RIQHE at high current bias are reminiscent of those observed in other pinned, spatially ordered systems such as CDWs in quasi-one dimensional metals or vortex lattices in type-II superconductors. However, while it is tempting to compare this behavior to the narrow-band "washboard" noise of conventional CDW compounds above their depinning threshold, the low observed

frequencies are difficult to justify. The fundamentals of the RIQHE breakdown phenomena are also described in refs. [4] and [8].

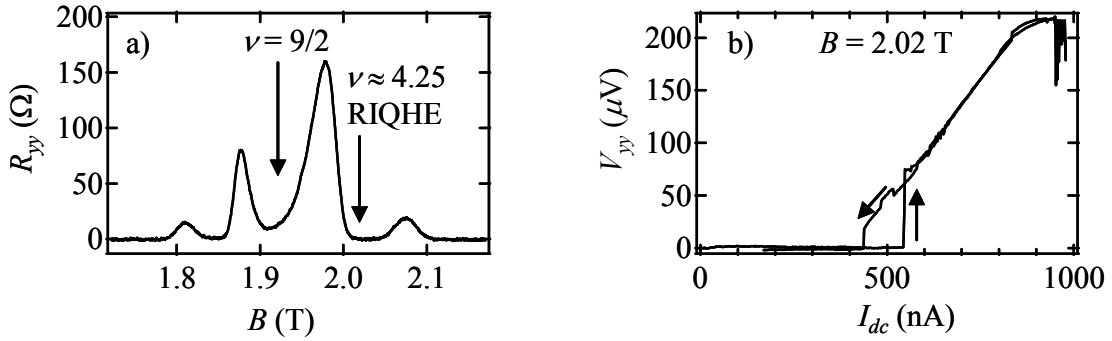

Figure 10.2: a) R_{yy} versus B through $\nu = 9/2$. b) V_{yy} versus I_{dc} at $B = 2.02$ T, in the $\nu \approx 4.25$ RIQHE. The I-V curve exhibits a discontinuous, hysteretic onset to conduction above ~500 nA. The arrows denote the direction I_{dc} was swept.

The final chapter, **Chapter 11**, synthesizes the unresolved issues of high LL physics and suggests specific directions that future experiments might take. Most importantly, direct experimental evidence of CDW formation is still lacking, and the problem of the orientational symmetry-breaking mechanism of the anisotropic states has not yet been solved. Despite the large amount of progress made so far, these fundamental questions will have to be left for others to answer.

---

1 *Physics Today*, December 1998, p. 23.

2 http://focus.aps.org/story/v3/st2.

3 M.P. Lilly, K.B. Cooper, J.P. Eisenstein, L.N. Pfeiffer, K.W. West, Phys. Rev. Lett. **82**, 394 (1999).

4 K..B. Cooper, M.P. Lilly, J.P. Eisenstein, L.N. Pfeiffer, K.W. West, Phys. Rev. B **60**, R11285 (1999).

5 K.B. Cooper, M.P. Lilly, J.P. Eisenstein, T. Jungwirth, L.N. Pfeiffer, K.W. West, Solid State Commun. **119**, 89 (2001).

6 M.P. Lilly, K.B. Cooper, J.P. Eisenstein, L.N. Pfeiffer, K.W. West, Phys. Rev. Lett. **83**, 824 (1999).

7 K.B. Cooper, M.P. Lilly, J.P. Eisenstein, L.N. Pfeiffer, K.W. West, Phys. Rev. B **65**, 241313(R) (2002).

8 K.B. Cooper, J.P. Eisenstein, L.N. Pfeiffer, K.W. West, to be published in Phys. Rev. Lett.; also at http://xxx.lanl.gov/abs/cond-mat/0210069.

Chapter 1:
Classical and Quantum Magnetotransport

1.1 Classical Magnetotransport in Two Dimensions

In the Drude model [1] of electron transport through a disordered solid, frequent collisions with impurities result in a characteristic transport relaxation time τ, yielding a dc conductivity in zero magnetic field of $\sigma_0 = ne^2\tau/m$, where n and m are the electron density and mass. This conductivity may also be written as $\sigma_0 = ne\mu$, where μ is defined as the electron mobility. Higher mobility electron systems have longer transport lifetimes and higher conductivities, and in this sense the mobility is a convenient way of characterizing the cleanliness or quality of a sample. If the electrons are confine to two dimensions and a perpendicular magnetic field is applied, the conductivity becomes a tensor relating the local current density and electric field as $\mathbf{J} = \boldsymbol{\sigma}\,\mathbf{E}$. The zero frequency conductivity tensor is

$$\boldsymbol{\sigma} = \frac{\sigma_0}{1+(\omega_c\tau)^2}\begin{pmatrix} 1 & -\omega_c\tau \\ \omega_c\tau & 1 \end{pmatrix}$$

where $\omega_c = eB/m$ is the cyclotron frequency in a magnetic field B. Equivalently, writing $\mathbf{E} = \boldsymbol{\rho}\,\mathbf{J}$, the resistivity tensor is

$$\boldsymbol{\rho} = \boldsymbol{\sigma}^{-1} = \rho_0\begin{pmatrix} 1 & \omega_c\tau \\ -\omega_c\tau & 1 \end{pmatrix} = \begin{pmatrix} \rho_0 & B/ne \\ -B/ne & \rho_0 \end{pmatrix},$$

with $\rho_0 = 1/\sigma_0$. Unlike in three dimensions, the resistivity components are expressed in the same units as resistance: the Ohm Ω.

The above relationships are applicable in magnetotransport measurements, where typically a current I is passed through a long and narrow "Hall bar" geometry as shown in Fig. 1.1. (The nineteenth-century physicist Edwin Hall pioneered magnetotransport measurements.) If the Hall bar is long and thin enough, the current density in its central region will not have a **y** component, and the electric field in that region will be

$$\mathbf{E} = \begin{pmatrix} \rho_{xx} & \rho_{xy} \\ -\rho_{xy} & \rho_{yy} \end{pmatrix} \begin{pmatrix} J_x \\ 0 \end{pmatrix} = \begin{pmatrix} \rho_{xx} J_x \\ -\rho_{xy} J_x \end{pmatrix} = \begin{pmatrix} \rho_0 J_x \\ -(B/ne) J_x \end{pmatrix}.$$

In this way, the electric field due to the current flow develops both a longitudinal and a transverse, or Hall, component. Physically, the Hall field comes from the Lorentz force pushing the moving electrons to one side of the sample (downward in the case of Fig. 1.1). The charge imbalance between the sample sides increases until the transverse electric field provides a force which exactly cancels the Lorentz force. At that point, equating the two forces $eE_y = ev_xB$ yields an electron drift velocity along **x** of $v_x = E_y / B$.

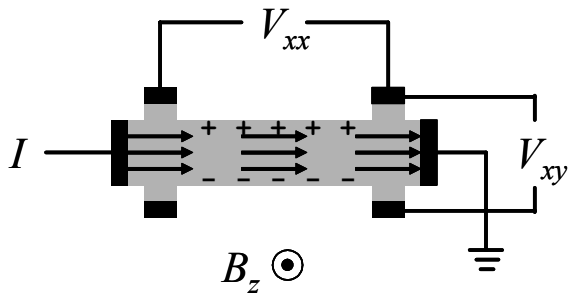

Figure 1.1: Magnetotransport in a Hall bar geometry. In a perpendicular magnetic field, the Lorentz force establishes a tranverse electric field, resulting in both a longitudinal voltage V_{xx} and a Hall voltage V_{xy}.

The longitudinal and Hall electric fields result in longitudinal and Hall voltages, as shown in Fig. 1.1. These voltages are $V_{xx} = I\rho_{xx}\frac{L}{W}$ and $V_{xy} = I\rho_{xy}$ where L and W are the length and width of the long, thin Hall bar. The ratio L/W is referred to as the "number of squares" between the longitudinal voltage contacts. This expression for V_{xx} is valid only for a uniform current density directed along **x**. In other geometries the relationship between V_{xx} and ρ_{xx} is more complicated, and the longitudinal *resistance* R_{xx}

is defined through the equation $V_{xx} = IR_{xx}$. On the other hand, the expression $V_{xy} = I\rho_{xy}$ remains true even for non-uniform current distributions as long as there is no net transverse current passing through a line connecting the two voltage contacts of the Hall measurement. In other words, while the ρ_{xx} and R_{xx} are in general different, R_{xy} and ρ_{xy} are the same and both equal to B/ne.

In the limit of very clean systems, for $\tau >> 1/\omega_c$, the conductivity and resistivity tensors become

$$\boldsymbol{\sigma} = \begin{pmatrix} 0 & -ne/B \\ ne/B & 0 \end{pmatrix} \text{ and } \boldsymbol{\rho} = \begin{pmatrix} 0 & B/ne \\ -B/ne & 0 \end{pmatrix}.$$

These equations mean that when collisions are negligible, the electric field **E** and the current density **J** are orthogonal to one another, i.e., the Hall angle $\theta_H = \tan^{-1}(\rho_{xy}/\rho_{xx}) = 90°$. Also, somewhat counter-intuitively, a vanishing diagonal resistivity $\rho_{xx} = 0$ means that $\sigma_{xx} = 0$ as well. Note that for a fixed current, a small ρ_{xx} implies that very little energy is dissipated in the bulk of a sample. However, a subtle consequence of the magnetic field is that even for $\rho_{xx} \to 0$, dissipation will still occur at the source and drain current contacts as long as ρ_{xy} is finite.

1.2 Quantum Magnetotransport in Two Dimensions

1.2.1 Quantum Description of a 2D Electron

In actuality, the condition $\tau >> 1/\omega_c$ cannot be treated accurately within the classical model of Drude theory because quantum mechanical effects become important in very clean 2DESs. One way of understanding this is that for a long transport lifetime τ, an electron in a magnetic field will come full circle before scattering. In a semiclassical sense, this results in the electron "interfering with itself," and therefore its wavelike

nature must be taken into account. The quantum nature of a clean 2DES in a magnetic field will turn out to have a dramatic impact on its transport properties.

Before considering these consequences, it is helpful to review the quantum mechanical solution of a single 2D electron in a magnetic field [3]. In the Landau gauge **A** = (0,*Bx*,0), where **B** = *B***z** is the magnetic field pointing in the **z** direction, the energy spectrum and wavefunctions of the electron are given by

$$\varepsilon_{Nk} = \left(N + \frac{1}{2} \right) \hbar \omega_c ,$$

$$\psi_{Nk}(x, y) \propto H_N \left(\frac{x - x_k}{l_B} \right) \exp\left[-\frac{(x - x_k)^2}{2 l_B{}^2} \right] \exp(iky) .$$

Here, $\omega_c = eB/m$ is the cyclotron frequency, $H_N(x)$ is a Hermite polynomial, and the parameter $l_B = \sqrt{\hbar / eB}$ is the "magnetic length." There are two quantum numbers: $N = 0$, 1, 2, …, and k, which is continuous unless a boundary condition in the y-direction is imposed. The energy spectum consists of an equally spaced ladder of levels called Landau levels (LLs) separated by $\hbar \omega_c$. This spectrum is an example of the close analogy between a 2D electron in a magnetic field and a one-dimensional harmonic oscillator. Because ε_{Nk} is independent of k, for a given N there may be many degenerate states.

The wavefunctions $\psi_{Nk}(x, y)$ consist of a plane-wave solution with constant probability density in the y-direction. In the x-direction the wavefunctions have N nodes and are given by the familiar one-dimensional harmonic oscillator solution centered at the location $x_k = -\hbar k / eB$. An important length scale is the cyclotron radius $R_c = v / \omega_c = l_B \sqrt{2N + 1}$, which is the size scale of the "spread" of an electron in the *Nth* LL. Thus these solutions to the Schrodinger equation consist of "strips" of probability density extending in the y-direction that are ~R_c wide in the x-direction and modulated with N nodes (see Fig. 1.2). Note that different gauge choices will result in a different set of eigenstates with the same energies; this is a consequence of the degeneracy within each LL.

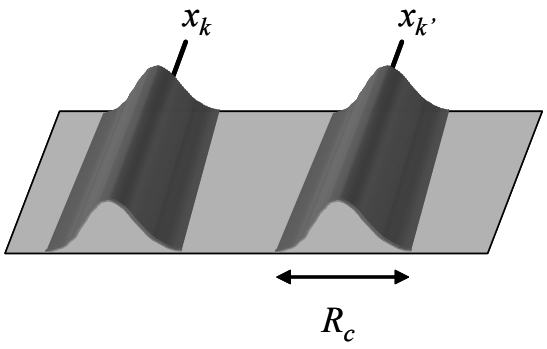

Figure 1.2: Schematic diagram of two $N = 0$ Landau gauge wavefunctions of a 2D electron in a magnetic field.

That degeneracy is given by $n_B = eB/h$, the number of states per unit area per spin in each LL. Because the quantum of magnetic flux is given by $\Phi_0 = h/e$ and the total magnetic flux is $\Phi = BA$, the degeneracy of each LL per spin is also the number of magnetic flux quanta passing through the sample.

The LLs are generated by a magnetic field, and so the spin of the electrons generates a Zeeman splitting of each LL. Although this Zeeman splitting is typically much smaller than the cyclotron gap, there is a substantial "spin gap" associated with the many-body energy penalty for an electron to reverse its spin. As a result, at magnetic fields large enough to resolve the LLs under realistic conditions, the electrons within each LL are generally spin-polarized.

The degeneracy of each spin-resolved LL allows a 2DES with a density n to fill $\nu = nh/eB$ total LLs, where ν is called the filling factor. For typical electron densities on the order of 10^{15} m^{-2}, several Tesla are required to force all the electrons in the 2DES into the same lowest LL, where $\nu \leq 1$. Fig. 1.3 shows a schematic representation of electrons at a filling factor $\nu = 9/2$, a value that will play a central role in this thesis. The filling factor can be adjusted either by varying the electron density or the magnetic field.

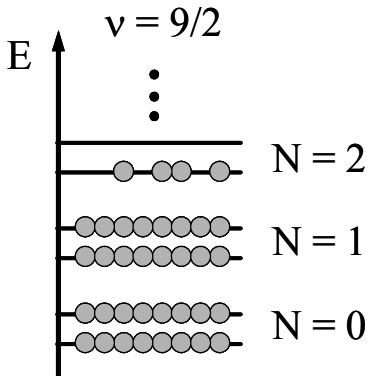

Figure 1.3: Spin-split Landau level ladder showing the electrons at a filling factor of $\nu = 9/2$.

1.2.2 Quantum Transport: the Integer Quantum Hall Effect

The LL structure of a 2DES in a perpendicular magnetic field has enormous consequences on the system's transport properties, most evidently in the integer quantum Hall effect (IQHE). The IQHE was discovered in 1980 by von Klitzing, who won a Nobel Prize in physics for his work [2]. Typical IQHE transport data taken by our group is shown in Fig. 1.4.

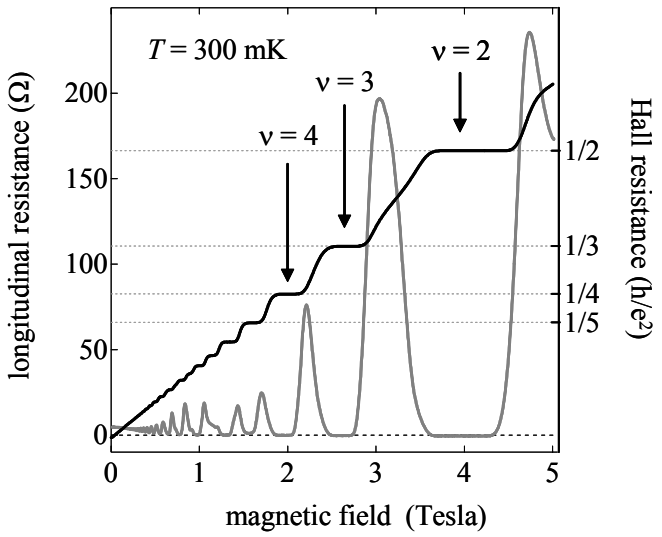

Figure 1.4: Magnetotransport data showing the integer quantum Hall effect (IQHE). As the Fermi level passes between two LLs, the longitudinal resistance R_{xx} (gray) vanishes while the Hall resistance R_{xy} (black) is quantized at the value h/ie^2. Data obtained by Laura Sinclair.

Fig. 1.4 shows that as B is varied, regions around the integer filling factors $\nu = i$ are characterized by a vanishing longitudinal resistance R_{xx} and a Hall resistance R_{xy} that is quantized to values of h/ie^2. The quantization of R_{xy} is so exact that it is used as a resistance standard with the definition that $h/e^2 = 25812.807\ \Omega$. The quantization of R_{xy} also represents an unusual way of measuring the fine structure constant $\alpha = e^2/\hbar c \approx 1/137$. The data in Fig. 1.4 are clearly much different than the prediction of the classical Drude theory, that $R_{xx} = constant$ and $R_{xy} = B/ne$.

A full explanation of the IQHE is difficult and lengthy; see refs. [3,4]. Briefly, the essential ingredients for the observation of the IQHE in a 2DES are LL formation, low temperatures, and disorder. The formation of LLs has already been discussed, and low temperatures $k_B T << \hbar\omega_c$ are necessary for the LLs to be resolved. (A typical cyclotron gap is $\hbar\omega_c / k_B = 20$ K at 1 T.)

Disorder in any real 2DES is inevitable, and its primary effect is to broaden the delta-function density of states of each LL, as shown in Fig. 1.5. Furthermore, the states within each LL may be classified into two categories. On the tails of the LLs, the states are *localized*; they cannot carry electric current across a sample. In the center of the LLs, the states are *extended*; they can carry current.

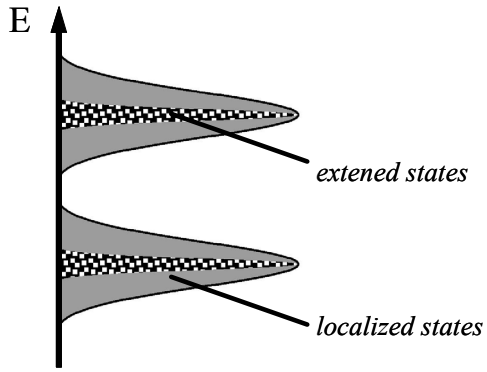

Figure 1.5: Two LLs broadened by disorder. Extended (conducting) and localized (insulating) states exist in the center and on the flanks of the LLs, respectively.

The formation of localized and extended states can be understood by modeling the disorder as a smoothly varying potential landscape of hills and valleys within the 2DES.

When the Fermi level lies in the low-energy tail of a LL, the electrons are confined to isolated valleys or pockets throughout the sample. This situation is shown schematically in Fig. 1.6a. The Fermi level electrons in the localized pockets carry a *circulating* current with an orientation determined by the sign of B.

As the Fermi level moves upward into the central region of a broadened LL, the potential valleys within the 2DES are filled up until a percolation threshold is reached. At that point, the "shorelines" of where the electrons fill the potential landscape become very long and percolate across the whole sample. This is shown in Fig. 1.6b. Rather than being confined within isolated pockets, the electrons extend across great distances and can easily scatter from one shoreline to another. These are the extended states at the center of the LLs. Note that the sample boundaries are essentially very steep potential profiles, along which electrons circulate in so-called "edge states."

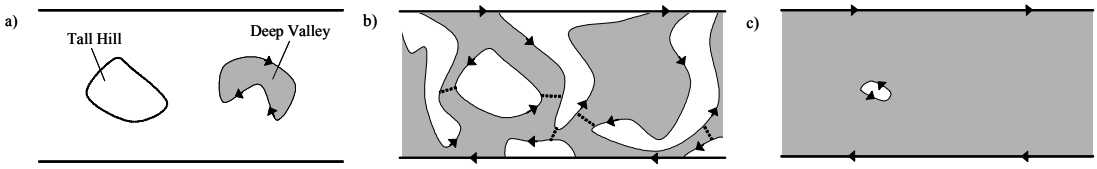

Figure 1.6: a) When the Fermi level lies below the center of a LL, the electron states are localized within potential valleys. b) When the Fermi level lies near the center of a LL, the electron states are extended and carry current through the 2DES. c) When the Fermi level lies above the center of a LL, the bulk electron states are localized, but edge states still carry current.

For even higher Fermi levels, the only unoccupied electron states in the bulk of the 2DES are at the very peaks of the potential topography. The electrons at the Fermi level circulate around these peaks and are thus localized again. Unlike where the Fermi level lies below the center of the LL, however, the localized bulk electron states are not the only states at the Fermi surface: the edge states still remain on the sample boundaries.

The phenomena associated with the IQHE follows from this picture of localized and extended states. When a single LL is partially filled with electrons only in its low-energy localized states, no current can conduct through the sample and that LL's contribution to the total conductivity is $\sigma_{xx} = \sigma_{xy} = 0$. When the Fermi level lies in the center of the LL, it possesses finite σ_{xx} and σ_{xy}. Finally, when the Fermi level lies above

the center of the LL, $\sigma_{xx} = 0$ because the bulk electron states at the Fermi level are localized and do not participate in the conduction of current. However, there are still current-carrying edge states at the sample boundaries. These edge states are chiral (i.e. they circulate in one direction), one-dimensional current-carrying channels, and therefore the Landauer-Buttiker formalism for 1D conduction can be applied [3]. Consequently, the contribution to conductivity of a filled (or nearly-filled) LL is $\sigma_{xx} = 0$ and $\sigma_{xy} = e^2/h$.

For many filled LLs, their contributions to the total conductivity add in parallel. When the net conductivity is then inverted to yield a resistivity, the result is that as the Fermi level passes through a LL, ρ_{xx} changes from zero to a finite value and back to zero again. Over the same range, ρ_{xy} changes from h/ie^2 to h/je^2, where the total number of filled LLs changes from i to j. This behavior of ρ_{xx} and ρ_{xy} can be clearly seen in Fig. 1.4, where the Fermi level is continuously adjusted by varying B at a fixed electron density. At the values of B where R_{xy} is quantized and R_{xx} is zero, the Fermi level resides in a LL's tail of localized states. When R_{xy} is not quantized and R_{xx} is finite, on the other hand, the Fermi level resides in the central region of the valence LL.

A crucial point about the explanation given for the IQHE is that interaction effects among the electrons were totally ignored. Indeed, the IQHE is inherently a *single-particle phenomenon*, whose ingredients are LL quantization and disorder in the 2DES. The next section will illustrate that some amazing new physics can appear in the quantum Hall regime when the interactions between electrons play a leading role in their behavior.

1.2.3 Quantum Transport: the Fractional Quantum Hall Effect

A major goal of early 2DES research in the quantum Hall regime was to probe the so-called extreme quantum limit, where only the lowest LL is occupied, i.e., where $\nu < 1$ [5]. Theoretical work had indicated that in this regime the 2D electrons would form a "Wigner solid" by arranging themselves on the vertices of a triangular lattice. This configuration was believed to minimize the interaction energy of the 2DES due to the repulsive Coulomb interaction.

A challenge in reaching the extreme quantum limit in the early 1980s was finding a 2DES of sufficiently low density and high mobility. The low density is necessary in

order to reach the regime of $\nu < 1$ at experimentally accessible magnetic fields of ~20 T (recall that $\nu = hn/eB$). On the other hand, lower density 2DESs tend to have lower mobilities and are easily localized by too-strong disorder even in the absence of B. A major breakthrough in developing low density, high-mobility samples came with the invention of the modulation doping technique in the growth of GaAs/AlGaAs heterostructures using molecular beam epitaxy (MBE). Details of this technique will be given in Section 2.1. In 1981, Gossard and Wiegmann used the modulation doping method to grow a sample with an electron density of $n = 1.23 \times 10^{11}$ cm^{-2} and an extremely high mobility (for the time) of $\mu = 90{,}000$ cm^2/Vs. (By comparison, growth technology has now advanced to the point where similar density samples have mobilities that are more than two orders of magnitude larger.)

Using this sample, Tsui and Stormer performed magnetotransport measurements up to magnetic fields corresponding to $\nu \approx 1/4$ [6]. To their astonishment, they observed what appeared to be the usual IQHE signature of a vanishing R_{xx} and a quantized R_{xy}, except that these features appeared around the filling factor $\nu = 1/3$, and the quantized value of R_{xy} was $3h/e^2$. This was the first observation of the fractional quantum Hall effect (FQHE). According to the IQHE theory, the vanishing of R_{xx} and the quantization of R_{xy} requires that the Fermi level lies in a gap between LLs. But no gap exists at $\nu = 1/3$ according to the single-particle picture, and Stormer and Tsui speculated that the transport signature might somehow be an indication of the sought-after Wigner solid.

The Wigner solid explanation turned out to be incorrect. Instead, the origin of the FQHE was shown by Laughlin [7] to be the formation of an extraordinary correlated quantum fluid in two dimensions, now called the "Laughlin liquid." One of its most remarkable aspects is how elegantly it may be described by the many-body wavefunction:

$$\Psi_3(r_1, r_2, \ldots r_N) = \prod_{i>j} (z_i - z_j)^3 \exp\left[-\sum_i |z_i|^2\right].$$

Here, the coordinate z_i refers to the *ith* electron located at a position (x,y) where $z = x + iy$. By forming a Laughlin liquid, the electrons at $\nu = 1/3$ filling are able to avoid each other particularly well—better than in the static Wigner solid—and thus minimize their

interparticle Coulomb repulsion. This property comes from the fact that Ψ rapidly approaches zero as the position of the *ith* and the *jth* electrons come close to one another. In addition, the exponent of 3 in the product ensures that Ψ is antisymmetric under an interchange of particles as required for Fermions.

Subsequent to Tsui, Stormer, and Gossard's initial discovery, the steady improvement in sample quality has allowed a plethora of other more delicate FQHE states to be discovered. Fig. 1.7 contains an example of transport data from a modern high-quality sample.

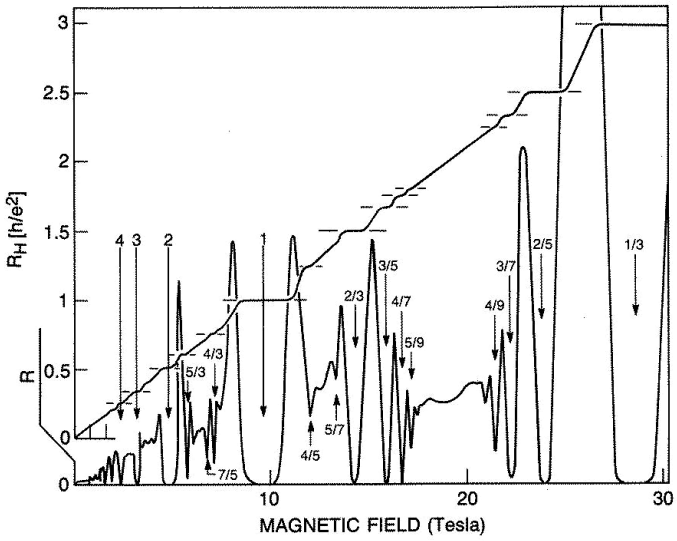

Figure 1.7: The fractional quantum Hall effect (FQHE) in a high-mobility 2DES. Like the IQHE, the FQHE exhibits vanishing R_{xx} and quantized R_{xy}, but these occur at certain fractional filling factors and the Hall resistance is quantized to a rational fraction of h/e^2. The FQHE states exist almost exclusively in the $N = 0$ LL and are inherently a many-body effect. Adapted from ref. [8].

Except for the integer filling factor points, each of the deep minima in R_{xx} and plateaus in R_{xy} signify a different FQHE state. These features always occur at filling factors ν that are rational fractions p/q, and the Hall resistance is quantized at the value $(q/p)h/e^2$. Most of these states can be accounted for using a hierarchical scheme or through the composite Fermion picture [9]. Note that all the FQHE states in Fig. 1.7 occur at filling factors $\nu < 2$, where the electrons occupy only the $N = 0$ LL. At very low temperatures and in very clean 2DESs, much more delicate FQHE states have also been

found in the $N = 1$ LL. These include one at $\nu = 5/2$ which is not readily accounted for by a Laughlin-type wavefunction and is the subject of ongoing investigation.

The reason the experimental signatures of the Laughlin liquid formation are so similar to those of the IQHE is that in both cases the Fermi level lies in an energy gap in the density of states of the 2DES. In the case of the IQHE, that energy gap comes from the spacing of the LLs. For the FQHE, the gap corresponds to the excitation energy required to make many-body quasiparticles in the Laughlin liquid. A fascinating aspect of these quasiparticles is that they are *fractionally charged*. In the case of the $\nu = 1/3$ FQHE, that charge is $e/3$—reminiscent (probably coincidentally) of quark physics! Investigations of the FQHE have produced advances in a rich variety physics concepts such as fractional quantum numbers, fractional statistics, skyrmions, composite particles, and chiral Luttinger liquids. Some FQHE theories have even been used by physicists probing the connection between quantum mechanics and gravity [10]. In 1998, Laughlin, Stormer, and Tsui were awarded the Nobel Prize in physics for the discovery of the FQHE.

1.2.4 The FQHE: Is That All?

Twenty years after its discovery, the FQHE remains an active research area, but by no means is it the last example of correlated electron physics in two dimensions. For instance, two fields showing intense recent activity are studies of the purported metal-to-insulator transition at zero magnetic field [11] and investigations of strongly coupled quantum Hall bilayers [12].

A third example of new many-body electron physics in two dimensions is the subject of this thesis. In 1996, Fogler et al. [13] and Moessner and Chalker [14] proposed that unlike in the $N = 0$ and $N = 1$ LLs, where FQHE physics dominates, electrons in the higher LLs should form into various CDW phases. Initially, this proposal was skeptically received because similar calculations pointing to a Wigner solid at $\nu < 1$ turned out to be incorrect. But experimentally, Willett and Eisenstein (since the late 1980s) and Stormer and colleagues (since the early 1990s) had known that the transport properties of very high-quality samples showed some unusual features in the $N = 2$ LL. At that time,

however, little attention was paid to their significance. In 1998, intrigued by a possible connection between the new CDW theory of high LLs and the old unresolved transport characteristics, we decided to look more closely at the transport properties of the latest generation high-mobility 2DESs. To our surprise, the transport results produced dramatic evidence for new many-body electronic phases in high LLs with properties that are consistent with the predictions of the CDW theory. From this research, a general new understanding of interaction physics in the quantum Hall regime has emerged. The following chapters describe the results of our investigations in detail.

---

1 See any elementary text on solid state physics, such as C. Kittel, *Introduction to Solid State Physics* (John Wiley, New York 1996).

2 K. von Klitzing, G. Dorda, and M. Pepper, Phys. Rev. Lett. **45**, 494 (1980).

3 J.H. Davies, *The Physics of Low-Dimensional Semiconductors* (Cambridge University Press, Cambridge 1998).

4 S.M. Girvin, *The Quantum Hall Effect: Novel Excitations and Broken Symmetries* in *Topological Aspects of Low Dimensional Systems*, ed. A. Comtet, T. Jolicoeur, S. Ouvry, F. David (Springer, Berlin 2000); also at http://xxx.lanl.gov/abs/cond-mat/9907002.

5 H.L. Stormer, Rev. Mod. Phys. **71**, 875 (1999).

6 D.C. Tsui, H.L. Stormer, and A.C. Gossard, Phys. Rev. Lett. **48**, 1559 (1982).

7 R.B. Laughlin, Phys. Rev. Lett. **50**, 1395 (1983).

8 J.P. Eisenstein, H.L. Stormer, Science **248**, 1510 (1990).

9 D. Yoshioka, *The Quantum Hall Effect* (Springer, Berlin 2002).

10 S.-C. Zhang and J. Hu, Science **294**, 823 (2001).

11 S.V. Kravchenko, G.V. Kravchenko, J.E. Furneaux, V.M. Pudalov, M. D'Iorio, Phys. Rev. B **50**, 8039 (1994).

12 See article by J.P. Eisenstein in *Perspectives in Quantum Hall Effects*, ed. S. Das Sarma and A. Pinczuk (John Wiley, New York, 1997).

13 M.M. Fogler, A.A. Koulakov, and B.I. Shklovskii, Phys. Rev. B **54**, 1853 (1996); A.A. Koulakov, M.M. Fogler, and B.I Shklovskii, Phys. Rev. Lett. **76**, 499 (1996).

14 R. Moessner and J.T. Chalker, Phys. Rev. B **54**, 5006 (1996).

Chapter 2:
Experimental Materials and Methods

2.1 GaAs/AlGaAs Heterostructures

2.1.1 Band Structure and the 2DES

Two-dimensional electron systems (2DESs) are created by confining electrons to a suitable surface or interface [1]. One way of doing this is by using an electric field to hold a sheet of electrons onto a flat insulating substance, such as liquid helium. A more common technique is to restrict the 2DES to an interface between a semiconductor and an insulator or between two different semiconductors. An example of the semiconductor-insulator 2DES is the metal-oxide-semiconductor field-effect transistor, or MOSFET, and it is the basis of modern electronics. A 2DES in a silicon MOSFET was used in the discovery of the IQHE in 1980, but the quality of these systems has only moderately improved since then. The most convenient measure of a 2DES's quality is its electron mobility, and the mobility is limited by processes that scatter electrons. At temperatures above ~10 K, electron-phonon scattering is dominant. The highest mobilities are achieved at temperatures near absolute zero where the scattering primarily comes from impurities or imperfections in the 2DES host material. In the case of MOSFETS, the highest low-temperature mobility yet achieved is roughly 80,000 cm^2/Vs. This number is limited by the inherent roughness of and the impurities contained within the glassy oxide layer confining the 2DES to the Si surface.

A superior method of confining a 2DES utilizes the much smoother interface between two semiconductor crystals. The most common such system is the modulation-doped GaAs/$Al_xGa_{1-x}As$ heterostructure grown by molecular beam epitaxy (MBE). In MBE, extremely pure elemental material is evaporated from furnaces onto a heated substrate in an ultrahigh vacuum environment, and virtually perfect crystalline material may be grown layer by atomic layer. GaAs and AlGaAs are ideal semiconductors for use

in heterostructures because they share the same crystal structure, and their lattice constants are equal to within a fraction of a percent. As a result, the interface between these two materials can be extremely smooth and defect-free.

Another important feature of GaAs/AlGaAs interfaces is the alignment of their bandgaps. The bandgap of GaAs is about 1.4 eV, while that of the most commonly used alloy $Al_{0.24}Ga_{0.76}As$ is roughly 1.7 eV. (For simplicity, AlGaAs is used as a substitute for the more accurate formula $Al_xGa_{1-x}As$; in the heterostructures referred to in this thesis, the aluminum concentration is $x = 0.24$.) While the Fermi level of the composite system will be equal across the interface of the two materials, a discontinuity in the conduction and valence band energies will exist at the interface. This discontinuity is primarily determined by a combination of the different bandgaps and electron affinities of GaAs and AlGaAs. The result is that the conduction band of GaAs lies about 0.19 eV below the conduction band of AlGaAs (see Fig. 2.1).

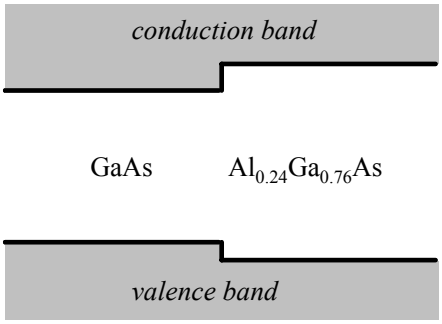

Figure 2.1: Alignment of conduction and valence bands at the interface of GaAs and AlGaAs.

With this conduction band offset, band structure engineering can be used to trap a 2DES at the interface between GaAs and AlGaAs. For example, Fig. 2.2a shows how a 2DES can be created at a single heterojunction of GaAs and AlGaAs. Because AlGaAs has a larger bandgap than GaAs, an n-doped region of AlGaAs will contribute some number of conduction electrons to an adjacent region of undoped GaAs. Once these electrons leave the AlGaAs, however, the charge imbalance from the ionized n-dopants (usually Si atoms) generates an electric field which bends the bands and creates a confinement potential for the conduction electrons in the GaAs region. In the case of the single-interface heterojunction shown in Fig. 2.2a, this confinement potential is

approximately triangular. At low temperatures, the electrons in the confining well fall into its lowest subband, and their motion becomes strictly two dimensional. (The subband separation is on the order of several tens of Kelvin.) Even though the electronic wavefunctions have a finite width in the **z** direction, typically ~10 nm, there is no freedom of movement outside of the x-y plane as long as the higher subbands of the confinement well remain unoccupied. Alternatively, a 2DES can become trapped in the quantum well heterostructure where two AlGaAs barriers form a symmetric sandwich structure to confine the 2DES. See Fig. 2.2b

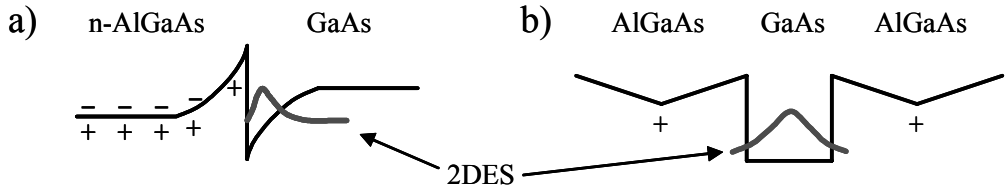

Figure 2.2: Two ways band structure engineering is used to confine a 2DES in GaAs/AlGaAs heterostructures. a) A single-interface heterojunction. b) A symmetric square quantum well.

A potentially important source of electron scattering in GaAs/AlGaAs heterostructures comes from the Si donor atoms that are responsible for generating the conduction electrons in the first place. A Si atom becomes positively charged when it gives up an electron to the conduction band, and such charged sites can strongly degrade the mobility of a 2DES. A major breakthrough in minimizing this scattering mechanism came with the invention of "modulation doping" by Stormer et al. [2]. In the variant of that technique known as "delta doping," the donor atoms are deposited during MBE into a single monolayer that is displaced from the 2DES by typically a few hundred Angstroms. In this way, the electrons of the 2DES and the ionized impurities that provide them are physically separated, and the scattering rate is significantly reduced. Note that the modulation doping technique is not possible in three-dimensional electron systems. This is the primary reason that electron mobilities in 2D far exceed those attainable in 3D systems. In addition to its use in scientific applications, modulation doping in GaAs/AlGaAs heterostructures is used in technologies such as cellular phone and radio telescope receivers.

Modulation doping is just one, albeit very important, ingredient in achieving high-quality 2DESs. Advances in MBE technology and expertise have also been crucial to improving 2DESs, and today the top crystal growers routinely achieve samples with low-temperature mobilities exceeding 10^7 cm^2/Vs. Our research group at Caltech is fortunate to have the MBE experts Loren Pfeiffer and Ken West of Bell Laboratories, Lucent Technologies, as close collaborators. They have supplied our laboratory with some of the best 2DES samples ever made, including a recently-grown quantum well heterostructure with a low-temperature mobility of roughly 3×10^7 cm^2/Vs. Using the Drude transport theory along with the measured electron density of $n = 3.0 \times 10^{11}$ cm^{-2}, this mobility corresponds to an extraordinary electron mean free path of ~300 μm!

Fig. 2.3 shows the schematic structure of a typical quantum well. From the bottom up, the sample begins with a thick GaAs substrate provided by a third-party manufacturer. Then a buffer of pure GaAs is grown, followed by a cleaning superlattice of hundreds of thin alternating layers of GaAs and AlGaAs for several microns. This superlattice planarizes the growth surface and traps background impurities. Next, the quantum well itself is grown, consisting of a few hundred nm of AlGaAs on either side of a 30 nm GaAs well. Two delta-doped layers of Si are also grown 80 nm away on either side of the quantum well. Finally, the structure is topped off with a thin 10 nm GaAs cap to prevent the oxidation of an exposed AlGaAs surface. In ultra-high-mobility structures such as this, modulation doping has eliminated the intentionally-placed donor atoms as a significant source of scattering. It is likely that unintentional background impurities in the AlGaAs ultimately limit the mobilities of such state-of-the-art samples.

Now the simplified band diagram of Fig. 2.2a can be revised to more accurately reflect the real band structure in a typical heterojunction 2DES. This is done in Fig. 2.4, and a generalization to quantum well structures is similar. The first thing to note about the band structure in Fig. 2.4 is that the Fermi level is determined by the high density of surface states on the GaAs surface and at the buried substrate interface. The surface states act as acceptors of charge and accumulate some fraction of the electrons provided by the dopant donor layer. This compensation process results in a downward slope of the conduction band from the surface to the donor layer. The other portion of the donors' charge is transferred to the GaAs/AlGaAs interface. The resulting electric field between

the donor layer and the single-interface heterostructure is approximately constant, and it creates a linear rise in the conduction band. The slope of the conduction band on the GaAs side of the band discontinuity is initially the same as for the AlGaAs side, but then the slope levels out as the delocalized charge of the electron layer is passed.

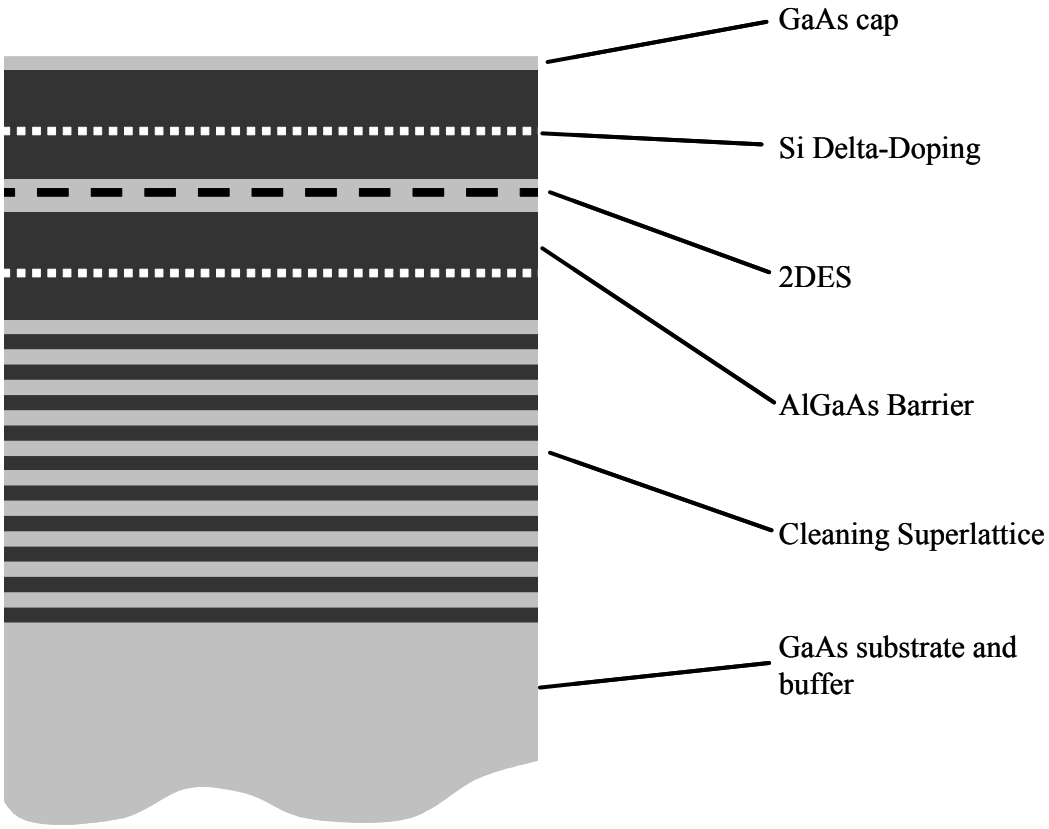

Figure 2.3: Schematic MBE structure of GaAs/AlGaAs wafer containing a 2DES in a symmetric square quantum well.

Finally, note from Fig. 2.4 that the conduction band at the donor layer typically lies only a small distance above the Fermi level. Therefore, if the system is too highly doped then the conduction band at the donor layer may dip below the Fermi level, and a second unwanted layer of electrons could form. If those electrons are sufficiently mobile, this may result in the phenomenon of "parallel conductivity" which plagues some of the samples that we study. When substantial parallel conductivity is present, the longitudinal resistivity of a 2DES does not reach zero around the integer filling factors of the IQHE.

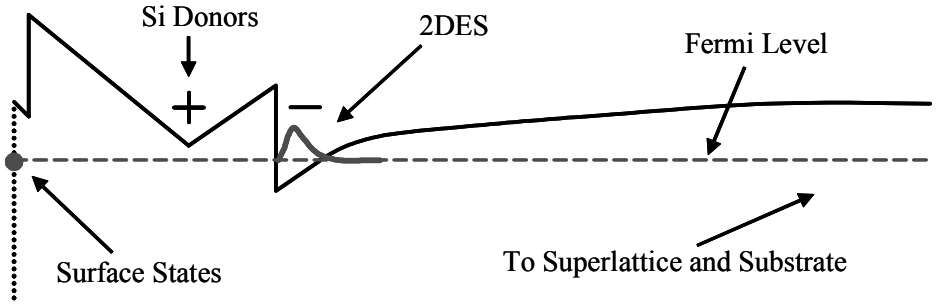

Figure 2.4: More detailed band diagram of 2DES confined to a single-interface heterojunction.

2.1.2 Crystal Axis Determination

The GaAs/AlGaAs heterostructure crystals are grown as two-inch diameter, 0.5 mm thick circular wafers. In the samples we use, the MBE conditions are set so that the growth direction is along the [001] GaAs crystal direction. GaAs and its lattice-matched alloy AlGaAs form a zinc-blende crystal structure with a cubic unit cell, shown in Fig. 2.5. Aside from the growth direction, the $[1\,\bar{1}0]$ and [110] crystal directions, which lie in the 2D plane of the electrons, require special attention.

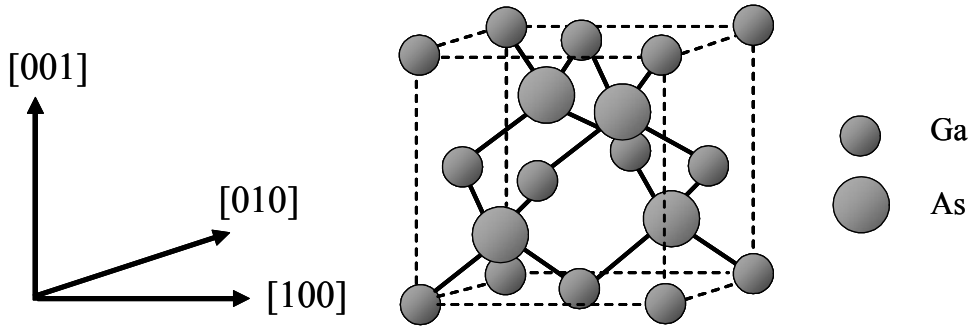

Figure 2.5: Unit cell and crystal axes of GaAs.

The first reason that $[1\,\bar{1}0]$ and [110] are important directions is that they point in the normal directions to the natural cleavage planes in a [001] GaAs wafer. When a sample is prepared for transport measurements, the first step is to cleave off a small

square piece of the parent wafer, typically 5 mm on a side. While wet etching is performed on some samples to define custom boundaries for the 2DES, most measurements are made on the bare cleaved squares. A second reason that these two directions are relevant is that they will turn out to be the principal axes of anisotropy in the high Landau level regime.

An unaided visual inspection of a GaAs crystal will not reveal any differences between the $[1\bar{1}0]$ and $[110]$ directions, and therefore determining these directions must be done by other means. One method is to look for a "major flat" of the original wafer. The major and minor flats refer to what appear to be cleaved sections in two orthogonal directions near the boundary of the circular wafer. This is shown schematically in Fig. 2.6, and the length of the major flat is longer than the minor one. These flats come from the original GaAs substrate used in the MBE growth process. The direction normal to the major flat points along $[1\bar{1}0]$ while the direction normal to the minor flat points along $[110]$, as determined through x-ray analysis by the original wafer manufacturer.

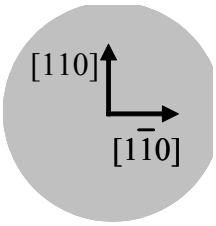

Figure 2.6: Crystal axes determination using wafer flat method. The major flat, at right, is perpendicular to the $[1\bar{1}0]$ direction.

Relying on the major and minor flats to determine the crystal axes of a given wafer can be problematic because we often receive only portions of wafers without knowing where the flats lie. Also, the orientation of the major and minor flats may not be known for samples that have already been cleaved from their parent wafer. Therefore, we almost always use alternative methods of determining the $[1\bar{1}0]$ and $[110]$ directions. One method is to perform a wet etch of a small portion of the wafer surface and examine the etch profiles in the different directions [3]. Processing details are given in Appendix A. Fig. 2.7 contains sketches of the etch profiles for the two relevant crystal directions.

For the etch boundary along $[1\bar{1}0]$, the etch digs an undercut with a distinctive notch shape. For a boundary along $[110]$, on the other hand, a gradual slope runs up the side of the resulting mesa.

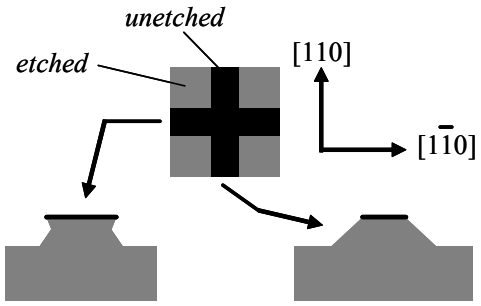

Figure 2.7: Anisotropic etching of [001] GaAs surface. The black cross represents a mask, and gray regions are exposed to the etch. The resulting etch profiles, shown at the bottom, depend on the direction of the in-plane crystal axes.

Because the etch depths are typically only a few microns, microscopy must be used to distinguish between the different profiles. High-magnification optical microscopy can be used if a sample is carefully cleaved through the etch boundary. A photograph of a typical cross-section is shown in Fig. 2.8a, where a notch etch profile reveals that the $[1\bar{1}0]$ direction lies out of the plane of the page. Alternatively, a scanning electron microscope (SEM) can be used to image the etch profile without a need to cleave the sample. As Fig. 2.8b shows, the SEM can clearly distinguish between the two etch profiles and thus determine the crystal directions of the sample.

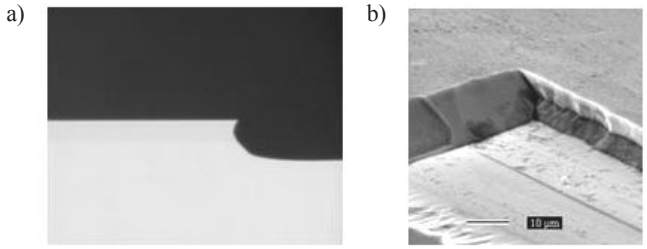

Figure 2.8: a) Optical microscope photograph of the notch-shaped etch profile resulting from a wet etch of a (001) GaAs surface. The notch-shaped profile indicates that the direction out of the plane of the page is $[1\bar{1}0]$. b) Scanning electron microscope image showing the two etch profiles resulting from etching through a corner of a mask; both the notch and the sloped profiles can be seen.

The third—and simplest—method of determining the crystal axes in MBE-grown $[001]$ GaAs heterostructures is to find certain telltale growth defects on the wafer surface using an optical microscope. The first surface defect we use is known as a "bowtie" defect because of its distinctive shape. Between about one and a few microns in size, the bowtie defects are always oriented in the same way with respect to the crystal axes: the direction along the length of the bowtie is $[110]$. A second structure with a consistent orientation is dubbed a "closed eye" defect. Often resembling the shape of a closed eye, this defect is circular or oval, also only a few microns in diameter, and has a line pointing along $[1\bar{1}0]$ running through it. Optical microscope images of the bowtie and closed-eye defects are shown in Fig. 2.9. These defects are generally randomly distributed over the wafer surface, and their coverage density can vary widely. On some wafers, neither type of defects can be found; on others, their coverage can be as high as several per cm^2. To our knowledge, the bowtie and closed-eye defects on GaAs have not been reported in the literature. However, bowtie-type defects have been reported on ZnSe surfaces [4], and certain "oval defects" with definite orientations have been observed on GaAs surfaces [5,6].

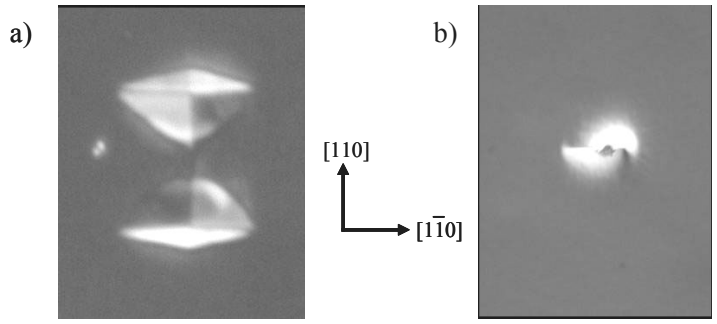

Figure 2.9: Optical microscope images of the a) bowtie and b) closed-eye defects that are common on GaAs surfaces. Their orientations determine the crystal directions as shown.

2.2 Sample Preparation and Measurement

2.2.1 Defining and Electrically Contacting the 2DES

The usual steps of sample preparation for the experiments described in this thesis are as follows: 1) cleavage from the parent wafer; 2) an optional mesa definition using a wet etch; and 3) diffusion of ohmic contact material into the 2DES. The wet etch recipe is described in Appendix A.

A sample begins as a cleaved square, usually 5 mm on a side. If a custom 2DES boundary such as a Hall bar is desired, the sample is etched using photolithography, as shown in Fig. 2.10a. Ohmic electrical contacts to the 2DES are then made by heat-diffusing high-purity indium at 425° C for 5-10 minutes from the sample surface into the region containing the 2DES. The indium is applied by hand with a soldering pencil. Square samples are made with eight indium contacts placed at the corners and midpoints of the sample perimeter, as shown schematically in Fig. 2.10b. Fig. 2.10c contains photo of the 5 × 5 mm sample F-2 with eight indium contacts. Samples will be denoted by a letter-number code; sample A-1, for example, refers to the #1 piece cleaved from the parent wafer labeled “A.”

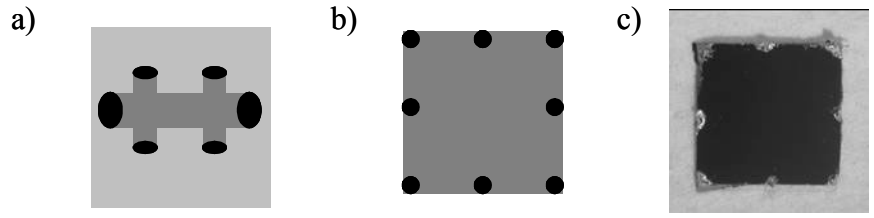

Figure 2.10: a) Schematic diagram of contact placement (black ovals) on a typical Hall bar mesa (dark gray) formed by etching the GaAs sample surface (light gray). b) Schematic diagram of typical contact placement for square samples. c) Photograph of a 5 mm square sample with eight indium contacts hand-placed along its perimeter.

2.2.2 Transport Measurement Technique

Longitudinal resistance measurements of 2DESs form the core of this thesis. In square samples, these transport measurements are made using the contact configuration shown in Fig. 2.11, where a current is driven between opposite side contacts while the voltage is measured across two adjacent corner contacts. Dividing the voltage by the current yields the longitudinal resistance. Two types of such longitudinal resistance measurements in square samples can be made depending on the direction of current flow within the square. For the rest of this thesis, the notation R_{xx} and R_{yy} will refer to the longitudinal resistance corresponding to current flow along $[1\,\bar{1}0]$ and $[110]$, respectively. In other words, $[1\,\bar{1}0]$ will refer to the **x** direction, while $[110]$ will refer to the **y** direction (see Fig. 2.11). For Hall resistance, or R_{xy}, measurements, voltage contacts on opposite sides of the current flow are used.

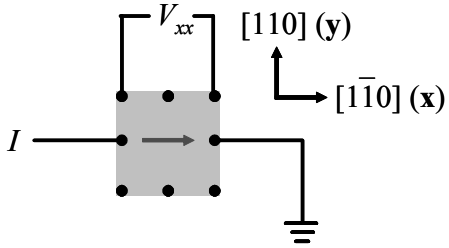

Figure 2.11: Schematic of the contact configuration for a four-terminal longitudinal resistance measurement on a square sample with eight contacts. Current is passed through opposing side midpoints while the voltage probes make contact to two adjacent corner contacts.

These four-terminal resistance measurements are made with the conventional lock-in amplifier technique shown in Fig. 2.12. A quasi-dc 13 Hz voltage is passed through a large resistor, typically 10 MΩ, to become a current source. For low-temperature magnetotransport measurements, currents in the range 2 to 20 nA are used. These currents have been empirically determined to be sufficiently small that no detectable ohmic heating of the 2DES occurs. They are also small enough that nonlinearities in the *I-V* curves are negligible, so that the resistance measurement remains in the linear response regime. The voltage detection is done with an averaging time of 0.3-3 seconds, depending on the signal-to-noise ratio desired and on how quickly the signal is varying because of a changing *B* or *T*. Most measurements were performed with a model 124A lock-in amplifier from EG&G/Princeton Applied Research, although a Stanford Research Systems SR830 was occasionally used.

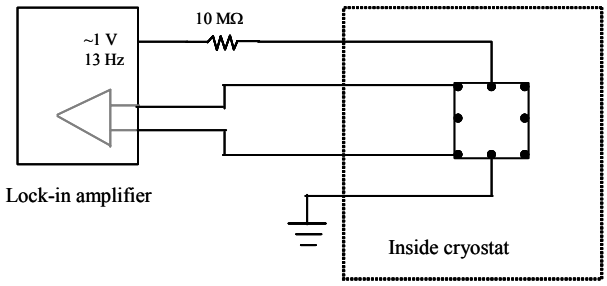

Figure 2.12: Schematic circuit diagram of lock-in amplifier measurement of longitudinal resistance of a square sample. The quasi-dc measurement is typically made at 13 Hz with a current bias of 2-20 nA.

2.2.3 Determining the Density and Mobility of a 2DES

The density of a 2DES may be measured in one of two ways. First, the slope of a sample's Hall resistance versus B line yields the 2DES density through the relationship $R_{xy} = B/ne$. At low temperatures, however, this relationship fails for magnetic fields larger than ~0.5 T, when Landau quantization effects become important. More commonly, the density of a 2DES is determined using the $1/B$-periodic oscillations of the longitudinal resistance in the IQHE. Recall from Section 1.2 that the minima of these so-called Shubnikov-de Haas (SdH) oscillations are located at integer filling factors $\nu = i = hn/eB$. By fitting a line to a sequence of (i,B^{-1}) points where low-field the resistance minima occur, the density n can be determined.

A sample's electron mobility is determined through the formula $\mu = 1/ne\rho$, where ρ is the zero-field resistivity of the 2DES. (The mobility is not well defined at nonzero magnetic fields.) While the resistivity can be measured trivially in long thin geometries where the current flow can be safely assumed to be uniform between voltage probes, in other geometries, such as squares, the "van der Pauw" technique must be used [7]. In that technique, various four-terminal resistances are measured among any four contacts on the perimeter of a 2DES, and then these resistances are plugged into a universal function to yield the resistivity.

2.2.4 Cooling and Rotating the Samples

Temperatures less than 150 mK are necessary to access the new physics described in this thesis, and an Oxford 200 TL dilution refrigerator was used to cool our samples to those low temperatures. This ^{3}He-^{4}He dilution refrigerator has a specified cooling power of 200 μW at 100 mK, and its base temperature is roughly 15 mK. The refrigerator temperature was measured with an Oxford calibrated carbon resistor using an ac resistance bridge. A photograph of the dilution refrigerator's internal components is shown in Fig. 2.13. During operation, the parts of the refrigerator shown in Fig. 2.13 are sealed in a vacuum can which is surrounded by a liquid helium bath.

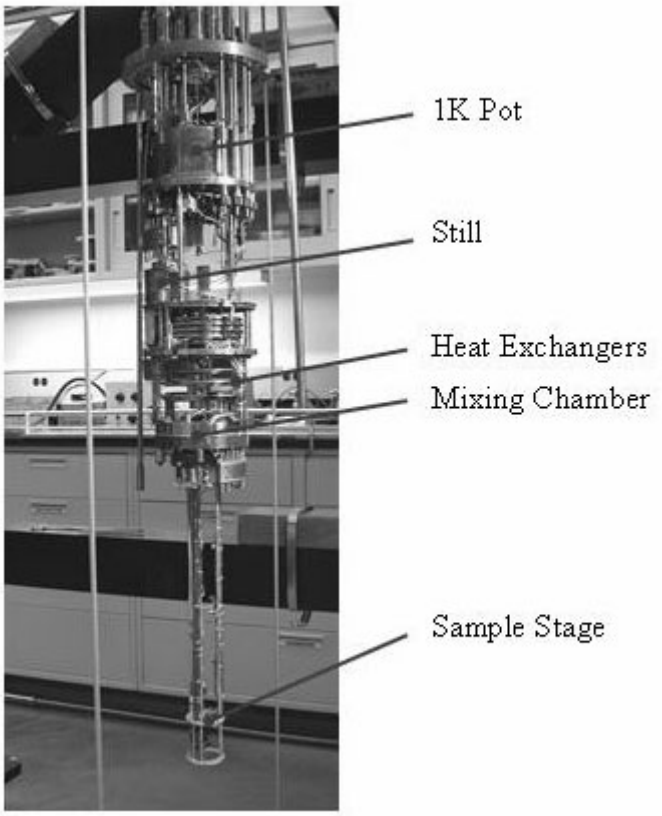

Figure 2.13: Photograph of inside of dilution refrigerator showing important componenets.

A detailed description of the principles of dilution refrigeration can be found in ref. [8], but briefly, the main stages of the refrigerator shown in Fig. 2.13 are

1) The 1K pot, where a reservoir of ^{4}He is pumped on and cooled to ~1.5 K in order to condense the 3He gas being recycled into the refrigerator.
2) The still, which operates at ~0.7 K and where ^{3}He is evaporated into a circulation pump at room temperature.
3) The heat exchangers, where ^{3}He leading to and exiting from the mixing chamber is allowed to thermally equilibrate.
4) The mixing chamber, where concentrated ^{3}He "evaporates" into into a dilute mixture of ^{3}He in ^{4}He. The refrigeration occurs through the latent heat of this evaporation, and the mixing chamber attains the lowest temperature in the refrigerator.

5) The silver sample stage, which extends into the superconducting solenoid magnet core and which is thermally sunk to the mixing chamber.

The 4K helium bath of the dilution refrigerator contains a 14/16 Tesla superconducting solenoid magnet that surrounds the sample stage. During measurements, magnetic field ramp rates must be kept low in order to prevent sample heating from eddy currents in the refrigerator's metal structures. Typical ramp rates are 0.001 T/min at the refrigerator's base temperature, 0.015 T/min at $T = 25$ mK, 0.05 T/min at 50 mK, and 0.1 T/min at 100 mK or higher.

The 2DES samples are secured to the sample stage of the dilution refrigerator in one of three ways. First, they were wired up to plastic-bodied circuit headers, which are then inserted into sockets on the sample stage. Second, they were wired to a gold-plated silver sample mount that attaches to the bottom of the sample stage shown in Fig. 2.13. The wire leads of this sample mount subsequently led to one of the sockets on the sample stage. Third, the samples were wired to a similar gold-plated silver sample mount that was customized to have a rotating paddle, as will be described below.

In each case, the sample contacts were attached to twisted pairs of wire (copper and manganin) that led out of the refrigerator to a room-temperature break-out box. Between the sample stage and room temperature, these wires were heat-sunk at the mixing chamber, the "50 mK plate" below the still, the 1K pot, and at 4 K either by running them across pads on copper laminate strips or by wrapping them many times around copper posts. Such care was taken in heat-sinking the wires because they are directly connected to the cold 2DES. Furthermore, we rely on the sample leads to provide the main thermal connection between the 2DES and the mixing chamber. Often, the extra precaution was taken to connect ~500 pF Mylar capacitors between the sample leads and the silver sample platform. To attain the lowest possible 2DES temperatures, it is important to provide this thermal sinking in close proximity to the samples. In the case of the gold-plated silver sample mounts we used, the 500 pF capacitors were combined with in-line 10 kΩ thin-film resistors in a low-pass configuration. This was done in an effort to minimize any high-frequency signals that might run down the wires and heat up the 2DESs.

An issue that plagues any low-temperature physics experiment in a 2DES is whether the electrons remain in thermal equilibrium with the refrigerator down to its lowest temperatures. Unfortunately, we have no direct method of verifying that the 2DES temperature is the same as the refrigerator temperature. However, we are reassured that the electrons are in good thermal contact with the mixing chamber because the *transport physics* of our best-quality 2DESs continue to evolve and exhibit new phenomena down to the lowest refrigerator temperatures attainable. A very dramatic example of this was obtained recently involving the very delicate FQHE states in the $N = 1$ LL. As shown in Fig. 2.14, the Hall resistance of sample K-1 (to be described further in Chapter 3) between the $\nu = 3$ and $\nu = 4$ IQHE states is almost featureless at a refrigerator temperature of 50 mK. However, as T is lowered to the base temperature of ~15 mK, the R_{xy} versus B trace continuously and dramatically evolves and a great deal of structure emerges, including plateaus indicating FQHE states at $\nu = 16/5$, 7/2, and 19/5. The physics responsible for the features in Fig. 2.14 are not the subject of this thesis; instead, a detailed account of the data can be found in ref. [9].

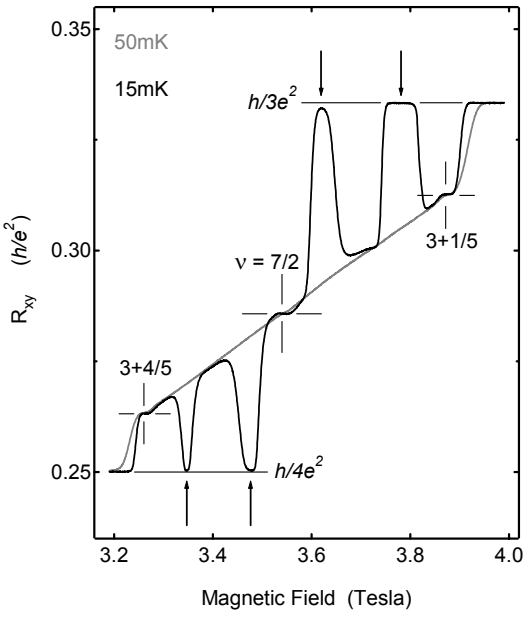

Figure 2.14: Hall resistance measurement surrounding the filling factor $\nu = 7/2$ in sample K-1. The dramatic increase in structure between 50 mK and 15 mK indicates that the 2DES is thermally grounded to the mixing chamber of the dilution refrigerator.

The magnetic field axis of the superconducting solenoid magnet in our system is fixed to point perpendicular to the plane of a 2DES lying flat on the sample stage. But occasionally it is desirable to introduce an adjustable magnetic field in the plane of a 2DES (see Chapters 8 and 9). To do this, we utilize a sample mount built by Ian Spielman that contains a rotating paddle (see Fig. 2.15). The paddle is held at some angle by a spring acting against a taut Kevlar string leading through a vacuum seal to room temperature. The paddle may be rotated *in situ* to any angle between -8° and +90° by pulling on the string with a linear motion feedthrough. The angles are typically determined with an uncertainty less than 1° by using a Hall probe installed perpendicular to the paddle to measure the strength of the in-plane field.

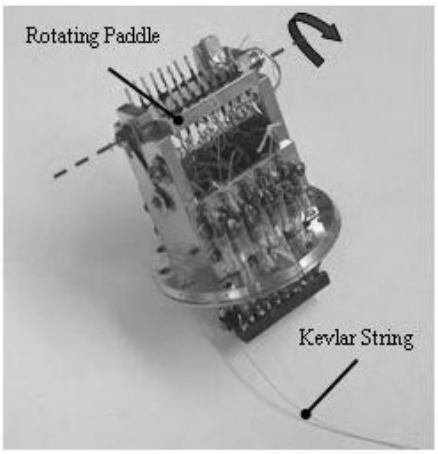

Figure 2.15: Photograph of the sample stage containing a rotating paddle. The rotation of samples allows an in-plane magnetic field to be applied.

2.2.5 Sample Illumination

Unless otherwise noted, all the magnetotransport measurements reported in this thesis were performed after a brief low-temperature illumination of the 2DES with a GaAs (red) light-emitting diode (LED). In the most common procedure, the sample is illuminated for 60 seconds during the cool-down process once the temperature reaches about 1.6 K. The LED is situated anywhere from one to a few cm away from the sample, and it is activated with about 1 mA of current.

The purpose of illumination is to improve the mobility and magnetotransport characteristics of a 2DES using the effect of persistent photoconductivity (PPC), which refers to the permanent increase in the low-temperature conductivity of 2DESs after illumination. PPC arises from a combination of the interaction of the light with "DX centers" in the doped AlGaAs layers and through the generation of particle-hole pairs in GaAs. The DX, or deep donor, sites occur when the substitution of a Si donor atom for a Ga atom is accompanied by a strain in the surrounding lattice. Unlike the normal hydrogenic donor configuration of Si donors, which have ionization energies of ~50 K, the electrons trapped in DX centers are confined with energies of ~150 K. As a result, a substantial number of would-be donor electrons remain trapped in the DX centers upon cooling to low temperatures. During illumination, the DX centers are converted into regular substitutional donors and their electrons can be transferred to the potential well of the 2DES. The photoexcited electrons may also help redistribute the residual charge in the dopant layer, and the conversion of the DX centers to normal hyrdogenic impurities may reduce the overall crystal strain near the 2DES. In general, the net result of illumination is an increased 2DES density and mobility.

However, in some cases the experimental consequences of illumination are unpredictable. For example, in one sample we studied, a 60-second illumination was found to cause severe parallel conductivity, while a 1-second illumination improved the transport quality. In another sample, the opposite situation occurred. In a third sample, the illumination was found to improve its transport characteristics but *reduce* its density. In a fourth, it was found that the transport was improved after illumination at 1.6 K by warming the sample to 2.2 K overnight before cooling further. Generally, the effect of illumination is more consistent in single-interface heterojunctions than in quantum wells (see Section 3.2). Thus, while PPC is an effective tool in improving the transport quality of 2DESs, some trial-and-error experimentation may be necessary in order to take full advantage of it.

---

1 For an overview of modern low-dimensional electron systems, see J.H. Davies, *The Physics of Low-Dimensional Semiconductors, an Introduction* (Cambridge University Press, Cambridge 1998).

2 H.L. Stormer, R. Dingle, A.C. Gossard, W. Wiegmann, and M.D. Sturge, Solid State Commun. **29**, 705 (1979).

3 Sadao Adachi and Kunishige Oe, J. Electrochem. Soc. **140**, 2427 (1983).

4 G. von Freymann, D. Lueren, C. Rabenstein, M. Mikolaiczyk, H. Richter, H. Kalt, Th. Schimmel, and M. Wegener, Appl. Phys. Lett. **76**, 203 (2000).

5 M. Bafleur, A. Munoz-Yague, and A. Rocher, Journal of Crystal Growth **59**, 531 (1982).

6 K. Fujiwara, K. Kanamoto, Y.N. Ohta, Y. Tokuda, and T. Nakayama, Journal of Crystal Growth **80**, 104 (1987).

7 L.J. van der Pauw, Philips Res. Rep. **13**, 1 (1958).

8 F. Pobell, *Matter and Methods at Low Temperatures* (Springer, Berlin 1996).

9 J.P. Eisenstein, K.B. Cooper, L.N. Pfeiffer, and K.W. West, Phys. Rev. Lett. **88**, 76801 (2002).

Chapter 3:
Anisotropic Transport in High Landau Levels

3.1 Basic Phenomenology of Anisotropic Transport

3.1.1 General Transport in a High-Mobility 2DES

Sample B-1 is a 5 mm cleaved square containing a high-mobility 2DES in a single-interface heterojunction. After illumination, the sample's low-temperature density and mobility were measured to be $n = 2.68 \times 10^{11}$ cm^{-2} and $\mu = 9 \times 10^{6}$ cm^2/Vs. The high quality of sample B-1 is evident in other ways besides its outstanding mobility. For example, Fig. 3.1 shows that at $T = 25$ mK the onset of Shubnikov de Haas (SdH) oscillations occurs at magnetic fields of only $B \approx 55$ mT, or equivalently, at a filling factor of $\nu \approx 200$. That such small magnetic fields are sufficient to resolve the Landau quantization suggests that the disorder-broadening of the LLs is very small. (The thermal broadening at 25 mK is negligible compared to the LL spacing at 55 mT of $\hbar\omega_c / k_B \approx 1$ K.) Note that in Fig. 3.1, the frequency of resistance oscillations doubles at $B \approx 130$ mT, signaling the spin-splitting of the LLs around $\nu \approx 83$.

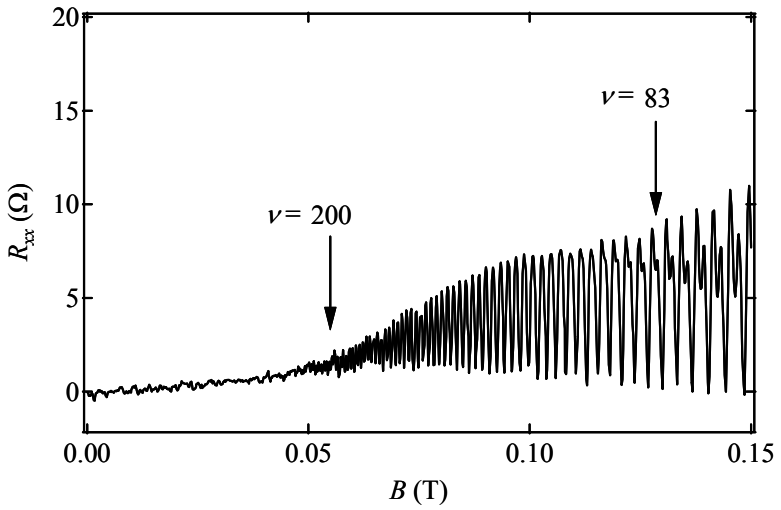

Figure. 3.1: Onset of SdH oscillations in sample B-1 at $T = 25$ mK. The disorder is so low that LLs can already be resolved by ~50 mT, or $\nu = 200$. The spin-splitting of the LLs occurs around $\nu = 83$.

Fig. 3.2 shows the longitudinal resistance R_{xx} from this sample over a broad range of magnetic fields $0 < B < 10$ T a 150 mK. At low magnetic fields $B < 2$ T, R_{xx} exhibits SdH oscillations. Once the magnetic field passes about 2 T, R_{xx} begins to show additional structure between the adjacent IQHE states where the longitudinal resistance vanishes. For example, in the $N = 2$ LL, where $4 < \nu < 6$, R_{xx} shows several extra "bumps and wiggles" around the $\nu = 9/2$ and 11/2 filling factors. This structure cannot be accounted for by the standard model of the IQHE in disorder-dominated systems, which predicts that the resistance should show a simple peak between integer quantum Hall states [1]. Electron interactions are already playing a role already by the third $N = 2$ LL.

At higher fields, evidence for electron correlations at 150 mK becomes even more pronounced. Significant structure appears in R_{xx} around filling factors $\nu = 5/2$ and 7/2 between about 2.8 and 5.5 T, and for fields $B > 5.5$ T, FQHE states begin to proliferate. For example, the 5/3 and 4/3 states surrounding the $\nu = 3/2$ structure are particularly well developed—another indication of the high sample quality. Although not shown, even higher magnetic fields would reveal more FHQE states, including the famous $\nu = 1/3$ state. The FQHE states above 5.5 T correspond to situations where the electrons occupy only the $N = 0$ LL. FQHE states occur in the $N = 1$ LL as well, but lower temperatures are required to detect them.

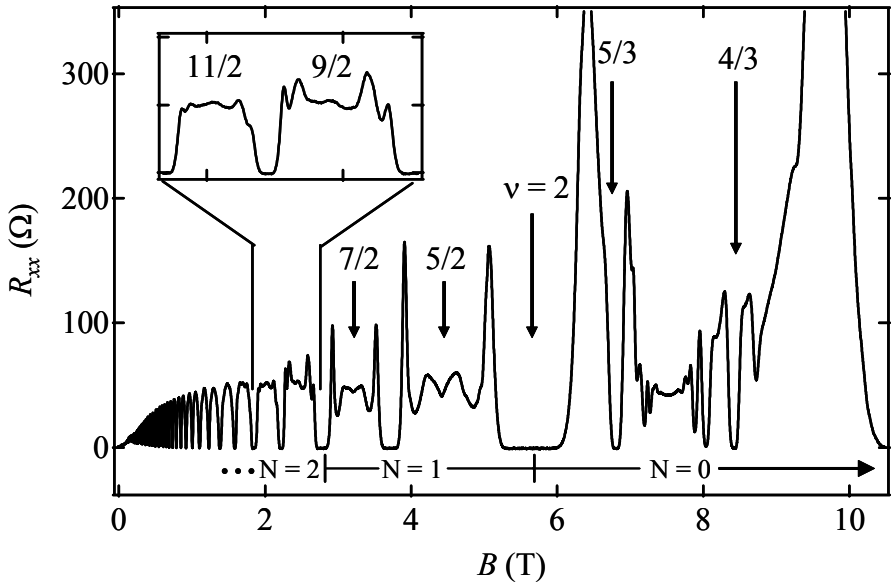

Figure 3.2: Longitudinal resistance at 150 mK in sample B-1. FQHE states are common in the lowest $N = 0$ LL. Structure in R_{xx} between IQHE states suggests that correlations are important into the $N = 2$ LL as well.

3.1.2 Low Temperature Transport and Anisotropy

Fig. 3.3 displays R_{xx} around the $\nu = 5/2$ structure at about 15 mK, the base temperature of our dilution refrigerator. In contrast to the 150 mK data, at this low temperature deep minima in R_{xx} signify that FQHE states exist at $\nu = 7/3$, 5/2, and 8/3. One might guess that FQHE states occur in the $N = 2$ LL as well because of the substantial structure evident there at 150 mK (Fig. 3.2). However, Fig. 3.4 demonstrates that a much more surprising feature appears in the low temperature transport in high LLs. Fig. 3.4 displays longitudinal resistance versus magnetic field at 25 mK. Unlike the previous figures, however, both R_{xx} and R_{yy} are displayed. As Section 2.2 explained, these resistances correspond to net current flowing along $[1\bar{1}0]$ and $[110]$, respectively. Thus, other than a 90° reorientation of the current and voltage contacts, the R_{xx} and R_{yy} data in Fig. 3.4 were taken under *identical* conditions.

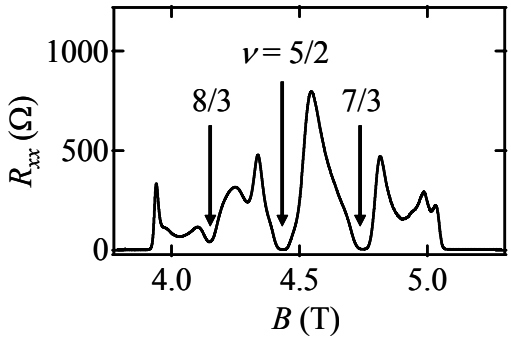

Fig. 3.3: Low-temperature $T = 15$mK structure of R_{xx} in the lower spin branch of the $N = 1$ LL. FQHE states at $\nu = 8/3$, 5/2, and 7/3 cause R_{xx} to approach zero.

For low fields $B < 0.75$ T and for high fields $B > 2.8$ T, R_{xx} and R_{yy} in Fig. 3.4 are roughly the same; the transport is relatively isotropic. The slightly larger values of R_{yy} over these magnetic field ranges is inconsequential and probably comes from inhomogeneities in the sample's resistivity. (The mechanism by which resistivity inhomogeneities affect resistance measurements will be discussed in depth in Chapter 6.) Although not shown in Fig. 3.4, isotropic transport is also observed for the $N = 0$ LL.

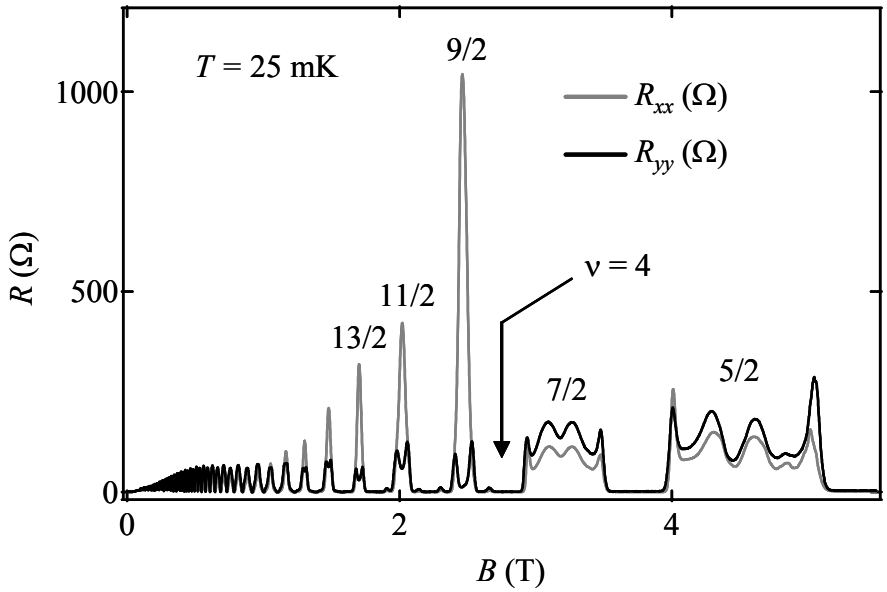

Figure 3.4: Magnetotransport of sample B-1 at 25 mK showing R_{xx} (gray) and R_{yy} (black). A dramatic anisotropy in longitudinal resistance develops only around the half-filling points of high LLs: at $\nu = 9/2$, 11/2, 13/2, etc.

In contrast, beginning abruptly in the third $N = 2$ LL and continuing into the next several higher LLs, R_{xx} and R_{yy} display a huge and striking anisotropy that is largest at the half filling points of the high LLs, i.e., at the filling factors $\nu = 9/2$, 11/2, 13/2, etc. For current flowing along $[1\bar{1}0]$ (the hard direction), large peaks in resistance occur around these half-filled LLs. For current flowing along [110] (the easy direction), deep valleys are observed. The strength of the anisotropy is greatest at $\nu = 9/2$ where the ratio R_{xx}/R_{yy} is about 80, and then it gradually diminishes over the next few half-filled LLs and disappears once $N = 5$. This remarkable anisotropy exists only around the half-filling points of the LLs for which $N \geq 2$. In the lower LLs, no similar resistance anisotropies develop at low temperatures.

The resistance anisotropy in half-filled high LLs is a low-temperature phenomenon that develops rapidly below about 150 mK. Fig. 3.5 shows how the anisotropy grows around $\nu = 9/2$ as the temperature is lowered from 200 mK to 25 mK. At 200 mK, R_{xx} and R_{yy} are virtually identical through $\nu = 9/2$, reaching about 50 and 60 Ω at half-filling, respectively. At 100 mK, however, a small peak has started to develop around $\nu = 9/2$ in R_{xx}, while a small dip in R_{yy} appears. The peak in R_{xx} grows to over 300 Ω by 80 mK, and by 25 mK it exceeds 1000 Ω. On the other hand, the minimum in R_{yy} drops gradually throughout the same temperature range until it is less than 3 Ω at 25 mK. A more detailed analysis of how the anisotropy develops with temperature will be presented in Section 3.4.

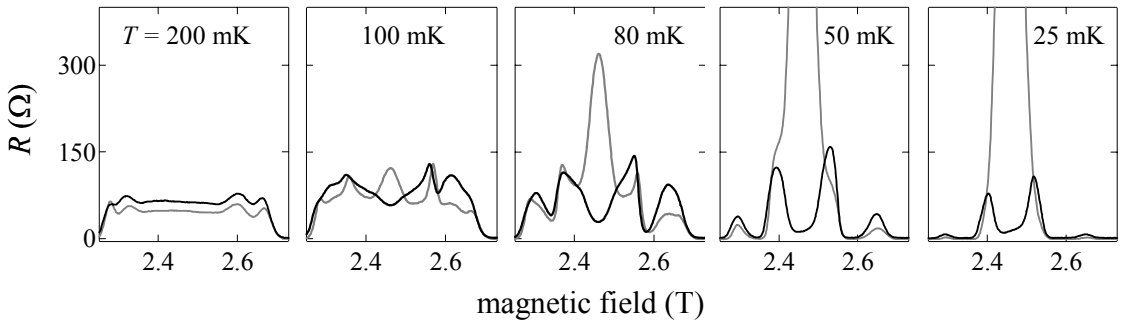

Figure 3.5: The development of anisotropic transport in sample B-1 around $\nu = 9/2$ as the temperature is lowered from 200 mK to 25 mK. Gray: R_{xx}; black: R_{yy}.

To test whether the $[1\bar{1}0]$ and $[110]$ directions are the principal axes of anisotropy, complementary longitudinal resistance measurements were made in sample B-1 with the net current flowing along the two diagonals of the square (the [100] and [010] directions). The two contact configurations and the corresponding transport results at 80 mK are shown in Fig. 3.6. Also shown are the conventional R_{xx} and R_{yy} measurements, where a large anisotropy is evident. Even though the resistance values along the sample's diagonals differ somewhat at $\nu = 9/2$, the anisotropy is weak and neither trace shows a deep minimum at half-filling. These results are not affected by either a reversal of the magnetic field direction nor by thermally cycling the sample to room temperature. Therefore, we conclude that the resistance anisotropy in sample B-1 has a twofold symmetry with principal axes that lie along the $[1\bar{1}0]$ and $[110]$ directions of the host GaAs heterostructure.

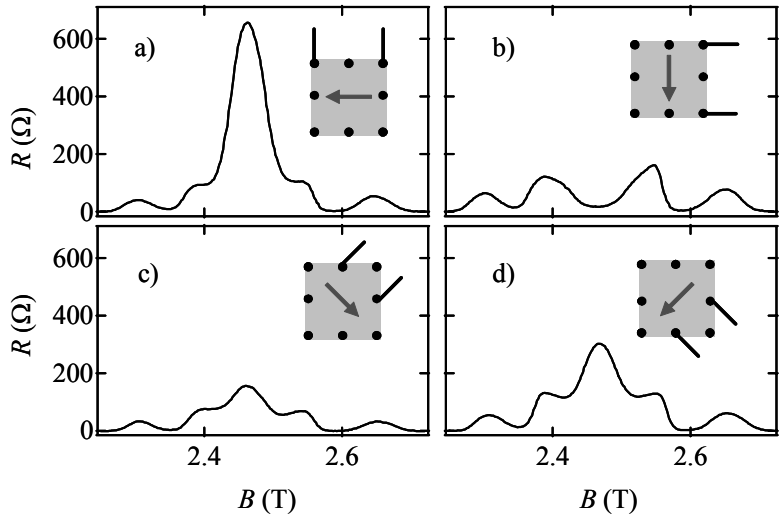

Figure 3.6: Longitudinal resistance of sample B-1 at $T = 80$ mK and $\nu = 9/2$. The contact configurations are shown in the insets with the arrows indicating the current flow direction and the lines indicating the voltage probes. a) Current along $[1\bar{1}0]$ (R_{xx}); b) current along $[110]$ (R_{yy}); c) current along $[100]$; d) current along $[010]$. While a) and b) show a strong anisotropy at half-filling, b) and c) do not.

While the large peak in R_{xx} in half-filled high LLs does not fit the conventional picture of a FQHE state where the longitudinal resistance vanishes isotropically, the deep minimum in R_{yy} is reminiscent of the FQHE. Therefore, the possibility of fractional quantum Hall physics in the anisotropic transport regime needs to be checked by

examining the Hall resistance for plateau formation. Fig. 3.7 shows both R_{xx} and R_{yy} versus filling factor through the $\nu = 9/2$ structure at 25 mK, along with two traces of the Hall resistance R_{xy}. The two R_{xy} traces correspond to current flow along $[1\,\bar{1}0]$ and $[110]$, although there is no substantive difference between the them. Note that unlike in the other data so far, these resistance traces are plotted versus filling factor $\nu = hn/eB$. The well-developed anisotropy in R_{xx} and R_{yy} can be seen to occur over a filling factor region $4.38 < \nu < 4.60$. Importantly, in this filling factor range there is no plateau in the Hall resistances that would indicate the formation of any FQHE state with $R_{xy} = h/\nu e^2$, and in fact there is very little structure in R_{xy} at all. Similar results are obtained for higher half-filled LLs, and therefore we conclude that there is no evidence that a FQHE state is somehow responsible for the anisotropic transport observed in these special regions.

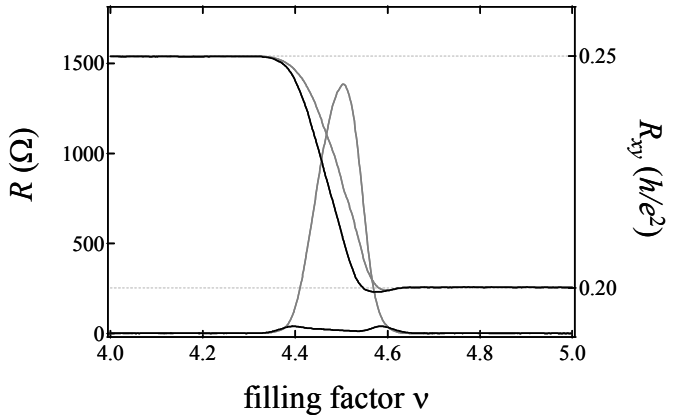

Figure 3.7: Longitudinal and Hall resistance of sample B-1 at $T = 25$ mK versus filling factor in the range $4 < \nu < 5$. R_{xx} (gray) and R_{yy} (black) show the usual low-temperature anisotropy. The two Hall traces were taken with average current flow along $[1\,\bar{1}0]$ (gray) and $[110]$ (black). No FQHE plateaus are evident.

3.1.3 Summary: Anisotropic Electronic Phases

In summary, this section has shown that huge resistance anisotropies develop around the half-filling points of excited LLs at low temperatures. These transport anomalies *cannot* be accounted for using the single-particle theory of the IQHE. Rather, the low temperatures and very clean systems required to observe these new effects point to a collective, many-body origin. The spontaneous development of an anisotropic electronic phase is inconsistent with the physics of the FQHE as well. The Laughlin liquid

represents an *isotropic* quantum fluid, and no evidence of fractional Hall resistance quantization exists in high LLs. Finally, the transport anisotropies are not consequences of any gross peculiarities of the 2DES or the measurement process. The anisotropies vanish by only ~150 mK, and they are totally absent anywhere except around half-filling of the $N = 2$ and several higher LLs. Therefore, these observations constitute dramatic evidence for new collective phases of 2D electrons that are generic to high LLs.

The discovery of new many-body electronic phases in excited LLs significantly changes the broad picture of 2DES physics in the quantum Hall regime. Prior to these experiments, it was widely believed that while the FQHE dominates the $N = 0$ and $N = 1$ LLs, the LLs $N \geq 2$ are too strongly affected by disorder to exhibit many-body effects. Furthermore, it was thought that if clean enough 2DESs could be made, then FQHE physics would be observed in those higher LLs as well. The observation of anisotropic transport in high LLs shows that this is not the case. In very clean samples, a distinct boundary exists at $N = 2$. Below that point, FQHE physics is the rule. Above it, anisotropic electronic phases prevail at least until $N = 4$ before disorder effects set in. The bulk of the research presented in this thesis is devoted to uncovering the nature of these new many-body states in high LLs.

3.2 Sample Survey: High LL Transport Below 150 mK

3.2.1 Wafers where Anisotropic Transport Is Observed

Table 3.1 contains a chart of all the wafers we have examined that show the high-LL anisotropic transport phenomena exhibited by sample B-1. Along with the wafer code, Table 3.1 lists the wafers' post-illumination density and mobility, and type of heterostructure (single-interface heterojunction or square quantum well).

Wafer	Density	Mobility	Heterostructure
A	2.3	7	HJ
B	2.7	9.0	HJ
C	2.1	16	HJ
D	2.6	10	HJ
E	2.0	4.4	HJ
F	1.5	11	HJ
G	2.1	9.2	HJ
H	2.5-2.9	23	QW
J	2.3	4	HJ

Table 3.1: A list of those samples showing the anisotropic transport phenomenon in high LLs. Units of density and mobility: 10^{11} cm^{-2} and 10^{6} cm^{2}/Vs. HJ = single-interface heterojunction; QW = square quantum well.

Fig. 3.8 shows low-temperature R_{xx} and R_{yy} transport data of samples taken from the nine wafers of Table 3.1. The data in Fig. 3.8 were obtained either at 50 mK or 25 mK, and in all cases the samples were 4 or 5 mm squares with eight contacts on their perimeters. The data in the panels of Fig. 3.8 cover a filling factor range $4 < \nu < 6$, which includes the $\nu = 9/2$ and $\nu = 11/2$ structures. Note that for each of the nine samples, the R_{xx} and R_{yy} traces exhibit essentially the same characteristics as those of sample B-1 that were discussed in Section 3.1. Albeit with differing strengths, each sample in Fig. 3.8 shows that for current flowing along $[1\bar{1}0]$, a peak in the longitudinal resistance occurs around $\nu = 9/2$ (and often $\nu = 11/2$); for current along $[110]$, a minimum is seen.

In none of the wafers were comparable anisotropies observed in the $N = 0$ or $N = 1$ LLs. This is significant because it rules out the possibility that there is a magnetic field threshold where the 2DES begins exhibiting anisotropic transport features. For example, the anisotropic transport of B-1, shown in Fig. 3.4, commences below about 2.8 T. In the low-density sample F-1, on the other hand, the anisotropies only appear below about 1.6

T, as shown in Fig. 3.8f. In all samples, the determining factor for the onset of anisotropic transport is that $N \geq 2$.

The data of Fig. 3.8 show that resistance anisotropies are observed in samples possessing a diversity of other characteristics. For example, both single-interface heterojunctions and quantum wells exhibit anisotropic transport. So do samples with mobilities down to at least 4×10^6 cm^2/Vs. The anisotropy is not restricted to samples grown by a single MBE machine, either. While eight of the samples of Fig. 3.8 were grown by Pfeiffer and West of Bell Laboratories, sample G-1 was grown by Werner Wegscheider using a separate MBE machine at the Walter Schottky Institute in Munich. Furthermore, other research groups have reported the same basic anisotropic transport phenomena in high LLs [2,3,4], although some of these groups may have been using samples from the same wafers listed in Fig. 3.8. In one case, high-LL transport anisotropies were reported in a two-dimensional *hole* system [5].

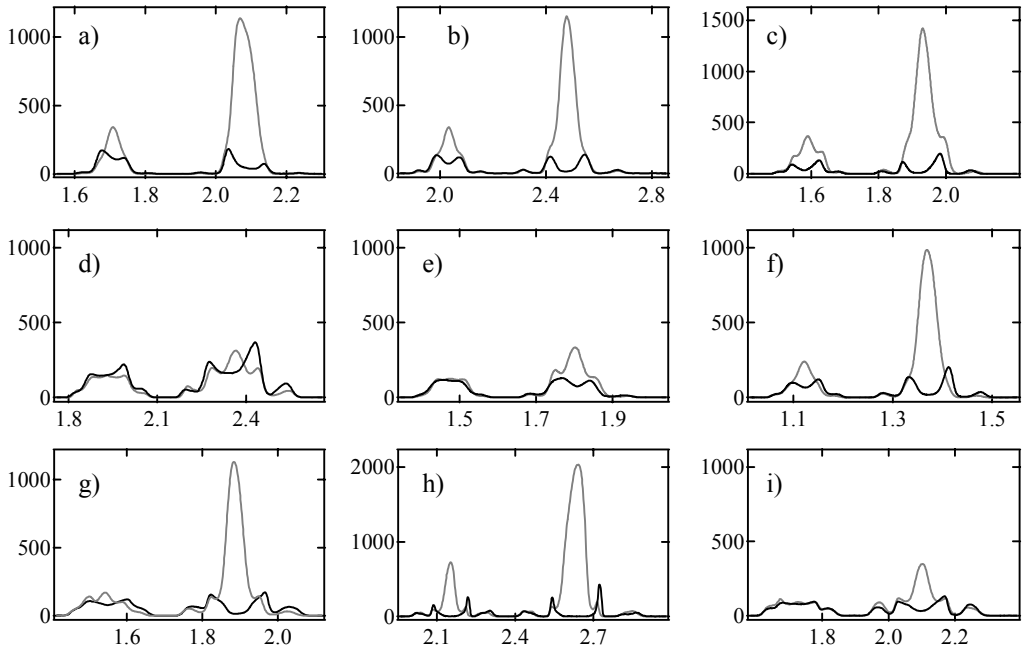

Figure 3.8: Low temperature transport R_{xx} (gray) and R_{yy} (black) in Ohms versus B (Tesla) through the $\nu =$ 9/2 and ν = 11/2 structures for a variety of samples and low temperatures: a) sample A-3, T = 25 mK; b) B-1, 50 mK; c) C-8, 25 mK; d) D-1, 50 mK; e) E-2, 25 mK; f) F-1, 25 mK; g) G-1, 50 mK; h) H-1, 50 mK; i) J-2, 50 mK.

Finally, we note that when multiple samples from the same wafer are investigated, the transport characteristics are consistent with one another. Thus there is strong evidence that the anisotropy is not a peculiarity restricted to one wafer or one sample. It is a generic transport feature in the high LL regime of high quality samples.

3.2.2 The Role of High Mobilities

The data of Fig. 3.8 show a wide variety of anisotropy strengths, and some of this diversity can be attributed to the samples having varying electron mobilities. For example, the sample D-1 ($\mu = 10 \times 10^6$ cm^2/Vs) shows only a weak anisotropy at $\nu = 9/2$ and $T = 50$ mK. At $\nu = 11/2$ the anisotropy is even less prominent. In contrast, Fig. 3.8h contains data from the extremely high mobility quantum well H-1 ($\mu = 23 \times 10^6$ cm^2/Vs). In that case, R_{xx} at $\nu = 9/2$ exceeds 2000 ohms at 50 mK, while R_{yy} vanishes to within the experimental uncertainty of ~1 Ω. At $\nu = 11/2$, the anisotropy is still very strong. The large discrepancy between the two samples is likely attributable to the more than a factor of two difference in their mobilities. However, the degree of anisotropy in high LLs is not strictly correlated with a sample's mobility. For example, the sample B-1 has a comparable mobility (and density) to D, yet it shows a much stronger anisotropy in high LLs (see Fig. 3.8b) at 50 mK.

Meanwhile, no anisotropic transport is observed if the mobility gets too low. Fig. 3.9 shows 50 mK R_{xx} and R_{yy} transport data from sample M-1, which has a mobility of only $\mu = 2.6 \times 10^6$ cm^2/Vs. In this case, no anisotropy in R_{xx} and R_{yy} exists in the high LL regime. In the $N = 1$ LL, the features around $\nu = 5/2$ and $\nu = 7/2$ also show significantly less structure than in sample B-1. The minimal amount of structure over all magnetic fields in this sample is typical of low mobility samples.

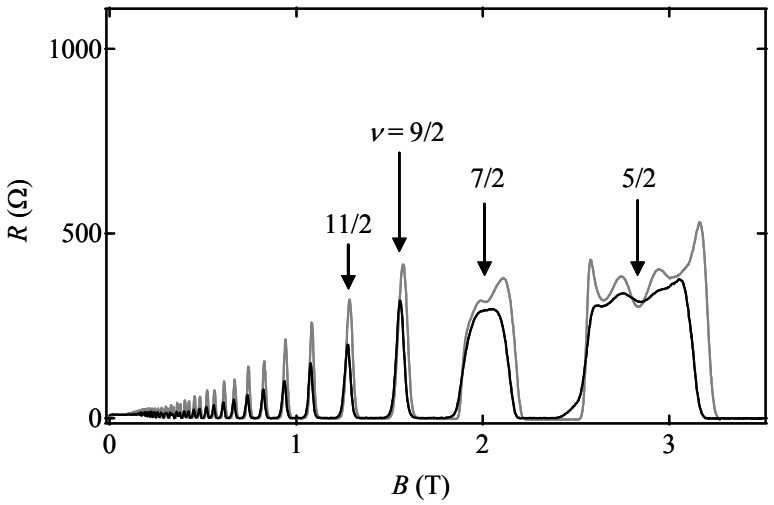

Figure 3.9: Longitudinal resistance R_{xx} and R_{yy} at 50 mK in the low-mobility sample M-1. Anisotropic transport in high LLs is not present.

3.2.3 Reproducibility of Transport Characteristics

The qualitative characteristics of the high LL transport anisotropies remain unchanged over repeated cool-downs of a given sample, but thermal cycling to room temperature can produce some small quantitative differences. Fig. 3.10 shows two examples of how the $\nu = 9/2$ structure at 25 mK changes between cool-downs. In Fig. 3.10a and b, R_{xx} and R_{yy} transport data are shown from the sample B-1 from two different cool-downs (solid and dashed traces). Clearly, the existence of the anisotropy, with the usual orientation, is unaffected by thermal cycling. Plus, the transport features differ only slightly in the two cases. The solid traces show a larger anisotropy, with the peak in R_{xx} being about 10% larger than in the dashed trace, and the valley in R_{yy} reaching as low as 14 Ω, compared to about 23 Ω in the dashed trace. Although those changes result in a substantial increase in the anisotropy ratio R_{xx}/R_{yy} (because $R_{yy} << R_{xx}$), the qualitative features of the $\nu = 9/2$ transport in the two cool-downs are the same. This example is typical of most of the samples we have measured.

Some samples show more variability, however. Fig. 3.10c and d contain R_{xx} and R_{yy} transport data from two cool-downs of the quantum well sample H-1, and this time

the differences between the two runs (solid and dashed traces) are more substantial. Most obviously, the 2DES density in the two cases differ by ~10% (2.6 and 2.9 × 10^{11} cm^{-2} for the dashed and solid traces, respectively). Also, in the dashed R_{xx} trace the $\nu = 9/2$ structure is more asymmetric, with the peak appearing to "lean" toward high fields. The peak height of the dashed trace is also substantially larger than the solid one. The R_{yy} data of this sample also show differences in their magnitudes and their symmetry about $\nu = 9/2$. These differences in the sample H-1 are an extreme example of how the transport characteristics change after thermal cycling, and such differences have only been observed in the quantum well heterostructures H-1 and K-1. (It is unclear why quantum wells show a greater variability of transport characteristics compared to single-interface heterojunctions; they are also more easily damaged by errant static electricity.) Nonetheless, the overall features of anisotropic transport in high LLs remains unaltered despite changes in the details of the transport characteristics in even the most extreme cases.

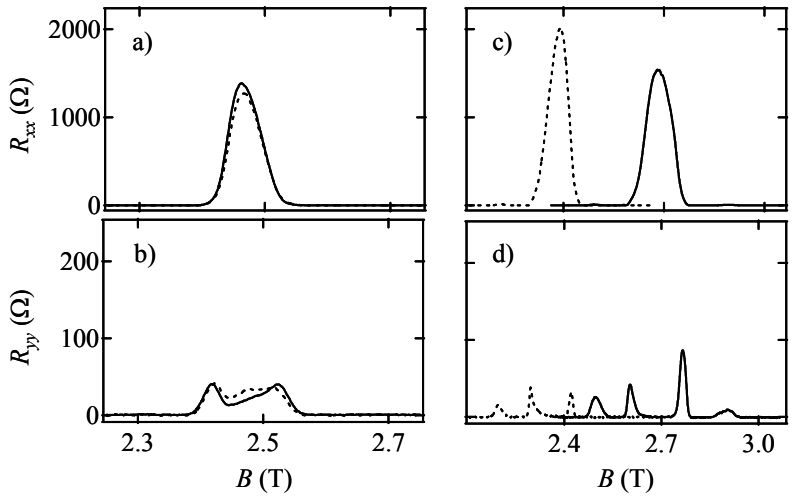

Figure 3.10: The variability of transport characteristics around $\nu = 9/2$ between cool-downs (solid versus dashed traces). a) R_{xx} in sample B-1; b) R_{yy} in sample B-1; c) R_{xx} in sample H-1; d) R_{yy} in sample H-1.

3.2.4 Effect of Illumination

Low temperature illumination, described in Section 2.2, is often essential in order to obtain high enough quality 2DESs for the observation of anisotropic transport in high LLs. Fig. 3.11 shows an example of the effect of illumination on sample B-1. In Fig. 3.11a, R_{xx} and R_{yy} versus B are shown after the sample is cooled down to 50 mK in the dark. Even though the temperature is very low, no significant anisotropy or other structure exists in the high LL region $\nu > 4$. Also, the amount of structure around $\nu = 7/2$ and 5/2 is suppressed.

After the data in Fig. 3.11a were taken, the sample was warmed to ~1.6 K, illuminated with a red LED for 1 minute, and then cooled again to 50 mK. The subsequent transport data is shown in Fig. 3.11b. Now there is a pronounced 50 mK resistance anisotropy at half-filled high LLs. The $\nu = 7/2$ region also shows significantly more structure, indicating that the quality of the 2DES improved in a global sense, and that the consequence of the illumination is not restricted to only the high LL regime. The illumination also increased the density in this sample from 2.48×10^{11} cm^{-2} to $n = 2.67 \times 10^{11}$ cm^{-2}.

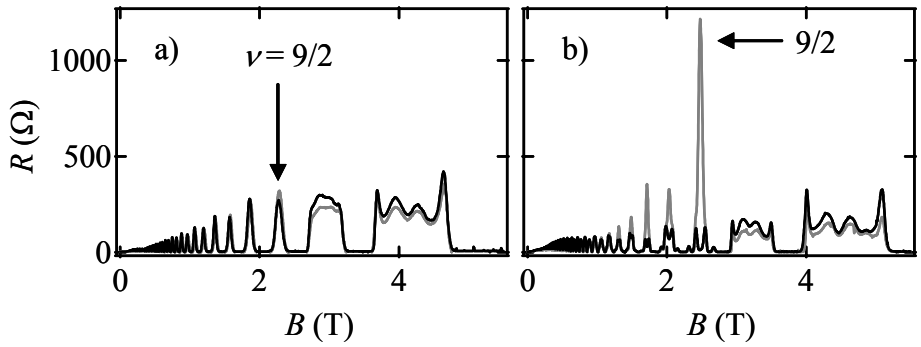

Figure 3.11: R_{xx} (gray) and R_{yy} (black) in sample B-1 at 50 mK before (a) and after (b) illumination with a red LED. Transport quality improves and resistance anisotropies appear only after illumination.

The effect of illumination outlined above for the sample B-1 is essentially the same for the other single-interface heterojunctions we have examined. For the quantum well samples, on the other hand, the picture is more complicated. Fig. 3.12 shows the effect of illumination on the sample H-1. This time, when cooled down in the dark to 50

mK, Fig. 3.12a shows that the resistance anisotropies in high LLs do exist (and are oriented in the usual way). Significant structure is also seen through $\nu = 7/2$ and 5/2. This observation is an indication of the very high quality of the 2DES in the sample H-1.

After following the standard procedure of warming to 1.6 K, illuminating for 1 minute, and then cooling back to 50 mK, the transport in the sample again changes significantly, as Fig. 3.12b indicates. The main effect of illumination is that the resistance anisotropy in several high LLs becomes much stronger. Also, the onset of SdH oscillations occurs around 0.2 T after illumination, compared to 0.5 T beforehand. Both of these facts indicated that the illumination improved the quality of the sample H-1. However, unlike the sample B-1, and contrary to the expectation of the persistent photoconductivity technique (see Section 2.2), the density of the quantum well after illumination actually *decreased* from $n = 2.75$ to 2.54×10^{11} cm^{-2}.

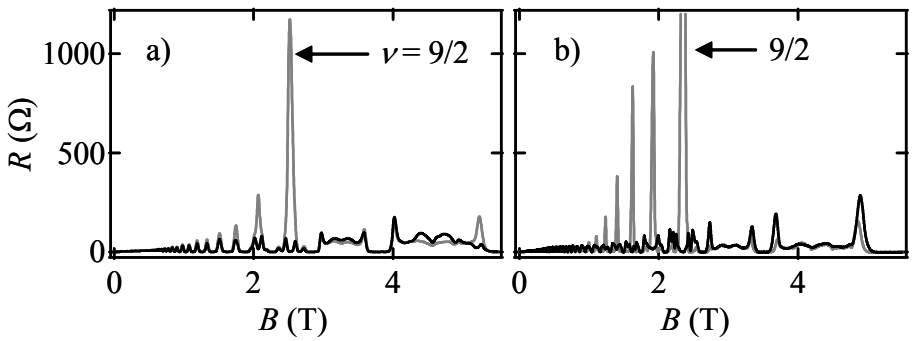

Figure 3.12: R_{xx} (gray) and R_{yy} (black) in sample H-1 at 50 mK before (a) and after (b) illumination. Transport quality improves, although the resistance anisotropy is already present before illumination.

3.2.5 Unconventional High-Mobility Samples

The transport phenomena in high-mobility 2DESs do not always fit the conventional picture outlined in this section, and there are two main classes of exceptions. First, there are samples where the transport characteristics are simply pathological. For example, Fig. 3.13 shows the 50 mK transport results of sample N-4, a single-interface heterojunction with a density and mobility of 2.2×10^{11} cm^{-2} and 12×10^{6} cm^2/Vs. This high mobility suggests that the sample would show excellent transport characteristics,

including a strong anisotropy in high LLs. In addition, its MBE structure is very similar to that of wafer C, which has produced good transport results (see Fig. 3.8c). However, as Fig. 3.13 makes clear, sample N-4 suffers from severe problems. First, R_{xx} does not exceed 50 Ω over the entire range shown, and for fields less than about 1.5 T it barely rises from zero. Also, R_{yy} exhibits wildly large quantum Hall oscillations at the larger fields and at smaller fields shows an approximately linear dependence on magnetic field. These problems probably arise from large-scale 2DES density inhomogeneities that result in highly nonuniform current flow. We often have to test multiple high-mobility samples before finding one with good transport characteristics. In these samples that are well-behaved, the usual resistance anisotropies in high LLs are almost always observed.

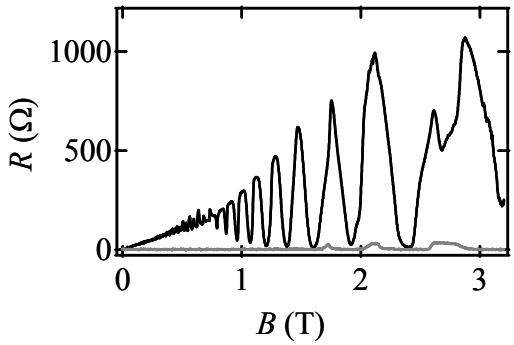

Figure 3.13: R_{xx} (gray) and R_{yy} (black) in sample N-4 at 50 mK, showing an example of pathological transport.

3.3 Testing Anisotropic Transport in Different Geometries

3.3.1 The Diamond Mesa

Sections 3.1 and 3.2 showed that the principal axes of anisotropic transport in high LLs are aligned to the underlying crystal structure so that $[1\bar{1}0]$ is the hard direction and $[110]$ the easy direction. However, so far all the data has been taken from square samples that had been cleaved along those same directions from their parent wafers. Therefore, the question arises whether the observed principal axes are associated with

orientation of the square boundary of the 2DES, or whether the crystal axes themselves determine the hard and easy axes.

A simple way of testing this is to construct a sample with a square boundary whose sides lie along directions other than $[1\bar{1}0]$ and $[110]$. This was done by etching a 2.5 mm square mesa from a larger piece of the wafer B so that the sides of the mesa were directed along [100] and [010]. Thus the resulting sample, B-5, contains a square mesa with an orientation that is rotated at a 45° angle with respect to the regular cleaved square samples. Eight indium contacts were then diffused in the usual locations around the mesa's perimeter, and the resulting transport data for four relevant configurations are shown in Fig. 3.14.

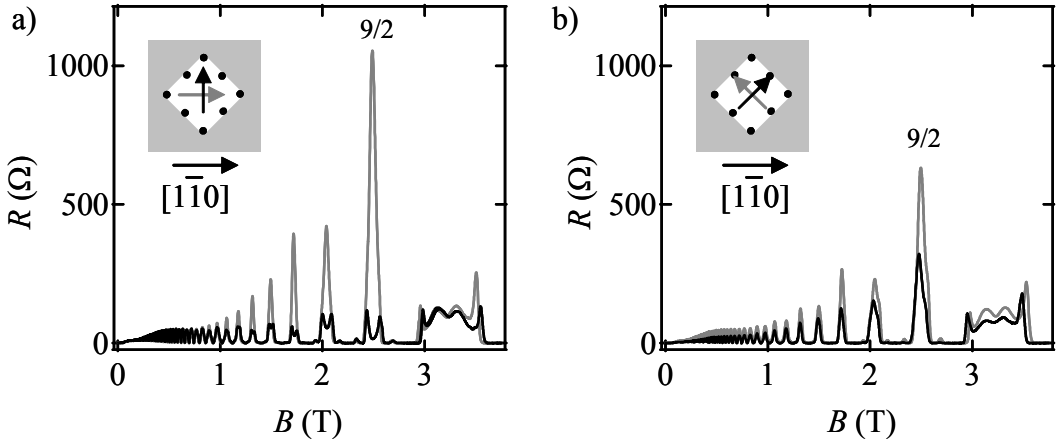

Figure 3.14: 50 mK longitudinal resistance in a square geometry rotated by 45° (sample B-5) with respect to the cleaved sample edges. a) Current along $[1\bar{1}0]$ (gray) and $[110]$ (black); b) current along $[010]$ (gray) and $[100]$ (black). Despite the diagonal mesa orientation, the principal axes of high LL anisotropy remain along $[1\bar{1}0]$ and $[110]$.

In Fig. 3.14a, the longitudinal resistance at 50 mK is shown over the range $3 < \nu < 6$, and the two traces correspond to a net current flow along the two diagonals of the square. The voltage probes in these configurations are placed on the midpoint contacts on the mesa's sides. These "diagonal" configurations essentially measure the resistance in the $[1\bar{1}0]$ and $[110]$ directions, and the transport data clearly show that a large anisotropy is present in half-filled high LLs with the usual orientation: $[1\bar{1}0]$ is the hard

direction and $[110]$ is the easy direction. Fig. 3.14b demonstrates that when the current is passed between the opposing midpoints of the squares, i.e., along the [100] and [010] directions, there is no substantial difference between the two orthogonal longitudinal resistances. Thus Fig. 3.14 proves that the principal axes of anisotropic transport are not determined by the directions of the square boundary of the 2DES. Rather, the anisotropy is robustly oriented along the underlying crystal directions $[1\bar{1}0]$ and $[110]$.

3.3.2 Hall Bars

Being long and thin, Hall bar geometries provide some advantages over squares. For example, their large aspect ratios increase the voltage signal of a longitudinal resistance measurement. Also, the current density along the length of a Hall bar is often assumed to be uniform across the width of the bar, making the conversion from resistance to resistivity simple.

Therefore, anisotropic transport was measured in Hall bar geometries to confirm its presence and orientation when the current path is better defined. Unlike the square geometry, where both R_{xx} and R_{yy} resistance measurements can be made in the same 2DES, two orthogonal Hall bars are necessary to compare the resistances along $[1\bar{1}0]$ and $[110]$. Two such pairs of Hall bars were made by etching pieces from the parent wafers B and C.

The first set of Hall bars are samples B-2 and 3, and their long axes lie along $[1\bar{1}0]$ and $[110]$, respectively. The Hall bars are approximately 1 mm wide and 4.5 mm long, with 3 contact tabs protruding from each side of the bar, as shown in the inset of Fig. 3.15. The 25 mK longitudinal resistance data of Fig. 3.15 were taken with the current running through the length of the Hall bars and with the voltage contacts on adjacent contact tabs. Fig. 3.15 covers a wider range of magnetic fields, and for low fields $B < 1$ T and higher fields $B > 2.8$ T, the two resistances are nearly equal. Consistent with the picture of anisotropic transport in high LLs, however, the resistances become significantly different starting in the $\nu = 9/2$ structure and continuing through the next several half-filled LLs. At $\nu = 9/2$, for example, the resistances differ by a factor of

6, with $[1\bar{1}0]$ the hard direction and $[110]$ the easy direction as usual. In addition, the Hall bars exhibit a rapid onset of anisotropy the temperature is lowered below ~150 mK.

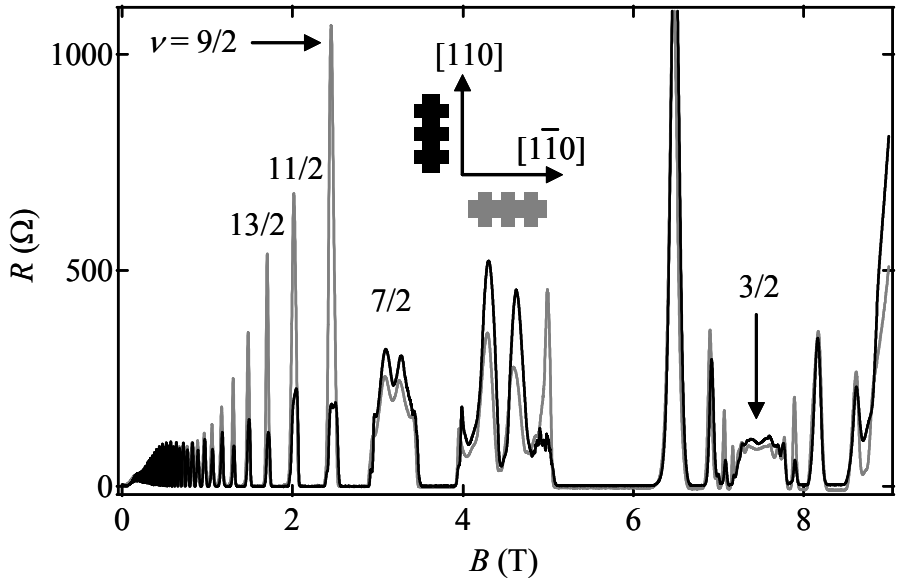

Figure 3.15: 25 mK longitudinal resistances for two orthogonal Hall bars: B-2 (gray, along $[1\bar{1}0]$) and B-3 (black, along $[110]$). The high LL anisotropy, though reduced, still exists at $\nu = 9/2$, 11/2, etc.

The factor of 6 anisotropy ratio at $\nu = 9/2$ in the Hall bar samples is significantly smaller than the factor of ~100 in the square sample B-1 from the same parent wafer (see Fig. 3.4). This discrepancy likely arises from a current-channeling effect. In square samples, Simon [6] pointed out that the ratio of R_{xx} and R_{yy} may be exponentially greater than the underlying ratio of the diagonal resistivity components ρ_{xx} and ρ_{yy}. This exaggeration essentially comes from the nonuniform current distribution in square samples. In Hall bar samples, the assumed uniform distribution of current yields a better match between measured resistances and underlying resistivities. Thus if the Hall bar and the square samples share the same anisotropic resistivity, then their resistances would be expected to yield different anisotropy ratios. Simon's analysis is able to reconcile the anisotropy discrepancy between squares and Hall bars, as will be discussed in Chapter 6.

The second set of Hall bars examined were samples C-9 and 10. They are about 460 μm wide and 3.5 mm long, with two contact tabs on either side of the central bar, as shown in the inset of Fig. 3.16. The lengths of the C-9 and C-10 Hall bars lie along the

$[110]$ and $[1\bar{1}0]$ crystal axes, respectively, and their longitudinal resistance data at 25 mK are shown in Fig. 3.16. (Note: the density of sample C-10 was found to be lower than C-9 by a factor of 0.97; in the figure, this has been accounted for by multiplying the magnetic field of the C-10 data by 1/0.97.)

The usual signatures of anisotropic transport in high LLs are apparent in the Hall bars C-9 and C-10. First, the transport around $\nu = 7/2$ is quite isotropic, as is the case for low fields $B < 1$. But for $\nu = 9/2$ and 11/2, the resistance around half-fillings of these LLs from sample C-10 greatly exceeds that obtained in sample C-9 (current along $[110]$). Furthermore, similarly to the case of the Hall bars B-2 and -3, the degree of anisotropy in the C-9 and C-10 Hall bars is reduced compared to a square sample from the same wafer at the same temperature. At $\nu = 9/2$, for example, the resistances from the two Hall bars differ by a factor of about 13, as compared to a factor of nearly 200 observed in a square sample from the same wafer (sample C-8, shown in Fig. 3.8c).

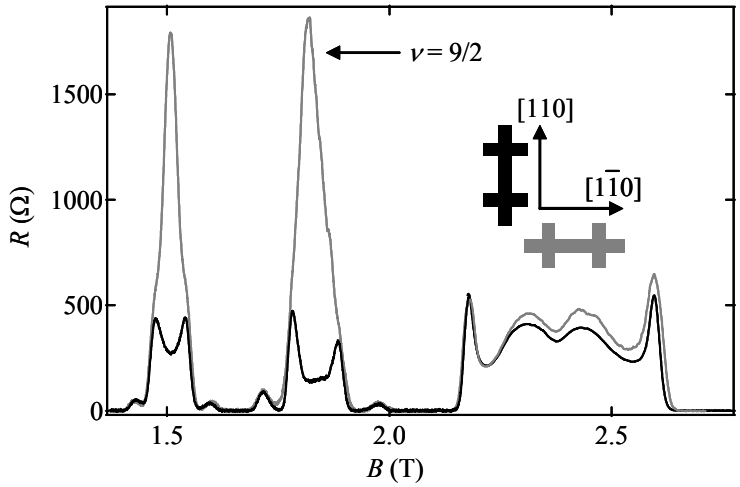

Figure 3.16: 25 mK longitudinal resistances for two orthogonal Hall bars: C-10 (gray, along $[1\bar{1}0]$) and C-9 (black, along $[110]$). The anisotropy with the usual principal axes is evident at $\nu = 9/2$ and 11/2.

3.4 Temperature Dependence of Anisotropic Transport

3.4.1 Sample Survey: $\nu = 9/2$

This section summarizes the temperature dependence of the anisotropic transport in greater detail and in a wider variety of samples. To begin, Fig. 3.17 shows an overview of how the resistance anisotropy in R_{xx} (top panels) and R_{yy} (bottom panels) develops around $\nu = 9/2$ in five different samples. From left to right, these are: H-1, B-1, G-1, C-8, and F-5. The order is also in decreasing density (not mobility): 2.9, 2.7, 2.1, 2.1, and 1.5 $\times 10^{11}$ cm^{-2} (see Table 3.1). For each panel, the four traces correspond to measurements taken at 25, 50, 100, and 150 mK.

In each of the samples in Fig. 3.17, there is a clear onset of anisotropy around $\nu = 9/2$ as the temperature is lowered. Also, with the exception of sample C-8, all the other R_{xx} peaks attain values in the range 1-2 kΩ by 25 mK, after having started between 50 and 100 Ω at 150 mK. The minima, on the other hand, typically fall in magnitude only by a factor of 2, except in the case of H-1 where R_{yy} vanishes to within the experimental uncertainty of ~1 Ω.

The most important trend in the temperature dependences shown in Fig. 3.17 is that the onset of anisotropy is sensitive to the 2DES density. For example, in the two highest density samples shown, H-1 and B-1, the growth of anisotropy is already underway by 100 mK, where the green traces show a shallow hump in R_{xx} and a corresponding dip in R_{yy}. In the highest density sample H-1, R_{yy} even reaches ~0 Ω by 100 mK, although only over a narrow magnetic field range. On the other hand, in the lower density samples the 150 and 100 mK data show virtually no differences around half-filling. In the lowest density sample F-5, the onset to anisotropy occurs at the lowest temperature of all the samples in Fig. 3.17. Higher density samples probably show larger resistance anisotropies at relatively higher temperatures because the energy scale of electron-electron interactions increases with the 2DES density. This is a consequence of the electrons being closer to one another.

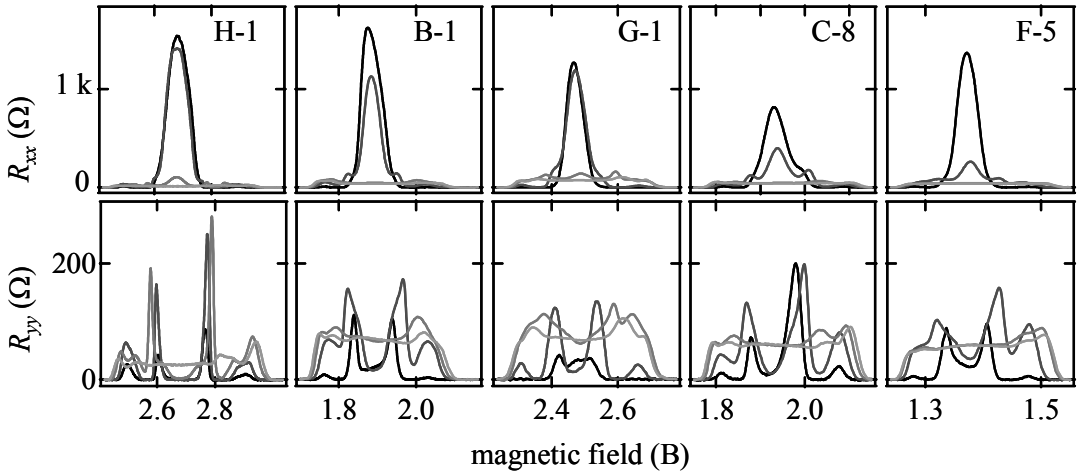

Figure 3.17: R_{xx} (top) and R_{yy} (bottom) through the $\nu = 9/2$ structure for the five samples indicated and at several temperatures. From lightest to darkest grayscale, the corresponding temperatures are $T = 25$, 50, 100, and 150 mK.

3.4.2 Temperature Dependence at Different Filling Factors

The transport anisotropy seen at $\nu = 9/2$ also occurs at higher half-filled LLs. The temperature dependence of the anisotropy in several high LLs for the sample B-1 is summarized in Fig. 3.18. In Fig. 3.18a, the longitudinal resistance R_{xx} is plotted versus magnetic field over the range $4 < \nu < 8$ and shows how the peaks around the half-filling points develop at $\nu = 9/2$, 11/2, 13/2, and 15/2. The six traces correspond to the temperatures 25, 35, 50, 65, 100, and 150 mK. Clearly, each half-filled high LL shows qualitatively similar behavior, with the peak in R_{xx} emerging quickly as the temperature is lowered. The increasing strength of the anisotropy from $\nu = 15/2$ to $\nu = 9/2$ can be understood by a theoretical model to be described in Chapter 6.

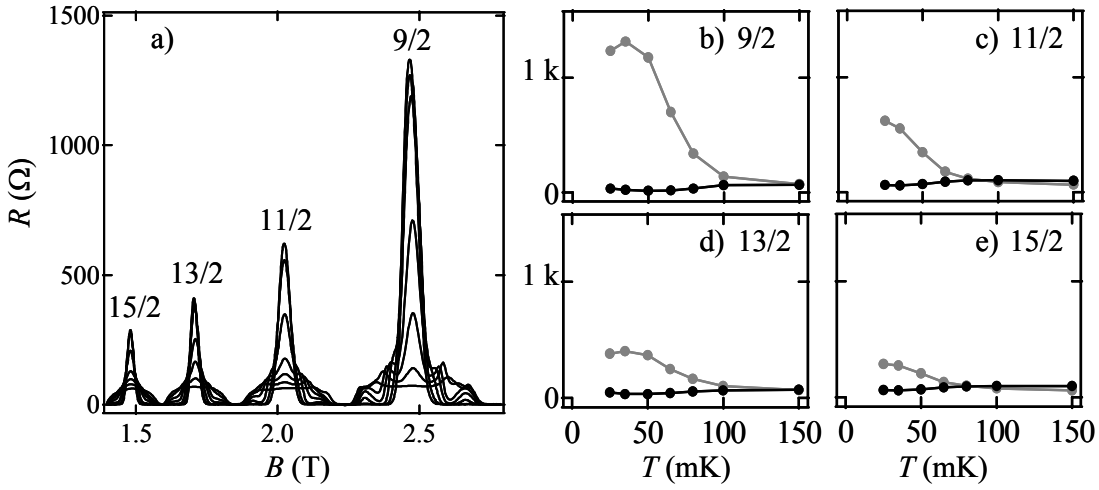

Figure 3.18: a) R_{xx} versus B in the range $4 < \nu < 8$ for sample B-1 at $T = 25$, 35, 50, 65, 100, and 150 mK; b) through e): R_{xx} (gray) and R_{yy} (black) versus T at the half-filling points $\nu = 9/2$, 11/2, 13/2, and 15/2.

The temperature dependence of the peaks in R_{xx} (gray), as well as the corresponding values of R_{yy} at half filling (black), are shown in Fig. 3.18b, c, d, and e for the filling factors $\nu = 9/2$, 11/2, 13/2, and 15/2. These data allow a visualization of how the anisotropy develops as the temperature is lowered, and they reveal an interesting trend. For $\nu = 9/2$ and 13/2, the peak in R_{xx}, which rapidly develops below 100 mK, appears to bend over or at least saturate by 25 mK. However, for 11/2 especially and also 15/2 no such saturation occurs.

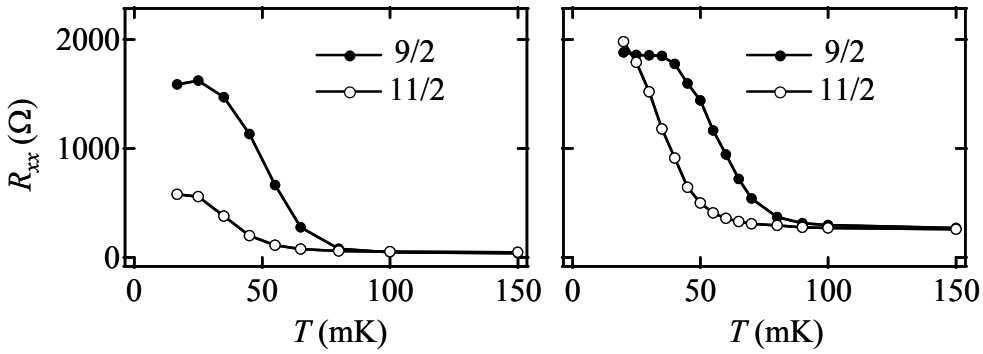

Figure 3.19: R_{xx} versus T measurements at $\nu = 9/2$ and 11/2 for the samples G-1 (left) and C-10 (right). For sample C-10, the low-temperature resistance at $\nu = 11/2$ exceeds that at $\nu = 9/2$.

The saturation of R_{xx} at $\nu = 9/2$ but not 11/2 has been observed in other samples as well, including G-1 and the Hall bar C-10. Peak height versus temperature data from these samples are shown in Fig. 3.19. In the case of the hall bar C-10, the $\nu = 11/2$ peak continues growing rapidly at low temperatures and by 20 mK it has even surpassed the peak at $\nu = 9/2$!

This distinction between the temperature dependence of R_{xx} and $\nu = 9/2$ and 11/2 is the first of many examples of an asymmetry between the spin-split LLs of the same index N. (Recall that while the spins of the valence electrons at $\nu = 9/2$, 13/2, etc., point in the same direction as B, those at $\nu = 11/2$, 15/2, etc. point in the opposite direction.) In the case of Fig. 3.18, this spin-splitting asymmetry applies to whether the peak values of R_{xx} saturate by 25 mK. It is not known what causes the difference between the half-even ($2N + 1/2$) and half-odd ($2N + 3/2$) high LLs. On the one hand, the trend is unexpected because the electrons with a given LL index N (e.g. 9/2 and 11/2 are both in $N = 2$) have the same spatial dependence of their wavefunctions. On the other hand, the spin polarization of the valence electrons alternates between successive levels, and the electrons of the submerged LLs possess a net spin polarization when an odd number of these LLs are filled.

3.5 Nonlinear Resistance of Anisotropic States

The resistance measurements described so far have all been in the linear response regime, where the measured resistance $R_{xx} = dV_{xx}/dI$ is obtained for a small ac excitation current $dI \leq 20$ nA. One reason the excitation current needs to be kept small is to avoid excessive heating of the 2DES. Another is that at too high currents, the resistance of the sample may become nonlinear. The nonlinearity of a sample's differential resistance can be measured by monitoring the signal dV_{xx}/dI in the presence of both a small ac current and a larger dc bias current I_{dc}. (Experimentally, the two currents are summed together via a low-frequency room-temperature transformer placed before the current-limiting resistor.) A sample's resistance may become nonlinear due to heating effects, but the physics of underlying electron phases also could play a role.

To probe for such new physics, dc biased differential resistance measurements were made on the anisotropic electron phases in high LLs, and Fig. 3.20 summarizes the essential result of such measurements. In Fig. 3.20a, the usual linear-response R_{xx} and R_{yy} traces of the sample B-1 at 25 mK are plotted versus filling factor for the range $4 < \nu < 10$. In Fig. 3.20b, six sets of differential resistance traces dV_{xx}/dI are shown corresponding to the six half-filled high LLs $\nu = 9/2$, 11/2, 13/2, 15/2, 17/2, and 19/2. For each set of traces, the dc current covers the range -200 nA $< I_{dc} <$ 200 nA and flows in the **x** (or $[1\,\bar{1}0]$) direction.

Several of the differential resistance traces exhibit strong nonlinearities. Most commonly, dV_{xx}/dI tends to initially increase until about I_{dc} = 100 nA before falling again. Because the linear-response resistance R_{xx} at these half-filling points of high LLs falls with increasing temperature, the initial rise in dV_{xx}/dI is *not* due to electron heating. Rather, it must arise from the nonlinear response of the underlying correlated electronic phase. At dc currents larger than 100 nA, the fact that dV_{xx}/dI drops with increasing I_{dc} may be consistent with electron heating. For currents along the **y** direction, the nonlinearities in R_{yy} are not as pronounced. Also, at temperatures where the resistance anisotropy vanishes, or when the filling factor is in the $N = 0$ or 1 LLs, the resistance nonlinearities are very weak or nonexistent.

An intriguing aspect of the data in Fig. 3.20b is that the spin-splitting asymmetry is very pronounced. For example, at $\nu = 9/2$ and $\nu = 13/2$ the differential resistances increase by over 50% from their initial value before falling again. Meanwhile, at $\nu =$ 11/2 and 15/2, dV_{xx}/dI does not increase more than ~8% before falling. This dramatic strong/weak pattern is repeated again for $\nu = 17/2$ and 19/2. The nonlinearity and the associated spin-splitting asymmetry has also been observed in other samples.

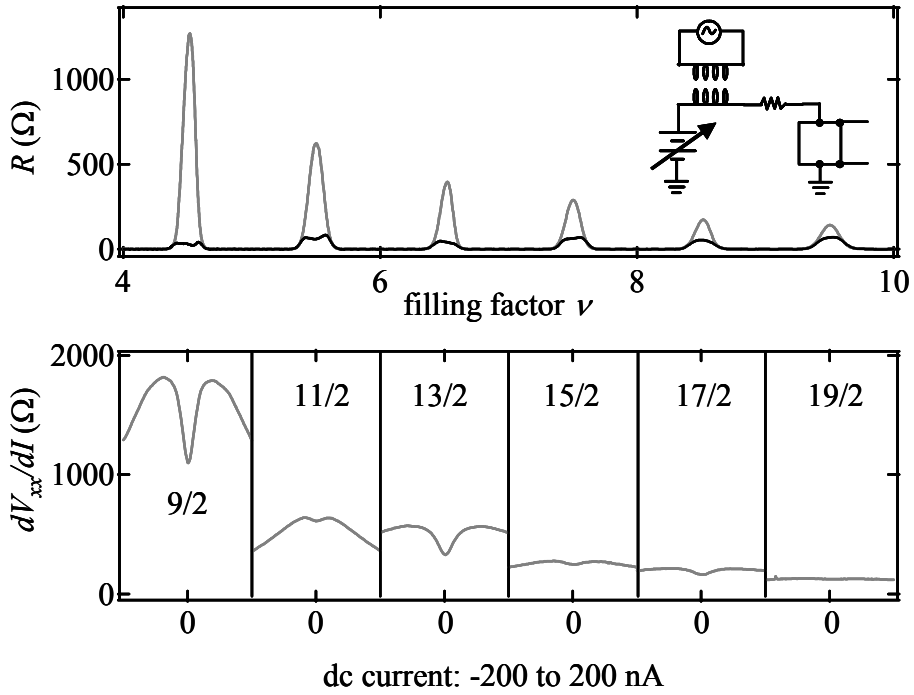

Figure 3.20: Top: R_{xx} (gray) and R_{yy} (black) versus filling factor at 25 mK in sample B-1. Bottom: nonlinearity in dV_{xx}/dI versus I_{dc} at the half-filled high LLs $\nu = 9/2$ through 19/2. For each case, the dc current varies from -200 to 200 nA. Inset: circuit diagram for coupling dc and ac currents.

A final feature of the nonlinear resistance behavior that might shed light on the underlying electron phases is summarized in Fig. 3.21. There, the differential resistance dV_{xx}/dI is shown versus I_{dc} for six different filling factors across the $\nu = 9/2$ region. As before, the data in Fig.3.21 were taken at 25 mK, and the span of I_{dc} is from -200 to 200 nA. Unlike the data in Fig. 3.20, the traces in Fig. 3.21 are plotted as changes in dV_{xx}/dI with respect to its value at $I_{dc} = 0$. The unusual aspect of Fig. 3.21 is that there is a very strong filling factor dependence of the nonlinearities across the $\nu = 9/2$ structure itself. On the one hand, the physics of the 2DES within a given LL should be symmetric with respect to half-filling because of particle-hole symmetry. However, that symmetry in Fig. 3.21 is clearly violated. For partial filling factors below half-filling, a very strong rise in dV_{xx}/dI with I_{dc} occurs, and this effect appears to be maximized around $\nu \approx 4.46$. Meanwhile, at higher partial fillings and on the other side of the half-way point the nonlinearity is weaker, and by $\nu \approx 4.57$ the sharp rise in dV_{xx}/dI with I_{dc} is completely gone. Like the spin-splitting asymmetry, this particle-hole symmetry-breaking within

high LLs appears in other transport measurements. In particular, Chapters 4 and 10 contain evidence of particle-hole asymmetries in the insulating phases that flank the anisotropies in high LLs.

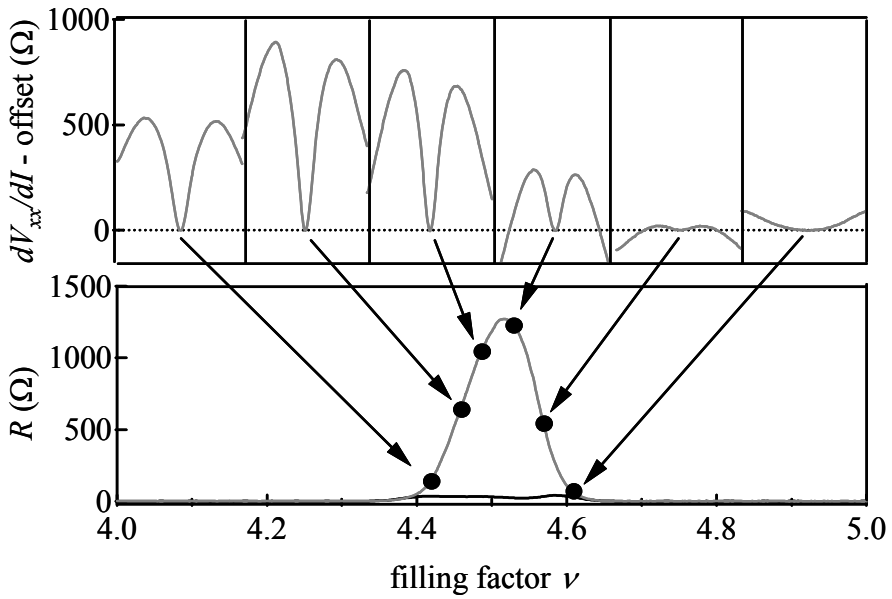

Figure 3.21: 25 mK nonlinearity in dV_{xx}/dI versus I_{dc} (top) at several filling factor across the $\nu = 9/2$ structure (bottom). The dV_{xx}/dI traces are offset to intersect 0 at $I_{dc} = 0$; in each case, I_{dc} varies from -200 to 200 nA.

---

1 See the chapter by S. Das Sarma in *Perspectives in Quantum Hall Effects*, ed. S. Das Sarma and A. Pinczuk (John Wiley, New York 1997).

2 R.R. Du, D.C. Tsui, H.L. Stormer, L.N. Pfeiffer, and K.W. West, Solid State Commun. **109**, 389 (1999).

3 R.L. Willett, J.W.P. Hsu, D. Natelson, K.W. West, and L.N. Pfeiffer, Phys. Rev. Lett. **87**, 126803 (2001).

4 F. Ertl, O. Jaeger, R.A. Deutschmann, M. Bichler, G. Abstreiter, E. Schuberth, C. Probst, and W. Wegscheider, submitted to 26th International Conference on the Physics of Semiconductors, Edinburgh 2002.

5 M. Shayegan, H.C. Manoharan, S.J. Papadakis, and E.P. DePoortere, Physica E **6**, 40 (2000).

6 S. Simon, Phys. Rev. Lett. **83**, 4223 (1999).

Chapter 4:
Re-entrant Insulating States in High Landau Levels

4.1 Basic Phenomenology of the Insulating States

Although not the focus of Chapter 3, other significant transport features develop in high LLs at low temperatures besides the resistance anisotropy. For example, condider Fig. 4.1, which is a reproduction of Fig. 3.5 and shows how R_{xx} and R_{yy} develop at low temperatures around $\nu = 9/2$ in sample B-1. While the most striking aspect of the data in Fig. 4.1 is the sudden development of anisotropic transport around half-filling, R_{xx} and R_{yy} exhibit other structural changes as well. At 80 mK, for instance, pronounced dips in both R_{xx} and R_{yy} appear on either side of half-filling, as indicated by the two arrows. The locations of these features correspond approximately to 1/4 and 3/4 partial filling. At lower temperatures these dips become deeper until by 25 mK the longitudinal resistance *isotropically vanishes* in the $\nu \approx 4.25$ and $\nu \approx 4.75$ regions. These regions are separated from the adjacent IQHE states by small, isotropic peaks in resistance ("satellite peaks") which shrink as the temperature is lowered.

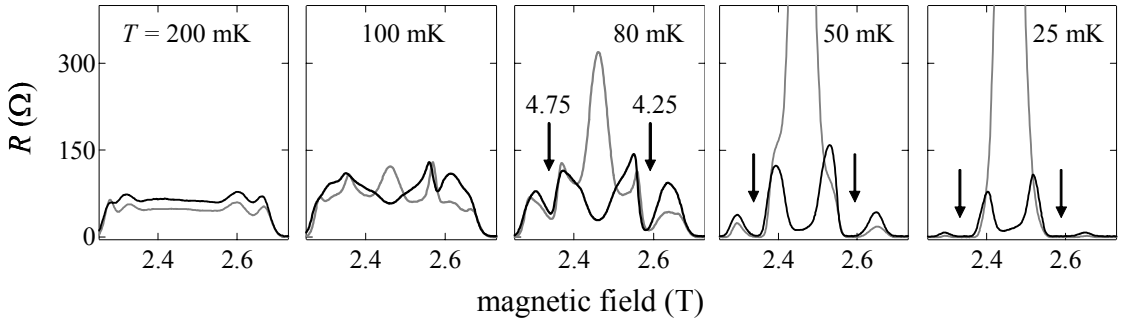

Figure 4.1: Temperature development of $\nu = 9/2$ structure in R_{xx} (gray) and R_{yy} (black) for sample B-1. The arrows indicate where the resistance minima at $\nu \approx 4.25$ and $\nu \approx 4.75$ form.

The observation of vanishing longitudinal resistance between adjacent IQHE states suggests that fractional quantum Hall physics might be at play in the flanks of $\nu =$

9/2. But a vanishing longitudinal resistance alone does not signify a FQHE state. Rather, the FQHE associated with some filling factor ν must also produce a Hall resistance R_{xy} that is *fractionally quantized* at the value $h/\nu e^2$. Therefore, if the insulating regions around $\nu = 4.25$ and $\nu = 4.75$ are FQHE states, then the corresponding R_{xy} at those filling factors should attain values around $h/(4.25)e^2$ and $h/(4.75)e^2$.

Fig. 4.2a shows the 50 mK longitudinal and Hall resistances of B-1 as a function of filling factor over a range $4 < \nu < 5$. The dark and light R_{xy} traces correspond to the net current driven along the $[1\,\bar{1}0]$ and [110] directions, respectively. (The small differences in the Hall resistance traces around half-filling are likely caused by the current-channeling effects discussed in Chapter 6.) If the Hall resistance were fractionally quantized at the filling factors $\nu \approx 4.25$ and 4.75, then it would exhibit a plateau at the values indicated by the short dotted line segments: at $R_{xy} = h/(4.25)e^2$ and $h/(4.75)e^2$. Clearly, fractional quantization of R_{xy} does not occur, and therefore the insulating states on the flanks of $\nu = 9/2$ are not generated by the FQHE.

While not fractionally quantized, however, the Hall resistance data in Fig. 4.2a appear to approximately maintain their *integer* quantized values even as the insulating regions are entered. The additional structure evident in R_{xy} nearer to half-filling is temperature dependent and does not represent a FQHE plateau. To provide a clearer picture of this, Fig. 4.2b shows both the longitudinal and the Hall data at a higher resolution over the range $4 < \nu < 4.3$. Starting at $\nu = 4$, both Hall resistance traces are accurately quantized at $h/4e^2$ while R_{xx} and R_{yy} are zero. (The values of R_{xy} in Fig. 4.2 have been adjusted by less than 1% to correct for an imperfect lockin gain and for integer Hall quantization.) This is classic integer quantum Hall behavior. At about $\nu = 4.12$, the IQHE state is lost as the Hall resistance falls off of its plateau, and the longitudinal resistances begin to form the satellite peak. As this peak is passed at about $\nu = 4.25$, the new insulating states emerge as R_{xx} and R_{yy} vanish again. Yet in the process, the Hall traces turn around and become re-quantized at the nearby integer value $h/4e^2$! In other words, the insulating region around $\nu = 4.25$ corresponds to a *re-entrant* integer quantum Hall effect, or RIQHE. Similar behavior occurs on the other flank of the LL near $\nu = 4.75$, as expected from the particle-hole symmetry of partially filled LLs.

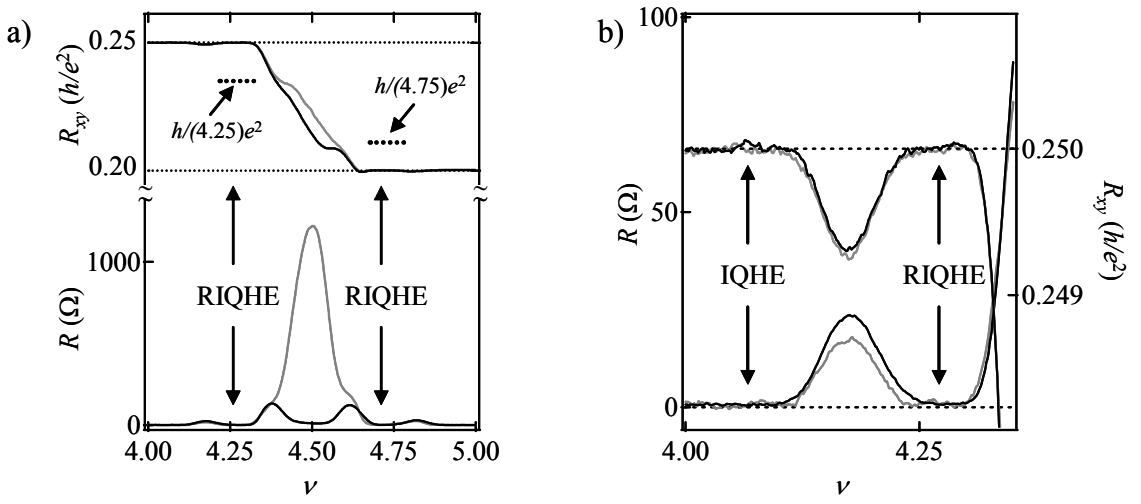

Figure 4.2: a) 50 mK longitudinal and Hall resistance between $4 < \nu < 5$ in sample B-1 for current along $[1\,\bar{1}0]$ (gray) and $[110]$ (black). The minima in R_{xx} and R_{yy} near $\nu = 4.25$ and $\nu = 4.75$ do not coincide with a fractionally quantized R_{xy} at the locations expected from the FQHE (short dashed lines). b) Close-up view of the longitudinal and Hall resistances demonstrating that the IQHE is re-entrant around $\nu = 4.25$.

An understanding of the mechanism for the RIQHE formation on a very general level comes from considering how the single-particle picture of the IQHE must be modified to account for the observations of Fig. 4.2. Hall resistance quantization and the vanishing of longitudinal resistance in an IQHE state arise from the single-particle localization by impurities (see Section 1.2). For example, as the filling factor is raised out of the $\nu = 4$ IQHE state, the longitudinal resistance becomes finite and R_{xy} falls off its plateau as the electrons begin to populate the current-carrying extended states in the center of the LL. As half-filling is approached, the IQHE predicts that R_{xx} increases along with the number of current-carrying electrons in the valence LL.

Fig. 4.2 therefore suggests that as the electron density in the valence LL increases, the particles at first participate in the conduction of current, and so R_{xx} and R_{yy} become finite. However, the subsequent decrease in the longitudinal resistance and the re-quantization of the Hall resistance around $\nu = 4.25$ indicate that as their density increases, the electrons *stop* participating in current conduction. This scenario is inconsistent with the single-particle picture of the IQHE, and we conclude that the electrons drop out as current carriers because of novel interaction physics.

4.2 Association of the RIQHE with Anisotropic Transport

The new RIQHE states are closely associated with the anisotropic electronic phases in half-filled high LLs. Like the resistance anisotropy, the RIQHE states described here only appear below about 150 mK in the highest quality samples. Also, they begin abruptly in the $N = 2$ LL, being most prominent around $\nu = 9/2$ and then tapering off in strength for higher LLs [1].

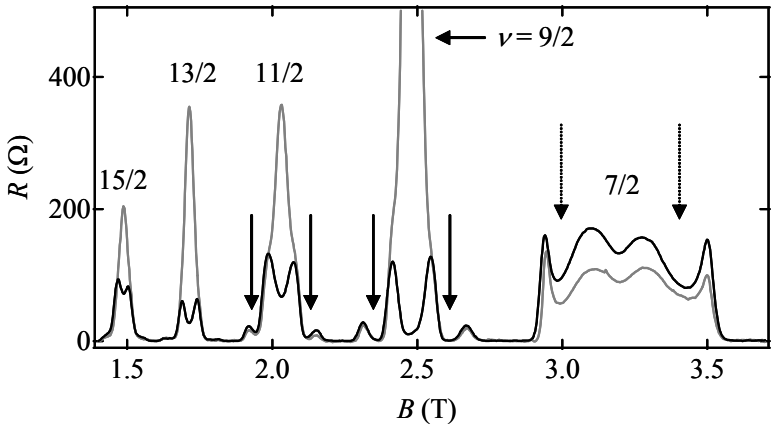

Figure 4.3: 50 mK R_{xx} (gray) and R_{yy} (black) data from sample B-1 demonstrating that the RIQHE (solid arrows) begins only in high LLs $N \geq 2$. The resistance minima on the flanks of $\nu = 7/2$ (dashed arrows) do not develop into RIQHE states at low temperature.

The sudden appearance of the RIQHE states in the $N = 2$ LL can be seen in Fig. 4.3, where the R_{xx} and R_{yy} data of sample B-1 are plotted versus magnetic field at 50 mK and over a range $3 < \nu < 8$. Around $\nu = 7/2$, no significant resistance anisotropy is present, and neither is any evidence for RIQHE states. The three local resistance minima in the $\nu = 7/2$ structure that do exist are likely the precursors of the FQHE states at $\nu =$ 16/5, 7/2, and 19/5 which were observed for the first time only recently in an ultra-high mobility sample [2]. Only when the filling factor exceeds 4, and the electrons begin to populate the $N = 2$ LL, do the RIQHE states appear. In Fig. 4.3, the two RIQHE states surrounding $\nu = 9/2$, at $\nu \approx 4.25$ and 4.75 are quite well developed. Likewise, there are also two RIQHE regions surrounding $\nu = 11/2$, but they are considerably weaker. In the $N = 3$ LL, only very weak shoulders adjacent to the main anisotropic regions point to the

existence of the RIQHE states even though the resistance anisotropies around $\nu = 13/2$ and 15/2 are still prominent.

The other samples we have studied also show the anisotropic transport persisting to higher LLs than the RIQHE, but in very high quality samples the RIQHE states are detectable up to the $N = 3$ LL. For example, Fig. 4.4 shows 50 mK longitudinal and Hall resistance data from the high-mobility quantum well H-1. The R_{xx} and R_{yy} data in the bottom panel show the usual large anisotropies around half-fillings of the high LLs: $\nu =$ 9/2, 11/2, 13/2, and 15/2. On the flanks of all these high LLs, the roughly isotropic RIQHE states are clearly visible, showing dips in R_{xx} and R_{yy} separated from the IQHE regions by the satellite peaks. The top panels of Fig. 4.4 contain portions of the corresponding Hall resistance data which have been offset so that the plateaus corresponding to the IQHE states all lie along the same line. These R_{xy} data show very clearly how the re-entrant nature of the quantized Hall resistance is reproduced from LL to LL.

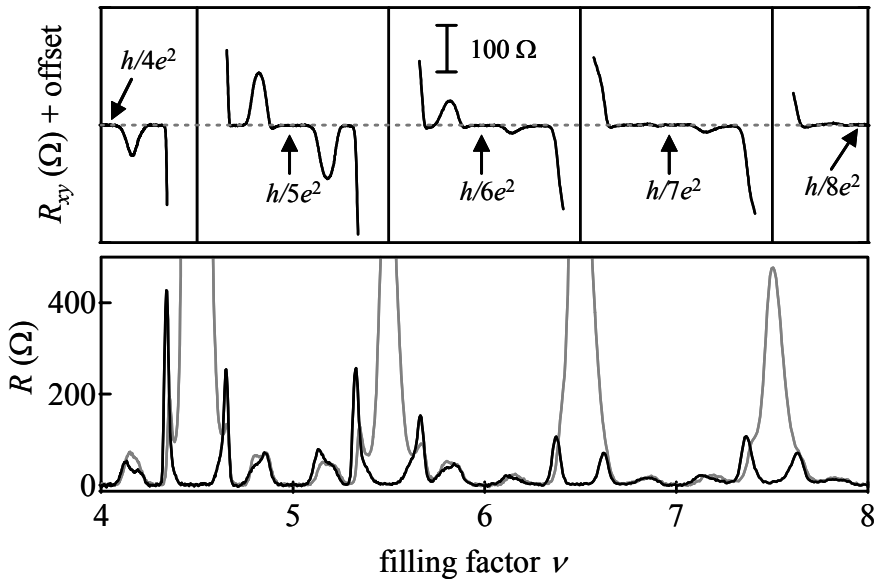

Figure 4.4: 50 mK Hall (top) and longitudinal (bottom) resistance data from sample H-1 through four high LLs. The longitudinal resistances shown are R_{xx} (gray) and R_{yy} (black). For each high LL, the Hall resistance exhibits re-entrant quantization where the RIQHE states occur.

Note that when the anisotropy is very strong, such as at $\nu = 9/2$, the RIQHE states are well developed on each side of half-filling. Also, the RIQHE gradually weakens

along with the resistance anisotropy at successively higher filling factors. Although not as visually striking as anisotropies, the RIQHE states are just as inconsistent with the single-particle model of the IQHE. Thus both the anisotropic and the insulating transport features in high LLs signify new collective phases of two-dimensional electrons.

4.3 Temperature Dependence and Activation Energies of the RIQHE

4.3.1 Sample C-1

To gain a deeper understanding of the RIQHE states in high LLs, it is helpful to analyze their development at low temperatures and to search for any Arrhenius-type activated behavior. One sample whose temperature dependence was extensively studied is sample C-1. For the purposes of an unrelated experiment, the boundary of this sample's 2DES has been modified by scratching lines on the sample surface as shown in the inset of Fig. 4.5b. Nonetheless, the sample still exhibits excellent transport properties in high LLs.

Fig. 4.5 summarizes the temperature dependence of the whole $\nu = 9/2$ structure of C-1 and includes an Arrhenius plot for the RIQHE state. In Fig. 4.5a and b, R_{xx} and R_{yy} versus B are shown at the seven temperatures 24, 40, 65, 80, 100, and 150 mK. Around $\nu = 9/2$, the resistance anisotropy develops strongly as the temperature is lowered below 150 mK. Over the same temperature range, the two RIQHE states form on the flanks of the LLs. The high-field RIQHE state, around $\nu = 4.25$, appears to be more robust to higher temperatures than its counterpart around $\nu = 4.75$. At 65 mK, for example, the $\nu \approx 4.25$ RIQHE still shows a deep dip in R_{xx} and R_{yy}, while only a very shallow feature is left in the $\nu \approx 4.75$ RIQHE state. This moderate violation of particle-hole symmetry within a LL is common in the quantum Hall regime, an spin effects and/or Landau level mixing may be possible culprits. Other evidence suggesting that the RIQHE states on the high magnetic field side of half-filling are stronger will be presented in Chapter 10, where the properties of the insulating phases at high current bias are studied.

The temperature development of the RIQHE states is also revealed by the R_{xy} data around $\nu = 9/2$ as shown in Fig. 4.5c. As with R_{xx} and R_{yy}, the re-entrant quantization of R_{xy} around $\nu = 4.25$ lasts to higher temperatures than the $\nu = 4.75$ state. Also, by 150 mK

there is no sign of any re-entrant behavior: R_{xy} monotonically rises from $h/5e^2$ to $h/4e^2$ as the filling factor changes from 5 to 4. Interestingly, the data show that the RIQHE states play a dominant role in affecting the structure of the Hall resistance traces between the adjacent integer LLs $\nu = 4$ and $\nu = 5$. This is in contrast to the case of the longitudinal resistances, where the anisotropy around half-filling is the most obvious low-temperature feature in high LLs.

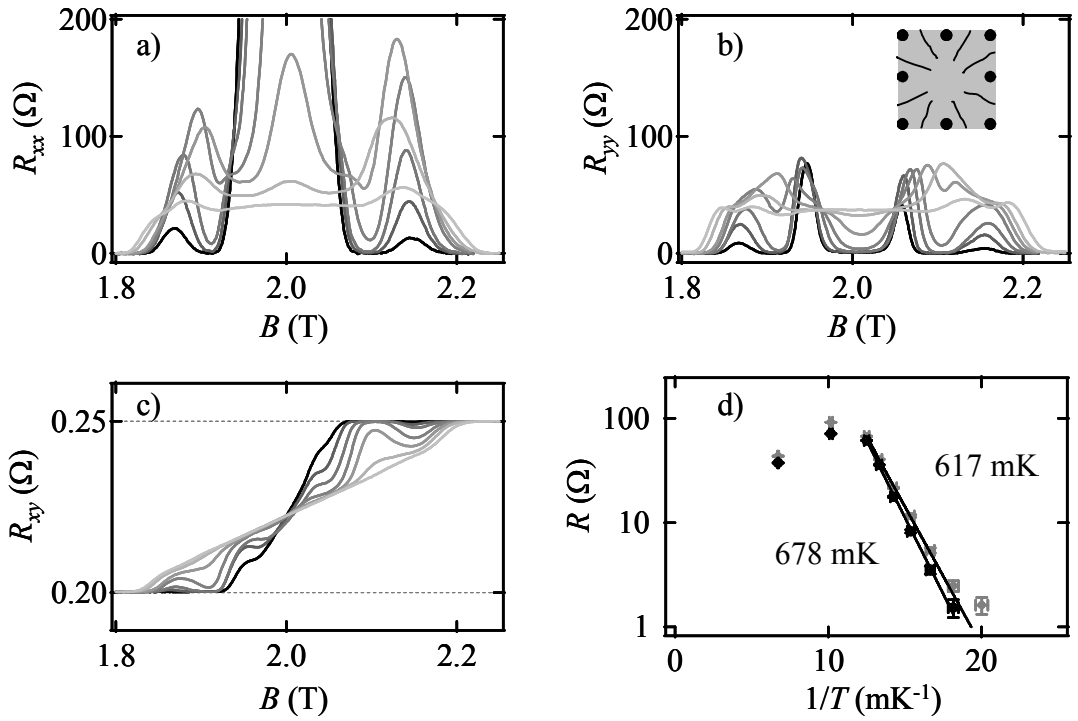

Figure 4.5: a), b), and c) R_{xx}, R_{yy}, and R_{xy} data through the $\nu = 9/2$ structure of sample C-1 at 25, 40, 50, 65, 80, 100, and 150 mK (dark to light). Inset to b): geometry of 2DES showing scratched sample surface. d) Arrhenius plot of R_{xx} (gray) and R_{yy} (black) taken at $B = 2.1$ T showing activation energies of ~650 mK.

The new RIQHE states are distinct from the IQHE and the FQHE phases, but all three share the property of being insulating. The insulating nature of the IQHE and the FQHE arises from the existence of an energy gap to conduction, and activated transport measurements in those states have been used to measure that gap and to elucidate the nature of the current-carrying quasiparticles. Activation measurements are based on the idea that the diagonal conductivity (and hence resistivity) of an insulating state in the quantum Hall regime is nonzero at any finite temperature and is proportional to the number of thermally excited quasiparticles. This, in turn, implies that the longitudinal

resistance obeys the Arrhenius formula $R_{xx} \sim \exp(-E_a/k_BT)$, where E_a refers to the activation energy of the quasiparticles. For example, in the IQHE, E_a is approximately equal to the LL spacing, while in the FQHE the activation energy refers to the energetic penalty of a creating a quasiparticle in the fractional quantum Hall fluid [3].

Therefore, the measurement of activation energies in the RIQHE regime might shed light on the properties of the underlying insulating electron states, and Fig. 4.5d contains an activation energy measurement of the $\nu \approx 4.25$ RIQHE state of sample C-1. In that figure several values of R_{xx} (gray) and R_{yy} (black) taken at 2.1 T are plotted logarithmically versus $1/T$. Before the R_{xx} and R_{yy} flatten out at high temperatures, they show good activated behavior with a fairly linear slope on the logarithmic scale for more than an order of magnitude of variation. The two straight line fits yield activation energies of 617 and 678 mK for the R_{xx} and R_{yy} measurements, respectively. The difference between these two energies should not be interpreted as an indication of an anisotropy in E_a because activation energy variations of ~10% are normal from measurement to measurement.

A revealing way of analyzing the activation energies is to track how they change throughout the RIQHE regions. Fig. 4.6 does this by plotting the measured values of E_a for sample C-1 across both RIQHE regions around $\nu = 9/2$. The values of E_a are plotted as black circles, and that data has been superposed onto 25 and 50 mK R_{yy} traces as a reference. The values of E_a here were obtained exclusively from the R_{yy} versus B traces at many different temperatures. The activation energies are not shown between 1.92 and 2.08 T because the R_{yy} values were *not* found to be linear over any reasonable range on a logarithmic scale such as in Fig. 4.5d. (This includes the central anisotropic $\nu = 9/2$ region where R_{yy}).

The data of Fig. 4.6 reveal three salient characteristics. First, the activation energies in the RIQHE regions reach a maximum where the RIQHE states are most robust. For example, in the low-field RIQHE state, E_a is largest at about 1.91 T. While at 25 mK the RIQHE is well developed from about B = 1.890 to 1.925 T, at 50 mK the R_{yy} trace shows a deep minimum centered almost precisely at 1.91 T. Thus 1.91 T is the magnetic field where the RIQHE persists to the highest temperatures. A similar correlation between the size of E_a and the strength of the RIQHE can also be seen on the

high-field side of the LL. The second important aspect of Fig. 4.6 is that the $\nu \approx 4.25$ activation energies reach about 30% larger values than the ones at $\nu \approx 4.75$. This is consistent with the previous observation that the $\nu \approx 4.75$ RIQHE is the more delicate of the two, but now the comparison may be made more quantitative. The third conclusion from Fig. 4.6 is that the activation energies begin to rise again once the satellite peaks are passed and the magnetic field moves into the IQHE regions of $\nu = 4$ and $\nu = 5$. Indeed, as the integer filling factors are approached, these energies are expected to reach tens of Kelvin at ~2 T because of the large LL spacing at a these magnetic fields.

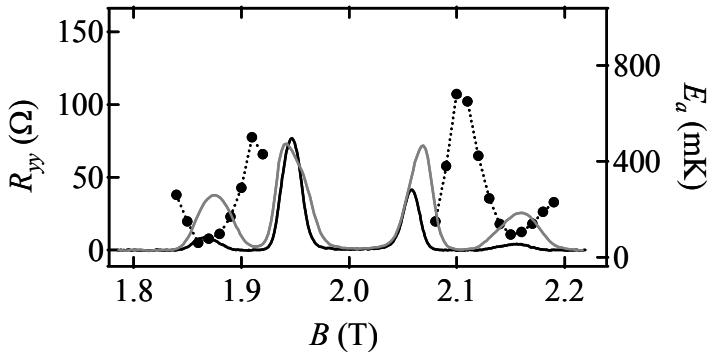

Figure 4.6: The solid circles denote activation energies E_a, in mK, as a function of B on the flanks of $\nu = 9/2$ in sample C-1. Longitudinal resistance R_{yy} is also shown at 25 mK (black) and 50 mK (gray). Where the RIQHE is strongest, E_a is largest.

4.3.2 Other Samples

The measured activation energies of the RIQHE states vary considerably from sample to sample, and a brief survey of this diversity in four different samples (G-1, F-5, H-1, and K-1) is shown in Fig. 4.7. In each case, low-temperature R_{xx} and R_{yy} transport data through the $\nu = 9/2$ structure are displayed along with an Arrhenius plot of R_{yy} taken in the center of the $\nu \approx 4.25$ RIQHE state. With the exception of K-1, the densities and mobilities of the samples in Fig. 4.7 are listed in Table 3.1. (Sample K-1 has a density and mobitlity of 3.0×10^{11} cm^{-2} and 30×10^{6} cm^2/Vs. Its transport features around half-filling of high LLs show anomalies that are currently being investigated. Nonetheless, the RIQHE states in sample K-1 are very well developed.)

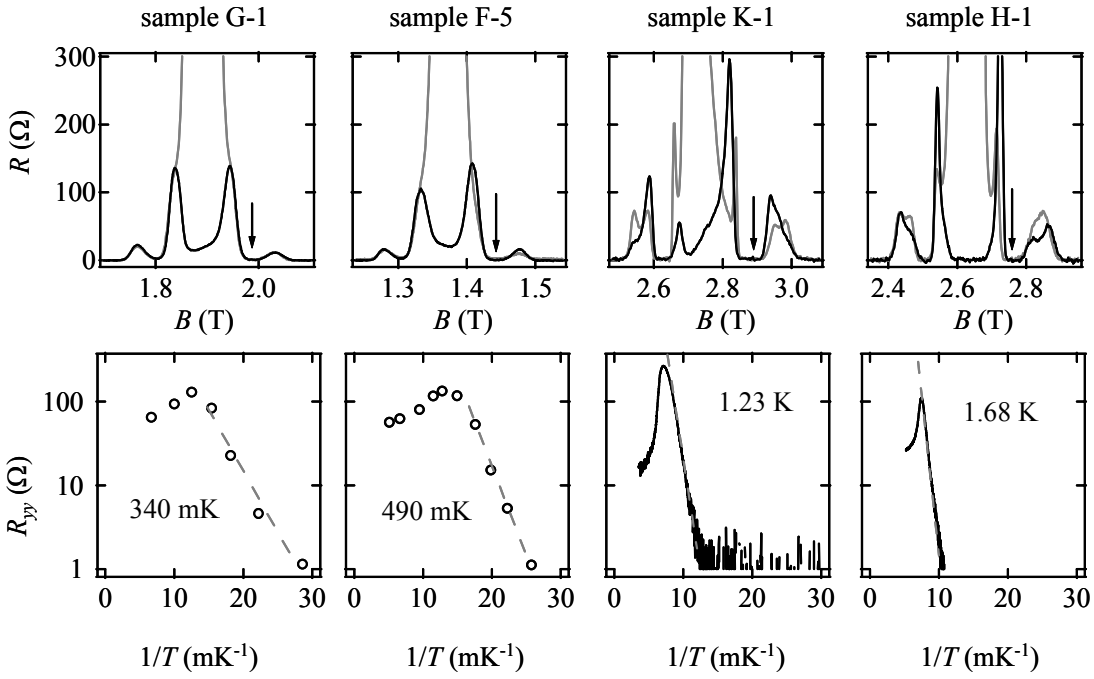

Figure 4.7: Top: low-temperature R_{xx} (gray) and R_{yy} (black) data from the four samples G-1, F-5, K-1, and H-1. Each span covers the $\nu = 9/2$ structure, and all data were obtained at 50 mK except for sample F-5, taken at 25 mK. Bottom: corresponding Arrhenius plots of R_{yy} versus $1/T$ taken at the magnetic fields indicated by the arrows. The dashed line fits yield the activation energies shown (in mK).

The activation energies of Fig. 4.7 span a wide range, from less than 400 mK in sample G-1 to nearly 1.7 K in sample H-1. The large activation energies and the high temperatures to which the RIQHE states persist in samples K-1 and H-1 are likely a result of their higher 2DES density. At higher densities, the electrons are closer together, and this raises the energy scale of an interaction-driven electronic phase. The same physics is likely behind the higher temperatures where anisotropic transport at half-filling occurs in higher density samples (see Section 3.4).

Another aspect of the RIQHE physics that deserves scrutiny is the temperature dependence of the satellite peaks separating the RIQHE regions from the IQHE states, and Fig. 4.8 illustrates how these peaks vary with temperature in several different samples. For each of six different samples, two or three low-temperature traces (usually 25, 35, and 50 mK) of R_{xx} versus ν are shown. As the temperature is lowered, both the RIQHE and the IQHE regions broaden, thus causing a constriction in the filling factor

range of the satellite peaks. Also, the height of the satellites in each sample becomes smaller for lower temperatures. Interestingly, in the case of sample B-1 (Fig. 4.8e), by 25 mK the satellite peaks have shrunk so rapidly that from this transport data there is no obvious boundary between the RIQHE and the IQHE. The disappearance of the satellite peaks in sample B-1 might be a result of disorder in the 2DES. After all, the samples in Fig. 4.8 are arranged from highest to lowest mobility (see Table 3.1), and there is certainly a rough trend of the higher quality samples showing taller satellite peaks. Dirtier samples, then, might be more likely to contain localization sites which assist in making the RIQHE or the IQHE more insulating.

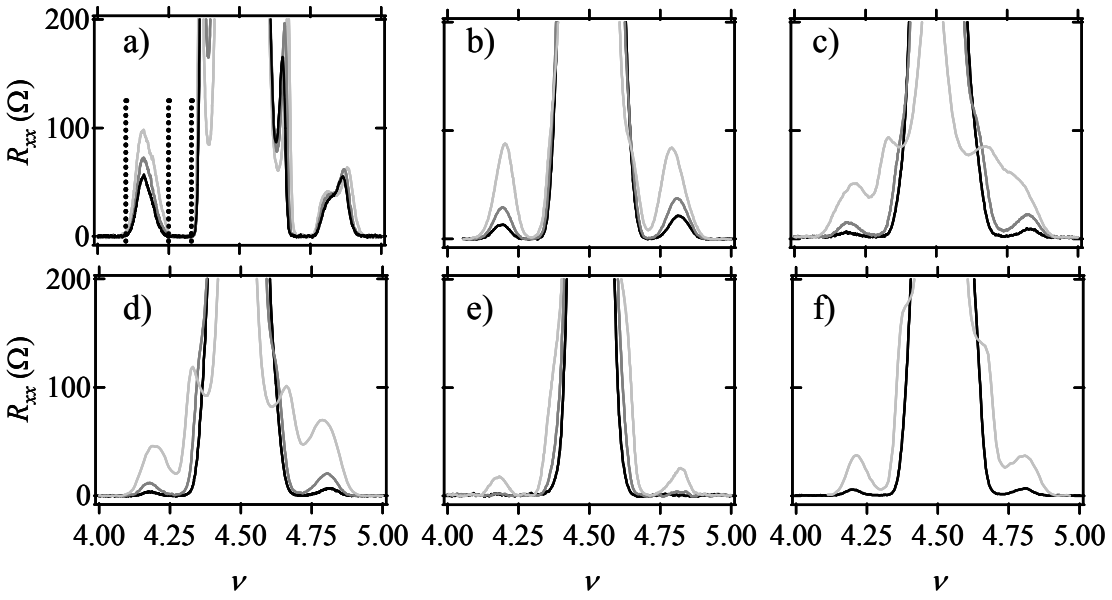

Figure 4.8: a) through f): R_{xx} through the $\nu = 9/2$ structure for the six samples H-1, C-1, F-5, G-1, B-1, and A-3. In a) through e), 25 mK (darkest), 35 mK, and 50 mK (lightest) data are shown. In f), only 25 mK and 55 mK data are shown. A variety of RIQHE strengths are present. Plotted versus filling factor, these results clarify the range of ν where the RIQHE occurs.

The data of Fig. 4.8 also help define the filling factor range where the RIQHE occurs. Of course, the absence of clear RIQHE boundary points in B-1 and the temperature-sensitive nature of the RIQHE's strength make a precise definition of the RIQHE range impossible. Nonetheless, the general location of the RIQHE in the $\nu = 9/2$ structures of Fig. 4.8 is remarkably reproducible from sample to sample, even when they contain 2DES densities varying over a factor of about 2. As a rule of thumb for the low-

temperature data in Fig. 4.8, with increasing ν from the $\nu = 4$ IQHE region, the satellite peak first appears at about 1/10 filling. Then the RIQHE sets in between about 1/4 and 1/3 filling before the central part of the LL structure is reached. The location of these three filling factors are denoted as vertical dashed lines in Fig. 4.8a and a rough phase diagram is shown in Fig. 4.9.

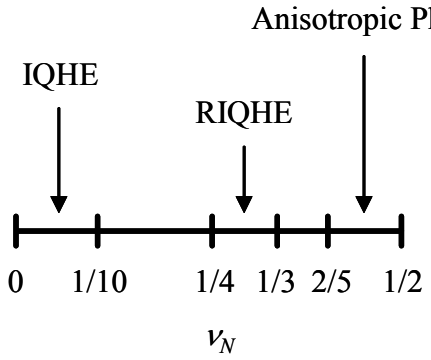

Figure 4.9: Approximate phase diagram, based on the data of Fig. 4.8, showing where the IQHE, RIQHE, and anisotropic transport occurs around $\nu = 9/2$. The partial filling factor of the valence LL is ν_N. The fractions 1/10, 1/4, etc. are meant only as convenient reference points.

---

1 Very recently, RIQHE states were discovered in the $N = 1$ LL at $T < 20$ mK, but we believe that they belong to a different class than the ones discussed here. See reference [2].

2 J.P. Eisenstein, K.B. Cooper, L.N. Pfeiffer, K.W. West, Phys. Rev. Lett. **88**, 076801 (2002).

3 R.L. Willett, H.L. Stormer, D.C. Tsui, A.C. Gossard, and J.H. English, Phys. Rev. B **37**, 8476 (1988).

Chapter 5:
Charge Density Waves in High Landau Levels

5.1 Stripes, Bubbles, and High LLs

The phenomena of anisotropic transport and re-entrant insulating states in high LLs are now widely believed to arise from charge density wave (CDW) formation. The proposal that CDWs are favored over FQHE states in the high LL regime was first made by Fogler, Koulakov, and Shklovskii (FKS) [1] and by Moessner and Chalker (MC) [2] in 1996. Both FKS and MC based their calculations on Hartree-Fock (HF) theory. FKS focused on the case of zero temperature and found two classes of CDW states in high LLs. First, around half-filling of the valence LL, they predicted that a unidirectional CDW forms. This "stripe" CDW consists of alternating rows of filled and empty states of the topmost LL. Second, FKS determined that the stripe CDW gives way to a triangular "bubble" CDW solution as the partial filling of the valence LL moves away from one half. These bubble phases consist of a triangular lattice of charge with two or more electrons per lattice site, depending on the LL index N. The CDW phases were found to prevail over FQHE alternatives for all LLs $N \geq 2$ [3]. Meanwhile, MC used a diagrammatic analysis incorporating finite temperatures to show that these HF solutions are actually exact in the limit of $N \to \infty$. Fig. 5.1a shows a cartoon of how the valence electrons are arranged in the stripe and bubble CDW states.

In the two years following the calculations of FKS and MC, the hypothesis that CDWs exist in high LLs received no experimental verification, and the quantum Hall community had good reason to be skeptical of the predictions of HF theory. After all, HF theory had previously predicted in that a Wigner solid, a cousin of the bubble CDW phase, would form at filling factors $\nu < 1$ [4]. But the subsequent discovery and explanation of the FQHE showed that the Laughlin liquid, not the electron solid, is the most prevalent ground state for $\nu < 1$ (with the exception of extremely low filling factors $\nu < 1/5$, where the Wigner solid is believed to finally form [5]). In fact, because it is

inherently a mean-field theory, HF theory is *incapable* of accounting for the fractional quantum Hall electron states.

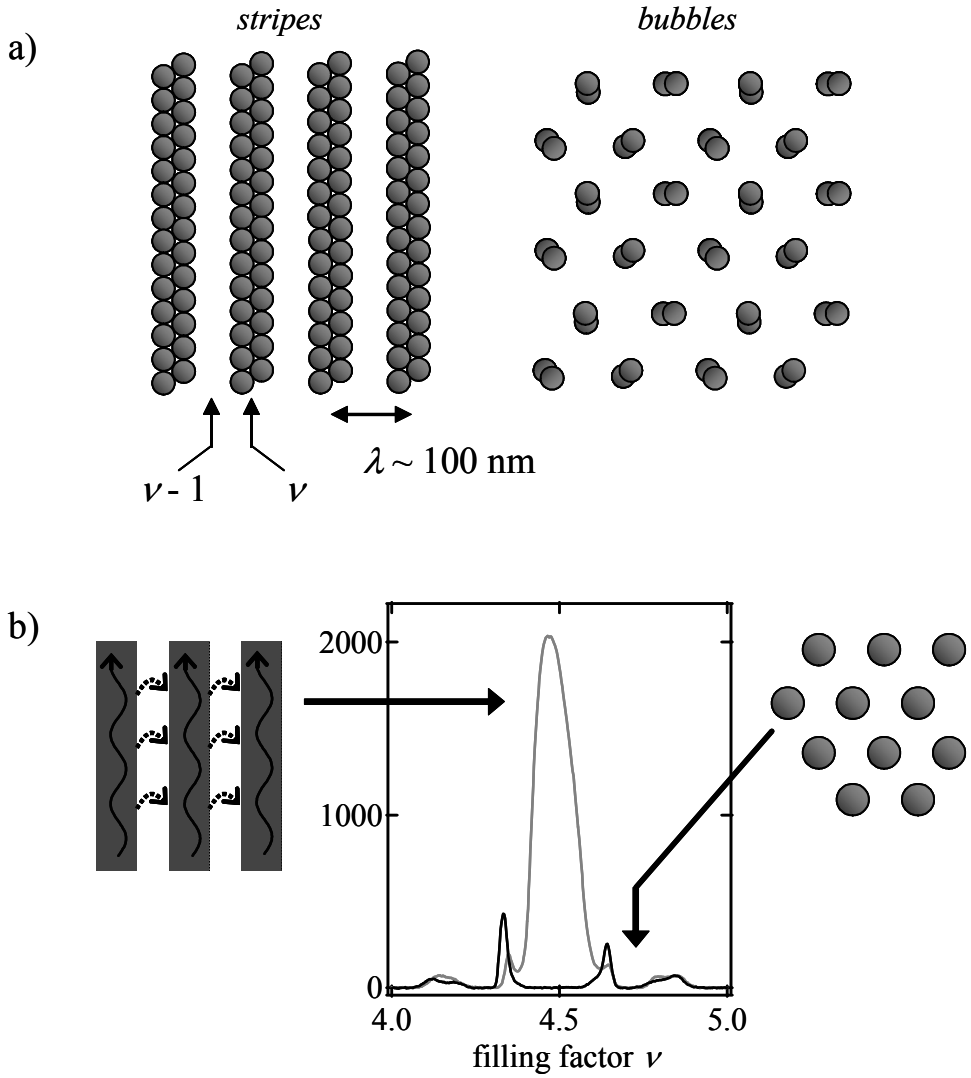

Figure 5.1: a) Cartoon showing stripe and bubble CDW phases. In the stripe phase, alternating regions of filled and empty states yield an average filling of 1/2. In the bubble phase, two electrons occupy each site of a triangular lattice. In both cases, typical modulation scales are ~100 nm. b) 50 mK R_{xx} (gray) and R_{yy} (black) from sample H-1 around $\nu = 9/2$. The stripe phase could account for the anisotropy at half-filling if electrons travel more easily along the stripes than between them. If pinned by disorder, the bubble phase would not conduct current, consistent with the RIQHE.

However, the outlook for HF theory in the quantum Hall regime changed dramatically in late 1998 when our group [6] and then Du et al. [7] first reported the anomalies of anisotropic transport and insulating phases in high LLs. Both effects can be

readily explained on a qualitative level by the CDW picture developed by FKS and MC. For example, because electrons would presumably encounter less resistance flowing along rather than across the stripes, a long-range orientation of the stripe CDW along the [110] crystal axis could account for the resistance anisotropies around half-filled high LLs. Also, the insulating nature of the RIQHE states follows immediately from the picture of the bubble CDW being pinned by disorder. With the valence LL electrons unable to participate in the 2DES conduction, the diagonal resistivity vanishes and the Hall resistivity is integrally quantized. Finally, strong evidence for CDW formation comes from the remarkable agreement of both theory and experiment that the new electron physics begins abruptly in the $N = 2$ LL and continues into higher LLs. Fig. 5.1b indicates how the stripe and bubble CDW phases are thought to account for the anisotropic transport and RIQHE states in the $\nu = 9/2$ structure.

5.2 The Physics of CDW Formation in High LLs

5.2.1 Hartree-Fock Theory

The origin of the stripe instability of two-dimensional electrons in high LLs can be understood by examining the HF energy of a unidirectional CDW whose Fourier component at a wavevector q is $\Delta(q)$. This energy is given by [1,8]

$$E_{HF} \propto \sum_{\mathbf{q}} U_{HF}(q)\left|\Delta(q)\right|^2 \qquad (1)$$

where $U_{HF}(q) = U_H(q) - U_F(q)$ is the Hartree-Fock potential in momentum space. For an unscreened Coulomb potential $v(q) = 2\pi e^2/q$, the Hartree and Fock terms are

$$U_H = \frac{e^2}{l_B}\left\{\frac{1}{ql_B}\exp\left(-\frac{q^2 l_B{}^2}{2}\right)\left[L_N\left(\frac{q^2 l_B{}^2}{2}\right)\right]^2\right\}$$

and

$$U_F = \frac{e^2}{l_B}\left\{\int_0^\infty dx J_0(q l_B x)\exp\left(-\frac{x^2}{2}\right)\left[L_N\left(\frac{x^2}{2}\right)\right]^2\right\}.$$

Here, l_B is the magnetic length and $L_N(x)$ is a Laguerre polynomial. These expressions are derived from the appropriate matrix elements of the Coulomb potential in the Landau gauge. See Section 1.2.

The Hartree, Fock, and total potentials for $N = 2$ are shown in Fig. 5.2. The optimum CDW state will have a Fourier expansion $\Delta(q)$ that minimizes the total energy E_{HF} with the constraint that the LL remains at some specified fixed partial filling factor. From equation (1), it is clear that the HF energy will be minimized if $\Delta(q)$ is *largest* where U_{HF} is *smallest*, i.e., most negative. Fig. 5.2 shows that this occurs where $ql_B \sim 1$. In other words, the optimum unidirectional CDW for $N = 2$ will have wavelength of approximately $\lambda \sim 2\pi l_B$. Note that for the CDW state to be stable, its HF energy must be negative. Because the direct part of the HF potential $U_H(q)$ is always positive (see Fig. 5.2), the exchange term $U_F(q)$ plays a crucial role in stabilizing the CDW state. In the more exact analysis of FKS, inter-LL screening is taken into account and the optimal CDW period of a general LL index N is found to be $\lambda = 2.7R_c$ where $R_c = \sqrt{2N+1}\, l_B$ is the cyclotron radius of an electron in the Nth LL. For example, at 2.5 T, where a typical 2DES would be in the $N = 2$ LL, the stripe CDW wavelength is $\lambda_{CDW} = 90$ nm.

Of course, this calculation was "rigged" to yield a stripe CDW state, and it is possible that other HF solutions exist with lower energies. Indeed, it can be shown that the stripe CDW is unstable to a small amount of modulation along the stripes in the y-direction [9,8]. Another CDW state that may be lower in energy than the stripe state is a bubble CDW with a lattice constant approximately the same as the stripe wavelength. While the stripe state dominates around half-filling, the bubble phase prevails at smaller partial fillings. This is consistent with the experimental results showing that the anisotropic phases exist around half-filling of high LLs and the insulating states are found only at lower partial fillings. However, the FKS theory predicts that *three* distinct bubble

CDWs (where the bubbles contain either one, two, or three electrons) exist at small partial fillings of the $N = 2$ LL, and that states with even more electrons per bubble exist at successively higher N.

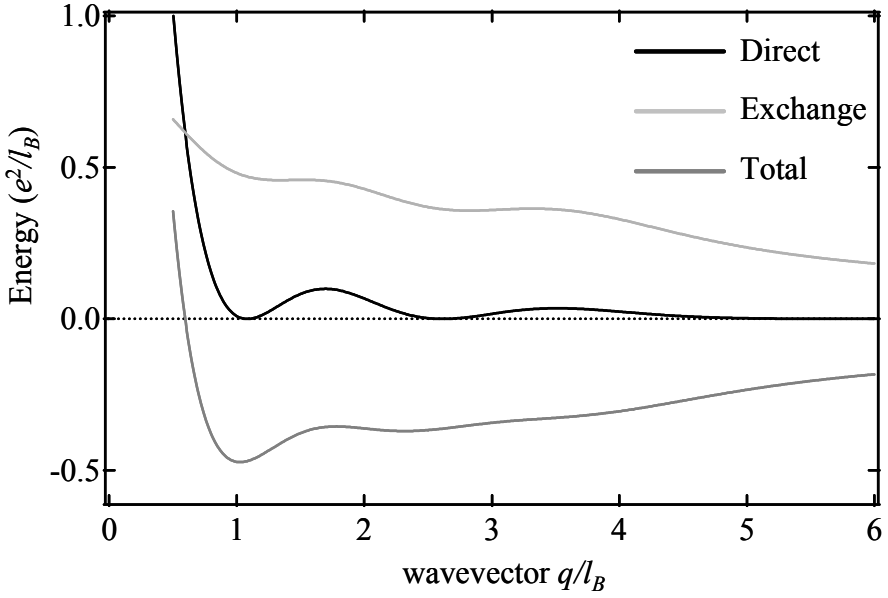

Figure 5.2: The direct, exchange, and total Hartree-Fock contributions to the energy of a stripe CDW. The deep minimum at $q/l_B \approx 1$ indicates that the stripe wavelength will be $\lambda_{CDW} \approx 2\pi l_B$.

5.2.2 An Intuitive Picture

At the qualitative level, CDW formation in high LLs can be understood as the result of a compromise between the repulsive direct and attractive exchange components of the Coulomb interaction. While the direct interaction operates at long distances as $1/r$, the advantage of the exchange interaction only occurs when the wavefunctions of two electrons overlap significantly, i.e., when the electrons are separated by less than $2R_c$. The net result is an interaction potential shown schematically in Fig. 5.3a, where a plateau forms around $r \sim 2R_c$ [10]. This plateau allows two electrons that are within a distance $2R_c$ of each other to come even closer together with only a small energetic penalty. Such a clustering may actually provide a net energetic *advantage* by reducing the repulsive interaction with neighboring electrons farther away. This instability toward clustering of electrons is the origin of the stripe and bubble CDW formation.

The reason that the CDW phases become more favorable only for high enough LLs can also be qualitatively understood [11]. As the LL index N increases, the electron wavefunctions become wider and they contain more and more nodes (see Fig. 5.3b and Section 1.2). This spreading of the electronic charge results in a rather small modulation in the actual charge density of a CDW state. The diminished charge modulation then favors CDW formation for large N by reducing the Hartree penalty of charge separation.

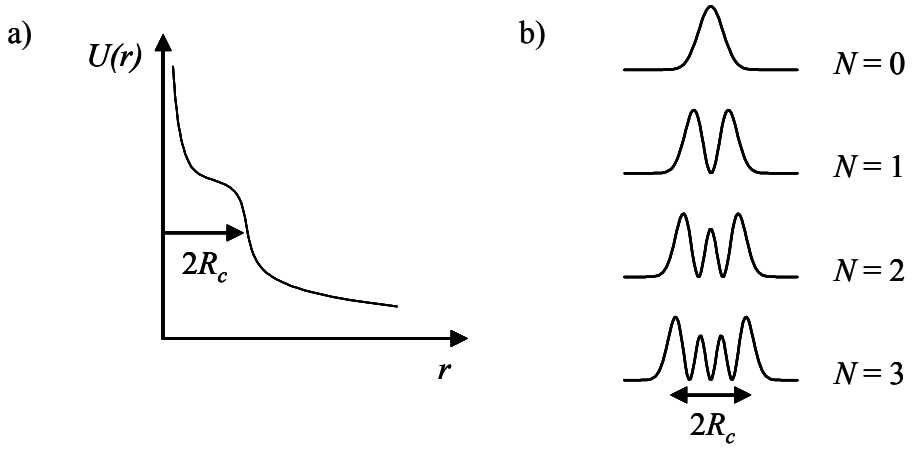

Figure 5.3: a) Real-space potential of two electrons in a single LL. The plateau extending to ~R_c arises from the advantageous exchange interaction. b) Profiles of electron probability in the Landau gauge.

5.2.3 Numerical Evidence Supporting CDW Formation

After the initial discovery of anisotropic transport and RIQHE states provided the first experimental evidence for CDW formation in high LLs, Rezayi et al. [12] and Haldane et al. [13] provided theoretical support for the CDW picture through exact diagonalization calculations of finite-sized electron systems. Although this method restricted their investigation to only a few partial filling factors in the $N = 2$ LL, clear evidence for stripe and bubble CDWs at the appropriate filling factors was obtained from the wave vector dependence of correlation functions and susceptibilities. This is in sharp contrast to the case of the lowest $N = 0$ LL, where such numerical studies show that FQHE states are prevalent.

A second numerical approach to the problem of electrons in high LLs was carried out by Shibata and Yoshioka [14] using the density matrix renormalization group (DMRG) method. They also found evidence for the stripe and bubble CDWs, and they

were able to construct a continuous phase diagram of CDWs in the $N = 2$ LL versus partial filling. Unlike the HF theory, which predicts that one-, two-, and three-electron bubble phases form on each side of half-filling of the $N = 2$ LL, the DMRG calculations predict only the one- and two-electron bubble phases. A comparison of the phase diagrams in the $N = 2$ LL for the HF theory and the DMRG theory is made in Fig. 5.4, along with the experimental phase diagram of the anisotropic and insulating regions taken from Fig. 4.9.

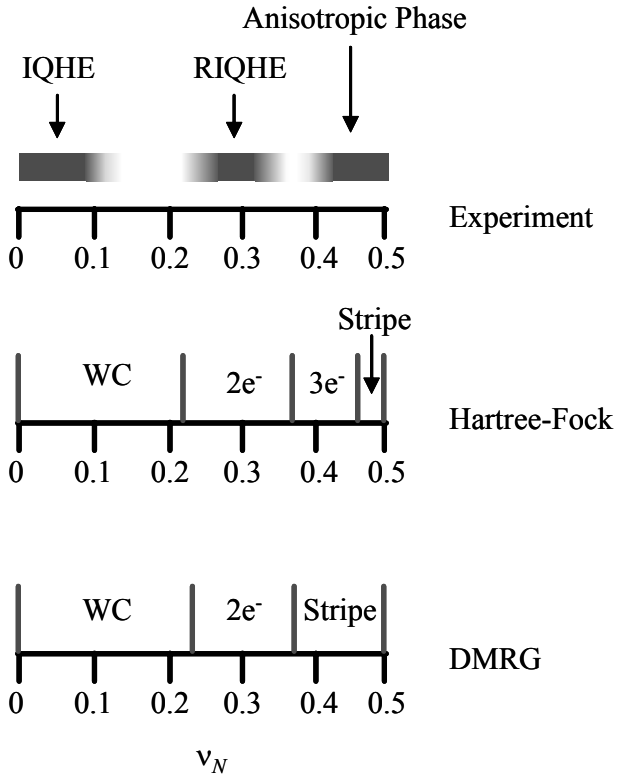

Figure 5.4: Comparison of experimental and theoretical phase diagrams of the electronic states in the $N = 2$ LL. Experimentally, only the IQHE, RIQHE, and anisotropic regimes are distinguished. Hartree Fock theory predicts two distinct bubble phases (with two and three electrons), while DMRG theory predicts only the two-electron bubble phase. Both anticipate a stripe phase near half-filling. The DMRG appears more consistent with the experimental results.

The experimental results appear to favor the DMRG predictions, if it is assumed that the one-electron bubble is hidden in the broad insulating IQHE region while the two-electron bubble is the basis of the RIQHE. (Some support for this hypothesis comes from very recent microwave conductivity measurements [15].) However, in the DMRG theory

still more bubble phases occur in the $N \geq 3$ LLs, while at those high LLs the experiments only reveal one insulating state flanking each side of half-filling.

5.3 Stripe and Bubble Motifs in Nature

Stripe and bubble CDW formation in high LLs is just one instance of the broad motif of pattern formation in nature. As with the 2DES in high LLs, the drive to satisfy two competing interactions commonly leads to a compromise of phase separation and pattern formation in a variety of physical systems. In their review on the topic, Seul and Andelman [16] cite the examples of type I superconducting films, chemical reaction-diffusion systems, organic (Langmuir) films, and Rayleigh-Benard instabilities of convection. Stripe CDWs in high-temperature superconductors are also thought to form within the two-dimensional copper oxide planes of the superconducting crystals [17].

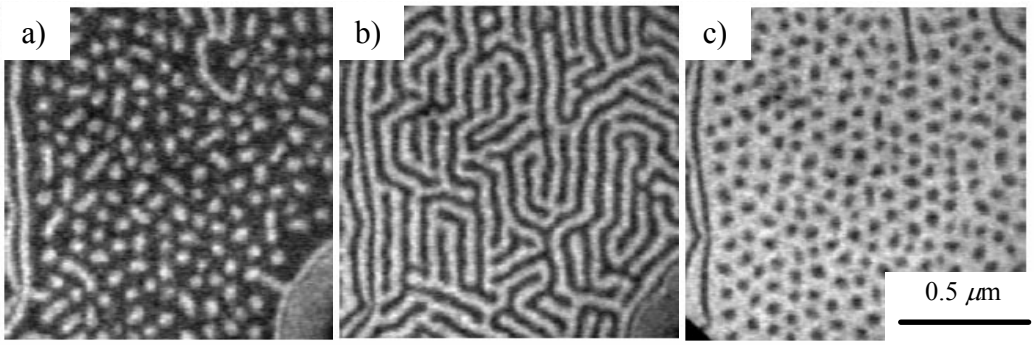

Figure 5.5: Self-assembled patterns of lead on a copper surface showing universality of bubble-stripe-antibubble transition in 2D systems. a) 0.33 monolayers of Pb; b) 0.38 monolayers; c) 0.48 monolayers. Reproduced from ref. [18] with permission by G.L. Kellogg.

One particularly striking example of bubble and stripe formation in two dimensions comes from recent low-energy electron microscope images by Plass et al. [18] of a lead coverage on a clean copper surface. Their data, shown in Fig. 5.5, demonstrate how, as the lead concentration increases, the surface pattern evolves from bubbles of lead droplets, to stripes of lead, to inverted bubbles of droplets again. This is in direct analogy to the case of electrons in high LLs which form bubbles at low partial fillings, stripes around half-filling, and bubbles again (of holes) at high partial fillings.

Furthermore, the length scales of the modulation in both the 2DES in high LLs and the lead on copper are almost identical, around 100 nm. (Unfortunately, a 2DES buried in GaAs at 25 mK is much more difficult to make images of!)

Still another vivid example of stripe formation occurs in thin layers of ferrofluids subject to a small perpendicular magnetic field. Following Rosensweig et al. [19], we built a Hele-Shaw apparatus for the purposes of demonstrating this example of pattern formation, and the results are shown in Fig. 5.6.

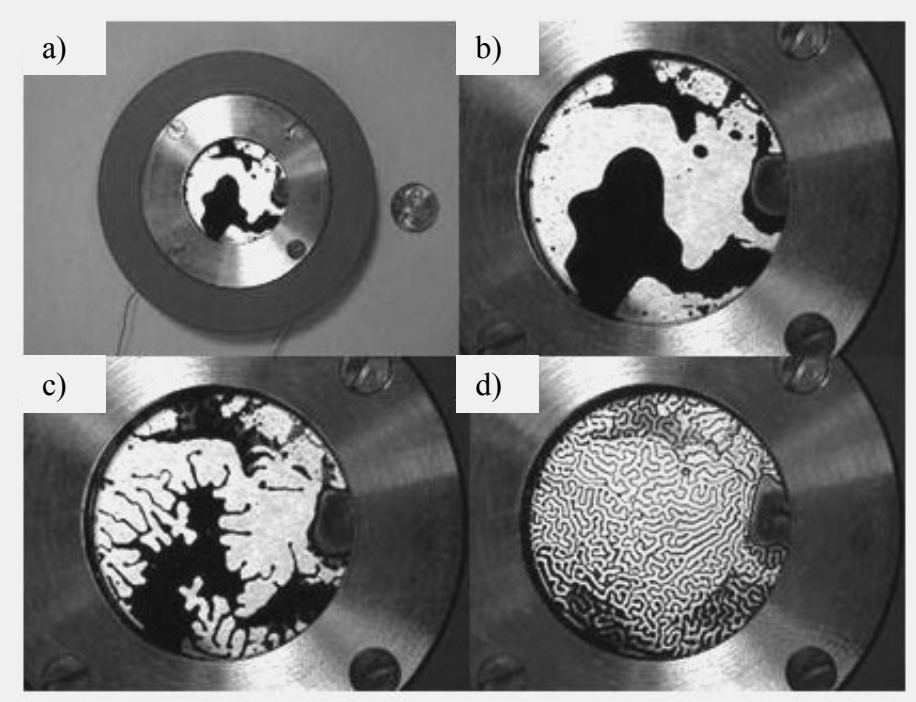

Figure 5.6: Photographs of homemade Hele-Shaw cell showing labyrinthine pattern formation in a thin layer of ferrofluid subjected to a modest magnetic field. a) View of entire cell and solenoid. b) through d): increasing the magnetic field to ~150 Gauss yields the stripe-like pattern.

The Hele-Shaw cell consists of two glass plates separated by a thin rubber gasket and containing a few grams of ferrofluid in a dilute isopropanol/water solution. The ferrofluid is an oily colloidal suspension of micron-sized magnetite particles. Surrounding the cell is a home-built solenoid coil capable of producing magnetic fields up to ~200 Gauss. As Fig. 5.6 shows, the ferrofluid develops an elaborate labyrinthine, or stripe, pattern on the millimeter length scale when the magnetic field is applied. In this case, the competing interactions driving the evolution of the ferrofluid are the dipole-

dipole repulsion of the magnetized fluid and the attractive force due to the fluid's surface tension. Unlike the stripe CDW in high LLs, the ferrofluid stripes are on macroscopic scales and are easily visualized.

---

1 M.M. Fogler, A.A. Koulakov, and B.I. Shklovskii, Phys. Rev. B **54**, 1853 (1996); A.A. Koulakov, M.M. Fogler, and B.I Shklovskii, Phys. Rev. Lett. **76**, 499 (1996).

2 R. Moessner and J.T. Chalker, Phys. Rev. B **54**, 5006 (1996).

3 M.M. Fogler, A.A. Koulakov, Phys. Rev. B **55**, 9326 (1997).

4 H. Fukuyama, P.M. Platzman, and P.W. Anderson, Phys. Rev. B **19**, 5211 (1979).

5 For a summary, see the chapters by H.A. Fertig and M. Shayegan in *Perspectives in Quantum Hall Effects*, ed. S. Das Sarma and A. Pinczuk (John Wiley, New York 1997).

6 M.P. Lilly, K.B. Cooper, J.P. Eisenstein, L.N. Pfeiffer, and K.W. West, Phys. Rev. Lett. **82**, 394 (1999).

7 R.R. Du, D.C. Tsui, H.L. Stormer, L.N. Pfeiffer, K.W. Baldwin, and K.W. West, Solid State Comm. **109**, 389 (1999).

8 D. Yoshioka, *The Quantum Hall Effect* (Springer, Berlin 2002).

9 E. Fradkin and S. Kivelson, Phys. Rev. B **59**, 8065 (1999).

10 M.O. Goerbig and C. Morais Smith, http://xxx.lanl.gov/abs/cond-mat/0301329

11 F. von Oppen, B.I. Halperin, and A. Stern, *Advances in Quantum Many-Body Theory*, vol. 3, ed. R.F. Bishop, N.R. Walet, and Y. Xian (World Scientific, Singapore 2000).

12 E.H. Rezayi, F.D.M. Haldane, and K. Yang, Phys. Rev. Lett. **83**, 1219 (1999).

13 F.D.M. Haldane, E.H. Rezayi, and K. Yang, Phys. Rev. Lett. **85**, 5396 (2000).

14 N. Shibata and D. Yoshioka, Phys. Rev. Lett. **86**, 5755 (2001).

15 R.M. Lewis, P.D. Ye, L.W. Engel, D.C. Tsui, L.N. Pfeiffer, and K.W. West, http://xxx.lanl.gov/abs/cond-mat/0205200; Y.P. Chen, R.M. Lewis, L.W. Engel, D.C. Tsui, P.D. Ye, L.N. Pfeiffer, and K.W. West, http://xxx.lanl.gov/abs/cond-mat/0301579.

16 M. Seul and D. Andelman, Science **267**, 476 (1995).

17 E.W. Carlson, V.J. Emery, A.S. Kivelson, and D. Orgad in *The Physics of Superconductors*, ed. K.H. Bennemann and J.B. Ketterson (Springer, Berlin 2003); also at http://xxx.lanl.gov/abs/cond-mat/0206217.

18 R. Plass, J.A. Last, N.C. Bartelt, G.L. Kellogg, Nature **412**, 875 (2001).

19 R.E. Rosensweig, M. Zahn, and R. Shumovich, J. Magnetism Magnetic Mater. **38**, 127 (1983); R.E. Rosensweig, *Ferrohydrodynamics* (Cambridge University Press, Cambridge 1985).

Chapter 6:
Transport Models of the Anisotropic Electronic Phase

6.1 Classical Transport in an Anisotropic Medium

6.1.1 Converting Resistance to Resistivity

Chapter 3 showcased examples of anisotropic transport in several different samples, and the degree of anisotropy, measured by the ratio R_{xx}/R_{yy}, varied greatly among them. At $\nu = 9/2$ and $T = 50$ mK, for example, Fig. 3.8 shows that the anisotropy ratio in sample B-1 is about 80, while in H-1 it is greater than 2000 but too large to be measured because R_{yy} vanishes to within the measurement resolution ($R_{yy} \leq 1\ \Omega$). These results suggest two important questions. First, do the vastly different anisotropy ratios reflect important differences in the electron phases of the two samples, for example in the properties of the stripe CDW that is thought to cause the anisotropy? And second, is the [110] transport in H-1 dissipationless in the sense that the IQHE is dissipationless?

The answer to both questions is "no," and an explanation comes from an important analysis by Simon of how an anisotropic resistivity tensor affects the current distribution in square geometries [1]. Simon assumed that the 2DES possesses a homogeneous resistivity tensor

$$\boldsymbol{\rho} = \begin{pmatrix} \rho_{xx} & \rho_{xy} \\ -\rho_{xy} & \rho_{yy} \end{pmatrix}, \qquad (1)$$

where the principal axes have been chosen to lie along the square's edges. Then, by solving the classical electrostatics problem of current being injected and withdrawn from point contacts placed at opposite midpoints of the square, Simon found that the measured longitudinal resistance of the square sample is

$$R_{xx} = \frac{4}{\pi}\sqrt{\rho_{xx}\rho_{yy}} \sum_{n=1,3,5\ldots} \left[n \sinh\left(\sqrt{\frac{\rho_{yy}}{\rho_{xx}}} \frac{\pi n}{2} \right) \right]^{-1} . \qquad (2)$$

The equivalent solution for R_{yy} can be found simply by interchanging ρ_{xx} and ρ_{yy}. Note that these solutions can be numerically inverted so that a given R_{xx} and R_{yy} will uniquely determine ρ_{xx} and ρ_{yy}, and vice versa.

The most important property of this conversion is that R_{xx}/R_{yy} can be *exponentially* sensitive to the ratio ρ_{xx}/ρ_{yy}. To show this, Fig. 6.1 displays R_{xx}/R_{yy} versus ρ_{xx}/ρ_{yy} on a log-linear graph. Note that as ρ_{xx}/ρ_{yy} changes from 1 to only 30, R_{xx}/R_{yy} increases by four orders of magnitude! Another interesting aspect of Simon's solution is that the anisotropy in resistivity can be removed from the problem by rescaling the aspect ratio of the square sample. Defining $\zeta = (\rho_{xx}/\rho_{yy})^{1/2}$, the transformation $y \to \zeta y$ will result in an equivalent problem but with an *isotropic* resistivity $\rho = \rho_{yy}$. In other words, the problem of finding the current distribution in a square with an anisotropic resistivity tensor is equivalent to finding the distribution in a rectangle with an aspect ratio ζ.

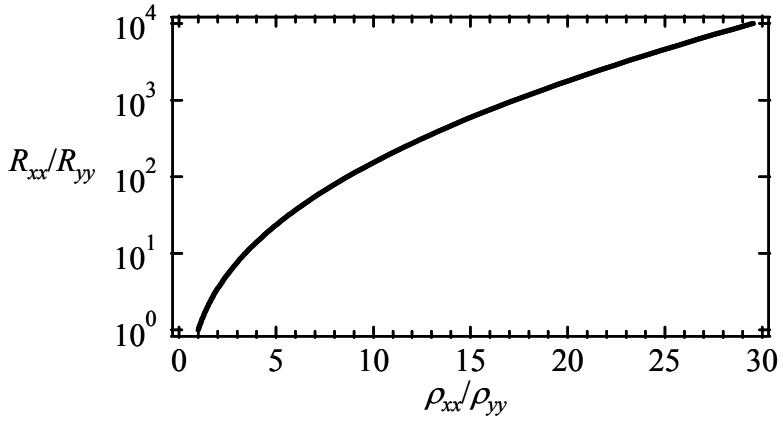

Figure 6.1: Relationship between the anisotropy ratio of resistance versus resistivity, calculated from eq. (2). Because of current-channeling effects, a modest resistivity ratio can result in a huge resistance ratio.

6.1.2 Resistance Anisotropy and Current Channeling

The exaggeration of the anisotropy ratio in square samples comes from how an anisotropic resistivity tensor affects the current density distribution in those samples. Fig. 6.2 shows contour lines of constant current for three different circumstances, calculated using the Finite Element Method (FEM) package of the Matlab software program. The left-hand image corresponds to current flowing in the **x** direction when the resistance is isotropic: $\rho_{xx} = \rho_{yy}$. The center and right images show current flowing in the **x** and **y** directions for $\rho_{xx}/\rho_{yy} = 10$.

For a fixed current through the square, the longitudinal resistance (R_{xx} or R_{yy}) is proportional to the voltage difference between two adjacent corners of the sample. This voltage difference, in turn, is given by either

$$V_{xx} = \rho_{xx} \int J_x dx \text{ or } V_{yy} = \rho_{yy} \int J_y dy , \qquad (3)$$

when the net current flow is along **x** or **y**, respectively. The line integrals run between adjacent corners of the square, where the voltage contacts are located. These expressions show that the ratio V_{xx}/V_{yy}, and hence R_{xx}/R_{yy}, is determined both by ρ_{xx} and ρ_{yy} *and* by the integrals of the current densities along a path connecting one voltage contact to the other.

Fig. 6.2 shows that when $\rho_{xx}/\rho_{yy} = 10$, the current distribution in the hard direction (middle panel) is only slightly more spread out than in the case where $\rho_{xx}/\rho_{yy} = 1$ (left panel). On the other hand, when the current flows along the easy direction (right panel), the current is strongly collimated into the center of the sample. Therefore, the current density J_y along the sample boundary is exponentially small, and from equation (3), R_{yy} becomes greatly suppressed.

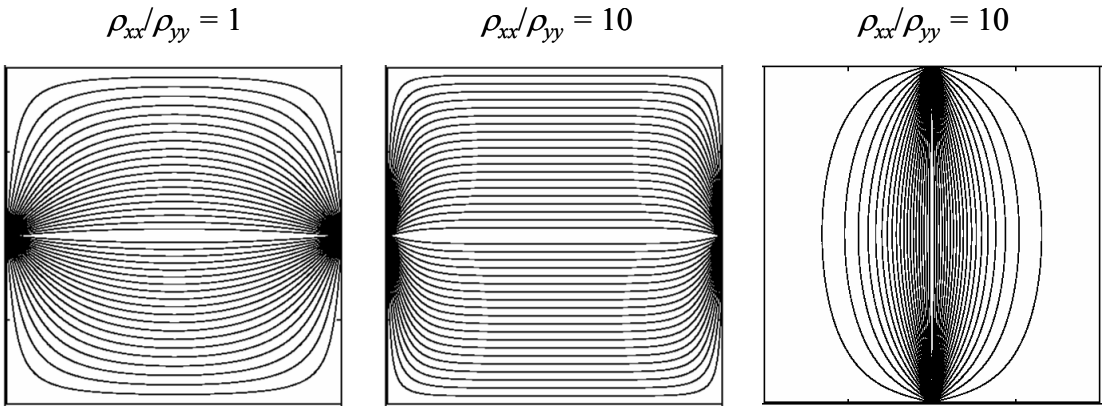

Figure 6.2: Left: isotropic resistivity and current flow along **x**. Middle: anisotropic resistivity $\rho_{xx}/\rho_{yy} = 10$ and current flow along **x**. The current is somewhat more spread out. Right: anisotropic resistivity $\rho_{xx}/\rho_{yy} = 10$ and current flow along **y**. The current distribution is heavily collimated away from the sample sides.

This effect can also be understood using the length-scaling principle mentioned above: that a square region with an anisotropic resistivity is equivalent to a rectangle with an isotropic resistivity. For example, if $\rho_{xx}/\rho_{yy} = 20$, then measuring R_{yy} is equivalent to measuring the four-terminal longitudinal resistance using the contact configurations shown in Fig. 6.3, where the voltage probes are quite far removed from the current contacts. This current-channeling effect is the likely reason that the easy resistance at $\nu = 9/2$ in H-1 is essentially zero. Rather than indicating dissipationless transport, the small value of R_{yy} simply reflects the fact that the anisotropic resistivity ratio exceeds about 20, so that $R_{xx}/R_{yy} > 2000$.

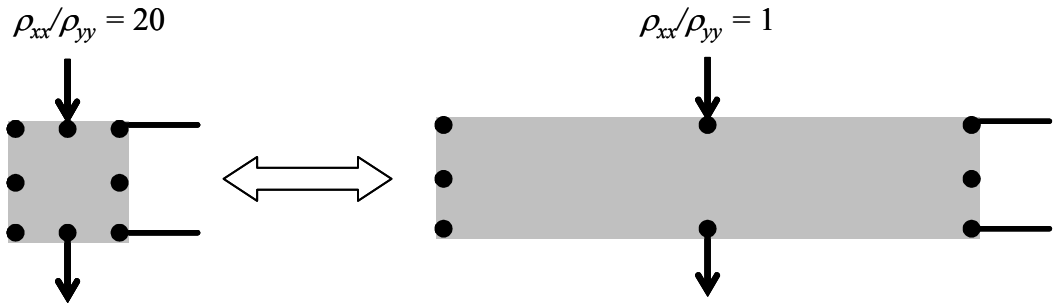

Figure 6.3: Equivalence between a square geometry with an anisotropic resistivity ratio of 20 and a rectangular geometry with an isotropic resistivity but an aspect ratio of $(20)^{1/2}$.

6.1.3 Problems with Resistivity Conversion

The derivation of equation (2) relies on some idealizations that are not met in practice. For example, the contacts on real samples are not point contacts, and their alignment is only as good as can be done by hand (see Fig. 2.10). Both of these issues will affect the current distribution, but a more drastic approximation of Simon's analysis is that the 2DES possesses a homogeneous (if anisotropic) resistivity tensor in the first place. Because of the inevitable disorder present, there must be some spatial dependence of ρ. Indirect experimental evidence of inhomogeneous resistivity tensors is plentiful in the form of contact-dependent resistance measurements. For example, longitudinal resistance measurements made on opposite sides of the same sample typically vary up to about 25%. This variation is probably too large to be caused by misaligned or finite-sized contacts. Rather, we believe that the differences in resistance from one side of the sample to the other reflects inhomogeneities in the conduction pathway of the current.

A final important way in which Simon's analysis is an idealization is that it neglects the known quantum nature of electron transport in the quantum Hall regime. For example, in an IQHE state, where $\rho_{xx} \approx \rho_{yy} \approx 0$, the chiral edge channels of the filled lower LLs are believed to contribute to the current conduction. Between IQHE states where the resistivities become finite, such as at $\nu = 9/2$, these edge channels still may participate in the current conduction, along with a parallel conduction channel corresponding to "bulk" current flow through the sample's interior. One consequence of this is that in thin Hall bar geometries the measured resistivities do not scale with the width of the bar because some fraction of the current is carried by the edge states rather than the bulk of the 2DES [2]. Predicting the effect of these edge states is made difficult because they are not necessarily in equilibrium with each other, nor with the bulk current-carrying channel [3,4]. In small geometries and high mobility samples especially, this complicated interaction between edge and bulk current flow can result in nonlocal resistances that defy a model based on a simple homogeneous resistivity tensor [5]. In the large, square geometries that have primarily been used for the experiments described in this thesis, these effects are likely minimized but are not necessarily negligible.

6.1.4 Example of Resistivity Conversion

With these caveats in mind, the resistance/resistivity analysis can be related to some experimental results. First, the geometrical exaggeration of the resistance anisotropy in square samples can account for the reduced anisotropy that is observed in Hall bar structures (see Section 3.3). Because they are relatively long and thin, Hall bars do not suffer as much from the current-channeling effect that plagues square samples. Within a classical transport model, the measured resistance of a Hall bar is given by $R_{xx} = \rho_{xx}(L/W)$, where L is the distance between voltage probes and W is the width of the current channel.

Thus the measured anisotropy ratio of $R_{xx}/R_{yy} \approx 6$ at $\nu = 9/2$ and $T = 25$ mK in the Hall bar samples B-2 and 3, described in Section 3.3, should give a rough measure of the underlying resistivity ratio ρ_{xx}/ρ_{yy}. Working backward from the observed ratio of $R_{xx}/R_{yy} \approx 80$ in B-1, the expected resistivity ratio is only $\rho_{xx}/\rho_{yy} \approx 8$, which is only about 30% off from the ratio derived from the Hall bar data. This is not too bad considering the manifold approximations that went into deriving equation (2) and the normal variation in the measured values of R_{xx} and R_{yy} from cool-down to cool-down. In the case of the Hall bars C-9 and 10, also discussed in Section 3.3, their resistance ratio was 13 at $T = 25$ mK, compared to a factor of 200 in the square sample C-8. Based on the data of Fig. 6.1, the anisotropy ratio of 200 could be generated by a resistivity ratio of only about 11, which is in even better agreement than the case of the experiments on the samples B-1, 2, and 3.

The effect of converting from resistance to resistivity over a broad magnetic field range, not just at $\nu = 9/2$, is shown in Fig. 6.4. Fig. 6.4a shows 25 mK transport data R_{xx} and R_{yy} from sample B-1 over several high LLs. The anisotropy ratio at $\nu = 9/2$ in this case is $R_{xx}/R_{yy} \approx 45$. (In the different cool-down of Fig. 3.4, the ratio was 80.) In Fig. 6.4b, this same data is plotted after having been converted to resistivities ρ_{xx} and ρ_{yy}. The diminished anisotropy in the half-filled high LLs is evident. Also, the minima at half fillings in the easy direction are not as deep in the ρ_{yy} data as they are in the R_{yy} data.

In Fig. 6.4c, the resistivities derived from Hall bar transport data from the samples B-2 and 3 are shown. These were converted from the resistances by taking into account the factor $L/W \sim 2/3$. Like the data of Fig. 6.4b, the resistivities in the easy direction do

not show deep minima in the half-filled high LLs. Also, the resistivity ratios in Fig. 6.4b are closer to those of the converted resistivities of the square sample than the original resistances. However, the overall the values of ρ_{xx} and ρ_{yy} in Fig. 6.4c are significantly smaller than in the resistivities of Fig. 6.4b. The origin of that difference may be from a number of factors, including an imperfect scaling from R to ρ, or from the fact that the samples were taken from separate areas of the parent wafer B. Nonetheless, we conclude that the resistances measured in square samples are poor representations of a sample's underlying resistivities. To determine ρ_{xx} and ρ_{yy}, either the mathematical conversion of equation (2) must be performed, or Hall bar measurements must be made.

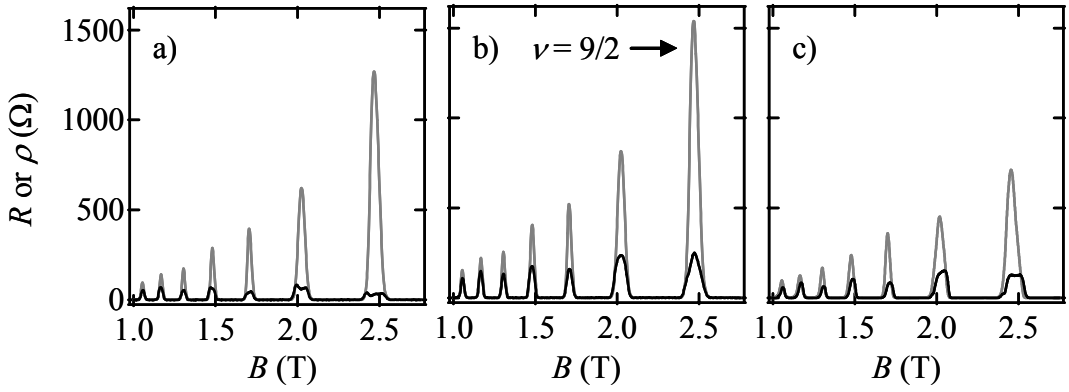

Figure 6.4: a) 25 mK R_{xx} (gray) and R_{yy} (black) data for sample B-1. b) Calculated ρ_{xx} (gray) and ρ_{yy} (black) values from a) using eq. (2). c) Estimated resistivities ρ_{xx} (gray) and ρ_{yy} (black) based on 25 mK Hall bar measurements from the samples B-2 and B-3.

The effect of current channeling due to an anisotropic resistivity tensor in high LLs has also been investigated recently by Willett et al. [6]. By using a square geometry with many contacts, closely spaced, placed around its edges, Willett et al. measured transport characteristics that are consistent with the current distribution spreading out when driven along $[1\,\bar{1}0]$ and collimating when driven along $[110]$. This is in agreement with the data presented here.

6.2 Quantum Transport of Stripe CDW Phase

6.2.1 Resistivity Product Rule

Apart from the classical treatment of current conduction described so far, significant theoretical work has been done to describe the transport properties of the stripe CDW model of half-filled high LLs.

The first attempt to formulate a transport theory of the stripe CDW state was made by MacDonald and Fisher (MF) [7]. In that work, the electronic structure in the valence LL is assumed to be a perfect unidirectional stripe CDW. Ignoring any defects in the stripes due to impurities or thermal fluctuations, MF further assumes that the stripes carry current along their boundaries. These are essentially the same kind of chiral edge states normally present along the sample boundaries in IQHE states. In this model, dissipation and transport orthogonal to the stripe CDW direction occurs via scattering events between adjacent edge channels, characterized by the hopping times τ_e and τ_h for electrons transversing filled (electron) or empty (hole) regions, respectively. To assist in visualizing this picture of stripe transport, Fig. 6.5 shows a cartoon of how current is carried in the MF model.

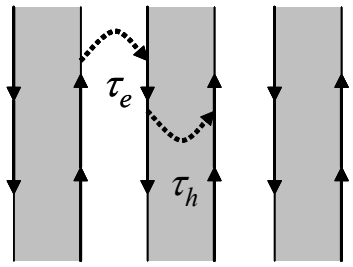

Figure 6.5: Schematic transport and scattering mechanisms based on MF theory. Electrons travel along one-dimensional chiral "edge states" running along the stripes. Scattering between these states (with relaxation times τ_e and τ_h) affects the net conductivity of the system.

Furthermore, the MF theory derives formulas for the components of a bulk resistivity tensor that depend in general on the unknown quantities τ_e and τ_h. However, at exactly half-filling, where the filled and empty regions of the stripe CDW are assumed to

be equivalent by particle-hole symmetry, the scattering times are equal and drop out of the formulas. This allows parameter-free comparisons to experiments to be performed. Assuming that the stripes lie either along **y**, so that the hard direction is along **x**, the prediction of the MF theory is:

$$\rho_{xx}\rho_{yy} = \left(\frac{h}{e^2}\right)^2 \frac{1}{\left\{\left([\nu]+1\right)^2 + [\nu]^2\right\}^2}, \qquad (4)$$

where $[\nu]$ is the largest integer less than ν.

To test the "product rule" of equation (4),Fig. 6.6 shows the relevant data for sample B-1. In Fig. 6.6a, the resistivities ρ_{xx} and ρ_{yy} are shown versus magnetic field for the filling factor range $4 < \nu < 11$ and at a temperature of 25 mK. These data are the same as those shown in Fig. 6.4b, and they were obtained by converting from resistance to resistivity using equation (2). In Fig. 6.6b, the resistivities over the same range are shown at 150 mK instead. At this elevated temperature, of course, no significant anisotropy exists in the high LLs. For both sets of data, the resistivities at half-fillings of the high LLs were multiplied together to form the product $\rho_{xx}\rho_{yy}$. (The value of ρ_{xx} at half-filling was taken to be the peak value in the case of the 25 mK data, and in some cases the peak is slightly shifted away from the half-filling point calculated by the average sample density. The uncertainty in resistivity between the two methods is no more than about 5%, which is well within the errors expected from inhomogeneities in the resistivity tensor.) The product $\rho_{xx}\rho_{yy}$ is plotted for several half-integer values of ν in Fig. 6.6c. The 25 mK values are blue, while the 150 mK values are red. Also shown, in black, are the theoretically predicted values from equation (4).

There is excellent agreement between the theory and experiment in Fig. 6.6c for the 25 mK data, where the anisotropy is well developed. The deviation from the theory is especially small considering that the resistivities were obtained indirectly from the raw resistance values. Also, an alternating overshoot/undershoot trend is visible in the experimental product $\rho_{xx}\rho_{yy}$ which is reminiscent of the spin-splitting asymmetry discussed previously in Section 3.4. Aside from the very good match between the theory

and experiment at 25 mK, Fig. 6.6c also shows that equation (4) does not work at 150 mK, when no substantial anisotropy is present. Because the anisotropy is hypothesized to signify the presence of an oriented stripe CDW, the fact that the product rule only holds when the anisotropy is well-developed suggests that a stripe CDW is indeed forming, and that the transport theory of MF is valid.

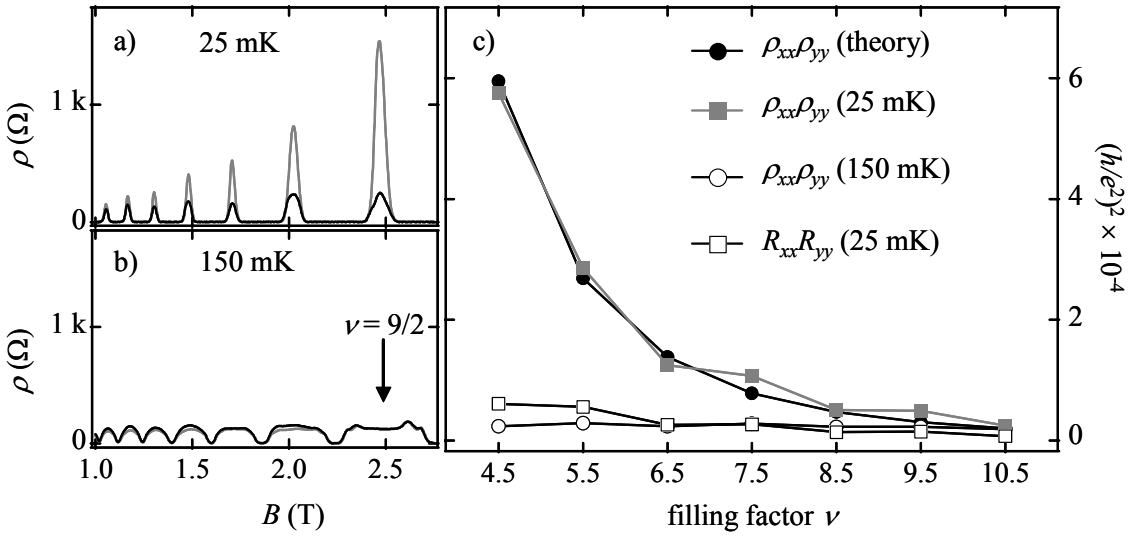

Figure 6.6: Product rule analysis of sample B-1. a) Resistivities ρ_{xx} (gray) and ρ_{yy} (black) calculated from 25 mK transport data using eq. (2). b) Resistivities at 150 mK. c) Comparison of the product rule theory eq. (4) with the 25 mK product $\rho_{xx}\rho_{yy}$, the 150 mK product $\rho_{xx}\rho_{yy}$, and the 25 mK product $R_{xx}R_{yy}$. Excellent agreement with the theory only occurs for the resistivity product at 25 mK, where the anisotropy is well-developed.

As another test of equation (4) for the sample B-1, raw resistance product $R_{xx}R_{yy}$ is shown in Fig. 6.6. Like the high temperature data, these values do not match the theoretical prediction of equation (4) at all. This fact attests to the importance of converting resistances to resistivities before comparing experiment to theory in the context of the MF analysis.

Next, consider how the product rule applies to the data of sample H-1, shown in Fig. 6.7a. There, the resistances R_{xx} (top) and R_{yy} (bottom) are shown versus magnetic field over the range $4 < \nu < 7$ for $T = 50$ mK. (Note that the two traces have different vertical scales). In each of the half-filled LLs shown, the anisotropy is so strong that R_{yy} actually vanishes, to within the experimental resolution of about 3 Ω, around $\nu = 9/2$,

11/2, and 13/2. According to the MF theory, then, the stripe CDW must be very well aligned along **y** to yield such a large anisotropy. Ideally, the product rule of equation (4) could be tested against the data in Fig. 6.7a. However, the fact that $R_{yy} \approx 0$ at half-fillings means that the geometrical conversion to resistivity for the square sample cannot be performed. Plus, no Hall bar measurements have been made from the parent wafer of this sample that could allow a measurement of ρ_{yy}.

Nonetheless, the data of Fig. 6.7a can still be checked for *consistency* with the product rule of equation (4). Fig. 6.7b shows the relationship between R_{xx} and R_{yy} that must hold at the filling factors $\nu = 9/2$, 11/2, and 13/2 if the equation (1) is valid. Interestingly, for the range covered in Fig. 6.7b, the dependence of R_{yy} on R_{xx} is very well-approximated as an exponential. For example, in the case of $\nu = 9/2$, a good fit to the line shown in Fig. 6.7b is $R_{yy} \approx 872*\exp(-R_{xx}/386)$, where R_{yy} and R_{xx} are measured in ohms. This exponential dependence ultimately comes from the current-channeling effect in the easy direction as discussed in Section 6.1.

Based on this relationship, the validity of the product rule for this sample may be checked for consistency by asking: Given that $R_{yy} < 3\ \Omega$ at $\nu = 9/2$, 11/2, and 13/2, are the values of R_{xx} large enough for the product rule of equation (4) to be true? For example, from Fig. 6.7b, if $R_{yy} < 3\ \Omega$ at $\nu = 9/2$, then R_{xx} must be larger than about 2200 Ω. That value is marked by a horizontal arrow above the $\nu = 9/2$ point in the R_{xx} data of Fig. 6.7a. While R_{xx} apparently does not quite reach 2200 Ω at $\nu = 9/2$, it comes quite close. Similarly, the arrows above the $\nu = 11/2$ and 13/2 peaks in Fig. 6.7 correspond to the R_{xx} values at those filling factors that are necessary account for R_{yy} to be less than 3 Ω. While the $\nu = 11/2$ peak is about a factor of two smaller than necessary for the product rule to be true, the $\nu = 13/2$ peak is large enough for equation (1) to hold. Thus the results are somewhat mixed for the sample H-1. The 11/2 data seems to rule out the validity of the product rule, but the 9/2 and 13/2 data show fairly good consistency. The apparent vanishing of R_{yy} in high LLs is therefore does not signify dissipationless transport in the sense of the IQHE; rather, the degree of anisotropy is just very large.

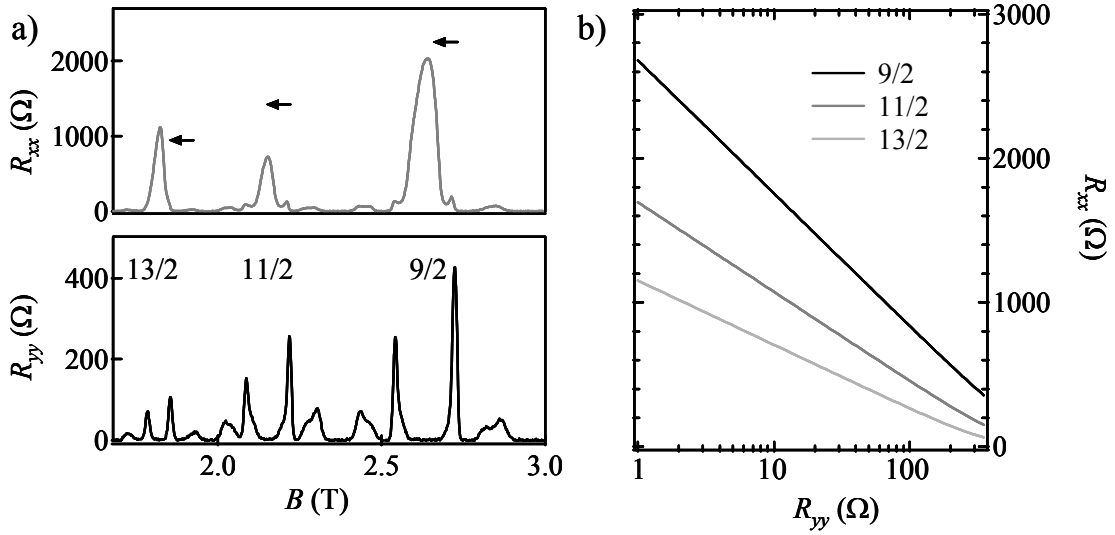

Figure 6.7: a) 50 mK R_{xx} (top) and R_{yy} (bottom) data of sample H-1. For product rule eq. (4) to hold, the peaks in R_{xx} at $\nu = 9/2$, 11/2, and 13/2 must exceed values indicated by the arrows in order for R_{yy} to be less than 3 Ω. b) Relationship between R_{xx} and R_{yy} assuming that the product rule and the current distribution analysis are correct.

One problem with comparing the experimental data to the predictions of the MF theory is that the resistance/resistivity conversion may be unreliable because of the various approximations made in its derivation. A more fundamental problem, however, is that the MF theory itself makes some unwarranted assumptions. One is that quantum interference effects during the stripe-stripe scattering events are unimportant, a justifiable assumption if the electrons travel a long distance before hopping between the stripe edge states [8]. The MF theory makes a prediction for this scattering length, $l \approx R_c(\rho_{xx}/\rho_{yy})^{1/2}$. The resistivity ratio in B-1, for example, is only around 7, so l is only a couple of cyclotron radii, or about 0.2 μm. This length is on the order of the stripe wavelength, meaning that quantum effects during scattering should be important [9].

6.2.2 Transport in Disordered Stripes

A possible reason for the reduced degree of resistivity anisotropy, given that the scattering length of electrons is expected to be very many cyclotron radii, is that the stripe CDW is not uniformly oriented throughout the whole sample. Indeed, the assumption by

MF of topologically perfect stripes, while being important to derive several transport properties, is a probable oversimplification. A more general model is that the stripes are variably oriented throughout the macroscopic sample, with only a net orientation over large distances caused by the weak crystal symmetry-breaking field. This picture actually anticipates the stripe nematic liquid crystal phase which will be discussed at length in Chapter 9, although here the stripe regions are assumed to be static.

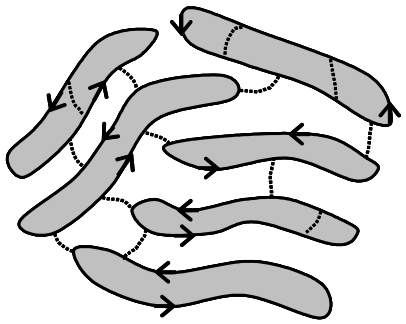

Figure 6.8: Schematic diagram of disordered stripe regions used as the basis of the OHS theory. Transport occurs through scattering between the stripe edges and results in the semicircle law of eq. (5).

The transport properties of this imperfect, static stripe CDW system have been explored by von Oppen, Halperin and Stern (OHS) [8]. Like the theory of MF, OHS assumed that electron transport occurs via the chiral edge states of the individual stripe regions, and that hopping between adjacent stripes occurs. But unlike the MF model, the distributions of the filled and empty regions can be random. Fig. 6.8 shows a cartoon picture of the situation, and the result of the OHS theory is a prediction of a general relationship among the components of the conductivity tensor:

$$\sigma_{xx}\sigma_{yy} + (\sigma_{xy} - \sigma_0)^2 = (e^2/2h)^2, \qquad (5)$$

where $\sigma_0 \equiv (e^2/2h)(2N + 1)$. This relationship, dubbed the "semicircle law," has also been derived within the context of a model for FQHE transport [10]. In fact, the semicircle law has been applied generally to quantum Hall system that consist of phase-separated regions of incompressible regions of the 2DES [11]. Unlike the predictions of the MF theory, equation (5) is parameter-independent *throughout* the *N*th LL, not just at the half-

filling point. However, at half-filling the two models are in agreement. This suggests that the good agreement between experiment and the product rule, for example in Fig. 6.6, does not depend on the assumption that the stripe CDW is uniformly oriented and perfectly aligned throughout the whole sample.

Fig. 6.9 summarizes how well the semicircle law applies to sample B-1, which already showed good agreement with the MF theory at half-filling of high LLs. In Fig. 6.9a, the top panel shows R_{xx}, R_{yy}, and R_{xy} data taken at 150 mK and plotted versus filling factor over the range $4 < \nu < 9$. These resistances were first converted to resistivities using the geometrical conversion from Section 6.1, and then to conductivities by inverting the 2×2 resistivity tensor. (A small offset and scale change was made to the R_{xy} data to ensure accurate quantization on the Hall plateaus.) Finally, the conductivity tensor components were combined and plotted in the bottom panel of Fig. 6.9a as $(\sigma_{xx}\sigma_{yy})^{1/2}$ versus σ_{xy} in units of e^2/h. Note that the range of both ν and σ_{xy} coincide in the x-axis of the figure. The data is shown in black, while the prediction of the semicircle law, equation (5), consists of the dashed semicircles. The agreement between the experiment and theory in the 150 mK data is not good, especially for $\nu < 7$. On the other hand, Fig. 6.9b shows a similar set of transport and semicircle data for the same sample but at 25 mK. This time, the agreement with the theory is impressive, particularly for the region around $\nu = 9/2$ and 13/2. The apparently systematic asymmetry about the half-integer points of σ_{xy} ultimately arises from the fact that as R_{xy} moves from one plateau to the next, it reaches the midpoint of the two plateaus substantially earlier than the half-filling point. More careful measurement of R_{xy} covering both positive and negative magnetic fields might yield a better agreement with the theory. Alternatively, a particle-hole asymmetry within the LL or inhomogeneities in the resistivity tensor may be at work.

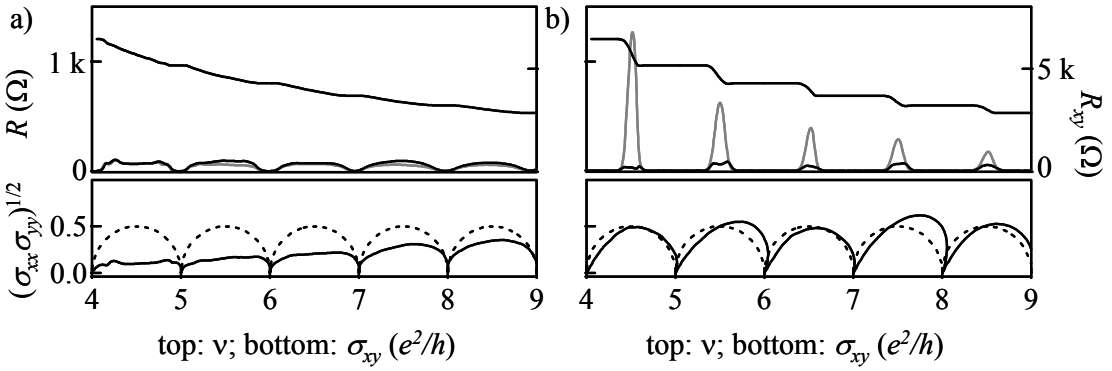

Figure 6.9: a) Top: 150 mK R_{xx} (gray), R_{yy} (black), and R_{xy} data versus filling factor in sample B-1. Bottom: resulting $(\sigma_{xx}\sigma_{yy})^{1/2}$ versus σ_{xy} curve (solid) compared to the semicircle law (dashed) of eq. (5). b) Corresponding semicircle law comparison for $T = 25$ mK. The agreement between theory and experiment is good at low temperatures where the anisotropy is well-developed.

The data in Fig. 6.9 suggest that overall, the semicircle law is in good agreement with the transport data in high LLs precisely when the resistance anisotropies are well developed at low temperatures. This is consistent with the transport model of OHS based on a disordered, albeit oriented, stripe CDW structure. It is also informative to consider why the 150 mK data of Fig. 6.9a do not obey the semicircle law. Naively, one might believe that the temperature is too high for the stripes to form and therefore the model is inapplicable. However, Chapter 9 will present strong evidence that at 150 mK the transport becomes isotropic because thermal fluctuations become too large for the native orienting mechanism of the GaAs host crystal. In this picture, the likely reason that the semicircle law does not hold at 150 mK is that the stripes are no longer static.

Interestingly, although the 150 mK data of Fig. 6.9 show that without anisotropic transport the semicircle law fails, a resistance anisotropy is *not* necessary for the law to hold. For example, Fig. 6.10 shows 50 mK R_{xx}, R_{yy}, and R_{xy} transport data of the low-mobility sample M-1, along with the corresponding fit to the semicircle law. The data are plotted in the same way as in Fig. 6.9, except the x-axis covers the range from 2 to 7. Although this sample shows none of the anisotropic transport features associated the hypothesized CDW physics, it still fits the semicircle law to a good degree, especially above $\nu = 4$.

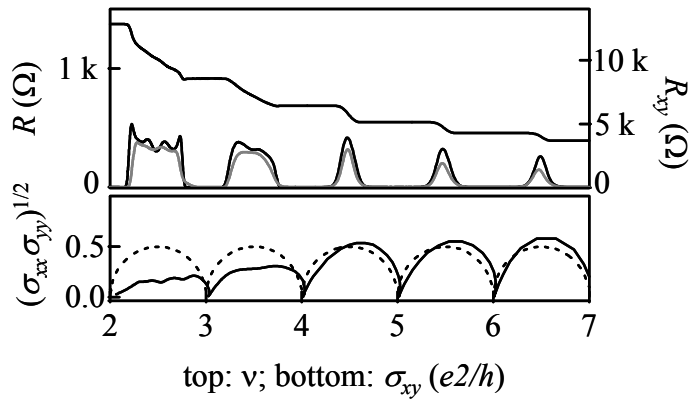

Figure 6.10: Comparison between experiment and theory of semicircle law following Fig. 6.9. Here, the data comes from sample M-1 at 50 mK. Although there is good agreement in the high LL regime $\nu > 4$, there is no evidence of a large transport anisotropy in half-filled high LLs.

This match could have at least two implications. First, it may simply arise from conventional properties of the transition between adjacent quantum Hall plateaus and be independent of CDW physics. The semicircle law has been proposed to account for such transitions previously [11]. A second possibility, and a more intriguing one, is that stripes may in fact exist in high LLs of low mobility samples such as M-1. Perhaps no resistance anisotropy is observed in the sample because its disorder is too great to permit any coherent orientation across macroscopic samples sizes. If this is the case, it might explain why the data in Fig. 6.10 fairly abruptly begin to fit the semicircle law above $\nu = 4$, where the stripe CDW physics is though to first form.

---

1 S. Simon, Phys. Rev. Lett. **83**, 4223 (1999).

2 B.E. Kane, D.C. Tsui, G. Weimann, Phys. Rev. Lett. **59**, 1353 (1987).

3 B.W. Alphenaar, P.L. McEuen, and R.G. Wheeler, Phys. Rev. Lett. **64**, 677 (1990).

4 P.C. van Son, F.W. de Vries, and T.M. Klapwijk, Phys. Rev. B **43**, 6764 (1991).

5 P.L McEuen, A. Szafer, C.A. Richter, B.W. Alphenaar, J.K. Jain, A.D. Stone, R.G. Wheeler, and R.N. Sacks, Phys. Rev. Lett. **64**, 2062 (1990).

6 R.L. Willett, K.W. West, and L.N. Pfeiffer, Phys. Rev. Lett. **87**, 196805 (2001).

7 A.H. MacDonald, M.P.A. Fisher, Phys. Rev. B **61**, 5724 (2000).

8 F. von Oppen, B.I. Halperin, A. Stern, Phys. Rev. Lett. **84**, 2937 (2000).

9 M.M. Fogler, Lecture Notes in Physics **595**: *High Magnetic Fields: Applications in Condensed Matter Physics and Spectroscopy*, ed. C. Berthier, L.P. Lévy, and G. Martinez (Springer, Berlin 2002).

10 A.M. Dykhne, I.M. Ruzin, Phys. Rev. B **50**, 2369 (1994).

11 I. Ruzin and S. Feng, Phys. Rev. Lett. **74**, 154 (1995).

Chapter 7:
Investigation of Orientational Symmetry-Breaking Mechanisms

7.1 Crystal Symmetry and GaAs

7.1.1 Electronic Equivalence of $[1\bar{1}0]$ and $[110]$

For the theory of stripe CDW formation in high LLs to agree with the experimental results, a symmetry-breaking mechanism due to the host GaAs/AlGaAs semiconductor must be present to orient the stripes along the $[110]$ crystal axis. To clarify how possible symmetry-breaking mechanisms may arise, it is helpful to consider the GaAs zinc-blende crystal structure shown in Fig. 7.1. In the alloy AlGaAs, the Al atoms randomly substitute the Ga atoms according to the stoichiometry. The MBE growth direction of our samples is along the $[001]$ axis and the 2DES exists in a plane perpendicular to that direction, denoted as the (001) plane.

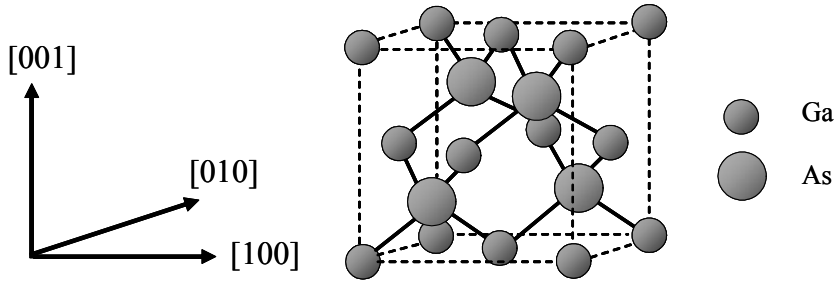

Figure 7.1: Crystal axes and structure of GaAs unit cell.

The fact that the GaAs unit cell is not invariant under rotations of $\pi/2$ about [001], but only under rotations of π, might lead one to believe that the $[1\bar{1}0]$ and $[110]$ directions are electronically inequivalent. However, as Kroemer pointed out in the context of the resistance anisotropy in high LLs, the symmetry of bulk GaAs does indeed

require the electronic transport to have a fourfold symmetry [1]. A derivation will be presented here for the case where the magnetic field and the electron spin are neglected.

First, consider the Bloch wavefunctions [2,3] for electrons in the crystal:

$$\psi(\vec{k},\vec{r}) = \exp(i\vec{k}\cdot\vec{r})u(\vec{k},\vec{r})$$

where the function $u(\vec{k},\vec{r})$ shares the spatial periodicity of the zincblende lattice. These wavefunctions have an energy $\varepsilon(\vec{k})$ which dictates the geometry of the Fermi surface. To prove that the transport properties are invariant under $\pi/2$ rotations about [001], it is sufficient to show that $\varepsilon(\vec{k})$ has the same cubic symmetry because electrons at the Fermi surface determine a system's transport properties [2].

Although the crystal potential is not invariant under $\pi/2$ rotations, it is invariant under the rotary reflection S_4. This symmetry operation consists of a $\pi/2$ rotation about the [001] direction combined with a reflection across a plane perpendicular to that axis. Equivalently, S_4 is a $-\pi/2$ rotation combined with an inversion. An inspection of the unit cell in Fig. 7.1 confirms that the S_4 symmetry is satisfied in zinc-blende. Because the crystal potential possesses this symmetry, the Hamiltonian commutes with the operator $\hat{S}_4$, and the transformation

$$\hat{S}_4\psi(\vec{k},\vec{r}) = \psi(\vec{k},\hat{S}_4^{-1}\vec{r})$$

yields a wavefunction with the *same energy* $\varepsilon(\vec{k})$. Effecting this transformation,

$$\begin{aligned}\hat{S}_4\psi(\vec{k},\vec{r}) &= \exp(i\vec{k}\cdot\hat{S}_4^{-1}\vec{r})u(\vec{k},\hat{S}_4^{-1}\vec{r}) \\ &= \exp(-i\vec{k}\cdot\hat{R}_{-\pi/2}\vec{r})u(\vec{k},\hat{S}_4^{-1}\vec{r}) \\ &= \exp\left[-i(\hat{R}_{\pi/2}\vec{k})\cdot\vec{r}\right]u(\vec{k},\hat{S}_4^{-1}\vec{r}),\end{aligned}$$

where the operator $\hat{R}_{\pi/2}$ represents a rotation by $\pi/2$ about [001]. Note that the equality

$$\vec{k}\cdot\hat{R}_{-\pi/2}\vec{r}=(\hat{R}_{\pi/2}\vec{k})\cdot\hat{R}_{\pi/2}(\hat{R}_{-\pi/2}\vec{r})=(\hat{R}_{\pi/2}\vec{k})\cdot\vec{r}$$

was used. Because the function $u(\vec{k},\hat{S}_4^{-1}\vec{r})$ is still periodic according to the crystal lattice, the transformed wavefunction is still in the Bloch form. Therefore, it's energy must be $\varepsilon(-\hat{R}_{\pi/2}\vec{k})$. But the fact that $\hat{S}_4$ commutes with the Hamiltonian means that the transformed wavefunction's energy is equal to the energy of the original wavefunction $\varepsilon(\vec{k})$, so that $\varepsilon(-\hat{R}_{\pi/2}\vec{k}) = \varepsilon(\vec{k})$. In other words, the function $\varepsilon(\vec{k})$ (and hence the Fermi surface itself) possesses cubic symmetry. Therefore, the transport also must be $\pi/2$ invariant. In bulk GaAs, $[1\bar{1}0]$ and $[110]$ will be indistinguishable using electronic transport measurements.

This analysis suggests a very general way of thinking about how orientational symmetry might be broken: $[1\bar{1}0]$ and $[110]$ become distinguishable when the S_4 symmetry is violated. The ways S_4 symmetry may be violated within a real sample can in turn be separated into two categories: extrinsic and intrinsic.

7.1.2 Extrinsic Symmetry-Breakers

An extrinsic symmetry-breaking source refers to some external influence in the sample growth, preparation, or measurement. For example, the GaAs substrate on which a heterostructure is grown might be initially miscut slightly away from the $[001]$ direction. As a result, the plane of the 2DES would not be exactly perpendicular to $[001]$, S_4 symmetry would be broken, and the two directions $[1\bar{1}0]$ and $[110]$ become distinguishable. Mechanistically, a miscut angle toward the $[1\bar{1}1]$ direction would result in steps in each atomic layer of the MBE growth with the step edges running along $[110]$. These terraces—located at both the heterostructure interfaces and the crystal surface—might then serve to somehow orient the stripe CDW phase along $[110]$ and account for the transport anisotropy. Because the GaAs unit cell is $a \approx 0.6$ nm, the miscut angle which would produce steps commensurate with typically $\lambda \approx 100$ nm stripe wavelength is

$\theta = \tan^{-1}(a/\lambda) \approx 0.3°$. Realistically, though, it is unlikely that miscut substrate wafers are responsible for the symmetry breaking mechanism in the case of the stripes in high LLs. After all, the surfaces of the GaAs substrates are specified to be normal to [001] to within 0.1°. Assuming that the statistical distribution of the azimuthally miscut angles is random, it would require a very unlikely coincidence for all of the multiple wafers we have investigated to exhibit anisotropic transport in high LLs keyed to the same crystalline axes. This is especially true considering that the same anisotropic transport phenomena have been observed in wafers grown over a span of nearly 15 years and from two different MBE systems. Furthermore, Ertl et al. reported that purposefully miscut substrates of 1° do not affect the anisotropy orientation [4].

Another example of an extrinsic symmetry-breaking source is a density gradient within the 2DES caused by imperfect MBE growth conditions that distinguish $[1\bar{1}0]$ and [110] from each other. Again, this scenario is unlikely considering the variety of different wafers where anisotropic transport in high LLs has been observed. Also, most of the wafers we have examined were rotated at ~10 rpm during the MBE growth, which would help smooth out any growth-induced gradients. Finally, the density variation from one side to another in typical ~5 mm samples is measured to be less than 0.3%.

Extrinsic symmetry-breakers need not originate in the MBE growth, and instead they might arise from measurement conditions that systematically favor one direction over the other. Normally no such symmetry-breakers are present to our knowledge, but they can be intentionally applied. For example, soon after the initial observation of the transport anisotropy in high LLs, our group [5] and Pan et al. [6] discovered that a small in-plane magnetic field could orient the stripes such that their hard transport direction lies parallel to the in-plane field. This remarkable phenomenon will be explored in Chapters 8 and 9.

7.1.3 Intrinsic Symmetry-Breakers

The second category of an S_4 symmetry-breaking mechanism is one that is intrinsic to the heterostructure crystal itself. Because the S_4 symmetry is only preserved in a pure, infinite GaAs crystal, any real heterostructure will inevitably violate the symmetry. For

example, the free (001) surface of a sample fails to be invariant under reflections, thus making $[1\bar{1}0]$ and $[110]$ inequivalent. This is not surprising, considering that the anisotropy in the GaAs surface chemistry is used to distinguish between the two directions in the first place, as discussed in Section 2.1. More generally, at any junction between GaAs and AlGaAs the S_4 symmetry is violated and the in-plane directions become twofold rather than fourfold symmetric.

The inequivalence of $[1\bar{1}0]$ and $[110]$ at any GaAs surface arises from the way the dangling bonds of the surface atoms link up. The most common type of GaAs surface reconstruction is called a (2×4) reconstruction, which refers to the doubled and quadrupled periodicity of the surface unit cell in the $[1\bar{1}0]$ and $[110]$ directions, respectively. These reconstructions obviously break the symmetry between $[1\bar{1}0]$ and $[110]$, and the difference between the two can be seen in striking scanning tunneling microscopy (STM) images obtained recently by LaBella et al. [7] and reproduced in Fig. 7.2. On that GaAs surface, the As atoms form conspicuous rows of dimers running along $[1\bar{1}0]$.

The reduced symmetry at the GaAs surface may play a role in orienting the stripe CDW in high LLs. For example, the railroad-track-like dimer rows of Fig. 7.2 might couple to orientation of the stripe CDW through an anisotropic crystal strain. Or, the GaAs surface reconstruction might orient a buried stripe CDW by through an anisotropic dielectric constant. It is plausible that the surface atoms or states would have an anisotropic dielectric screening capability, and in fact dielectric anisotropies on GaAs surfaces have been studied extensively at optical frequencies using the technique of reflectance-difference (or anisotropy) spectroscopy [8]. To our knowledge, any similar anisotropy in the dielectric constant at dc frequencies has not been studied.

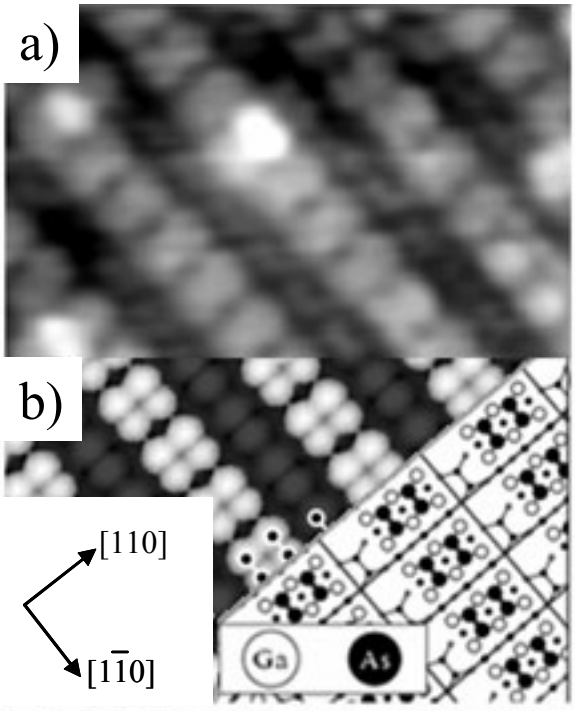

Figure 7.2: Image reproduced from ref. [7] with the permission of P.M. Thibado. a) STM image of GaAs surface showing As dimer pairs running along $[1\,\bar{1}0]$ with a periodicity of ~2 nm. b) Theoretical simulation of STM image (upper left) based on the $\beta 2(2\times4)$ surface reconstruction shown (bottom right).

A less obvious potential intrinsic symmetry-breaking source is the shape of the 2DES confinement potential. As Kroemer pointed out [1], S_4 symmetry in the immediate environment of a 2DES in a heterostructure will be violated if the confinement potential of the electrons lacks reflection symmetry. For example, a 2DES confined to a single-interface heterojunction resides in a roughly triangular potential well which explicitly breaks the reflection symmetry across the (001) plane, as shown in Fig. 7.3a. Associated with the triangular potential is a large internal electric field along [001] of ~10^4 V/cm. Rosenow et al. [9] and Takhtamirov et al. [10] have found that these band structure effects in typical single-interface heterojunctions lead to small (~0.1%) anisotropies in the effective mass of the two-dimensional electrons. This anisotropic effective mass was predicted to favor an orientation of the stripes that is consistent with the experiment.

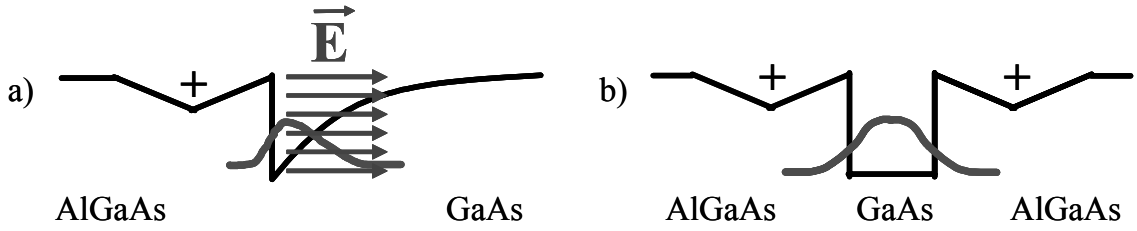

Figure 7.3: a) The asymmetric confinement potential of a single-interface heterojunction has a built-in electric field breaking the S_4 symmetry. b) Symmetric confinement in a square quantum well has no such electric field. Nevertheless, the anisotropy orientation in both structures is the same.

However, the experimental evidence suggests that the symmetry of the 2DES confinement potential is not the symmetry-breaker of the striped CDW state. In the sample B-1, for example, the 2DES resides in a conventional single-interface heterojunction that lacks reflection symmetry. In the sample H-1, on the other hand, reflection symmetry is preserved because the 2DES is confined to a square quantum well with Silicon doping layers positioned symmetrically about 100 nm above and below the quantum well, as shown in Fig. 7.3b. Yet both samples—the asymmetric heterojunction and the symmetric quantum well—show the same qualitative resistance anisotropies, with the same orientation, in half-filled high LLs (see, for example, Fig. 7.4 below). While some small-scale irregularities in the quantum well might technically destroy its symmetry, it has been convincingly demonstrated in two-dimensional hole systems that the symmetry of the confinement potential can be readily detectable using transport measurements under the appropriate circumstances [11,12]. The lack of any significant differences in transport between B-1 and H-1 implies that the symmetry of the confinement potential is not the most important factor determining the stripe orientation in high LLs.

7.2 Anisotropic Roughness in GaAs Heterostructures

7.2.1 Mounding on GaAs

One possible intrinsic symmetry-breaking mechanism of the stripe CDW states that has attracted considerable attention is anisotropic roughness on the sample surfaces. Section 7.1 already explained how the symmetry between $[1\bar{1}0]$ and $[110]$ in a bulk crystal is naturally broken at the (001) surface of GaAs, and this often leads to anisotropies in morphological features that develop during MBE growth. The oriented "bowtie" and "closed eye" defects described in Section 2.1 are examples of this process. Another is the common feature of anisotropic mounding or island formation.

Several groups have detected shallow, elongated mounds on the surfaces of MBE-grown GaAs using atomic force microscopy (AFM) [13,14,15,16]. In each of those cases, the long axis of the surface mounds was found to be along $[1\bar{1}0]$. Generally, the mounds have lateral scales of ~1 μm and are less than 10 nm tall. The mounds' precise morphology and prevalence depend on the details of the GaAs growth conditions. For example, the surface roughness of GaAs/AlGaAs heterostructures has been reported to be very sensitive to the Al concentration and the type of dopants used [17].

Mounding on GaAs is believed to arise from the growth mode of island nucleation prevailing over the smoother step-flow process of MBE growth. Island formation becomes favorable when a so-called "Schwoebel" barrier prevents an adatom from falling off of a step edge despite it being energetically favorable to do so [14]. The origin of the mound *anisotropy*, on the other hand, is not clear. It might come from an energy anisotropy of edges aligned along the $[1\bar{1}0]$ or $[110]$ directions [18], or from the anisotropic diffusion of adatoms on the growing MBE surface [19].

In terms of a CDW symmetry-breaking mechanism, the anisotropic surface mounds might generate a periodic potential modulation in the 2DES. For example, the mounds have been observed to induce changes in the local 2DES density [20]. Artificial periodic potentials are known to affect other aspects of quantum Hall transport features [21,22,23], and they might also couple to the energetics of the stripe orientation. Indeed,

Aoyama et al. [24] and Yoshioka [25] have shown theoretically how a periodic potential modulation could orient a stripe CDW in the high LL regime. Interestingly, Aoyama et al. showed that the effect of a periodic potential on the stripe CDW orientation is not obvious: the stripes may align along or against the direction of modulation, depending on its strength and periodicity.

Using AFM, Willett et al. [26] reported an apparent correlation between anisotropic surface morphologies of GaAs/AlGaAs heterostructures and various transport characteristics of the buried two-dimensional electron systems. One of their central results was that the (001) heterostructure surfaces consistently exhibited micron-scale mounds or ridges with long axes aligned along the $[1\bar{1}0]$ direction. The orientation of these features were in agreement with those reported in the literature for MBE-grown GaAs. This led those authors to speculate that surface roughness may play an important role in orienting the stripe CDW electron phases of half-filled high LLs.

7.2.2 Mound Orientation not Correlated with Anisotropy

Unlike Willett et al., we find [27] that while micron-scale surface roughness on GaAs heterostructures is common, its orientation (if present) may lie along either $[1\bar{1}0]$ *or* $[110]$. For example, Fig. 7.4 displays 20×20 μm surface images of three different GaAs heterostructures as a demonstration of the variety of surface morphologies we have observed. The full grayscale in Fig. 7.4 corresponds to a height deviation of 5 nm in the $[001]$ direction, and the in-plane $[1\bar{1}0]$ and $[110]$ directions are indicated in Fig. 7.4b. The three wafers are B, G, and H, and the scan direction of the AFM cantilever was chosen to be at a 45° angle to the principal $[1\bar{1}0]$ and $[110]$ axes in order to avoid artifacts from the rastering tip interfering with judgments regarding the orientation of anisotropic features. Images from sections of the same wafer separated by several cm were found to share very similar surface morphology characteristics. This indicates that each wafer exhibits its own distinct surface morphology.

Fig. 7.4 shows that while anisotropic surface roughness exists, it may be oriented along either $[1\bar{1}0]$ or $[110]$. For example, the surface of Fig. 7.4a is covered with

rounded mounds elongated along [110] and separated by narrow valley running in the same direction. Though harder to discern, the smooth surface of Fig. 7.4b also contains shallow features elongated along [110]. In contrast, the surface of Fig. 7.4c contains prominent ridges uniformly lying along $[1\bar{1}0]$ instead. The anisotropic mounds visible in Fig. 7.4a and c are roughly 1 μm wide and up to several times that length long. Despite this variability in the surface roughness orientation, however, the corresponding transport data indicates that in all three samples the resistance anisotropy in high LLs is oriented with the hard direction along $[1\bar{1}0]$ and the easy direction along [110]. In other words, there is no apparent correlation between the orientation of elongated surface mounds and the orientation of the anisotropic electronic states.

Furthermore, Fig. 7.4 shows that the strength of the surface roughness varies greatly from sample to sample. On the 5 nm height scale, the morphologies of Fig. 7.4a and c are clearly visible while the surface of Fig. 7.4b is virtually featureless. Quantitatively, the rms surface roughness of the three images in Fig. 7.4 was calculated to be 0.64, 0.09, and 0.71 nm, respectively, corresponding to a variation of almost an order of magnitude. Yet this variation is not strongly correlated to the apparent strength of the anisotropy in high LLs, at least when measured by the low temperature resistance anisotropy at $\nu = 9/2$. For example, sample G-1, with an rms roughness of 0.09 nm, has virtually the same ratio of R_{xx}/R_{yy} at $\nu = 9/2$ as in sample B-1, which has a roughness of 0.64 nm. Indeed, the differences in anisotropy strength are more closely associated with the sample mobility and density, as described in Sections 3.2 and 3.4.

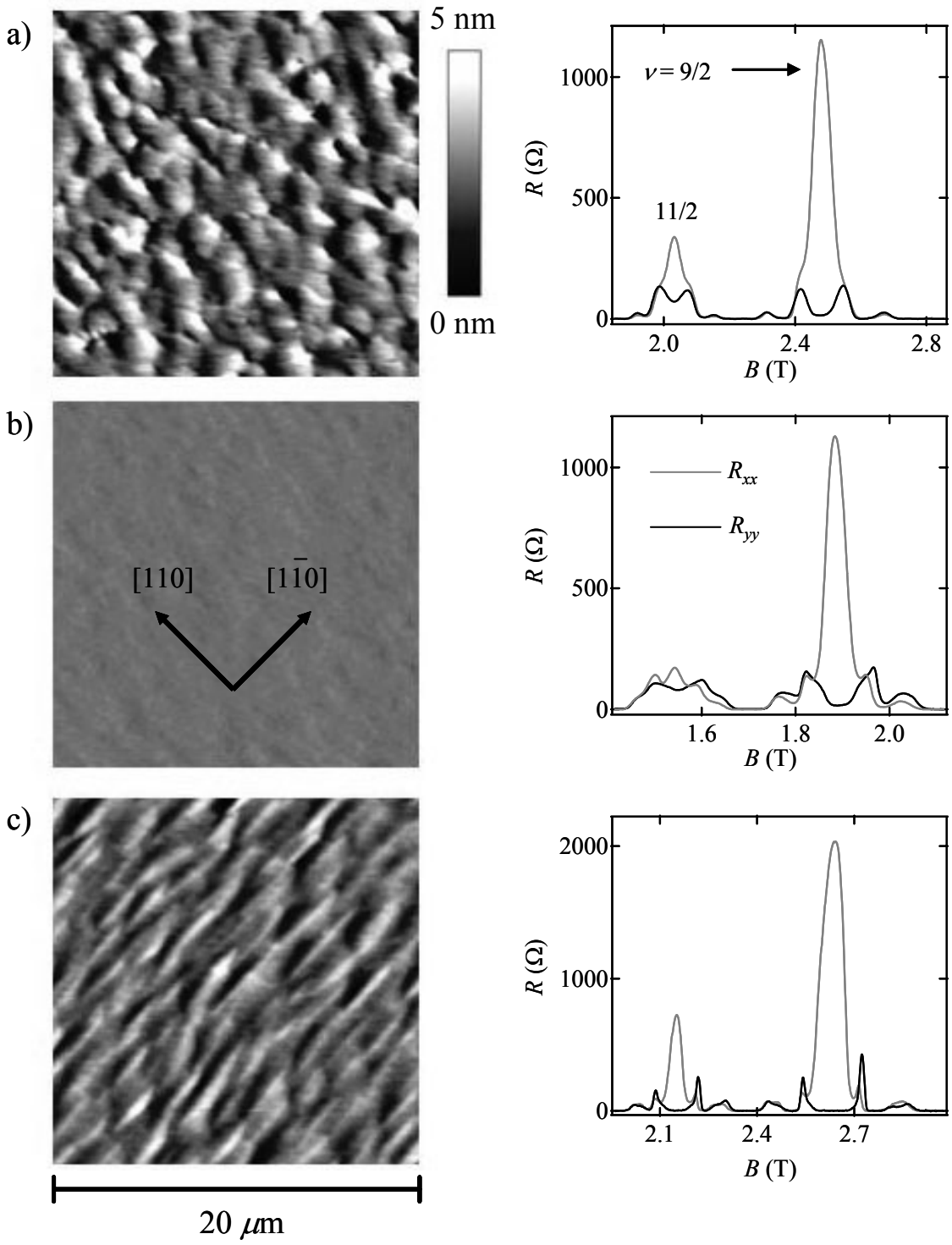

Figure 7.4: $20 \times 20\ \mu m^2$ AFM images and 50 mK longitudinal resistance data (R_{xx}: gray; R_{yy}: black) for the samples: a) B-1, b) G-1, and c) H-1. The grayscale spans 5 nm. The crystal axes directions for each sample are shown in b). While each sample exhibits anisotropic transport with the hard axis along $[1\,\bar{1}0]$, the surface morphology strengths vary and may possess orientations either along $[110]$ or $[1\,\bar{1}0]$.

A similar diversity of surface features was detected on six other wafers not shown in Fig. 7.4. Of those six samples, three possess surface roughness oriented along $[110]$, two have no obvious orientation, and one shows an orientation along $[1\bar{1}0]$. A large variation of the surface roughness strengths was also measured. To our knowledge, no other reports of elongated mounds along $[110]$ on GaAs surfaces have been made; only $[1\bar{1}0]$-oriented mounds can be found in the literature. Considering that the mound formation is so sensitive to the detailed growth conditions, and that the mechanism for mound formation is poorly understood, the greater diversity of our results seems less surprising. In any case, all of these samples examined with the AFM exhibit high LL anisotropies keyed to the usual principal axes. Therefore we conclude that the micron-scale surface roughness of GaAs/AlGaAs heterostructures is not the sought-after orientational symmetry breaker of the anisotropic electronic phases in half-filled high LLs.

Although surface mounding has been ruled out as an orientational symmetry-breaker of the stripe CDW state in high LLs, other structural anisotropies in the GaAs crystal might have an influence on the 2DES. For instance, the anisotropic morphologies on the finished MBE wafers presumably built up gradually during the sample growth. Therefore, anisotropies in the roughness of the GaAs/AlGaAs interfaces *where the 2DES resides* might play a role in orienting the stripe CDW state. Such anisotropic interface roughness in buried GaAs/AlGaAs layers has been detected before in magnetic resonance experiments [28].

Anisotropic roughness at buried interfaces has also been blamed for small anisotropy ratios of ≤ 2 for 2DES mobilities in the $[1\bar{1}0]$ and $[110]$ directions at zero magnetic field [29,30]. But in our samples, the zero-field and low-field resistances R_{xx} and R_{yy}, are not correlated with the orientation of the anisotropic electron phase in high LLs. Any broad background transport anisotropy that might exist does not affect the orientation of the resistance anisotropy in high LLs at low temperatures. Thus if anisotropic roughness at the heterostructure interfaces plays any role in orienting the stripe CDW, it has not been detected in any other of our transport measurements.

7.3 Piezoelectric Orienting Mechanism

A totally different mechanism that might play a role in orienting the stripe CDW is the piezoelectric interaction of the CDW with the GaAs crystal. GaAs is piezoelectrically active because its crystal structure lacks inversion symmetry [31]. One consequence this has on electron transport in 2DESs is that the dominant phonon scattering mechanism at low temperatures involves piezoelectric phonons [32]. Another way piezoelectricity is known to affect 2DES transport is through crystal strain effects when gates or dielectric materials are deposited on top of GaAs/AlGaAs heterostructures. For example, the electron density in field effect transistors (FETs) [33,34] and lateral surface superlattices (LSSLs) [35] is affected by the piezoelectric polarization charge arising from surface crystal stain. Interestingly, these piezoelectric effects exhibit a sensitivity to the *orientation* of the surface structures with respect to the crystal axes: When the FETs and LSSLs are oriented along either $[1\bar{1}0]$ or $[110]$, the piezoelectric effects are maximized relative to orientations along [100] and [010].

For the problem of anisotropic transport in high LLs, Fil [36] proposed that the piezoelectric interaction, combined with the anisotropy in the elastic moduli of GaAs, might play a role in orienting the stripe CDW. Defining ϕ to be the angle of the stripe CDW with respect to the [100] direction, Fil calculated the total energy $U(\phi)$ of the CDW with respect to its orientation within the (001) plane of a bulk GaAs crystal. Fil's central result is shown in Fig. 7.5, where the anisotropic part of the total energy, $U_{an}(\phi)$, is plotted versus angle ϕ. Here, the experimentally reasonable values of $\lambda_{CDW} = 100$ nm for the stripe wavelength and $n = 0.3 \times 10^{11}$ cm^{-2} for the valence LL electron density were chosen, and the units of energy are mK per electron. Fig. 7.5 shows that $U_{an}(\phi)$ possesses a fourfold invariance with minima approximately along $\phi = \pi/4$ and $3\pi/4$, meaning that the stripes would equally prefer to lie along either $[110]$ or $[1\bar{1}0]$. Interestingly, there are actually two minima on either side of $\phi = \pi/4$ and $3\pi/4$, separated by a very shallow barrier. These would presumably serve to broaden the distribution of stripe orientations but still maintain a preferential direction along either $\phi = \pi/4$ or $3\pi/4$.

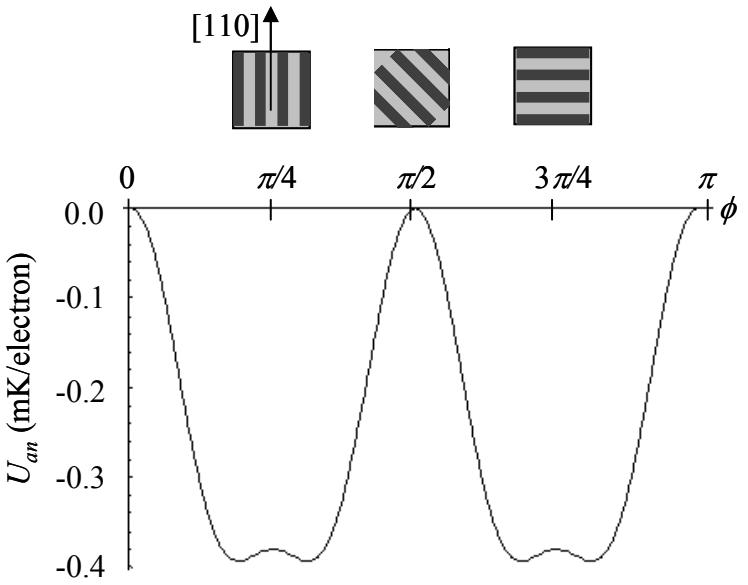

Figure 7.5: Piezoelectric anisotropy energy of a stripe CDW oriented in GaAs at an angle ϕ with respect to the [100] direction. The energy was derived using the method of Fil [36] for a stripe CDW with a wavelength of 100 nm and an electron density of 3×10^{10} cm^{-2}.

The depth of the potential wells in Fig. 7.5 is approximately -0.4 mK per electron, and this value can be very roughly determined with a quick order-of-magnitude calculation as follows [36]. With no piezoelectricity, the energy per electron of a stripe CDW is on the order of $e^2/\varepsilon\lambda_{CDW}$, which is about 10 K for the experimental situation (for GaAs, $\varepsilon \sim 13\varepsilon_0$). This essentially comes from the Coulomb penalty of separating electrons by a distance λ_{CDW}. In the presence of piezoelectricity, the electric displacement is reduced by the amount of polarization present: $D \to D - P$. This polarization is roughly the strain, u, times the piezoelectric modulus value β, so that $D \to D - \beta u$. The strain, in turn, is related to the electric displacement through the elastic constant c as $u \sim \beta D / c$. Therefore, the electric displacement is reduced by a factor of $\chi = (1 - \beta^2 / c\varepsilon)$. In GaAs, $\beta \sim$ -0.2 C/m^2 and c $\sim 10^{11}$ N/m^2, so that $\chi \approx (1\text{-}10^{-4})$. The total energy is proportional to the electric field times the electric displacement, so that the energetic *advantage* gained by introducing piezoelectricity is roughly $10^{-4} \cdot 10$ K $\approx$ 1 mK per electron. Chapter 8 will show that this energy scale of the piezoelectric

interaction is indeed on the same order of magnitude as the native symmetry-breaking energy of real samples.

Note that the piezoelectric analysis does not solve the symmetry-breaking problem in high LLs because the in-plane symmetry is still fourfold-symmetric; according to piezoelectricity, alignment along $[1\bar{1}0]$ and [110] are equivalently favorable. An additional symmetry-breaking field would still be necessary to pick out [110] as the preferred stripe orientation. However, the piezoelectric interaction is still intriguing because its favored directions and its energy scale are experimentally relevant.

---

1 H. Kroemer, http://xxx.lanl.gov/abs/cond-mat/9901016.

2 C. Kittel, *Quantum Theory of Solids* (John Wiley, New York 1987)..

3 M. Tinkham, *Group Theory and Quantum Mechanics* (McGraw-Hill, New York 1964)

4 F. Ertl, O. Jaeger, R.A. Deutschmann, M. Bichler, G. Abstreiter, E. Schuberth, C. Probst, and W. Wegscheider, submitted to 26th International Conference on the Physics of Semiconductors, Edinburgh 2002.

5 M.P. Lilly, K.B. Cooper, J.P. Eisenstein, L.N. Pfeiffer, K.W. West, Phys. Rev. Lett. **83**, 824 (1999).

6 W. Pan, R.R. Du, H.L Stormer, D.C. Tsui, L.N. Pfeiffer, K.W. Baldwin, K.W. West, Phys. Rev. Lett. **83,** (1999) 820.

7 V.P. LaBella, H. Yang, D.W. Bullock, and P.M. Thibado, Phys. Rev. Lett. **83**, 2989 (1983).

8 I. Kamiya, D.E. Aspens, L.T. Florez, and J.P. Harbison, Phys. Rev. B **46**, 15894 (1992).

9 B. Rosenow and S. Scheidl, Int. J. Mod. Phys. B **15**, 1905 (2001).

10 E.E. Takhmatirov and V.A. Volkov, JETP Letters **71**, 422 (2000).

11 J.P. Eisenstein, H.L. Stormer, V. Narayanamurti, A.C. Gossard, and W. Wiegmann, Phys. Rev. Lett. **53**, 2579 (1984).

12 R. Winkler, S.J. Papadakis, E.P. DePoortere, and M.Shayegan, Phys. Rev. Lett. **84**, 713 (2000).

13 C. Orme, M.D. Johnson, J.L. Sudijono, K.T. Leung, and B.G. Orr, Appl. Phys. Lett. **64**, 860 (1994).

14 M.D. Johnson, C. Orme, A.W. Hunt, D. Graff, J. Sudijono, L.M. Sander, and B.G. Orr, Phys. Rev. Lett. **72**, 116 (1994).

15 G.W. Smith, A.J. Pidduck, C.R. Whitehouse, J.L. Glasper, and J. Spowart, J. Crystal Growth **127**, 966 (1993).

16 G. Apostolopoulos, J. Herfort, L. Daweritz, K. Ploog, and M. Luysberg, Phys. Rev. Lett. **84**, 3358 (2000).

17 F. Alexandre, L. Goldstein, G. Leroux, M.C. Joncour, H. Thibierge, and E.V.K. Rao, J. Vac. Sci. Technol. B **3**, 950 (1985).

18 E.J. Heller and M.B. Lagally, Appl. Phys. Lett. **60**, 2675 (1992).

19 A. Kley, P. Ruggerone, and M. Scheffler, Phys. Rev. Lett. **79**, 5278 (1997).

20 Y. Yayon, M. Rappaport, V. Umansky, and I. Bar-Joseph, Phys. Rev. B **66**, 033310 (2002).

21 D. Weiss, K. von Klitzing, K. Ploog, and G. Weimann, Europhys. Lett. **8**, 179 (1989).

22 R.L Willett, K.W. West, L.N. Pfeiffer, Phys. Rev. Lett. **78**, 4478 (1997).

23 J.H. Smet, K. von Klitzing, D. Weiss, W. Wegsheider, Phys. Rev. Lett. **80**, 4538 (1998)

24 T. Aoyama, K. Ishikawa, and N. Maeda, Europhys. Lett. **59**, 444 (2002).

25 D. Yoshioka, J. Phys. Soc. Jpn. **70**, 2836 (2001).

26 R.L. Willet, J.W.P. Hsu, D. Natelson, K.W. West, and L.N. Pfeiffer, Phys. Rev. Lett. **87**, 126803 (2001).

27 K.B. Cooper, M.P. Lilly, J.P. Eisenstein, T. Jungwirth, L.N. Pfeiffer, K.W. West, Solid State Comm **119**, 89 (2001).

28 H.W. van Kesteren, E.C. Cosman, W.A.J.A. van der Poel, and C.T. Foxon, Phys. Rev. B **41**, 5283 (1990).

29 Y. Markus, U. Meirav, H. Shtrikman, and B. Laikhtman, Semi. Sci. Tech. **9**, 1297 (1994).

30 Y. Tokura, T. Saku, S. Tarucha, and Y. Horikoshi, Phys. Rev. B **46**, 15558 (1992).

31 J.F. Nye, *Physical Properties of Crystals* (Oxford University Press, Oxford 1985).

32 J.H. Davies, *The Physics of Low-Dimensional Semiconductors* (Cambridge University Press, Cambridge 1998).

33 C.P. Lee, R. Zucca, and B.M. Welch, Appl. Phys. Lett. **37**, 311 (1980).

34 P.M. Asbeck, C.P. Lee, and M.-C.F. Chang, IEEE Trans. Electron. Devices **ED-31**, 1377 (1984).

35 E. Skurkas, A.R. Long, I.A. Larkin, J.H. Davies, and M.C. Holland, Appl. Phys. Lett. **70**, 871 (1997).

36 D.V. Fil, Low Temp. Phys. **26**, 581 (2000).

Chapter 8:
High LLs and In-Plane Magnetic Fields

8.1 The Tilted Field Technique

A common experimental method in the field of quantum Hall physics is the *in situ* rotation of a 2DES about an axis perpendicular to the fixed magnetic field direction. This "tilted field" technique permits the application of an adjustable in-plane magnetic field component $B_{||}$ in addition to the perpendicular field $B_{\perp}$ generating Landau quantization. In our experiments, the samples were rotated about a fixed axis using a rotating sample platform described in Section 2.2. The in-plane and perpendicular fields are functions of the tilt angle θ through $B_{||} = B\sin(\theta)$ and $B_{\perp} = B\cos(\theta)$.

The in-plane field $B_{||}$ affects the 2DES in two ways. First, $B_{||}$ contributes to the spin-flip Zeeman energy of the electrons, which depends on the total magnetic field B. Second, $B_{||}$ can affect a 2DES via the finite width of the electron layer in the perpendicular (or **z**) direction. While the motion of electrons confined to an infinitely thin layer will be independent of an in-plane field, real samples contain a 2DES that is typically ~10 nm wide. As a result, $B_{||}$ can influence the transport properties of a 2DES regardless of the spin. The following sections demonstrate that the interaction of $B_{||}$ with the finite width of the electrons has a dramatic effect on the transport properties of the $N \geq 1$ LLs.

8.2 $B_{||}$ as an Orientational Symmetry-Breaker

8.2.1 $B_{||}$ and High LL Transport in Sample F-5

Fig. 8.1 shows how the 25 mK transport characteristics of the $\nu = 9/2$ anisotropy in sample F-5 responds to an in-plane magnetic field pointed along [110], the easy transport direction. The three panels show R_{xx} and R_{yy} versus $B_\perp$ for the tilt angles $\theta = 0°$, 22°, and 31°. At $B_\perp$ = 1.38 T (the half-filling point), the corresponding in-plane fields are 0.0, 0.56, and 0.83 T. At $\theta = 0°$, the data exhibit the usual resistance anisotropy, with $[1\bar{1}0]$ the hard direction and [110] the easy direction. At $\theta = 22°$, however, the transport appears to be relatively isotropic. The peak in R_{xx} has dropped from over 1200 Ω to less than 200 Ω, and the minimum in R_{yy} has risen to roughly 300 Ω. By $\theta = 31°$, the resistance anisotropy has reemerged, but now with a minimum in R_{xx} and a large peak in R_{yy}. In other words, by a tilt angle of 31° the principal axes of anisotropy have rotated by 90° with respect to their original configuration.

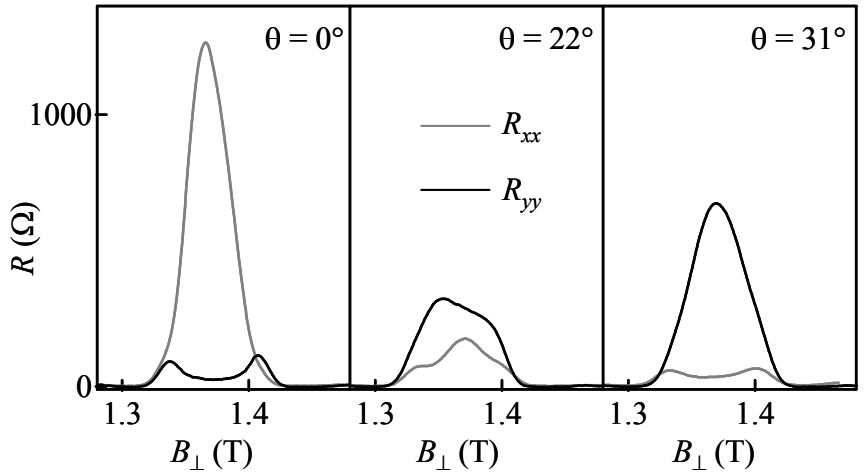

Figure 8.1: 25 mK R_{xx} (gray) and R_{yy} (black) data through $\nu = 9/2$ in sample F-5 for tilt angles of 0°, 22°, and 31°. The in-plane magnetic field lies along [110], and its strength at half-filling is 0 T, 0.6 T, and 0.8 T for the three angles. The principal axes of anisotropy interchange with $B_{||}$ along [110].

Fig. 8.2a compares how the $\nu = 9/2$ anisotropy is affected by $B_{||}$ directed along both [110] and $[1\bar{1}0]$. For $B_{||}$ along $[1\bar{1}0]$, a separate cool-down was required in order to reorient the sample on the rotator paddle by 90°. At $B_{||} = 0$, R_{xx} and R_{yy} at $\nu = 9/2$ approximately coincide for the two cool-downs, and the anisotropy is in the usual orientation with $R_{xx} > R_{yy}$. When $B_{||}$ in the [110] direction exceeds about 1 T, the anisotropy reverses, with $R_{yy} > R_{xx}$. This is the same effect shown in Fig. 8.1, and the crossing-point where $R_{xx} \approx R_{yy}$ occurs at about $B_{||} = 0.5$ T. On the other hand, no anisotropy reversal occurs for $B_{||}$ along $[1\bar{1}0]$; R_{xx} remains larger than R_{yy} for $B_{||}$ up to ~9 T. Meanwhile, Fig. 8.2b shows a similar comparison of how $B_{||}$ affects the anisotropy at $\nu = 11/2$. Again, the anisotropy reverses for $B_{||}$ along [110], while its orientation is unaffected by an in-plane field along $[1\bar{1}0]$.

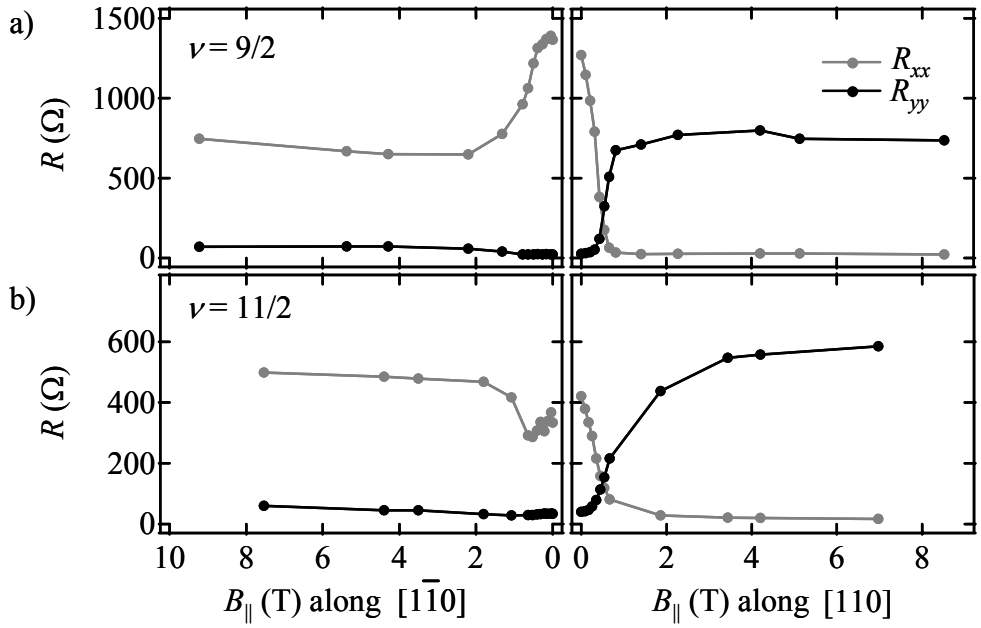

Figure 8.2: a) 25 mK R_{xx} (gray) and R_{yy} (black) values at $\nu = 9/2$ in sample F-5 as a function of $B_{||}$. Left: $B_{||}$ along $[1\bar{1}0]$, and the anisotropy axes remain unchanged. Right: $B_{||}$ along $[110]$, and the anisotropy axes reverse. b) Corresponding data for $\nu = 11/2$; $B_{||}$ has similar effect.

These results indicate that $B_{||}$ acts like an *external* orientational symmetry-breaker of the stripe CDW in high LLs. For $B_{||} = 0$, the stripe orientation is determined by the native symmetry-breaking mechanism of the GaAs crystal, as discussed in Chapter 7.

However, this mechanism can apparently be overcome by an in-plane field of ~1 T directed along $[110]$, resulting in an interchange of the hard and easy transport directions. On the other hand, these directions remain unchanged for $B_{||}$ along $[1\bar{1}0]$. This suggests that the stable orientation of the stripe CDW is with the stripes running perpendicular to the direction $B_{||}$, so that hard transport direction is *along* $B_{||}$. Section 8.4 will review the theoretical picture of how $B_{||}$ is believed to orient the stripe CDW, but first the experimental phenomenon will be explored in more detail.

8.2.2 $B_{||}$ and High LL Transport in Other Samples

In sample B-1, tilted field data for filling factors $\nu = 9/2$ through 15/2, are displayed in Fig. 8.3. This figure shows that applying $B_{||}$ along $[110]$ causes a reversal of the anisotropy in each of these half-filled high LLs. Interestingly, the "critical" in-plane field $B_{||}^{*}$ where R_{xx} and R_{yy} cross is very close to 0.5 T for each high LL. For $B_{||}$ along $[1\bar{1}0]$, the results are somewhat more complicated than in the case of sample F-5. For $\nu = 9/2$, the relative magnitudes of R_{xx} and R_{yy} reverse for intermediate in-plane fields, but once $B_{||}$ exceeds 5 T the original anisotropy orientation is restored. This reversal does not occur for the other half-filled high LLs in Fig. 8.3, although a significant reduction in anisotropy is apparent at $\nu = 13/2$. (The spin-splitting asymmetry is evident again, with the tilt results for $\nu = 9/2$ and 13/2 being distinct from those at $\nu = 11/2$ and 15/2.)

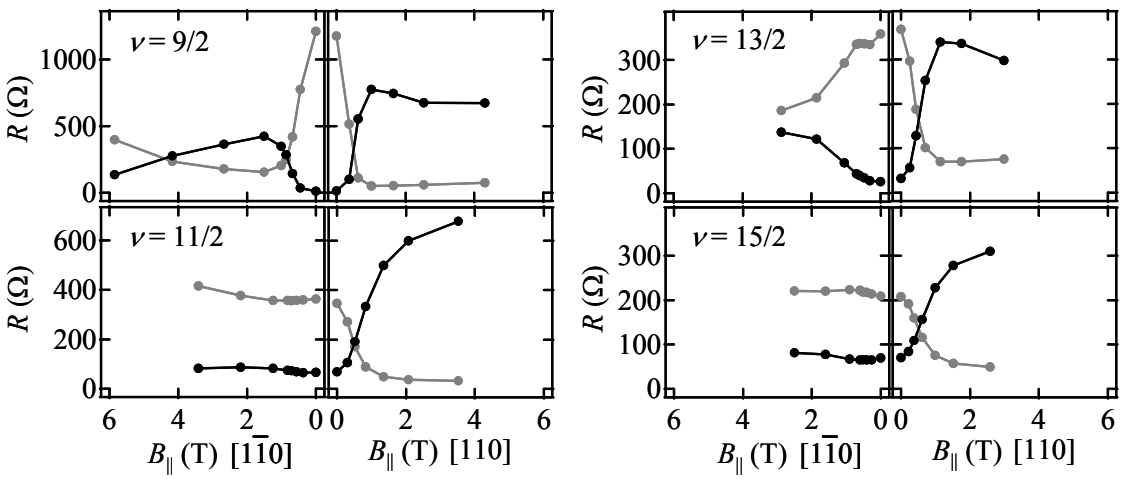

Figure 8.3: R_{xx} (gray) and R_{yy} (black) data versus $B_{||}$ for sample B-1 at 50 mK. $B_{||}$ lies along $[1\bar{1}0]$ (left) and $[110]$ (right) for $\nu = 9/2$, 11/2, 13/2, and 15/2. Interchange of anisotropy axes occurs for $B_{||}$ along $[110]$.

In sample H-1, the influence of $B_{||}$ on the anisotropy was only investigated for $B_{||}$ along $[110]$, and the results are shown in Fig. 8.4 for $\nu = 9/2$ and 11/2. The anisotropy reversal effect is again evident, and this time it is particularly strong. The resistances cross at only $B_{||}^{*} \approx 0.3$ T, and by only $B_{||}^{*} \approx 0.5$ T the resulting anisotropy is approximately as strong as it was for $B_{||} = 0$.

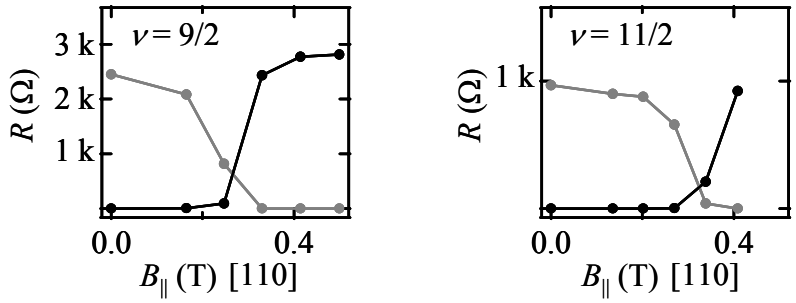

Figure 8.4: R_{xx} (gray) and R_{yy} (black) versus $B_{||}$ for sample H-1 at 50 mK. $B_{||}$ lies only along $[110]$ for $\nu =$ 9/2 (left) and 11/2 (right). Interchange of anisotropy axes occurs by only $B_{||} \approx 0.5$ T.

The effect of an in-plane field on the anisotropic transport in high LLs has also been studied by Pan et al. [1] in yet another sample, and they observed the same anisotropy reorientation phenomenon. Interestingly, those authors observed that $B_{||}$ along

$[1\,\bar{1}0]$ affects the $\nu = 9/2$ anisotropy in a similar way to that seen in Fig. 8.3, where R_{xx} falls considerably before rising again for high $B_{||}$.

8.2.3 Influence of $B_{||}$ Outside of Anisotropic Regime

Above it was hypothesized that the anisotropy reorientation in the presence of $B_{||}$ arises from the energetic advantage gained from a reorientation of the stripe CDW. However, an alternative explanation for the reorientation effect is that $B_{||}$ introduces a strong *global* transport anisotropy that is independent of the existence of any stripe CDWs. After all, $B_{||}$ explicitly breaks the orientational symmetry of the 2DES.

To rule out this possibility, Fig. 8.5 shows the transport data around $\nu = 9/2$ at three tilt angles for $B_{||}$ along $[110]$. Around half-filling, the anisotropy reversal occurs by $\theta = 34°$. Crucially, however, the RIQHE regions and the satellite peaks flanking $\nu = 9/2$ show almost no change between $\theta = 0°$ and $\theta = 34°$. Specifically, no strong anisotropy has been introduced anywhere in the $\nu = 9/2$ structure except in the central region where the stripe CDW is believed to form. (A small amount of anisotropy is induced in the RIQHE satellite peaks by 34°; see Fig. 8.8.) Although not shown, $B_{||}$ also does not introduce strong anisotropies in very high LLs or in the $N = 0$ LL either. An important exception to this rule is the response of the $N = 1$ LL, which will be discussed in Section 8.3. Thus there is strong evidence that the reversal in anisotropy in half-filled high LLs does not come from $B_{||}$ introducing a global transport anisotropy at all magnetic fields. Rather, the in-plane field has a very specific and striking effect on the anisotropic electronic phases in half-filled high LLs.

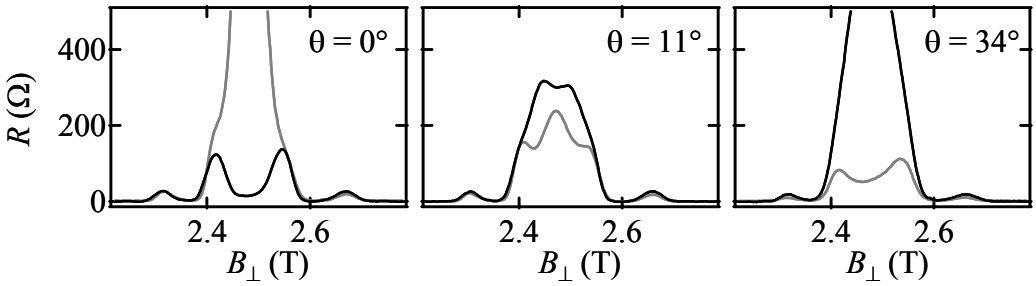

Figure 8.5: R_{xx} (gray) and R_{yy} (black) through $\nu = 9/2$ for sample B-1 at 50 mK. The tilt angles 0°, 11°, and 34° are for $B_{||}$ along $[110]$. Despite anisotropy reversal at half-filling, little change in the transport occurs in the flanks of the LL.

8.3 Other Effects of $B_{||}$ on High LL Transport

8.3.1 High Temperature Transport

In addition to being able to reorient the principal axes of anisotropy at low temperatures, an in-plane field also affects the transport characteristics in half-filled high LLs at higher temperatures. For example, Fig. 8.6 compares how R_{xx} and R_{yy} at $\nu = 9/2$ and 11/2 evolve as a function of $B_{||}$ in sample F-5 at 100 mK. At $B_{||} = 0$, the transport is virtually isotropic because of the elevated temperature, and $R_{xx} \approx R_{yy}$. For increasing $B_{||}$, however, a prominent anisotropy is *induced*. For example, at $\nu = 9/2$, when $B_{||}$ is directed along $[110]$, R_{yy} steadily rises from about 50 Ω to over 600 Ω, while R_{xx} is largely unaffected. On the other hand, when $B_{||}$ lies along $[1\bar{1}0]$, the induced anisotropy has the opposite orientation: R_{xx} rises to ~600 Ω while R_{yy} changes only modestly. Fig. 8.6 shows essentially the same effect for $\nu = 11/2$ as well. Note that the ultimate orientation of the anisotropy for large $B_{||}$ is the same at 100 mK as it is at 25 mK (see Fig. 8.2). In both cases, the direction of $B_{||}$ is the hard transport direction.

These observations suggest that anisotropic transport in high LLs can be observed at relatively high temperatures, provided that $B_{||}$ is large enough and in the appropriate

direction. The implications of this observation in terms of the stripe CDW picture will be discussed at length in Chapter 9.

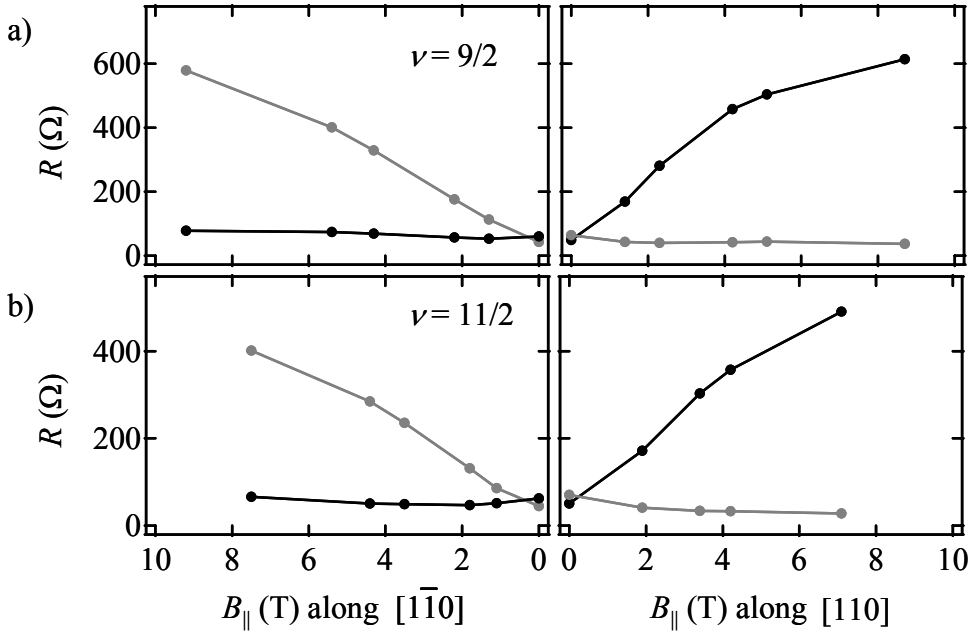

Figure 8.6: a) R_{xx} (gray) and R_{yy} (black) for sample F-5 at $\nu = 9/2$ and 100 mK. Left: $B_{||}$ along $[1\,\bar{1}0]$; right: $B_{||}$ along $[110]$. b) Corresponding data for $\nu = 11/2$. $B_{||}$ induces anisotropic transport at this elevated temperature such that the hard transport direction is along $B_{||}$.

8.3.2 Nonlinear Transport

As described in Section 3.5, a telltale property of the anisotropic phases in high LLs is that the resistance R_{xx} exhibits a distinctive nonlinear dependence on the dc current I_{dc} that is passed through the sample. Fig. 8.7 shows how the nonlinearities in R_{xx} and R_{yy} evolve in the presence of an in-plane field along $[110]$ for the sample B-1 at 25 mK. For $B_{||} = 0$, the two prominent humps in R_{xx} versus I_{dc} indicate that the usual resistance nonlinearity is present. For $B_{||} = 1$ T, the axes of anisotropy have interchanged, with $R_{yy} > R_{xx}$. Importantly, the nonlinearity has interchanged as well, although it is somewhat weaker. Without a model of the nonlinearity, it is difficult to explain why its strength is weaker after the reorientation. However, because the nonlinearity was judged to be a property specific to the stripe CDW, its appearance in R_{yy} after the reorientation is consistent with the interpretation of $B_{||}$ causing a 90° rotation of the stripes.

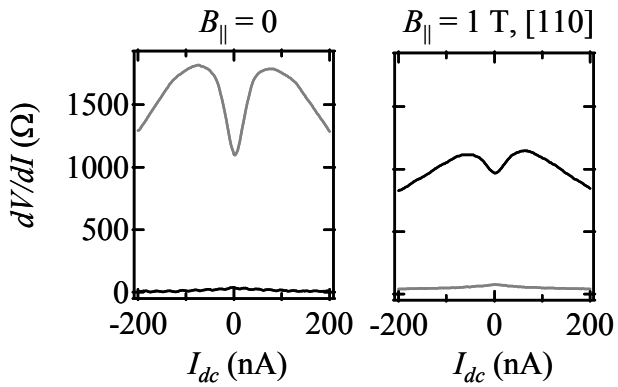

Figure 8.7: Effect of $B_{||}$ on nonlinear differential resistance at 25 mK in sample B-1. As the anisotropy axes interchange with $B_{||}$ along $[110]$, so do the nonlinearities in R_{xx} (gray) and R_{yy} (black).

8.3.3 RIQHE

Fig. 8.8a features a how R_{xx} evolves with $B_{||}$ along $[110]$ over the range $4 < \nu < 5$ at $T =$ 50 mK, focusing on values of R_{xx} less than ~100 Ω to highlight the physics of the RIQHE. The seven traces shown were obtained at tilt angles from 0° to 60° corresponding to increasing values of $B_{||}$. (For $\nu = 9/2$, the corresponding values of $B_{||}$ run from 0 to 4.3 T.) For clarity, each trace is also offset by a constant shift, and the 0 Ω level is indicated by the short dashed horizontal lines. At $\theta = 0°$, the RIQHE is well developed around $\nu = 9/2$ and exhibits prominent satellite peaks separating the IQHE regime from the deep minima of the RIQHE insulating states. The RIQHE is less well-developed around the $\nu = 11/2$ structure, but is still clearly visible at $\theta = 0°$. As the tilt angle is increased, however, the signatures of the RIQHE gradually disappear. The minima in R_{xx} around 1/4 and 3/4 partial fillings lift upward, while the height of the satellite peaks become smaller. By $\theta = 60°$, only a small inflection in R_{xx} indicates any unusual physics due to the RIQHE.

The weakening of the RIQHE is in contrast to the anisotropic region around half-filling, which remains prominent up to in-plane fields in excess of many Tesla. It is perplexing why the RIQHE and the anisotropy would behave differently even though they are both thought to arise from the same essential physics of CDW formation. One

possibility is that a large in-plane fields anisotropically distorts the cyclotron orbits of the electrons that constitute the bubble CDW [2]. This in turn might render transport through the bubble CDW somewhat anisotropic. If this scenario is correct, the one would expect the transport in the RIQHE regions to become more anisotropic as $B_{||}$ increases. Indeed, Fig. 8.8b shows that compared to the case at $\theta = 0°$, for the large tilt angle of $\theta = 60°$ the transport in the weakened RIQHE is somewhat anisotropic, with the hard direction being the same as that observed in the half-filling region.

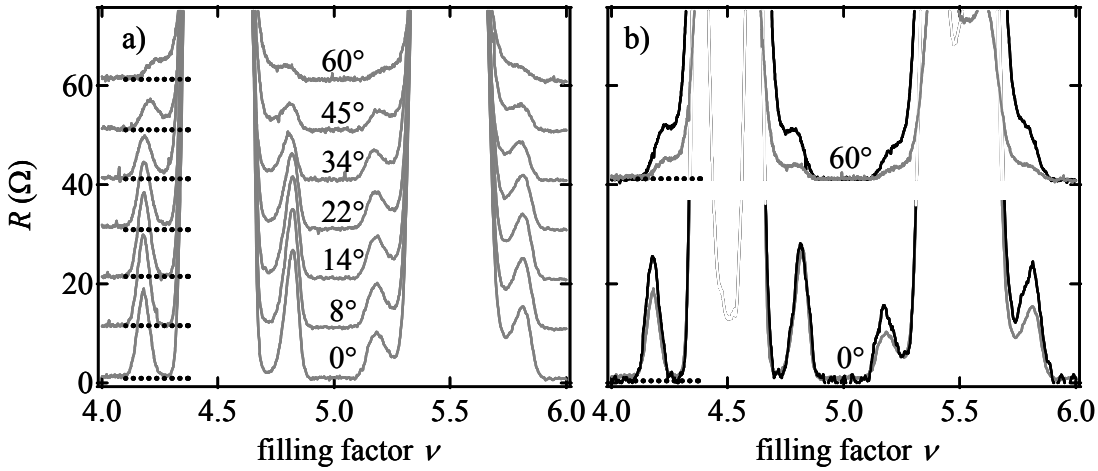

Figure 8.8: Effect of $B_{||}$ (along $[110]$) on the RIQHE at $\nu = 9/2$ and 11/2. a) R_{xx} versus ν at 50 mK for tilt angles 0°, 8°, 14°, 22°, 34°, 45°, and 60°. Each trace is offset by a constant, with the zero resistance level indicated by the short dashed lines. b) R_{xx} (gray) and R_{yy} (black) at 0° and 60° tilt. For large $B_{||}$, the RIQHE is less distinct and somewhat anisotropic.

8.3.4 $N = 1$ LL

An in-plane field induces surprising changes in the transport of the $N = 1$ LL. Fig. 8.9a, b, and c show 50 mK transport data in sample B-1 over a wide range of $B_{\perp}$ for three cases: $\theta = 0°$, $\theta = 46°$ with $B_{||}$ along $[110]$, and $\theta = 47°$ with $B_{||}$ along $[1\bar{1}0]$. First consider Fig. 8.9b, where $B_{||}$ lies along $[110]$. In the high LL regime, the usual 90° rotation of the transport anisotropy in the $N \geq 2$ LLs has occurred. Also, at very low perpendicular magnetic fields where $N >> 1$ or at high perpendicular fields where $N = 0$, any relative anisotropy between R_{xx} and R_{yy} is small and approximately the same as it is at

$\theta = 0°$ (Fig. 8.9a). However, in the $N = 1$ LL a strong anisotropy has been *induced* by the in-plane magnetic field, and its orientation is such that the hard direction lies along $B_{||}$. Thus, the transport around filling factors $\nu = 5/2$ and 7/2, which is normally isotropic at $\theta = 0°$, become highly anisotropic with the application of a substantial in-plane magnetic field. A similar, although weaker, anisotropy is also induced in the $N = 1$ LL when $B_{||}$ is applied along $[1\bar{1}0]$, as shown in Fig. 8.9c, and again the hard direction lies along $B_{||}$.

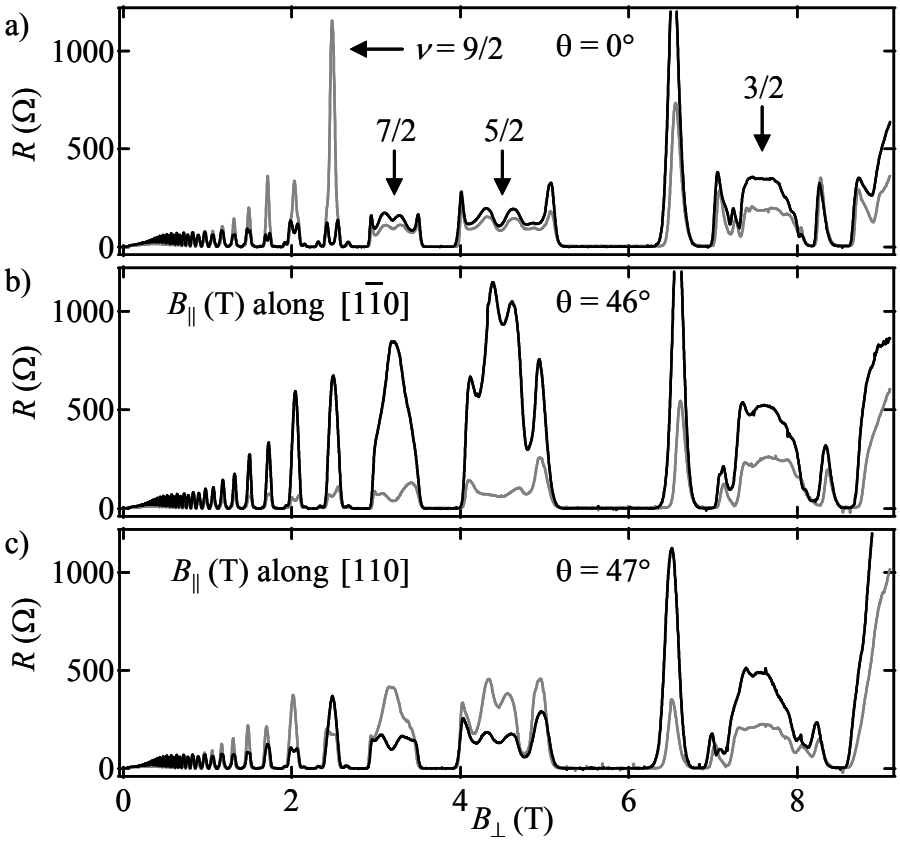

Figure 8.9: R_{xx} (gray) and R_{yy} (black) data for sample B-1 at 50 mK over a wide field range. a) $\theta = 0°$; b) $\theta = 46°$ and $B_{||}$ along $[1\bar{1}0]$; c) $\theta = 47°$ and $B_{||}$ along $[110]$. $B_{||}$ introduces anisotropy in the $N = 1$ LL.

These observations are encapsulated in Fig. 8.10, which shows how R_{xx} and R_{yy} evolve at the half-filling points $\nu = 3/2$, 5/2, and 7/2 for $B_{||}$ directed along $[1\bar{1}0]$ and $[110]$. In the case of $\nu = 3/2$, which is in the $N = 0$ LL, in-plane magnetic fields up to about 8 T in either direction have virtually no impact on the relative values of R_{xx} and R_{yy}.

For $\nu = 5/2$ and 7/2, on the other hand, such fields induce a substantial anisotropy. In both cases, the hard direction is along $B_{||}$. Interestingly, the more rapid development of anisotropy for $B_{||}$ directed along $[110]$ compared to $B_{||}$ along $[1\bar{1}0]$ in the $N = 1$ LL has also been observed by us in the sample F-5. The data from Pan et al. [1] reveal the same trend as well, indicating that it is a generic phenomenon.

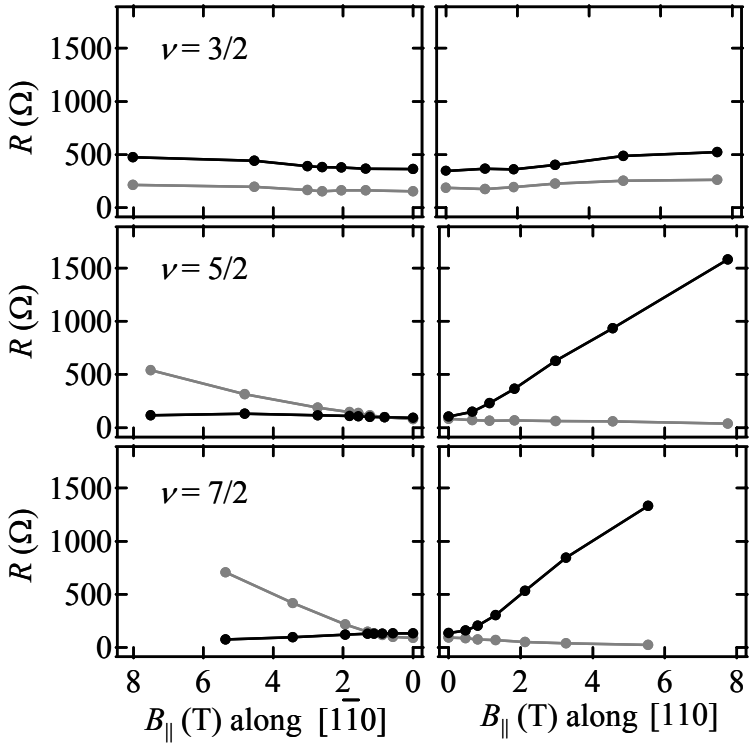

Figure 8.10: Effect of $B_{||}$ on R_{xx} (gray) and R_{yy} (black) at $\nu = 3/2$, 5/2, and 7/2. Data from sample B-1 at 50 mK. Anisotropic transport is induced for $\nu = 5/2$ and 7/2, but not for $\nu = 3/2$.

The fact that anisotropic transport can be induced in the $N = 1$ LL is very important because the physics of electrons in that regime has been a long-standing mystery. Situated intermediately between the $N = 0$ LL where FQHE states dominate and the high LL regime where CDW formation likely rules, the $N = 1$ LL is somewhat of a misfit. It does exhibit FQHE states, but only at very low temperatures, and these include the poorly-understood $\nu = 5/2$ and 7/2 even-denominator states. Earlier research found that an in-plane field suppresses the energy gap of the $\nu = 5/2$ state [3,4], and this was interpreted as evidence that the state is spin-unpolarized. However, other interpretations

of the gap suppression can be constructed, and mounting theoretical work suggests that the $\nu = 5/2$ state is spin-polarized [5,6]. This earlier work on the $\nu = 5/2$ state must now be reconciled with the present experiments which show that an in-plane magnetic field favors an anisotropic state over the FQHE.

8.4 Theoretical Picture of $B_{||}$ as a Symmetry-Breaker

8.4.1 Orbital Coupling of $B_{||}$ with the Stripes

The experimental evidence indicates that the favorable orientation of the stripe CDW with respect to the direction of $B_{||}$ is such that the stripes lie perpendicular to $B_{||}$. This section summarizes the results of a persuasive theoretical picture developed by Jungwirth et al. [7], and Stanescu et al. [8] to account for these results. The central idea is that in the presence of an in-plane field, the orbital motion of the two-dimensional electrons composing the stripe CDW is altered because $B_{||}$ mixes together the higher subbands of the electrons' confinement potential. This subband mixing, in turn, affects the energetics of the stripe CDW and generates a difference in energy for the stripes aligned along versus across the direction of $B_{||}$. By accounting for this effect at the Hartree-Fock level, Jungwirth et al. were able to estimate the so-called anisotropy energy, E_A, associated with an in-plane magnetic field. The anisotropy energy E_A is defined as the difference in energy of the stripes aligned along versus against the in-plane magnetic field (see Fig. 8.11).

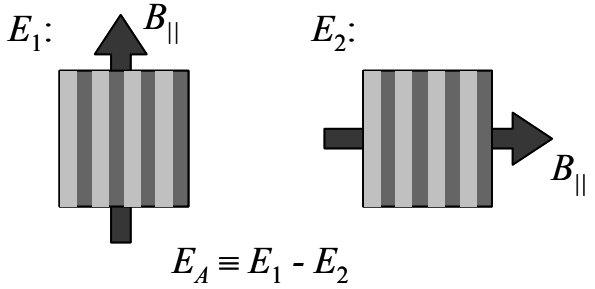

Figure 8.11: Definition of anisotropy energy E_A. If $E_A > 0$, the stripe CDW phase is stabilized with the stripes running perpendicular to $B_{||}$ (right).

Positive values of E_A are in agreement with our experiments in that they indicate that the hard transport direction (where electrons move across the stripes) is along $B_{||}$. However, the sign of E_A is not obvious *a priori*. In fact, Jungwirth et al. found that the sign of E_A is sensitive to such subtle effects as the screening by filled LLs and the exact shape of the 2DES confinement potential. After taking those factors into account, they found that for the samples and in-plane fields we have investigated, E_A is positive. Further confirmation of the theory of Jungwirth et al. comes from its success in accounting for anisotropies in high LLs for a 2DES occupying two subbands of a wide quantum well in the presence of $B_{||}$ [9]. Also, by explaining the experimental observation of anisotropy reorientation caused by $B_{||}$, the theory lends strong support to the overall stripe CDW picture of anisotropic phases in high LLs.

8.4.2 Limitations of the Theory

An aspect of the data that does not fit neatly into the picture of Jungwirth et al. is the sometimes complicated way the anisotropy orientation responds to an in-plane field directed along $[1\bar{1}0]$. If the effect of $B_{||}$ were only to orient the stripe CDW, and if applying $B_{||}$ along $[1\bar{1}0]$ only reinforces the native crystal orientating mechanism, then one would expect the degree of anisotropy to remain the same and possibly even increase. However, Fig. 8.2 shows that the peak height of R_{xx} for both $\nu = 9/2$ and 11/2 is seen to vary considerably at low $B_{||}$ along $[1\bar{1}0]$ before stabilizing at approximately constant values. This indicates that $B_{||}$ does more than simply serve as an orienting field of the stripes. For example, one potential effect of $B_{||}$ not taken into account by the theory of Jungwirth et al. is how an in-plane field affects the microscopics of electron transport along or across the stripes. Such an effect might be able to account for the apparently reduced anisotropy at large values of $B_{||}$ along $[1\bar{1}0]$. This affect could also explain why the strength of the reoriented anisotropy is also reduced by approximately the same amount when $B_{||}$ lies along $[110]$ (see Fig. 8.2).

8.4.3 Estimating the Strength of the Native Symmetry-Breaker

The ability to determine the anisotropy energy E_A of a stripe CDW in an in-plane magnetic field permits an estimate to be made of the strength of the *native* orienting mechanism of the crystal. This is done by evaluating E_A at $B_{||}^*$, the magnetic field along [110] necessary to render the transport isotropic. At $B_{||}^*$, the in-plane field is presumed to just cancel the effect of the native orienting mechanism.

Using the specific structural parameters of the samples F-5, B-1, and H-1, Jungwirth determined the theoretical field-induced anisotropy energies as a function of $B_{||}$ [10], and the results are shown in Fig. 8.12 for the case of $\nu = 9/2$. Note that for in-plane fields up to 1 T, the calculated values of E_A in each sample are positive, indicating that the stripes should lie perpendicular to $B_{||}$. It is remarkable how different the dependence of E_A on $B_{||}$ is for sample B-1 and the H-1, despite their densities being so similar (2.67 and 2.54×10^{11} cm^{-2}, respectively). The reason for the apparent discrepancy is that the unoccupied second subband in the heterojunction of sample B-1 is much closer to the chemical potential than for the square quantum well of sample H-1, and subband mixing is more pronounced. Jungwirth et al. found that such mixing generally yields smaller anisotropy energies.

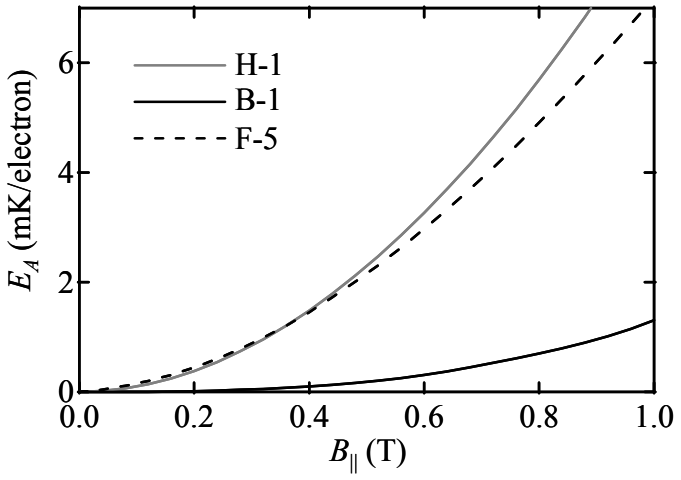

Figure 8.12: Theoretical results of anisotropy energy versus in-plane magnetic field of a stripe CDW in the samples H-1, B-1, and F-5. Evaluated at the switching field $B_{||}^*$, E_A yields an estimate of the strength of the native symmetry-breaking mechanism. Calculations were performed by T. Jungwirth.

The experimentally determined values of $B_{\|}^{*}$ for the three samples at $\nu = 9/2$ are 0.50, 0.55, and 0.24 T, respectively. From Fig.JunwirthEA, then, the native orienting energies for the three samples B-1, F-5, and H-1 are found to be 0.2, 2.4, and 0.5 mK/electron. These energies are much smaller than the ~100 mK temperature scale where the onset of anisotropy occurs. This supports the picture that the anisotropic phases consist of a CDW that forms from robust interaction physics, and then is oriented by a relatively weak native symmetry-breaking field. Also, these estimates of E_A should offer useful constraints on the strength of an proposed crystal orienting mechanisms. Indeed, the candidate mechanism of piezoelectricity, discussed in Section 7.3, yields orienting energies on the same order of magnitude as those determined by the present comparison of theory and experiment.

8.5 Stripes Oriented along Diagonals?

Can the stripes be made to lie along either of the "diagonal" directions [100] or [010]? Answering this question will provide a good test of whether $B_{||}$ can be used as an orienting mechanism to align the stripes in an arbitrary direction. According to the theory of Jungwirth et al., this should be the case. However, the underlying orientational symmetry-breaking field of the host crystal may complicate matters. For example, the native symmetry-breaking mechanism might have a double-minimum structure favoring alignment along the usual $[110]$ and $[1\bar{1}0]$ directions. For example, the piezoelectric mechanism might generate this double-minimum potential (see Section 7.3). Also, the recent experiments of Zhu et al. [11] suggest that in a given sample, the stripes can be made to lie along $[1\bar{1}0]$ or $[110]$, but not along either of the diagonals, as the 2DES density changes. If two local minima exist in the orientational energy of a stripe CDW, then the experiments described below might reveal this by testing whether it is relatively difficult to orient the stripes along one of the unfavorable directions.

First, consider the longitudinal resistances obtained with current flowing along the diagonal [100] and [010] directions in the more familiar case of $B_{||}$ directed along [110]. To simplify the notation, these longitudinal resistances will be labeled R_{pp} and R_{qq}, so that [100] represents the **p** direction and [010] the **q** direction. The directions **p** and **q** are rotated by 45° with respect to **x** and **y**. (To measure R_{pp} and R_{qq}, the current is driven between opposite corner contacts while the voltage is measured between two side contacts.) Fig. 8.13 contains 25 mK data of R_{xx}, R_{yy}, R_{pp}, and R_{qq} versus $B_{||}$ for the filling factors $\nu = 9/2$ and 11/2 in sample B-1. The top panels, containing R_{xx} and R_{yy}, show essentially the same physics as in lower-temperature data of Fig. 8.3. For $B_{||}$ along [110], the orientation of the anisotropy changes by 90° once $B_{||}$ exceeds ~1 T. The lower panels demonstrate that as this reorientation occurs, R_{pp} and R_{qq} remain roughly isotropic for the whole range of $B_{||}$.

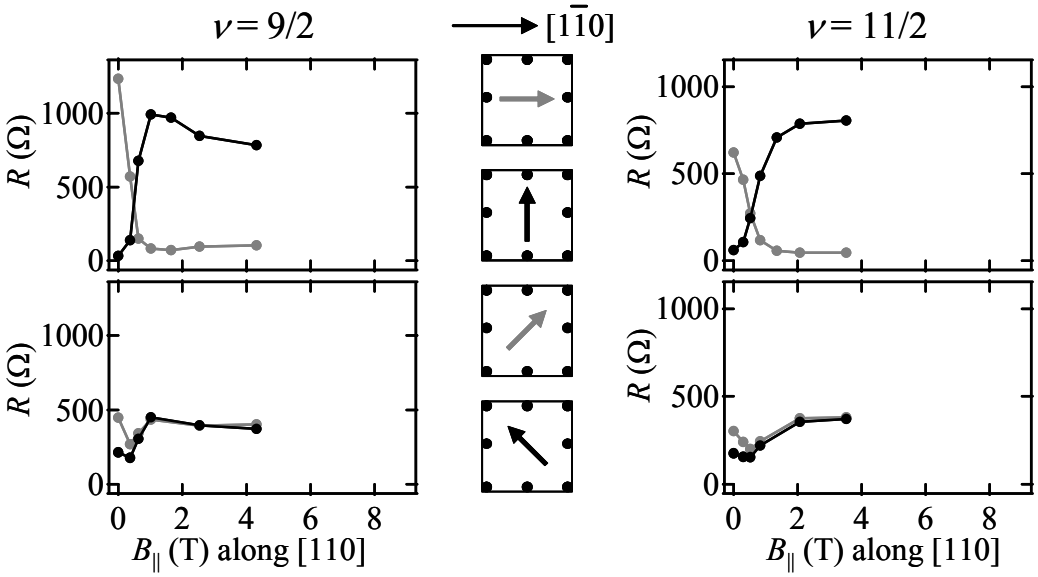

Figure 8.13: Effect of $B_{||}$ along [110] on longitudinal resistances in four directions. Top panels: R_{xx} (gray), R_{yy} (black). Bottom panels: R_{qq} (gray), R_{pp} (black). Whereas the R_{xx}, R_{yy} anisotropy reverses, no anisotropy appears in R_{qq} and R_{pp}.

This will be important for comparing the situation to $B_{||}$ directed along [010], but it also is a good demonstration that as the 90° reorientation occurs, the anisotropy orientation is *not* continuously rotated through the whole span. In other words, at $B_{||} \approx$ 0.5 T, the R_{xx} and R_{yy} values are not roughly the same because the stripe CDW has rotated

by 45°. The R_{pp} and R_{qq} values, also being roughly equal at $B_{||} \approx 0.5$ T, indicate that the transport at that point is isotropic with respect to all four directions (and presumably with respect to any direction within the 2DES plane).

Next, Fig. 8.14 shows how R_{xx}, R_{yy}, R_{pp}, and R_{qq} respond to an in-plane field along [010], i.e., the **q** direction, and the results are not as clear-cut as in Fig. 8.13. In the case of $\nu = 9/2$, $B_{||}$ along [010] does not produce a strong anisotropy with the anticipated orientation of the hard direction along $B_{||}$ (i.e., $R_{qq} > R_{pp}$). The resistance R_{qq} does seem to gradually pull away from R_{pp} at quite high in-plane fields, but the eventual anisotropy at $B_{||} \geq 8$ T is not as striking as that which results when $B_{||}$ is applied along [110] instead (see Fig. 8.13). The resistances R_{xx} and R_{yy}, meanwhile, show a substantial degree of anisotropy at moderate fields before becoming roughly equal at the highest $B_{||}$ examined. Because a strong anisotropy in R_{pp} and R_{qq} does not develop for $B_{||}$ along [110] at $\nu = 9/2$, it appears that indeed it may be more difficult to reorient the stripes along a diagonal than along one of the usual principal axes.

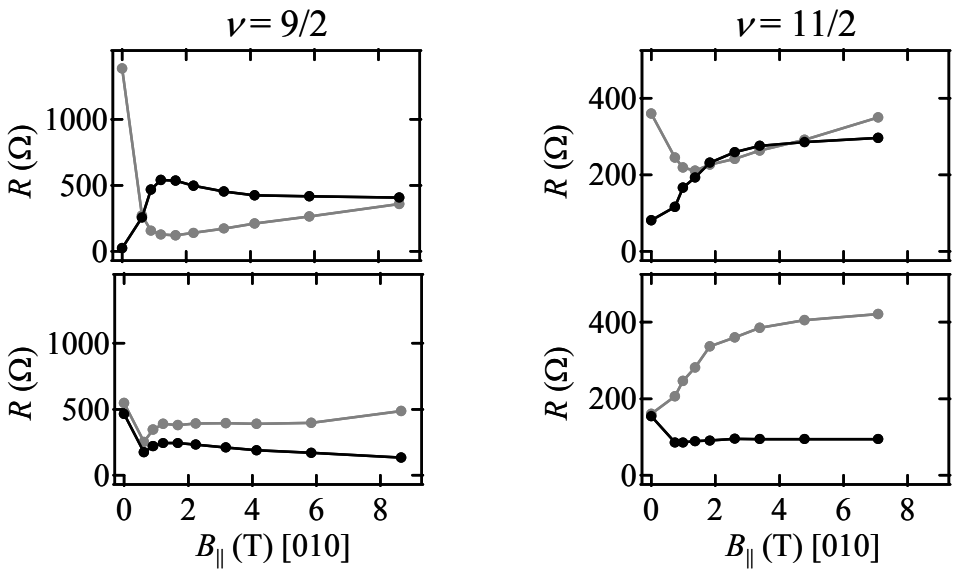

Figure 8.14: Same four panels as in Fig. 8.16, but now $B_{||}$ lies along [010]. A moderate anisotropy appears to be induced in R_{qq} and R_{pp} at $\nu = 11/2$, but the results at $\nu = 9/2$ are more ambiguous.

However, basing this conclusion on the $\nu = 9/2$ data alone is risky, especially considering that the anisotropy at $\nu = 9/2$ in sample B-1 does not conform to the orienting

theory of Jungwirth et al. when $B_{||}$ is directed along $[1\bar{1}0]$ (see Fig. 8.3). The anisotropy orientation at $\nu = 11/2$, on the other hand, is consistent with the reorientation theory (again, see Fig. 8.3). Therefore, it is important to consider the situation at $\nu = 11/2$, shown in the lower panels of Fig. 8.14. This time, $B_{||}$ along [010] does indeed appear to induce a substantial anisotropy in R_{pp} and R_{qq}, with the hard direction being along the expected [010] axis. By $B_{||}$ = 2-3 T, as much anisotropy is present in R_{pp} and R_{qq} as was initially present in R_{xx} and R_{yy}. The latter resistances, meanwhile, show good isotropy for $B_{||}$ along [010]. The $\nu = 11/2$ data thus suggest that $B_{||}$ along [010] can easily reorient the stripe CDW to lie along the diagonal [100].

In summary, the experiments described in this section yield somewhat ambiguous results. Apparently, $B_{||}$ along a diagonal direction may reorient the anisotropy by 45° for $\nu = 11/2$, but the results for $\nu = 9/2$ are less clear. Thus firm conclusions cannot be drawn regarding whether piezoelectricity or some other native orienting mechanism that favors $[1\bar{1}0]$ and [110] orientations over [100] and [010].

---

1 W. Pan, R.R. Du, H.L. Stormer, D.C. Tsui, L.N. Pfeiffer, K.W. Baldwin, and K.W. West, Phys. Rev. Lett. **83**, 820 (1999).

2 Rosenow and S. Scheidl, Int. J. Mod. Phys. B **15**, 1905 (2001).

3 J.P. Eisenstein, R.L. Willett, H.L. Stormer, D.C. Tsui, A.C. Gossard, and J.H. English, Phys. Rev. Lett. **61**, 997 (1988).

4 See the chapter by J.P. Eisenstein in *Perspectives in Quantum Hall Effects*, ed. S. Das Sarma and A. Pinczuk (John Wiley, New York 1997).

5 G. Moore and N. Read, Nucl. Phys. B **360**, 362 (1991).

6 R.H. Morf, Phys. Rev. Lett. **80**, 1505 (1998).

7 T. Jungwirth, A.H. MacDonald, L. Smrcka, S.M. Girvin, Phys. Rev. B **60**, 15574 (1999).

8 T. Stanescu, I. Martin, P. Phillips, Phys. Rev. Lett. **84**, 1288 (2000).

9 W. Pan, T. Jungwirth, H.L. Stormer, D.C. Tsui, A.Hl MacDonald, S.M. Girvin, L. Smrcka, L.N. Pfeiffer, K.W. Baldwin, and K.W. West, Phys. Rev. Lett. **85**, 3257 (2000).

10 K.B. Cooper, M.P. Lilly, J.P. Eisenstein, T. Jungwirth, L.N. Pfeiffer, and K.W. West, Solid State Commun. **119**, 89 (2001).

11 J. Zhu, W. Pan, H.L. Stormer, L.N. Pfeiffer, and K.W. West, Phys. Rev. Lett. **88**, 116803 (2002).

Chapter 9:
Evidence for a Liquid-Crystal Phase Transition

9.1 Going beyond the Hartree-Fock Solution

9.1.1 Fluctuations and Electronic Liquid Crystals

Various aspects of the transport phenomena in high LLs have been successfully attributed to the formation of stripe and bubble CDWs in high LLs: Stripe and bubble formation is consistent with the anisotropic transport and RIQHE states in high LLs; transport models of conduction through the stripe phase are in fair agreement with the experiments; and the reorientation of the resistance anisotropy by an in-plane magnetic field $B_{||}$ has been accounted for using a stripe-based model.

Despite these successes, however, the straightforward stripe CDW picture of Chapter 5 is widely believed to be incomplete. As a mean-field solution, the Hartree-Fock (HF) ground state tends to exaggerate the amount of order in a system by neglecting its fluctuations due to thermal or quantum agitation. The first researchers to consider possible embellishments to the HF solution of a stripe CDW were Fradkin and Kivelson (FK) [1]. Using very general symmetry arguments, FK proposed qualitative phase diagrams of electrons in high LLs in the absence of disorder but in the presence of quantum fluctuations at zero temperature and thermal fluctuations at finite temperature. These phase diagrams provide an important way of classifying the possible modifications to the basic stripe CDW solution in terms of electronic liquid crystals. Listed in order of the increasing importance of fluctuations, the possible phases are (see Fig. 9.1) [1,2]:

1. *A stripe crystal*, where the unidirectional stripe CDW with a wave vector along **x** also possesses a periodic modulation along the stripes in the **y** direction. As mentioned in Section 5.3, this state is actually a Hartree-Fock solution to the interacting problem, but the modulations along the stripes are

small. In the stripe crystal, translational symmetry is broken in both the **x** and **y** directions, and hence rotational invariance is also violated.

2. *A smectic liquid crystal*, where modulations along the a given stripe have no long-range correlations with stripes farther away. In this case, translational invariance is restored along **y** but is still broken along **x**. Rotational symmetry is also still broken.
3. *A nematic liquid crystal*, where translational symmetry along both **x** and **y** is preserved while rotational symmetry is still broken. Essentially an anisotropic liquid, the nematic liquid crystal phase arises naturally from the smectic phase when the stripes are allowed to terminate.
4. *An isotropic liquid*, where now all symmetries (rotational and translational) are restored. Importantly, an isotropic liquid may still possess short-range stripe order, but over large distances the positions and orientations of these "stripe moments" are randomized.

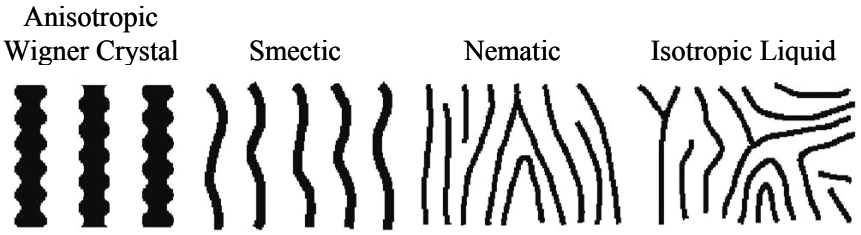

Figure 9.1: Four possible variants of the stripe CDW phase in order of increasing symmetries. Reproduced from ref. [2] with permission of M. Fogler.

Each of the first three possibilities listed above has a broken rotational symmetry and thus is consistent with the experimental observation of anisotropic transport. Note that because it is a continuous symmetry, true long-ranged orientational order cannot exist at finite temperatures in two dimensions. This is the well-known result of the Mermin-Wagner theorem [3]. Nonetheless, a state with quasi-long-ranged, algebraically-decaying orientational order can still account for the experimental anisotropies. When some background anisotropy is present to pick out a preferred direction, the collective electronic state will exhibit a large net anisotropy over macroscopic length scales.

At present there is no firm consensus regarding which possibility—the stripe crystal, smectic, or nematic—accurately describes the experimental situation around half-filling of high LLs at low temperatures. The stripe crystal has been argued to be unlikely because it should be pinned by impurities and therefore be insulating, much like the bubble CDW states at small partial filling factors [1]. Other calculations also suggest that the stripe crystal will melt into a smectic at inaccessibly low temperatures [4,5]. At finite temperatures, FK favor the nematic over the smectic because the energy of a dislocation in two dimensions is finite and because the experiments suggest that dissipation along the easy direction remains finite even as $T \to 0$ [1].

9.1.2 The Nematic-to-Isotropic Phase Transition

One of the most attractive features of the electronic liquid crystal picture of the anisotropic states in high LLs is that it can reconcile a nagging discrepancy between Hartree-Fock theory and experiment about the temperature below which the resistance anisotropies are observed. According to the Hartree-Fock theory, the melting temperature of the stripe CDW phase is on the order of a few Kelvin [6,2]. This is too large by about an order of magnitude: experimentally, the resistance anisotropy sets in only below about 100 mK. Disorder, known to affect the temperature at which the FQHE is observed [7], might account for some of this difference.

However, a more interesting possibility is that the onset of anisotropy at low temperatures does not signify the initial development of CDW formation; rather it reflects the orientational ordering of local regions that have pre-existing stripe order. This possibility was first suggested by FK [1], who proposed that the transition from anisotropic to isotropic transport around 100 mK reflects a nematic-to-isotropic liquid crystal phase transition. In this picture, for temperatures less than 100 mK the stripes constitute an anisotropic nematic liquid crystal. Above 100 mK, defects in the nematic proliferate until the 2DES becomes an isotropic liquid. Rather than melting, the stripes simply become orientationally disordered over the macroscopic sample dimensions. Only at much higher temperatures of a few Kelvin would the stripe formation on some microscopic scale vanish. The sequence of this proposed scenario is sketched in Fig. 9.2.

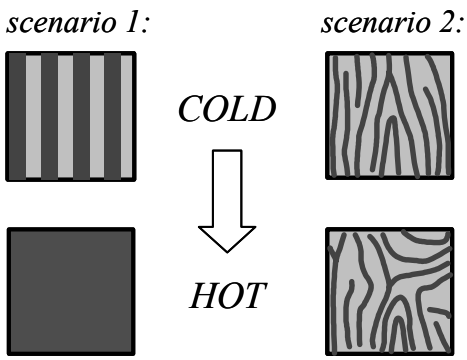

Figure 9.2: Two scenarios for the transition from anisotropic to isotropic transport in the stripe CDW phase as T increases. Left: the stripes melt. Right: the stripes lose their net orientation.

The nematic-to-isotropic phase transition occurs via a Kosterlitz-Thouless (KT) transition due to the unbinding of "disclination pairs," which are analogous to the vortex pairs in systems that obey a 2D XY model, such as superfluid ^{4}He [3]. Based on that analogy, Fradkin et al. [8] addressed the problem of the temperature dependence of anisotropic transport in high LLs by using a classical 2D XY model with a director order parameter. They found that one set of our data is well-described by a 2D XY model with an orienting field strength of ~3.5 mK and a phase transition temperature of ~65 mK. (Note: the 3.5 mK energy is not per electron but per some grouping of electrons that constitute a small stripe domain.) The relatively small orienting field is consistent with the anisotropic phase being weakly oriented by some native symmetry-breaking mechanism of the 2DES host crystal. Subsequent to the work of Fradkin et al., Wexler and Dorsey (WD) [9] formulated a parameter-free theory of the nematic-to-isotropic phase transition and found that the nematic-to-isotropic phase transition temperature occurs at ~200 mK for typical 2DES densities. This is in much better agreement with the experiments than the Hartree-Fock melting temperature of a few Kelvin.

Of course, the classical models of Fradkin et al. and Wexler and Dorsey are inherently incomplete because the quantum nature of the nematic state is completely ignored. To remedy this, Radzihovsky and Dorsey [10] recently derived a microscopic theory of a quantum nematic pertaining to the anisotropic states in half-filled high LLs. Experiments designed to test this model have not yet been performed.

9.1.3 Searching for Stripes at Elevated Temperatures

A striking prediction of the electronic liquid crystal picture of the anisotropic phases in high LLs is that the stripe structure persists on some microscopic scale above the temperatures where resistance anisotropies are observed. Therefore, any evidence of stripe formation at elevated temperatures will lend strong support to the nematic-to-isotropic phase transition hypothesis. A hint of such evidence has already been presented in Section 8.3, where an in-plane magnetic field was shown to induce anisotropic transport in high LLs at 100 mK in sample F-5. Because $B_{||}$ acts like an orientational symmetry-breaking field, a natural interpretation of that data is that $B_{||}$ generates a net orientation in the otherwise isotropic distribution of local stripe regions. A cartoon of this scenario is shown in Fig. 9.3.

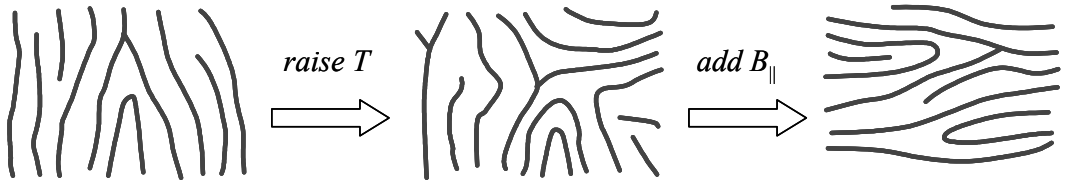

Figure 9.3: Cartoon showing how local stripe CDW order might be detected at high T by using an in-plane magnetic field to overcome thermal fluctuations and orient the liquid-crystal-like phase.

9.2 Symmetry-Breaking in the 2D XY Model

9.2.1 Setting Up the Problem

Before examining how $B_{||}$ affects transport in high LLs at elevated temperatures, it is helpful to consider how the 2D XY model proposed by FK is affected by a strong symmetry-breaking field. The model approximates the nematic liquid crystal as a lattice of individual "nematogens" that interact with each other through an exchange interaction J and with an external symmetry-breaking field h. Each nematogen represents a small stripe "moment" with some orientation in the range $0° < \varphi < 180°$, where φ is measured from the **x** axis (see Fig. 9.4). In the conventional two-dimensional XY model, the individual moments are treated as spins, but in this case the 180° rotational periodicity of

a stripe moment means that each nematogen should be treated as a director. The resulting Hamiltonian is:

$$H = -J\sum_{\langle i \neq j \rangle} \cos\left[2\left(\varphi_i - \varphi_j\right)\right] + h\sum_i \cos\left(2\varphi_i\right),$$

where the first summation is over nearest neighbors only. Meanwhile, the "magnetization" M of the entire system is:

$$M = \left\langle \cos\left(2\varphi_i\right)\right\rangle.$$

Note that the symmetry-breaking field h has been taken to be along **x**, and so M is necessarily along the same direction.

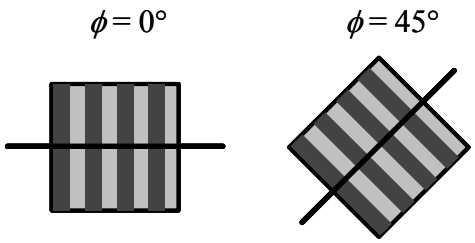

Figure 9.4: Cartoon of two nematogens, or stripe CDW regions, oriented at $\phi = 0°$ and $\phi = 45°$.

The magnetization of the nematogen lattice is meant to be analogous to the degree of anisotropy in a stripe CDW system. For $M = 1$, each nematogen is aligned along **x,** while $M = 0$ results when their orientations are randomized. However, there is no general relationship between M and the transport coefficients measured in resistance measurements. Certainly M should be independent of the sample geometry and be a function of the resistivities ρ_{xx} and ρ_{yy} rather than the geometry-dependent resistances R_{xx} and R_{yy}. Fradkin et al. suggested on general symmetry principals that the quantity $(\rho_{xx} - \rho_{yy})/(\rho_{xx} + \rho_{yy})$ is a measure of M at least in some temperature regimes. But this makes the probably wrong assumption that a complete alignment of the stripes ($M = 1$) exhibits a vanishing easy resistivity $\rho_{yy} = 0$.

The symmetry-breaking field h is intended to capture the physics of both the native crystal orienting mechanism and the in-plane magnetic field. As with M, however, the field h should not be interpreted explicitly in terms of real physical parameters. For example, it is known experimentally that $B_{||} \rightarrow -B_{||}$ has no significant effect on the resistance anisotropy, while $h \rightarrow -h$ clearly will change the net magnetization of the model system. Also, $B_{||}$ seems to affect the transport through the stripe phases in other ways than simply by orienting the stripes (see Section 8.4). Thus the results of the 2D XY model are only meant to provide a qualitative description of the nematic-to-isotropic phase transition believed to occur in stripe CDW systems.

9.2.2 Monte Carlo Solution of $M(h,T)$

The solution of the 2D XY model described above consists of an equation of state $M(h,T)$ relating the magnetization to the temperature and the strength of the symmetry-breaking field. For the case of $h = 0$, the solution is trivial: $M = 0$ for any finite T. This is a consequence of the Mermin-Wagner theorem [3]. Even when $h = 0$, however, the system exhibits the KT phase transition at a temperature $T_{KT} = 0.88J$, where the vortex-pair unbinding transition occurs [8]. For $h \neq 0$, $M(h,T)$ should be nonzero at all T because the orientational symmetry is explicitly broken. Furthermore, any small h should result in $M(h,T)$ being close to 1 as long as $T < T_{KT}$, and then falling toward 0 as the temperature is increased. This represents the nematic-to-isotropic phase transition, and its sharpness depends on the magnitude of h.

To see this behavior, we follow Fradkin et al. [8] and compute the function $M(h,T)$ numerically using the Metropolis Monte Carlo method [11,12] on a 100×100 grid. The Metropolis method uses an iterative importance-sampling technique to search phase space for an equilibrium configuration. We are confident of its validity because the Monte Carlo results of Fradkin et al. were reproduced and the computed values of $M(h,T)$ for a free system ($J = 0$) matched the analytical result. For a detailed description of our Monte Carlo solution and the code used for its implementation, see Appendix B.

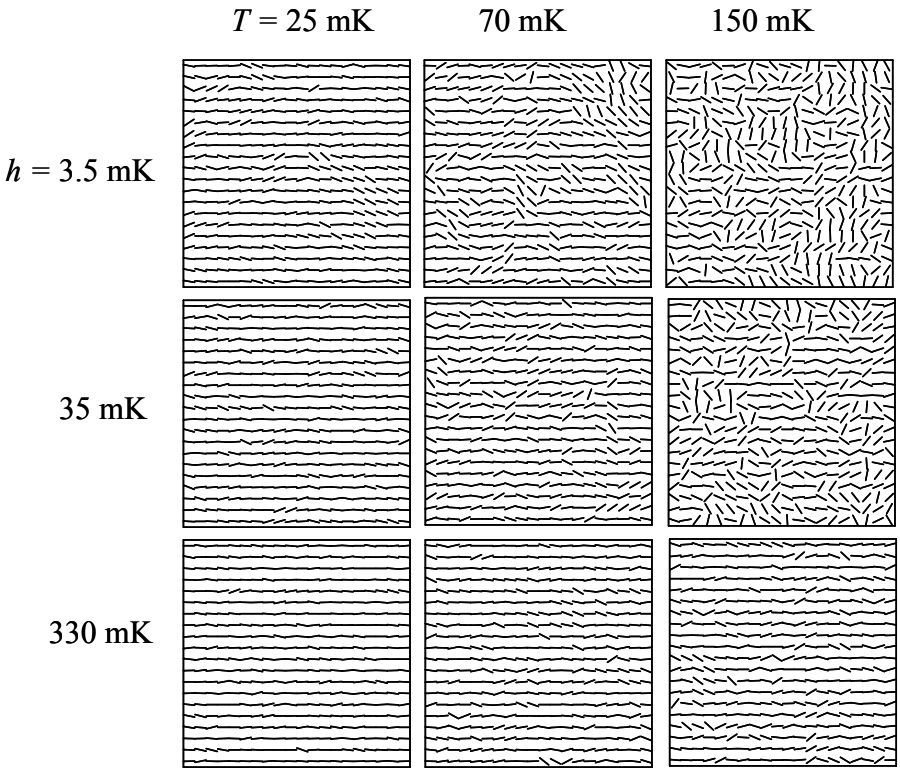

Figure 9.5: Snapshots of 20 × 20 lattice sites of the nematogen orientations from a 2D XY Monte Carlo calculation. The nearest-neighbor coupling energy is $J = 73$ mK, and the nine panels correspond to combinations of the three temperatures T and orienting fields h as shown. The magnetization M increases at either lower T or higher h.

Fig. 9.5 gives a visual impression of the behavior of $M(h,T)$ by showing selected 20 × 20 "snapshots" of the full 100 × 100 grids for the cases of $T/J = 0.34$, 0.96, and 2.1, and $h/J = 0.05$, 0.5, and 4.5, where for simplicity the energy units are taken to be the same as those of temperature (i.e. the Boltzmann constant $k_B = 1$). Each short line in one of the panels represents a nematogen oriented at some angle $0° < \varphi < 180°$. From left to right, the temperature increases; from top to bottom, the symmetry-breaking field increases. The computed values of M for the full 100 × 100 systems are written for each case. The images show two general trends. First, the magnetization decreases with increasing temperature, as can be seen by the nematogen orientations' increasing randomization for higher T. This reflects the thermal fluctuations overcoming the exchange energy J keeping nearest-neighbor nematogens aligned. Second, increasing the

symmetry-breaking field h increases the M. For example, at the highest temperature $T/J = 2.1$, there is virtually no order when h/J is only 0.05. On the other hand, for $h/J = 4.5$, the system reaches 85% of full magnetization. This trend comes from the symmetry-breaking field overwhelming the thermal fluctuations that normally randomize the nematogen orientations.

Fig. 9.6 shows M as a function of T/J for $h/J = 0.05$, 0.5, 1.5, and 4.5. For $h/J = 0.05$, M exhibits a sharp drop as T/J exceeds about unity. This signifies the transition from an anisotropic nematic to a nearly isotropic phase. The transition temperature is set by the KT phase transition temperature $T_{KT} = 0.88J$, indicated by an arrow in Fig. 9.6. As h/J increases, the transition from anisotropy to isotropy becomes systematically broader because the increasing strength of the symmetry-breaking field permits larger magnetizations at higher temperatures.

The general properties of $M(h,T)$ for the two-dimensional XY model are similar to those of the magnetization of a ferromagnet in an external magnetic field. Very weak external fields merely break rotational symmetry and orient the magnetization below the Curie temperature T_c. In the presence of a strong magnetic field, however, the ferromagnetic transition is broadened out in temperature and substantial magnetization is present at temperatures $T > T_c$. For $T >> T_c$, the magnetization is that of the free spins in the system [13].

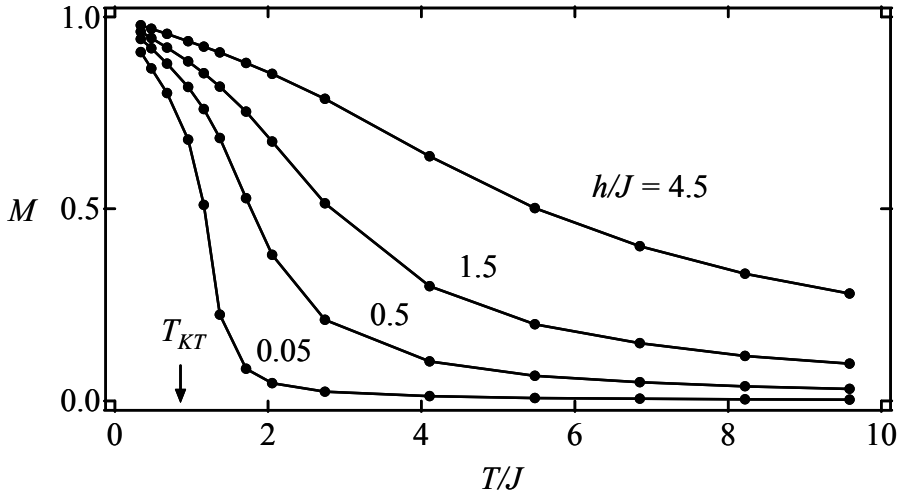

Figure 9.6: The Monte Carlo solution of $M(h,T)$ versus T/J at four values of h/J. The anisotropic-to-isotropic transition is broadened out for increasing h. The Kosterliltz-Thouless phase transition temperature $T_{KT} = 0.88J$ is indicated by the arrow.

In the context of the experiments to be described below, the salient feature of each of these systems—the isotropic liquid crystal above T_{KT} or the ferromagnet above T_c—is that the individual moments *still exist* at the high temperatures. A symmetry-breaking field is still capable of generating a magnetization in the systems even at those high temperatures where no large magnetization is otherwise present. The next section will show data suggesting that the same physics is at work in the case of the anisotropic phases in high LLs.

9.3 An In-Plane Field and the Onset of Anisotropy

9.3.1 Broadening of the Onset to Anisotropy

All data presented in this section come from sample F-5, and Fig. 9.7 illustrates the basic effect of an in-plane magnetic field on the transition from anisotropic to isotropic transport. In Fig. 9.7a, $B_{||} = 0$ transport data is shown for the $\nu = 9/2$ structure at $T = 25$, 40, 50, and 100 mK. The strong anisotropy at 25 mK is completely gone by 100 mK. Meanwhile, Fig. 9.7b shows how the $\nu = 9/2$ transport evolves with temperature when the sample is tilted by $\theta = 58°$ with $B_{||}$ along $[1\bar{1}0]$. At $\nu = 9/2$, this angle corresponds to an in-plane field of 2.2 T. Note that this is well above the value of $B_{||} \approx 1$ T required to overcome the native orienting mechanism from the host crystal (see Fig. 8.2), and so the external orienting field is presumably stronger than the native crystal field present when $B_{||} = 0$. Unlike the case where $B_{||} = 0$, the data in Fig. 9.7b show that significantly higher temperatures are needed before the transport becomes isotropic. Only by 300 mK do R_{xx} and R_{yy} reach approximately the same value at $\nu = 9/2$.

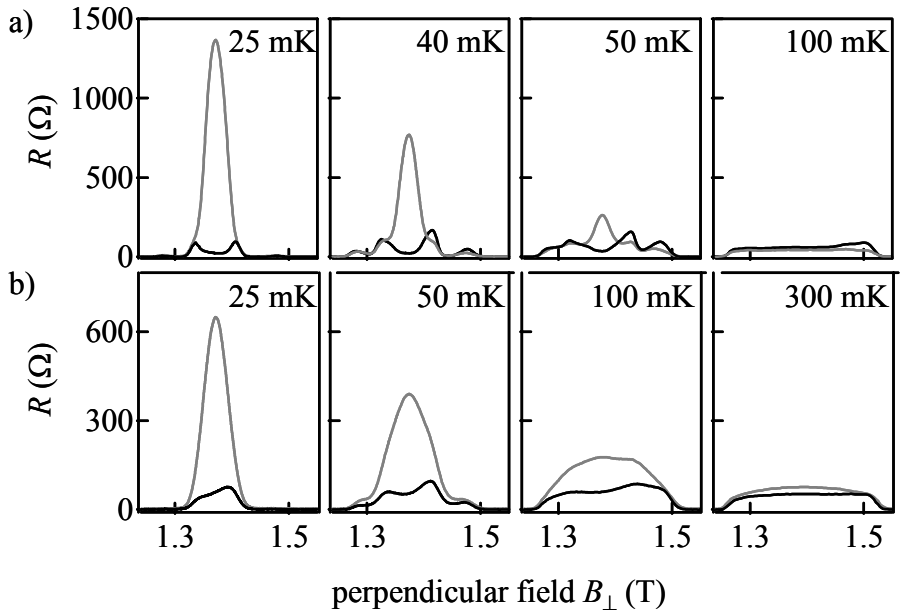

Figure 9.7: Thermal broadening of anisotropic-to-isotropic transition in sample F-5 due to $B_{||}$. a) R_{xx} (gray) and R_{yy} (black) through $\nu = 9/2$ for $B_{||} = 0$. The anisotropy vanishes by ~100 mK. b) $B_{||} = 2.2$ T along $[1\,\bar{1}0]$ at $\nu = 9/2$. The anisotropy persists until ~300 mK.

To give a more complete picture of the transition from anisotropic to isotropic transport, Fig. 9.8 displays the temperature dependence of the longitudinal resistance in the hard and easy directions, R_{hard} and R_{easy}, at $\nu = 9/2$ for several values of $B_{||}$. The data in the left-hand panels were taken with $B_{||}$ directed along $[1\,\bar{1}0]$. In this case, $B_{||}$ does not interchange the principal axes of anisotropy and thus $R_{hard} = R_{xx}$. For the right-hand panels, however, $B_{||}$ is along $[110]$ and therefore *does* interchange the hard and easy directions, provided $B_{||} > 0.5$ T. Therefore, with the exception of the $B_{||} = 0$ data, the traces in the right-hand panels are of $R_{easy} = R_{yy}$.

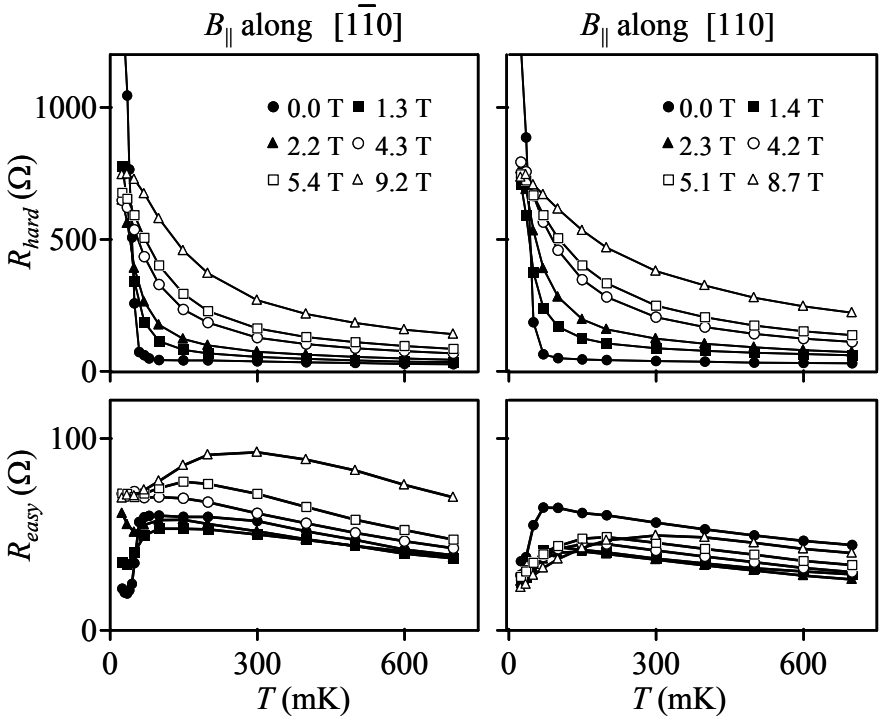

Figure 9.8: Temperature dependencies of longitudinal resistance in the hard (top) and easy (bottom) directions at $\nu = 9/2$ for sample F-5. For increasing $B_{||}$ along either $[1\bar{1}0]$ (left) or $[110]$ (right), the onset to anisotropic transport at low T is broadened.

It is clear from Fig. 9.8 that a large $B_{||}$ systematically broadens out the variation of R_{hard} at low temperatures. The temperature dependence of R_{hard} at $B_{||} = 0$ is extremely steep, falling below 50 Ω by 100 mK and then remaining steady at temperatures above that. As $B_{||}$ increases, the transition becomes steadily broadened, until at $B_{||} \approx 9$ T R_{hard} is still falling noticeably with increasing T even above 600 mK. This qualitative broadening effect occurs for both orientations of the in-plane field relative to the crystal directions. Note that the broadening effect is not obviously present in R_{easy}, although some softening in the temperature dependence occurs for low temperatures and large in-plane fields.

Fig. 9.9 shows data taken in the same situation as Fig. 9.8, except that R_{hard} and R_{easy} were obtained at $\nu = 11/2$. Essentially the same qualitative behavior occurs for $\nu = 11/2$. Although higher filling factors were not studied as carefully in this sample, we presume that the effect is generic for all high LLs that exhibit anisotropic transport.

The broadening effect shown in Fig. 9.8 and Fig. 9.9 is in good qualitative agreement with the results of the Monte Carlo calculation of Section 9.2. Just as the nematic-to-isotropic transition in Fig. 9.6 becomes more and more gradual for increasing h, so does the transition from anisotropic to isotropic transport at $\nu = 9/2$ and 11/2.

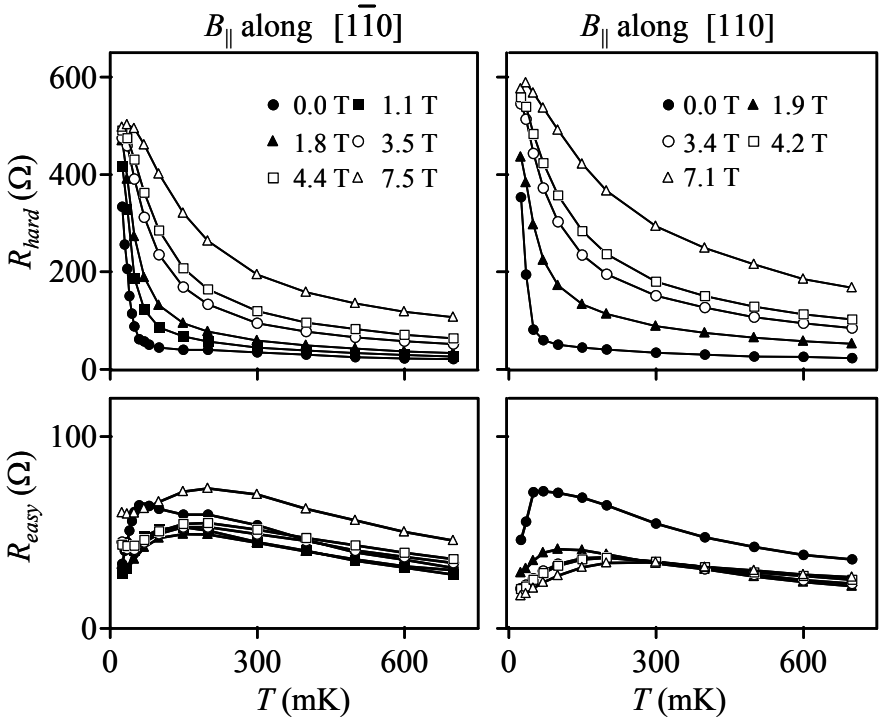

Figure 9.9: Temperature dependencies of longitudinal resistance in the hard (top) and easy (bottom) directions at $\nu = 11/2$ for sample F-5. For increasing $B_{||}$ along either $[1\bar{1}0]$ (left) or $[110]$ (right), the onset to anisotropic transport at low T is broadened.

9.3.2 Broadening of Resistivities

Recall that unlike R_{hard}, R_{easy} versus T does not show a strong or systematic dependence on $B_{||}$. A possible reason is that the easy resistance is strongly affected by unpredictable changes in the current distribution arising from $B_{||}$. After all, Chapter 6 showed how R_{easy} can be extremely sensitive to current inhomogeneities. To really examine how $B_{||}$ affects transport in the easy direction, it would be best to use a long, thin Hall bar geometry to avoid the current-channeling effects. This has not been done; instead, the resistivity values ρ_{xx} and ρ_{yy} were computed from the resistance values R_{xx}

and R_{yy} using the methods of Chapter 6. The resulting ρ_{xx} and ρ_{yy} versus T data are shown in Fig. 9.10a and Fig. 9.10b for the case of $B_{||}$ along $[1\,\bar{1}0]$. (Because the axes of anisotropy are not reversed for $B_{||}$ along $[1\,\bar{1}0]$, $\rho_{xx} = \rho_{hard}$ here.) The figure shows that ρ_{xx} exhibits the same basic broadening of its temperature dependence as does R_{hard} when a large in-plane magnetic field is applied. Also, unlike the R_{easy} traces in Fig. 9.8 and Fig. 9.9, here ρ_{yy} shows a substantial broadening as well.

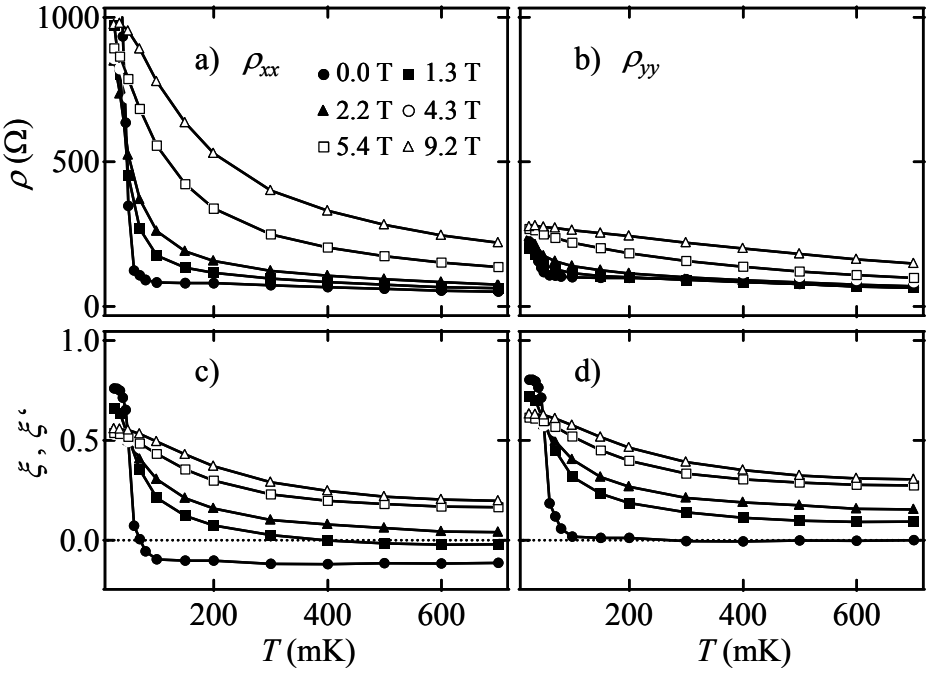

Figure 9.10: a) and b) Broadening of ρ_{xx} and ρ_{yy} versus T for various $B_{||}$ along $[1\,\bar{1}0]$ in sample F-5 at $\nu = 9/2$. c) Temperature dependence of the "order parameter" $\xi \equiv (\rho_{xx} - \rho_{yy})/(\rho_{xx} + \rho_{yy})$ at different $B_{||}$. d) Temperature dependence of the order parameter with ρ_{yy} scaled by 0.8 so that $\xi' \rightarrow 0$ for large T and for $B_{||} = 0$.

Fradkin et al. proposed that the quantity $\xi \equiv (\rho_{xx} - \rho_{yy})/(\rho_{xx} + \rho_{yy})$ represents the magnetization M of the XY model discussed in Section 9.2. Fig. 9.10c shows the temperature dependence of ξ (computed from the data in Fig. 9.10) at several values of $B_{||}$. The usual broadening is present, but there is an obvious problem with associating the quantity ξ with M: for low temperatures ξ does not approach 1 and for high temperatures ξ actually turns negative. The latter problem essentially comes from a background

anisotropy in ρ_{xx} and ρ_{yy} even at high temperatures. To get around this, all the values of ρ_{yy} can be scaled by value of 0.8, which forces the $B_{||} = 0$ values to approach 0. The result, ξ', is shown in Fig. 9.10d. However, these traces of ξ' still suffer from the problem of not approaching unity at low temperature, and except for the $B_{||} = 0$ traces they appear to be saturating at nonzero values for high temperatures.

Thus we conclude that the data show a broadened transition from anisotropic to isotropic transport as $B_{||}$ increases, which is *qualitatively consistent* with that expected from the calculations based on the XY model. Most importantly, these results constitute evidence that at temperatures above 100 mK, the electronic phases at half-filled high LLs still possess local stripe moments. This is in agreement with the nematic liquid crystal picture of the anisotropic electronic phases in half-filled high LLs.

9.3.3 Comparison to the $N = 0$ Landau Level

To strengthen the case for the electronic liquid crystal picture of high LL electrons, it is important to control for the effect of $B_{||}$ in a regime where stripes are not thought to exist, for example in the $N = 0$ LL. For consistency with the higher LLs, transport at the half-filling factor $\nu = 3/2$ will be studied here. Fig. 9.11 displays R_{xx} and R_{yy} versus T at the filling factors $\nu = 11/2$, 9/2, 5/2, and 3/2. In each case, the tilt angle was adjusted so that at half-filling an in-plane field of either 4.3 or 4.4 T was applied in the $[1\bar{1}0]$ direction. For $\nu = 11/2$ and 9/2, there is a broadened onset to anisotropy at low temperatures compared to the case where $B_{||} = 0$ (as in Fig. 9.9 and Fig. 9.8).

At $\nu = 5/2$, anisotropic transport also sets in over approximately the same temperature range as at the other high half-filling factors. In this case, however, the onset to anisotropy has not been broadened with respect to the $B_{||} = 0$ situation. As explained in Section 8.3, the $\nu = 5/2$ evolves from an isotropic to an anisotropic state as $B_{||}$ is applied.

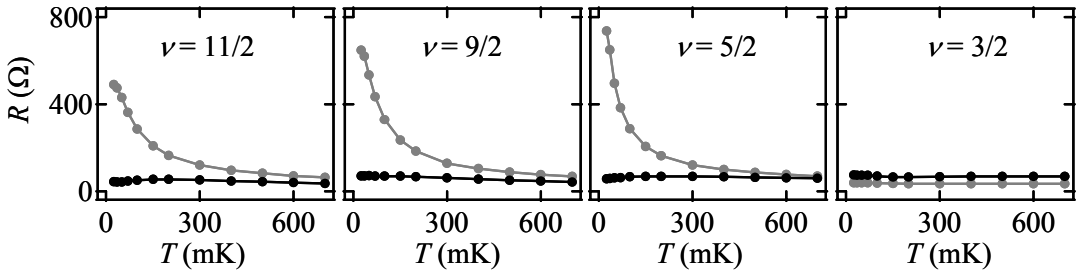

Figure 9.11: Temperature dependence of R_{xx} (gray) and R_{yy} (black) at $\nu = 11/2$, 9/2, 5/2, and 3/2 in sample F-5 when $B_{||} = 4.4$, 4.3, 4.3, and 4.4 T along $[1\,\bar{1}0]$, respectively. Anisotropic transport at low T does not occur at $\nu = 3/2$, where $N = 0$.

Meanwhile, the $\nu = 3/2$ temperature dependence shows no onset to anisotropy at low temperatures even though the same in-plane field $B_{||} = 4.4$ T is applied. Clearly, then, $B_{||}$ does not affect all LLs equally by introducing anisotropic transport. Only at the half-filled high LLs $N \geq 2$ for $B_{||} = 0$, and $N \geq 1$ for $B_{||} \neq 0$, does the in-plane magnetic field induce anisotropic transport. This suggests that there must be a specific interaction between $B_{||}$ and the collective phases of high LLs.

9.3.4 Data Collapse and Scaling $B_{||}$ by T

This final section concerns an intriguing scaling property of R_{hard}. Fig. 9.12a and Fig. 9.12b contain the same R_{hard} data for $\nu = 9/2$ that was shown in Fig. 9.8 for $B_{||}$ along both $[1\,\bar{1}0]$ and $[110]$. However, this time the data are plotted against the *scaled* temperature $T/B_{||}$ (for nonzero $B_{||}$). Plotted in this way, the data collapse onto a single curve with impressive precision. This means that R_{hard} depends on T and $B_{||}$ essentially through the single ratio $T/B_{||}$.

To discern the functional form of this dependence, the same scaled data is shown in Fig. 9.12c and Fig. 9.12d using log-log axes. The dashed lines in the figures, placed there only as guides to the eye, are proportional to $(T/B_{||})^{-0.8}$. Although the R_{hard} points do not fall on a straight line, it is still apparent that R_{hard} depends on the ratio $T/B_{||}$ in this approximately linear manner. A similar data-collapse occurs for $\nu = 11/2$ as well.

(Incidentally, the easy resistance values do not obey this scaling relationship. This may be related to the current-channeling effects discussed above.)

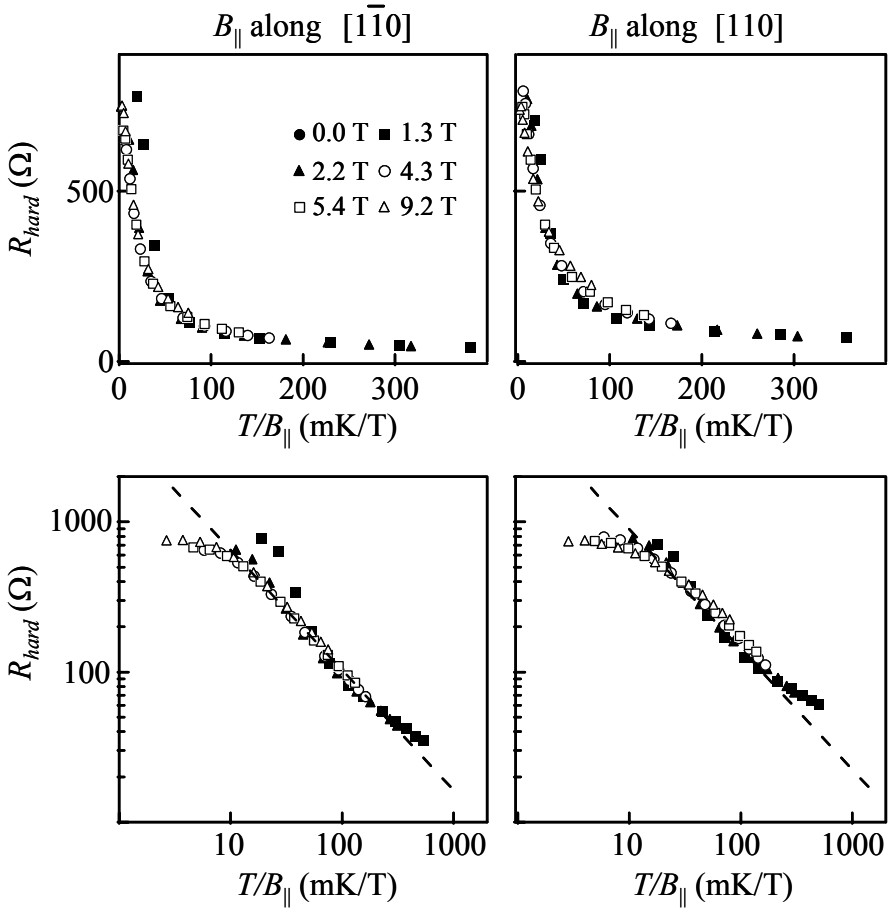

Figure 9.12: Hard resistance dependence on the quantity $T/B_{||}$ at $\nu = 9/2$ for sample F-5. The top graphs reveal a scaling relationship so that R_{hard} is nearly a single function of $T/B_{||}$. The bottom log-log plots contain the same data but with dashed lines corresponding to the power law dependence $R_{hard} \sim (T/B_{||})^{-0.8}$.

The connection, if any, between the scaling behavior of R_{hard} and the purported nematic-to-isotropic phase transition is not understood. While at a high enough temperature T the two-dimensional XY model of the anisotropic nematic must eventually approach a Curie law with $M \sim h/T$, this limiting behavior is not well developed in the (h,T) parameter range which seems most relevant to our experimental data. In any case, the relationship between h and $B_{||}$ is unclear and certainly not linear. Nonetheless, the sublinear power law behavior indicated in Fig. 9.12 and Fig. 9.13 still might help rule out an alternative model of how $B_{||}$ induces anisotropy in high LLs. In this alternative model,

in contrast to the nematic liquid crystal model, the function of $B_{||}$ is twofold: to *create* stripes and to *orient* stripes.

However, if this alternative scenario were correct, then one would expect to see a stronger power law dependence of the anisotropy on $B_{||}$. This is in analogy to a paramagnetic system where the polarization is $M \sim \mu^2 B/T$. If the spin moments μ were also generated by B, then a superlinear dependence of M on B will occur. Therefore, the degree of anisotropy in high LLs should be superlinear as well if the role of $B_{||}$ is to create and orient the stripe CDW phase at high T. Therefore, we conclude that the weak dependence of R_{hard} on $B_{||}$ in Fig. 9.12 and Fig. 9.13 provides yet stronger evidence that local stripe moments of the anisotropic electronic phases in high LLs do exist at relatively high temperatures.

---

1 E. Fradkin and S.A. Kivelson, Phys. Rev. B **59**, 8065 (1999).

2 M.M. Fogler, Lecture Notes in Physics **595**: *High Magnetic Fields: Applications in Condensed Matter Physics and Spectroscopy*, ed. C. Berthier, L.P. Lévy, and G. Martinez (Springer-Verlag, Berlin 2002).

3 P.M. Chaikin and T.C. Lubensky, *Principles of Condensed Matter Physics* (Cambridge University Press, Cambridge 1995).

4 H.A. Fertig, Phys. Rev. Lett. **82**, 3693 (1999).

5 A.H. MacDonald and M.P.A. Fisher, Phys. Rev. B **61**, 5724 (2000).

6 T. Stanescu, I. Martin, and P. Philips, Phys. Rev. Lett. **84**, 1288 (2000).

7 R.L. Willett, H.L. Stormer, D.C. Tsui, A.C. Gossard, and J.H. English, Phys. Rev. B **37**, 8476 (1988).

8 E. Fradkin, S.A. Kivelson, E. Manousakis, and K. Nho, Phys. Rev. Lett. **84**, 1982 (2000).

9 C. Wexler and A.T. Dorsey, Phys. Rev. B **64**, 115312 (2001).

10 L. Radzihovsky and A.T. Dorsey, Phys. Rev. Lett. **88**, 216802 (2002).

11 N. Metropolis, A.W. Rosenbluth, M.N. Rosenbluth, A. Teller, and E. Teller, J. Chem. Phys. **21**, 1087 (1953).

12 D. Chandler, *Introduction to Modern Statistical Mechanics* (Oxford Univ. Press, New York 1987).

13 R.K. Pathria, *Statistical Mechanics* (Butterworth-Heinemann, Oxford 1996).

Chapter 10:
Breakdown and Narrow-Band Noise in the RIQHE

10.1 General Properties of Spatially Ordered Electronic Systems

Based on the CDW theory of electronic phases in high LLs (Chapter 5), the insulating RIQHE states are believed to arise from a lattice of electron bubbles pinned in place by disorder. If the bubble CDW picture of the RIQHE states is accurate, then it would represent one of several examples of pinned, spatially ordered electronic systems in nature. For example, quasi-one-dimensional metals such as $NbSe_3$ or $K_{0.3}MoO_3$ undergo a Peierls transition that generates a periodic modulation of the atomic lattice [1]. In response, the conduction electrons form a CDW with a wavelength on the order of a few atomic lattice constants of the host materials.

Perhaps closer analogs to the hypothesized bubble CDW of high LLs are pinned, spatially-modulated systems in *two* dimensions. The prime example is the triangular CDW lattice of the Wigner crystal (WC) electron solid, and at least three classes of these phases exist. First, a classical WC occurs at very low electron densities on liquid helium films [2]. Second, a still-undiscovered WC is believed to exist for more moderate electron densities where quantum fluctuations are relevant [3]. Third, Wigner crystallization might occur at very high magnetic fields (i.e. at very low filling factors $\nu << 1$) in a 2DES [4]. Aside from the WC, another spatially ordered electronic state in two dimensions is the Abrikosov vortex lattice in thin films of type-II superconductors, where the vortices have a spacing of ~50 nm [5].

The CDWs, WCs, and vortex lattices share certain common characteristics that might be relevant to the purported bubble CDW in high LLs. For example, each of the systems is insulating because the modulated structures are pinned by impurities or lattice defects. In the case of the CDWs and WCs, this means that linear response electrical transport measurements yield infinite resistances. The pinning of the vortex lattices, on

the other hand, means that the superconducting system remains in a zero resistance state; the vortex lattice itself, not the electron fluid, is "insulating."

A second common feature of the CDWs, WCs, and vortex lattices is that each exhibits a depinning transition when subjected to some critical level of stress. For the 1D CDW $NbSe_3$, electric fields exceeding a few mV/cm cause a sudden onset of conduction as the CDW dislodges from its pinning potential and starts to slide [1]. Similar sharp onsets to conduction have been observed in WCs on liquid helium [6] and at high magnetic fields [7,8]. Finally, vortex lattices exhibit depinning transitions above some critical current where superconductivity breaks down and dissipation occurs [9,5].

A third commonality among CDWs, WCs, and vortex lattices involves their dynamics above the depinning threshold. Most dramatically, these dynamics can generate a temporally periodic electrical response reflecting the spatial periodicity of the sliding elastic medium. These oscillating signals are dubbed "narrow-band noise" or "washboard noise," which refers to a model of the sliding CDW as a single particle falling down a tilted washboard potential. Washboard noise was first observed in the 1D CDW system of $NbSe_3$ by Fleming and Grimes [10]. In these systems, the sliding CDW above its depinning threshold generates ac voltages with frequencies that are directly proportional to the velocity of the CDW according to $f = v/a$, where v is the velocity and a the lattice constant of the CDW. Typical observed frequencies are hundreds of kHz, but in very clean samples frequencies as low as 1 Hz have been observed [11]. More complicated temporal phenomena, including ac-dc interference, memory effects, and signatures of chaos, are also commonly observed in 1D CDWs [1].

Narrow-band noise has also been searched for in WC and vortex lattice systems, but the results have been more ambiguous than in 1D CDWs. In the case of the WC state at very low filling factors, broad-band noise has been observed above the depinning threshold [12], but only a small amount of indirect evidence exists for washboard oscillations [13]. For vortex lattices, narrow-band noise has been recently reported for the first time in a high-T_c superconductor [14]. Broad-band noise signatures are more common in vortex lattices [15], possibly because of the relatively incoherent motion of elastic media in two dimensions where multiple pathways of current flow may occur. A final dynamical effect seen in WCs and vortex lattices is random switching between

distinct dissipative states in the vicinity of the depinning transition [8,16]. The switching behavior may be accompanied by hysteresis with respect to the strength of the stress being applied to the systems, and some theoretical work suggests that it reflects the opening of filamentary conduction channels through the lattice media [17].

The presence of any of these common characteristics of 1D CDWs, WCs, and vortex lattices in the RIQHE states would provide good evidence that the bubble CDW model of the RIQHE is accurate. The first criterion of insulation is certainly met in the RIQHE. As discussed in Section 5.2, the vanishing of the longitudinal resistance at low temperatures and around 1/4 and 3/4 filling of high LLs signals the presence of an insulating electronic phase. What about a depinning threshold and dynamics? As the rest of this chapter will show, these effects occur in the RIQHE as well. While major questions about their nature remain unanswered, the depinning and dynamical properties of the RIQHE still provide evidence that bolsters the case for bubble CDW formation in high LLs.

10.2 Sharp Thresholds to Conduction in the RIQHE

10.2.1 The Basic Effect

In a 1D CDW system, the depinning transition is normally measured in a voltage-biased configuration, where current conducts through the system only once some threshold electric field is reached. It might be expected that a similar set-up is appropriate for the RIQHE in high LLs. After all, the bubble lattice consists of charge centers that should respond to an electric field. However, unlike in 1D CDW systems, the RIQHE states exist in the quantum Hall regime where the filled lower LLs serve as parallel channels of conduction. At any voltage bias, the 2DES will conduct current. While changes in that conduction would be expected at a depinning transition of the bubble CDW, a superior method of searching for this transition involves the current-biasing technique shown in Fig. 10.1. In this technique, a dc current I_{dc} is passed through the RIQHE state while the longitudinal voltage is monitored. Because the longitudinal resistance vanishes in the RIQHE, this voltage should remain zero as long as the bubble CDW stays pinned.

However, the current I_{dc} generates a transverse Hall electric field due to the Hall voltage $V_{xy} = I_{dc}R_H$, where R_H is the Hall resistance. Thus the current-biasing technique is essentially the same as a field-biasing technique, where the electric field is in a direction perpendicular to the bias current. At a depinning transition, the Hall electric field becomes strong enough to dislodge the pinned bubble CDW, and it will start to conduct current. Because these electrons are in a partially occupied LL, they will dissipate energy and exhibit a finite longitudinal resistance. In other words, a depinning transition will be signaled by a sudden deviation of V_{yy} from zero above some threshold dc current.

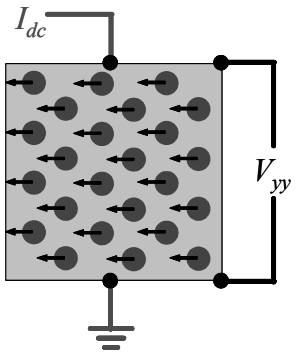

Figure 10.1: Schematic of measurement technique for detecting a depinning transition in the bubble CDW. A dc current I_{dc} along **y** creates a transverse Hall field along **x** which exerts a force on the bubble CDW. If the pinned bubbles break free, the longitudinal voltage V_{yy} becomes nonzero.

Fig. 10.2 shows the basic result of such a measurement in sample C-8. In Fig. 10.2a, the longitudinal resistance R_{yy} is shown through the $\nu = 9/2$ structure at 25 mK, and the two insulating RIQHE states are evident. Fig. 10.2b shows the dc current-voltage (I-V) measurement of V_{yy} versus I_{dc} obtained at $T = 25$ mK and $B = 2.022$ T, which is indicated by an arrow inside the $\nu \approx 4.25$ RIQHE region of Fig. 10.2a. The data in Fig. 10.2b were obtained by sweeping the dc current from zero to nearly 1000 nA and then back to zero again at a rate of about 6 nA/s. (As a comparison, the linear-response resistance measurements are typically made with an excitation current less than 20 nA.) The longitudinal voltage is monitored after amplification by a room-temperature preamplifier (model PAR-113), and a small constant offset due to the preamplifier has been subtracted from the data so that $V_{yy} = 0$ at $I_{dc} = 0$.

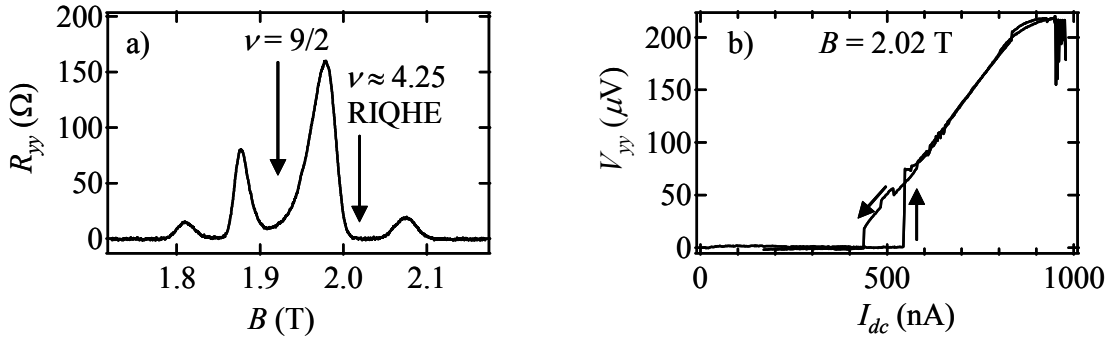

Figure 10.2: a) R_{yy} versus B from sample C-8 at 25 mK. b) V_{yy} versus I_{dc} at B = 2.02 T, in the $\nu \approx 4.25$ RIQHE. The *I-V* curve exhibits a discontinuous, hysteretic onset to conduction above ~500 nA. The arrows denote the direction I_{dc} was swept.

As I_{dc} increases to about 500 nA, V_{yy} remains approximately zero and the RIQHE state stays intact. However, once I_{dc} exceeds a threshold of about 540 nA, V_{yy} suddenly jumps to about 75 μV and the RIQHE state breaks down. The voltage V_{yy} continues to increase with a fairly constant slope of about 500 Ω as I_{dc} increases. On its way up, V_{yy} jumps around slightly at certain points, and at the highest currents the voltage falls repeatedly by several tens of μV before recovering. On the way back down, a counter-clockwise hysteresis loop occurs. Thus, the *I-V* measurement of the $\nu \approx 4.25$ RIQHE in sample C-8 exhibits precisely the kind of signature expected for a depinning transition of the bubble CDW. Above a threshold current of ~500 nA, or equivalently a threshold Hall field of ~10 mV/cm , the breakdown of the insulating state occurs as the bubble CDW suddenly starts to conduct. (The threshold electric field is estimated by dividing the transverse Hall voltage by the width of a sample, in this case 5 mm.) The very sharp onset to conduction implies that a large region of the bubble CDW is dislodged from its pinning potential simultaneously. If the system were less well correlated, one would expect the conduction to begin gradually, as different small regions of the bubble CDW are depinned at different fields. It will be demonstrated later that these sharp onsets to conduction are only observed where the RIQHE states form: around 1/4 and 3/4 filling of high LLs with $N \geq 2$.

The purely dc measurement shown in Fig. 10.2b obscures the fact that the longitudinal voltage actually increases above zero slightly before the sudden breakdown

to a highly conducting state. In Fig. 10.3, a plot of V_{yy} versus I_{dc} is shown along with the differential resistance dV_{yy}/dI versus I_{dc} for a magnetic field near $\nu \approx 4.25$. The differential measurement, using the usual lockin technique with an added dc current component, provides a more sensitive measure of what happens below threshold. The differential resistance data show that the resistance of the 2DES creeps up to above 50 Ω prior to breakdown. One possible scenario for this is that the 2DES consists of a mixture of pinned bubble CDW regions of various sizes. Then, low-level dissipative conduction may appear gradually as a few small bubble regions begin to conduct before the major depinning event of a large region.

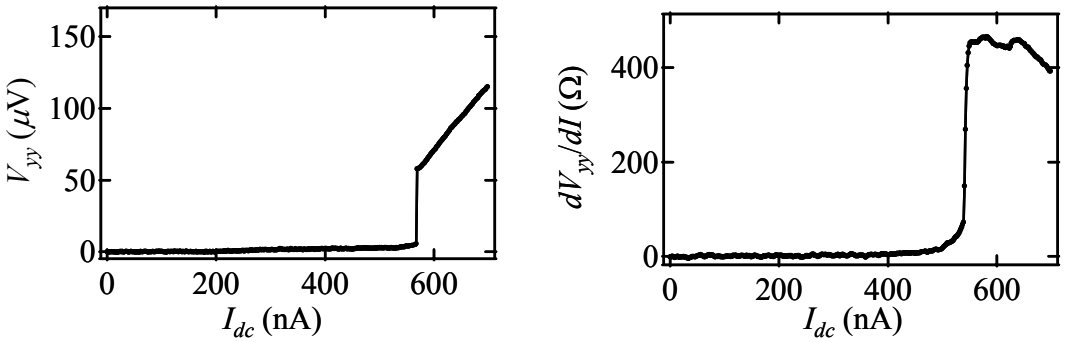

Figure 10.3: a) V_{yy} versus I_{dc} for $B = 2.04$ in sample C-8 at 25 mK. b) dV_{yy}/dI versus I_{dc} under same conditions. The differential resistance rises above 50 Ω before breakdown occurs. The variation in threshold current is typical between any two measurements.

Although the RIQHE breakdown data of Fig. 10.2 focus only on V_{yy} versus I_{dc}, quite similar *I-V* curves are found with the current running along $[1\,\bar{1}0]$ instead. The details of any two *I-V* traces will differ, but there are no significant qualitative differences of the RIQHE breakdown phenomenon for current along [110] or $[1\,\bar{1}0]$. This is perhaps unsurprising because the longitudinal resistances R_{xx} and R_{yy} show no significant anisotropies in the RIQHE regions. Aside from V_{yy} and V_{xx}, a third voltage which can be monitored as a function of I_{dc} is V_{xy}, the Hall voltage. Fig. 10.4a shows how V_{xy} depends on I_{dc} in the $\nu \approx 4.25$ RIQHE state. At first, V_{xy} increases linearly with current with a slope given by $h/4e^2$. Above the breakdown current of $I_{dc} \approx 400$ nA, however, V_{xy} begins to deviate from the straight line. At these high currents, V_{xy} is less than it would be if the

RIQHE had not broken down, but only by a few percent. The magnitude of that difference is plotted versus I_{dc} in Fig. 10.4b.

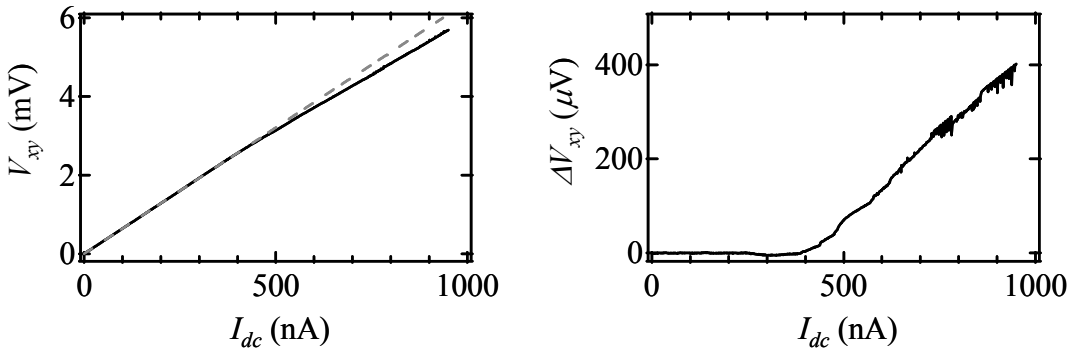

Figure 10.4: a) V_{xy} versus I_{dc} for $B = 2.02$ in sample C-8 at 25 mK. Above breakdown, V_{xy} falls below the linear slope indicated by the dashed line. b) Magnitude of the difference between the straight line and the measured V_{xy} in a).

10.2.2 Restriction to the RIQHE Regime

A major clue that the nonlinear *I-V* curves of Fig. 10.2 really do reflect the depinning of a bubble CDW is that they are restricted to the narrow magnetic field ranges where the RIQHE states occur. To demonstrate this, Fig. 10.5 contains a sampling of V_{yy} versus I_{dc} curves for the whole magnetic field range of Fig. 10.2. For clarity, only sweeps with increasing current are displayed. These data are taken at equally spaced magnetic fields from approximately $\nu = 5$ to $\nu = 4$. Also shown is the longitudinal resistance R_{yy}, and the *I-V* curves have been offset so that they intersect the magnetic field axis of the R_{yy} versus B plot at the corresponding field where they were obtained. The data show that large jumps in V_{yy} versus I_{dc} occur in a cluster of *I-V* curves near the $\nu \approx 4.25$ RIQHE. Around the $\nu \approx 4.75$ RIQHE, only one of the two or three curves shows a jump in V_{yy}, and it is relatively weak. The relative weakness of the nonlinearities in the *I-V* curves around $\nu \approx 4.75$ versus $\nu \approx 4.25$ is reminiscent of the disparity in strength of the RIQHE states in the two regions generally. For example, Section 4.3 showed that lower temperatures are required for the $\nu \approx 4.75$ RIQHE to form (see Fig. 4.6).

Outside the RIQHE regions, V_{yy} has only a weak dependence on I_{dc}. Around the half-filling point $\nu = 9/2$, the *I-V* curves are mostly flat and show only slight nonlinearities. The corresponding V_{xx} curves at $\nu = 9/2$ show a steeper dependence on I_{dc} because of the resistance anisotropy around half-filling. However, no discontinuities in V_{xx} or V_{yy} occur around half-filling. In the context of the depinning picture, this suggests that no depinning transition occurs in the anisotropic region where the stripe CDW is thought to exist. This conclusion is consistent with the results of Section 3.5, where smooth features were found in the *dV/dI* versus I_{dc} traces but no sign of a depinning transition—such as kinks in *dV/dI*—were seen. It is also consistent with the interpretation of the stripe CDW as an anisotropic *conducting* medium, because depinning transitions are characteristic of *insulating* systems.

Especially significant in Fig. 10.5 is the contrast in the *I-V* curves between the RIQHE and the IQHE regions. Recall from Chapter 4 that the longitudinal and Hall resistance measurements show the same phenomenology in the RIQHE and the IQHE: $R_{xx} = R_{yy} = 0$ and $R_{xy} = h/ie^2$, with i an integer. On the other hand, Fig. 10.5 illustrates that a huge different exists in how the RIQHE and IQHE states respond to large dc currents. While the *I-V* curves are highly nonlinear and contain abrupt voltage jumps in the RIQHE regions, deep in the $\nu = 5$ or $\nu = 4$ IQHE V_{yy} remains zero up to $I_{dc} = 1000$ nA. This is true up to even much higher currents, as will be shown later in Fig. 10.13. The distinction between the *I-V* curves in the IQHE and the RIQHE regions reflects the vastly different physics behind the two insulating states. The IQHE comes from single-particle localization by disorder of small numbers of electrons in the valence LL (see Section 1.2). In the RIQHE, many-body electron interactions are responsible for the state's insulating nature. First, the interactions generate the bubble CDW phase; subsequently, that charge lattice becomes immobilized by disorder. In the IQHE, there is no spatially ordered electronic system to depin and the *I-V* curves are therefore flat. In the RIQHE, the *I-V* curves contain sharp thresholds to conduction due to the simultaneous depinning of large numbers of electrons comprising the bubble CDW.

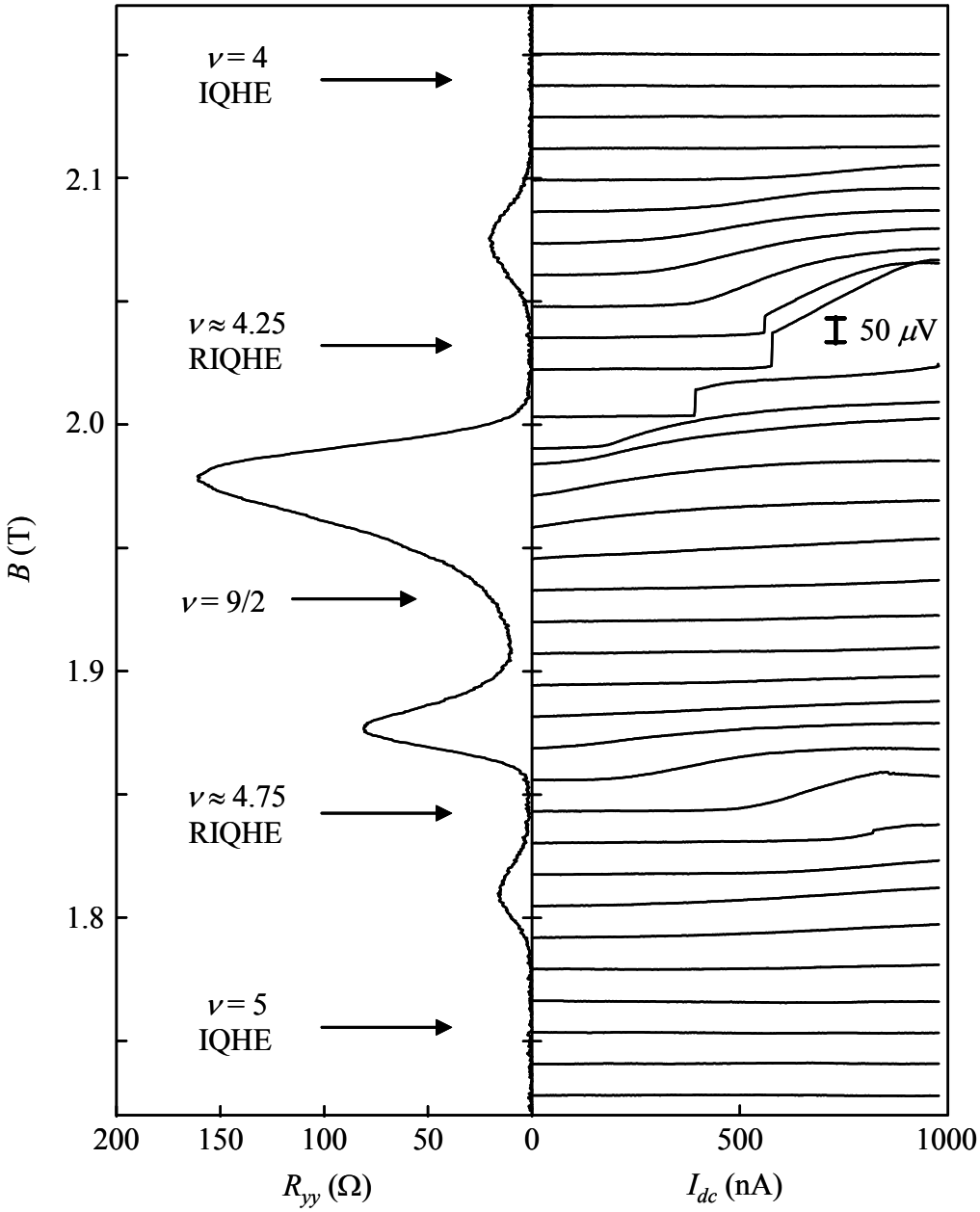

Figure 10.5: Left: R_{yy} (bottom axis) versus B (left axis) through the entire $\nu = 9/2$ structure of sample C-8 at 25 mK. Right: dc I-V curves, sweeping up only, offset so that they intersect the vertical axis at the magnetic field where they were obtained. The sharp discontinuous onsets to conduction only occur in the $\nu \approx 4.25$ RIQHE. Smaller discontinuities are present in the $\nu \approx 4.75$ RIQHE, but nowhere else for $4 < \nu < 5$.

10.2.3 Breakdown in Other Samples and Higher LLs

While Fig. 10.5 indicates that discontinuities in the *I-V* curves are confined to the RIQHE regions around $\nu = 9/2$ in sample C-8, Fig. 10.6 shows that these features also occur in other samples that exhibit RIQHE physics. In the upper panels of Fig. 10.6, transport data of R_{xx} and R_{yy} through the $\nu = 9/2$ structure are shown for several samples. The lower panels contain V_{yy} versus I_{dc} traces taken in the vicinity of the $\nu \approx 4.25$ RIQHE. All the data were obtained at temperatures $T \leq 50$ mK, where the RIQHE is well developed.

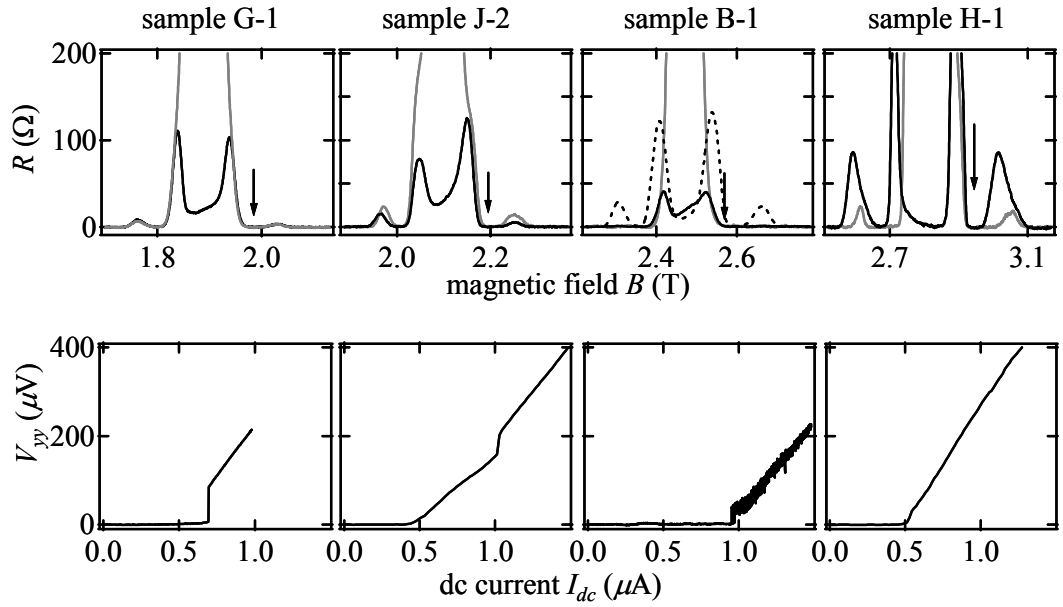

Figure 10.6: A selection of longitudinal resistance data and RIQHE breakdown *I-V* curves from different samples. Top: R_{xx} (gray) and R_{yy} (black) through the $\nu = 9/2$ structure for samples G-1 (25 mK), J-2 (25 mK), B-1 (solid 25 mK; dashed 50 mK), and H-1 (50 mK). Bottom corresponding V_{yy} versus I_{dc} traces (sweeping up) at the magnetic fields indicated by the arrows in the $\nu \approx 4.25$ RIQHE regions.

Note that the onset to conduction may or may not occur discontinuously. For example, sample G-1 exhibits the RIQHE breakdown around $I_{dc} = 700$ nA, with a strong signature of V_{yy} jumping up from zero. On the other hand, the *I-V* curve from sample J-2 shows that the breakdown of the insulating state just below 500 nA occurs in a continuous fashion with the slope of V_{yy} versus I_{dc} changing suddenly above the threshold current. However, closer to 1 μA a sharp discontinuity in V_{yy} does occur. In sample H-1,

a very small discontinuity around 500 nA appears at the threshold current. Finally, in sample B-1, the threshold current is large—almost 1 μA—and the initial jump in V_{yy} is small. Above threshold, V_{yy} also shows many fluctuations as it increases.

Interestingly, the *I-V* curve for sample B-1 was taken at 25 mK, where the satellite peaks separating the RIQHE from the IQHE have disappeared (see Section 4.3). Transport data for B-1 at 50 mK is shown as a dashed trace, in addition to the 25 mK data, to indicate where the RIQHE occurs. It is noteworthy that even though at 25 mK there is no distinction between the RIQHE and the IQHE in the R_{xx} and R_{yy} data, the sharp discontinuities in the *I-V* curves occur only in the vicinity of the RIQHE. Thus, the sharp breakdown features can be a more reliable way of distinguishing between the two very different insulating states.

As for the RIQHE states in higher LLs with $\nu > 5$, methodical *I-V* data has only been obtained in sample H-1 because most other samples show only weak evidence of the RIQHE in higher LLs (see Section 4.2). Fig. 10.7 displays a sampling of *I-V* curves (in this case, with V_{xx} versus I_{dc}) in the RIQHE of several higher LLs: around the filling factors $\nu \approx$ 4.25, 4.75, 5.25, 5.75, 6.25, and 6.75. Note how in each case, either a sharp jump in V_{xx} or a sudden discontinuity in its slope signals the breakdown of the RIQHE and the onset to conduction. As expected, these features have not been detected outside the RIQHE regions.

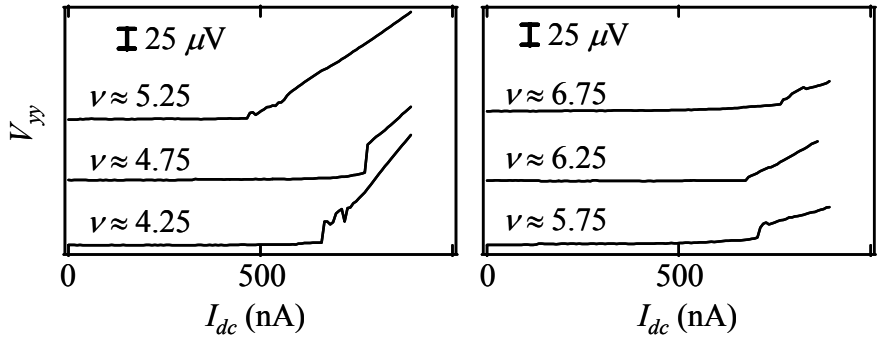

Figure 10.7: 25 mK dc *I-V* curves from sample H-1. The sweep-up traces were obtained in the RIQHE regions $\nu \approx$ 4.25 through $\nu \approx$ 6.75. Each one shows signs of the RIQHE breakdown phenomenon.

10.2.4 Temperature and Field Dependence

The temperature dependence of the discontinuous *I-V* curves in the RIQHE states is important for at least two reasons. First, the RIQHE states themselves are known to vanish by 100 mK or so. Therefore, if the sudden onsets to conduction evident in the *I-V* curves are to be interpreted as evidence for a depinning transition in the bubble CDW, then these curves should also smooth out as the temperature is increased. Second, the dc currents needed for the RIQHE breakdown are large. Although the majority of that current is probably carried by the edge channel pathways of the filled lower LLs that lie below the Fermi level in the bulk of the sample, the possibility of electron heating must be considered.

Fig. 10.8a shows how a typical *I-V* curve near $\nu \approx 4.25$ in sample C-8 evolves with temperature. As the temperature is raised from 25 mK, the conduction threshold shifts to lower dc currents and the size of the discontinuity and hysteresis generally decreases. By 65 mK, no threshold to conduction is evident. But by that temperature, the RIQHE no longer exists, as can be seen from the longitudinal resistance data in Fig. 10.8b. Note that a vanishing longitudinal resistance in the RIQHE is not necessary for discontinuities in the *I-V* curves to be seen. For example, the data in Fig. 10.8 show that by 50 mK the RIQHE region around $\nu \approx 4.25$ has already become conducting, while a distinct threshold behavior in the *I-V* curve at 55 mK still exists. However, at 50 mK R_{xx} and R_{yy} show a distinct minimum where the RIQHE is forming, indicating that the necessary correlations among the electrons are becoming significant by that point. The fact that the sudden onset to conduction appears below approximately the same temperature where the RIQHE becomes insulating constitutes further evidence that the conduction thresholds are associated with the many-body physics responsible for RIQHE formation. The data of Fig. 10.8a also indicate that electron heating is not a severe problem: the *I-V* curves remain quite sensitive to temperature changes down to at least 25 mK. This is somewhat surprising because the large currents needed for the RIQHE breakdown should generate significant heat. Presumably, that heat is carried away by the sample's leads before it affects the bulk of the 2DES. Further consideration of possible heating effects will be discussed in Section 10.3.

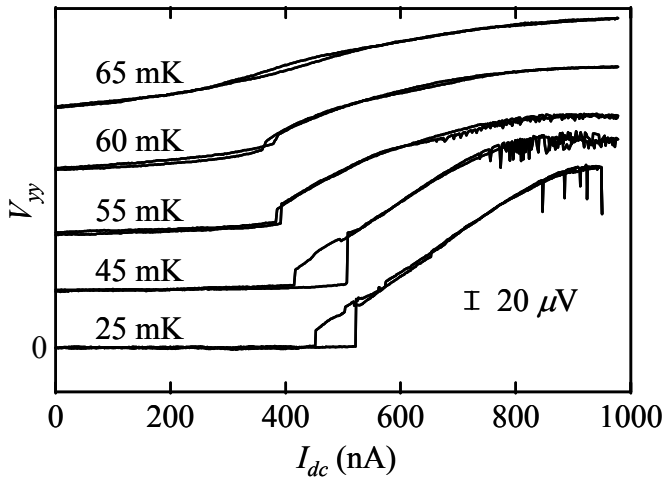

Figure 10.8: V_{yy} versus I_{dc} curves from sample C-8 at B = 2.02 T. As the temperature increases from 25 to 65 mK, the discontinuous onset to conduction gradually vanishes.

Various aspects of the $\nu \approx 4.25$ *I-V* curves systematically change with B through the RIQHE region. For example, Fig. 10.9 shows a plot of the temperature T_d (solid circles) at which the discontinuity in the *I-V* curve disappears. The temperature T_d is largest (~60 mK) at the center of the RIQHE, and falls off rapidly on either side. This might be related to the fact that the activation energy of the RIQHE is also largest in its center (see Fig. 4.6).

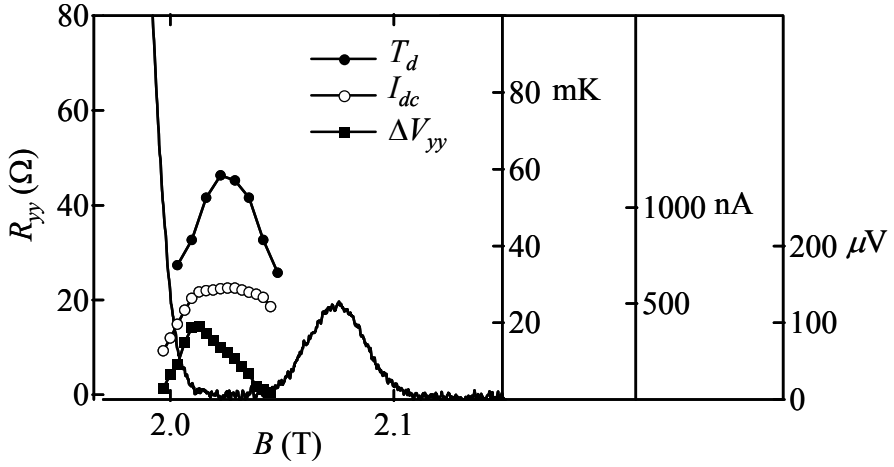

Figure 10.9: Three measures of the RIQHE breakdown versus magnetic field superimposed on R_{yy} versus B data (left axis) of sample C-8 at 25 mK. Solid circles: T_d, the temperature above which no discontinuity in the *I-V* curves are observed. Open circles: the sweep-up threshold current at 25 mK. Solid squares: the magnitude of the longitudinal voltage jump at threshold.

Fig. 10.9 also shows how the magnitude of the initial threshold dc current (open circles) and the size of the voltage step ΔV_{yy} at breakdown (solid squares) depend on B through the RIQHE. These values were obtained from the set of data shown in Fig. 10.5. The threshold current is largest near the center of the RIQHE and tapers off toward its boundaries. The magnitude of the voltage step, on the other hand, is largest near the low-field end of the RIQHE, but it falls rapidly on either side of the RIQHE. Thus like the activation energy (Fig. 4.6) and the discontinuity disappearance temperature T_d, the threshold current and voltage step also appear to be measures of the strength of the RIQHE. Take together, these observations are consistent with the bubble CDW picture. At the magnetic fields where the bubble CDW is the most robust, higher temperatures are required to generate dissipative transport; the highest threshold currents are necessary to depin the bubble CDW; and the discontinuities in the *I-V* curves persist to the highest temperatures.

It should be cautioned that a quantitative analysis of the RIQHE breakdown properties could be misleading because an *I-V* curve is not entirely reproducible from measurement to measurement even under identical conditions. For example, at $B = 2.022$ T and $T = 25$ mK, five traces of V_{yy} versus I_{dc} in sample C-8 taken at different times over several weeks exhibited depinning threshold voltages between 521 and 576 nA. However, the threshold currents of two traces obtained consecutively are normally in agreement within 5 nA of each other. The *I-V* curves in Fig. 10.5 were taken consecutively.

The fact that there is no fixed threshold dc current of the RIQHE breakdown is reinforced by the data shown in Fig. 10.10. In Fig. 10.10a, an *I-V* curve at $B = 2.016$ T is shown, with the breakdown occurring at about 500 nA. In Fig. 10.10b, V_{yy} is plotted versus time as I_{dc} is ramped to slightly above 400 nA and stopped. About 200 seconds later, the insulating state spontaneously breaks down and V_{yy} becomes nonzero. This suggests that the RIQHE may break down over some range of high threshold currents rather than at a specific current.

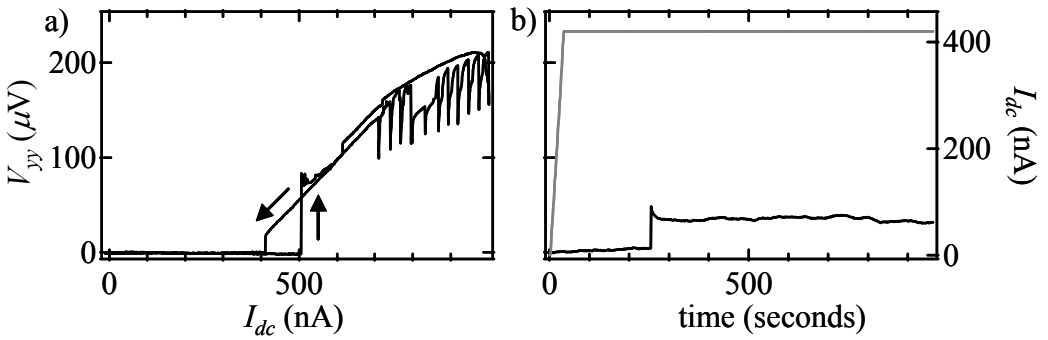

Figure 10.10: a) V_{yy} versus I_{dc} for sample C-8 at 25 mK and B = 2.02 T. Breakdown occurs around I_{dc} = 500 nA. b) Under same conditions, V_{yy} versus time (black) as I_{dc} (gray) is ramped to 420 nA and stopped. After about 250 seconds, the RIQHE state spontaneously breaks down.

10.2.5 Dynamics above Breakdown

Fig. 10.11 shows that the voltage spikes occurring in V_{yy} above threshold are actually time-dependent and can be quite periodic. Fig. 10.11a shows an *I-V* curve from $\nu \approx 4.25$ in sample C-8 at 25 mK taken with I_{dc} ramping at 2 nA/sec. In Fig. 10.11b, the same measurement is made, except I_{dc} is halted at 900 nA while V_{yy} continues to be monitored. Although steady at first, V_{yy} soon starts to exhibit sudden drops at approximately equal time intervals of around 10 to 18 seconds. A simple two-level switching model is not applicable because the distribution of times is clearly *not* random.

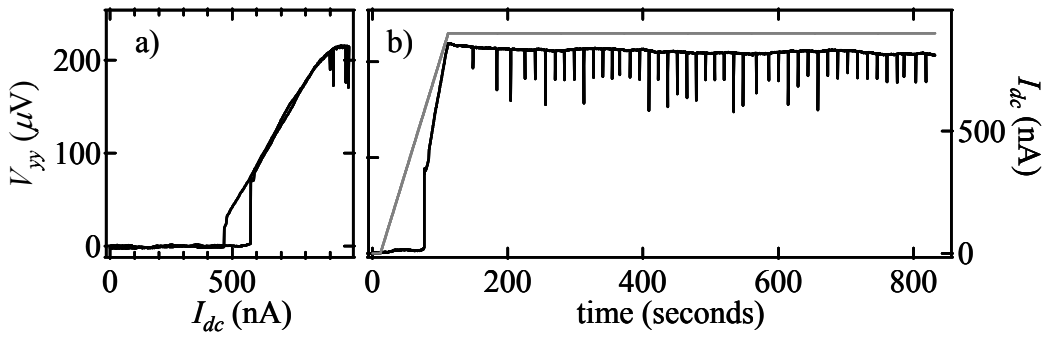

Figure 10.11: a) V_{yy} versus I_{dc} at 25 mK and B = 2.02 T from sample C-8. b) V_{yy} (black) versus time as I_{dc} (gray) is ramped to 900 nA and halted. Quasiperiodic voltage spikes in V_{yy} occur about every 15 seconds.

Fig. 10.12 shows how the periodicity of these voltage spikes varies with temperature. The data in Fig. 10.12 were obtained by recording a series of many tens or

hundreds of voltage spikes in V_{yy} at I_{dc} = 900 nA and then extracting the average time between spikes, $\langle \Delta t \rangle$. The error bars on $\langle \Delta t \rangle$ are simply the standard deviations of that sampling and are meant to give an idea of the spread of $\langle \Delta t \rangle$ and hence the periodicity. In Fig. 10.12a, $\langle \Delta t \rangle$ is plotted versus T on a log-log scale to check for a power law dependence. The best fit, shown as a gray line, is $\langle \Delta t \rangle \sim T^{-5.67}$. Note that from 20 to 50 mK, $\langle \Delta t \rangle$ decreases from about 50 seconds to less than one second. In Fig. 10.12b, $\langle \Delta t \rangle$ is plotted versus $1/T$ on a long-linear scale to check for activated behavior $\langle \Delta t \rangle \sim \exp(-E_A/T)$, and the line fit gives an activation energy of 166 mK. It should be emphasized that the fitting functions made in Fig. 10.12 are simply guesses of two possible relationships between $\langle \Delta t \rangle$ and T.

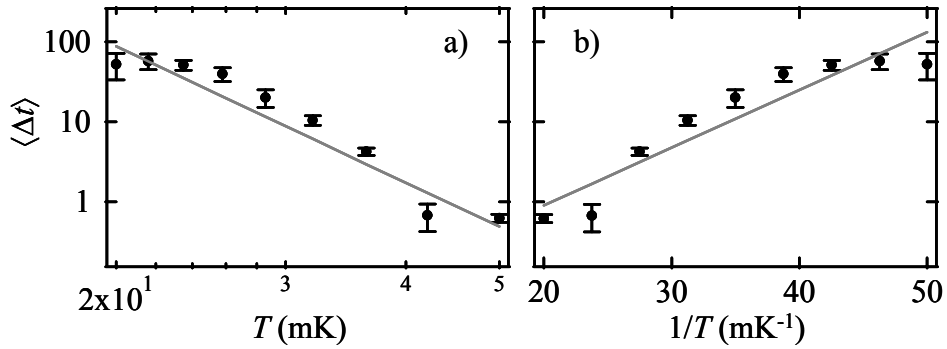

Figure 10.12: Average period of voltage spikes under the conditions of Fig. 10.11 as a function of a) temperature, and b) inverse temperature. Linear fits to the data (gray lines) are made to reveal possible power law or activated behavior; neither fit works very well.

One possible explanation for the voltage fluctuations is that individual current filaments or pathways through the CDW open and close over time and with a changing dc current. This mechanism has been proposed to account for similar data observed in the depinning of vortex lattices [16,17]. However, this explanation does not account for the strong periodicity of the voltage spikes.

10.2.6 Alternate Breakdown Models and Heating

So far, the phenomenon of RIQHE breakdown has been interpreted as a depinning transition in the bubble CDW. The sharp threshold to conduction above a critical dc current is reminiscent of the depinning of other spatially ordered electronic systems such as 1D CDWs, WCs, and vortex lattices. The hysteresis and dynamical switching behavior of the transition to conduction is also similar to what is observed in the depinning events of some two-dimensional WC [8] and vortex lattice [16,17] systems. However, alternative models for the RIQHE breakdown that have nothing to do with pinned bubble CDWs can be constructed. For example, the nonlinear *I-V* curves discussed in this chapter are qualitatively similar to what is observed in the breakdown of the IQHE. Discontinuous *I-V* curves, hysteresis, and excess noise near the onset of conduction have all been reported [18]. Numerous mechanisms [18] for the breakdown have been proposed, including runaway heating, Zener tunneling, inter-LL transitions, backscattering filament formation, and magneto-exciton generation [19].

No single theory of IQHE breakdown satisfactorily explains all the experimental results, and the application of these theories to the RIQHE is further complicated by some important differences between the RIQHE and the IQHE. For example, the RIQHE is only observed at temperatures below ~100 mK in the highest quality samples available. Most IQHE breakdown studies, on the other hand, have been made at much higher temperatures and pertain to samples with much lower mobilities where interaction physics is negligible. Another significant difference is that the observed threshold fields for conventional IQHE breakdown in comparable bulk 2D samples exceed those we find in the RIQHE by large factors, typically 10^3 to 10^4.

Efforts were made to directly compare the physics of the RIQHE and the IQHE breakdown, but no threshold behavior was ever observed in the latter case. For example, Fig. 10.13a compares the *I-V* curves in the RIQHE and the IQHE regimes for sample H-1 at a refrigerator temperature of 50 mK. The magnetic fields where the *I-V* curves were obtained are indicated by arrows above the longitudinal resistance transport data shown in Fig. 10.13b. For the case of the RIQHE, V_{yy} breaks down well below $I_{dc} = 1\ \mu$A and rises very rapidly after that. For the IQHE case, no sharp rise in V_{yy} is seen even up to I_{dc}

= 9 μA. By that point, V_{yy} has only slowly begun to rise up from zero. Also, such high currents cause so much heat to be dissipated that the refrigerator has difficulty maintaining low temperatures; by that point the 2DES is certainly much hotter than 50 mK. Finally, after running such a large current through the sample, its transport quality—at all magnetic fields—can become significantly degraded, requiring a thermal cycling to room temperature.

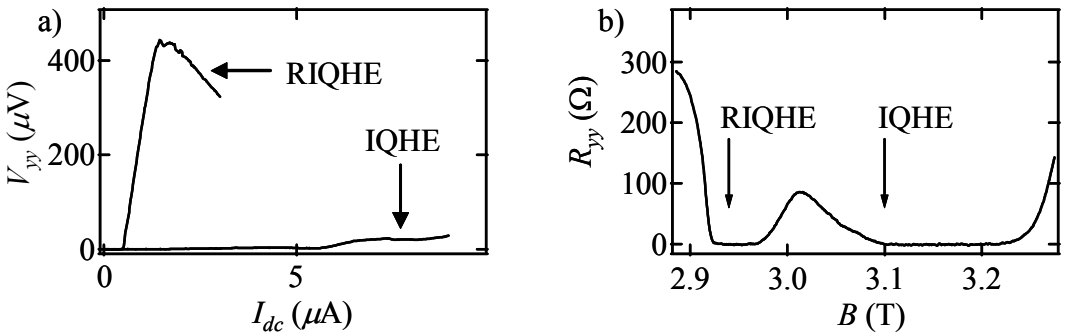

Figure 10.13: a) Comparison of the RIQHE and IQHE breakdown in sample H-1 up to high dc currents. b) Arrows indicate the magnetic fields where the *I-V* curves were obtained. Although V_{yy} in the IQHE regime eventually becomes nonzero for large I_{dc}, a sharp onset to conduction only occurs in the RIQHE.

Despite these major differences between the RIQHE and the IQHE breakdown features, it is still worthwhile to investigate how our data might fit one of the leading candidate models of IQHE breakdown: runaway heating [20]. An essential element of that model is that the longitudinal resistance R_{xx} in the IQHE regime rises with increasing temperature so that the thermal runaway will be initiated at some threshold power input to the 2DES.

To investigate the relevance of this heating model of RIQHE breakdown, Fig. 10.14 compares the temperature dependence of the resistance R_{yy} at two filling factors of sample C-8, one inside the RIQHE and one on the IQHE side of the satellite peak (Fig. 10.14a). At both locations, the temperature dependence (Fig. 10.14b) of R_{yy} behaves in an activated manner: $R_{yy} = R_0 \exp(-E_A/T)$, and the measured activation energies in the two cases are comparable ($E_A \sim 0.3$ K). On the other hand, *only* the *I-V* curves in the RIQHE show sharp thresholds to conduction. This is true regardless of whether the actual R_{yy} value is smaller, equal to, or larger than the value inside the RIQHE where a sharp onset to conduction was observed. A simple thermal runaway model of the RIQHE

breakdown, on the other hand, would predict that a similar breakdown should occur on the $\nu = 4$ side of the satellite peak as well because the temperature dependence of the two points are so similar. That this does not happen suggests that the discontinuities in the RIQHE *I-V* curves cannot be accounted for by the runaway heating model.

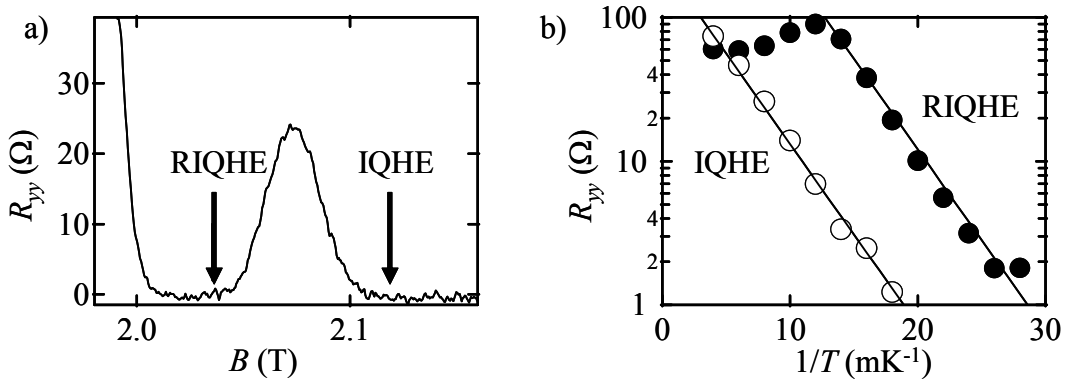

Fig. 10.14: a) R_{yy} versus B at 25 mK in sample C-8 showing locations where the RIQHE and the IQHE are scrutinized. b) An Arrhenius plot of R_{yy} taken at the two locations. Both the IQHE and the RIQHE exhibit activated behavior with $E_a \sim 300$ mK. Despite that similarity, discontinuous *I-V* curves are only observed in the RIQHE state.

Another piece of evidence suggesting that the heating model is not appropriate for the RIQHE breakdown is shown in Fig. 10.15. There, two traces of the differential resistance dV_{yy}/dI are plotted versus I_{dc} for sample B-1. The two traces were obtained simultaneously with two pairs of longitudinal voltage contacts (gray and black) on opposite sides of the sample (see inset). Interestingly, the "gray" side breaks down almost 200 nA earlier than the "black" side. If electron heating were the culprit for the RIQHE breakdown, then one would expect the whole 2DES to heat up once breakdown occurs. However, the RIQHE on one side of the sample remains intact, and presumably cold, even after the other side starts conducting. On the other hand, the data are consistent within the picture of a depinning transition of a bubble CDW because the bubble phase could begin to flow in some portions of the sample but not in others for an intermediate value of I_{dc}.

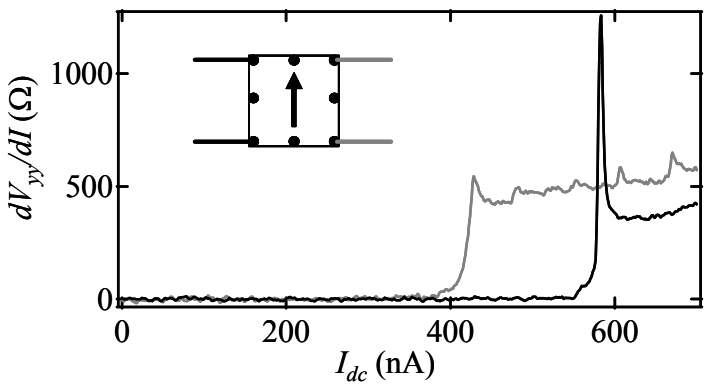

Figure 10.15: Breakdown of the $\nu \approx 4.25$ RIQHE in sample C-8 at 25 mK. The differential dV_{yy}/dI versus I_{dc} curves were taken simultaneously using contact pairs (black and gray) on opposite sides of the sample (see inset). The threshold currents for the two sides are substantially different.

10.3 Narrow-Band Noise Accompanying RIQHE Breakdown

10.3.1 Time Domain

Subsequent to the discovery and investigation of the RIQHE breakdown phenomena described in Section 10.2, another remarkable aspect of the RIQHE physics at high I_{dc} was uncovered: that the abrupt onset of conduction is often accompanied by narrow- and broad-band noise throughout frequencies in the kHz range. The basic result is summarized in Fig. 10.16. Fig. 10.16a shows the longitudinal resistances R_{xx} and R_{yy} in sample H-1 at $T = 50$ mK over the range $4 < \nu < 5$. In Fig. 10.16b, the *I-V* curve taken at $\nu = 4.27$ is plotted. In this case, the $\nu \approx 4.25$ RIQHE breakdown occurs at $I_{dc} \approx 1.1$ μA, where V_{yy} abruptly rises from zero.

Unlike the data of Section 10.2, here the dc *and* ac components of V_{yy} are monitored simultaneously in a manner shown schematically in the inset to Fig. 10.16b. After a room-temperature amplification stage with a gain of typically 10^4, the dc and ac voltages V_{dc} and V_{ac} are read by a digital voltmeter and a digital oscilloscope (Hewlett Packard Infinium), respectively. The bandwidth of the circuit, about ~100 kHz, is limited

by the *RC* roll-off time arising from sample impedance (~5 kΩ) and the cable capacitance running up from the sample stage in the dilution refrigerator.

Fig. 10.16c shows that along with the sharp dc response, a nonzero V_{ac} appears as the RIQHE breaks down. Four 10 ms traces of the net longitudinal voltage $V_{ac} + V_{dc}$ taken at different values of I_{dc} are displayed. For $I_{dc} = 0.5\ \mu$A, V_{ac} is very small and displays only background noise. Above the dc threshold current of 1.1 μA, however, V_{ac} begins to fluctuate. Immediately above threshold, at $I_{dc} = 1.2\ \mu$A, V_{ac} displays a reproducible burst-like pattern separated by irregular intervals. At higher currents V_{ac} shows unambiguous narrow-band noise, oscillating around 3 kHz for $I_{dc} = 1.4\ \mu$A. As I_{dc} is increased further, the noise frequency rises and higher harmonic content is present. By $I_{dc} = 1.7\ \mu$A, fluctuations on time scales of less than 0.1 ms are seen. It is noteworthy that this noise in V_{ac} develops *spontaneously* in the RIQHE regions of high LLs under *purely dc* current excitation. The noise arises from the 2DES itself and is not due to interactions with the external circuitry. For example, the noise can be measured in a four-terminal or a two-terminal configuration, and it is not affected by the value of the large blocking resistor (5-10 MΩ) used in the dc current source. Also, the noise has been detected using a current preamplifier as well as a voltage preamplifier.

The voltage oscillations in Fig. 10.16c are somewhat reminiscent of the voltage spikes observed in some of the dc *I-V* curves shown in Section 10.2. However, it is not known whether there is any connection between the two. At the time of their detection, the voltage spikes of Section 10.2, which were recorded only on the time scale of seconds, were not investigated thoroughly. Since the discovery of the kHz-frequency oscillations, the samples that did show the slower dynamics have not been investigated again.

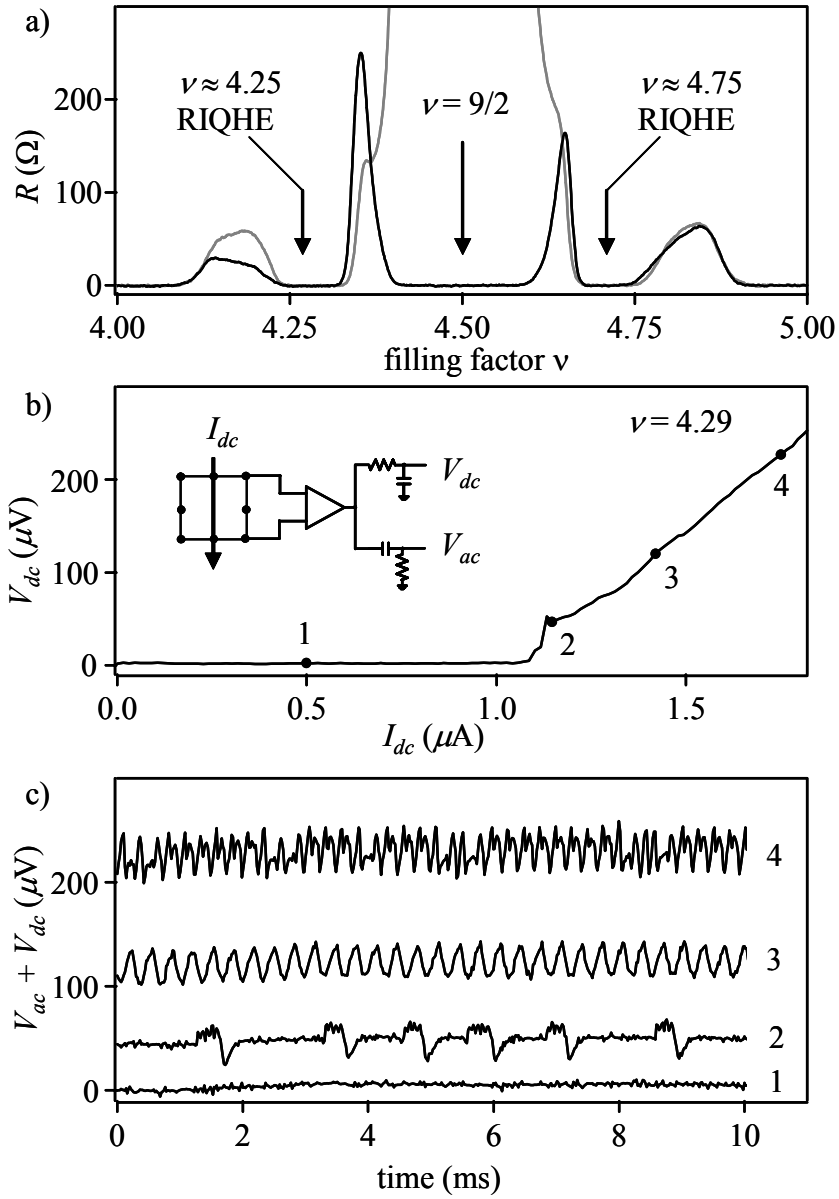

Figure 10.16: Overview of the time-dependent breakdown phenomenon in sample H-1 at 50 mK. a) R_{xx} (gray) and R_{yy} (black) versus filling factor in the range $4 < \nu < 5$. b) Non-linear dc I-V curve taken near the center of the $\nu \approx 4.25$ RIQHE. Inset: schematic circuit diagram showing separation of V_{dc} and V_{ac}. c) Time dependences of the net longitudinal voltage $V_{ac} + V_{dc}$ taken at the values of I_{dc} labeled in b).

10.3.2 Frequency Domain

Fig. 10.17 illustrates how the spectral content of the noise associated with the breakdown of the RIQHE near $\nu \approx 4.25$ varies with I_{dc}. The lower panel of Fig. 10.17a shows a typical dc *I-V* characteristic, and the threshold to conduction occurs close to 1.0 μA. Meanwhile, the upper panel displays a logarithmic plot of the simultaneously recorded Fourier power spectrum of V_{ac}. The Fourier spectrum was calculated by the digital oscilloscope using the fast Fourier transform (FFT) algorithm. The spectral data shown in Fig. 10.17 were obtained by averaging 64 FFT spectra at each one of 200 values of I_{dc} between 0 and 3 μA. Care was taken to minimize aliasing effects by having a sufficiently high sampling rate and by adjusting the preamplifier filters. The full gray scale in the image of Fig. 10.17 corresponds to a noise power variation of 37 dB. The faint horizontal lines running across the entire image are artifacts arising from background electronic pick-up. Such pick-up signals come largely from the vibrations of the leads in the dilution refrigerator and are exacerbated by the presence of the ~2 T magnetic field.

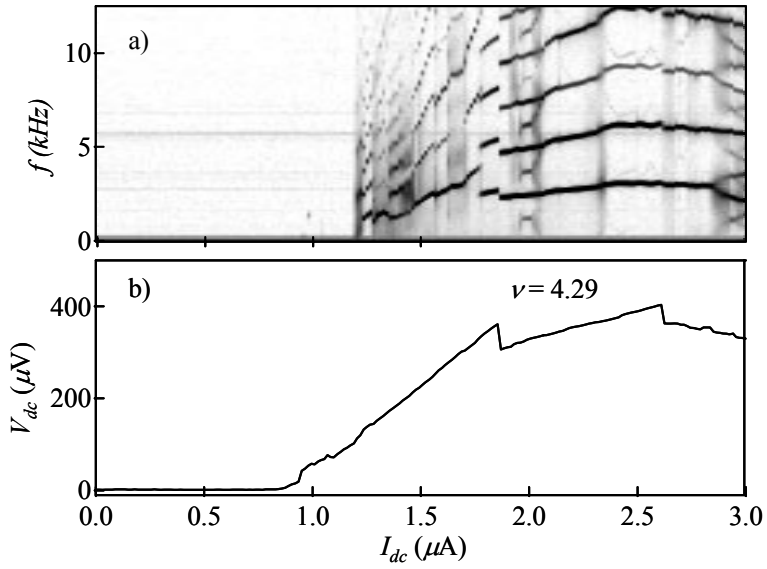

Figure 10.17: a) Spectral characteristics of noise associated with RIQHE breakdown in sample H-1 at 50 mK and $\nu = 4.29$. The grayscale span covers a noise power variation of 37 dB. The frequencies of the narrow-band noise modes initially increase with I_{dc} above breakdown. b) Corresponding dc *I-V* curve.

It is apparent from Fig. 10.17 that as the dc breakdown current is exceeded, the power spectrum erupts from quiescence into a rich pattern of sharp spectral lines and their harmonics. These noise modes can be quite distinct, although they tend to jump around in frequency at certain values of I_{dc}. Weaker broad-band features are also evident. The frequencies of the noise modes in Fig. 10.17 are strongly dependent on the dc current flowing through the sample. Indeed, in some respects the noise power spectrum mirrors the dc *I-V* characteristic. Immediately above threshold, V_{dc} rises linearly with I_{dc}; at the same time, the dominant mode frequencies also rise roughly linearly. At higher dc currents, V_{dc} exhibits sharp step-like features and ultimately begins to fall. Likewise, the power spectrum undergoes abrupt structural changes and, eventually, the dominant mode frequencies also begin to subside.

Just as the detailed shape of the dc *I-V* curves at a given *B* and *T* will vary from measurement to measurement over the course of an experiment, so will the precise noise spectral "fingerprint" such as that shown in Fig. 10.17. The fingerprints also change within the RIQHE region at slightly different filling factors or with different choices of voltage contacts on the sample. However, certain qualitative features of the noise are robust: the onset of noise near dc breakdown; modes with fundamental frequencies in the kHz range; a strong current dependence with frequencies that increase (along with V_{dc} and I_{dc}) immediately following breakdown; and a complex mix of regions with narrow-band and broad-band noise. The presence of kHz noise, with the same qualitative behavior, has also been observed accompanying the RIQHE breakdown in four different samples: H-1, J-2, K-1, and L-4. The wafers H and J are included in the list of samples of Table 3.1 which exhibit normal anisotropic transport characteristics. Sample K-1 was discussed in Section 4.3, and while its resistance anisotropy is somewhat anomalous, it shows excellent RIQHE features. Sample L-4, with a density and mobility of 2.1×10^{11} cm^{-2} and 12×10^{6} cm^2/Vs, also exhibits a clean RIQHE around $\nu = 9/2$. However, because its transport characteristics elsewhere are somewhat pathological, sample L-4 was omitted from Table 3.1.

To give an idea of how the character of the noise varies from one sample to the next, Fig. 10.18a shows a spectral fingerprint taken near $\nu \approx 4.25$ at 25 mK in sample L-4. In this figure, the dc *I-V* curve (with its y-axis on the right) is overlaid on the spectral

fingerprint. As with the sample H-1, after the abrupt rise of V_{dc} signals the breakdown of the RIQHE, oscillations in V_{ac} start. A complex and beautiful pattern of noise modes is generated as I_{dc} increases to 1.5 μA. Interestingly, the fact that V_{dc} shows a kink only at the threshold current and then proceeds to increase quite smoothly may lead one to think that the RIQHE breakdown behavior is more mundane in this sample than in cases where sharp discontinuities in V_{dc} are observed (such as in Fig. 10.2). However, the dramatic spectral content of V_{ac} leaves no doubt that interesting physics occurs in the breakdown of the RIQHE.

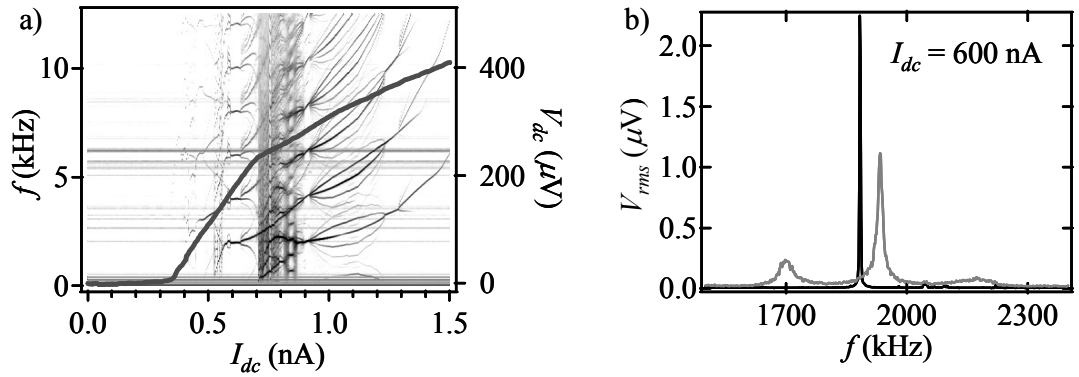

Figure 10.18: a) Spectral fingerprint of breakdown in the $\nu \approx 4.25$ RIQHE in sample L-4 at 25 mK. The thick trace superposed on the noise data is the corresponding dc *I-V* curve. b) Two high-resolution spectra (gray and black) taken a few minutes apart at I_{dc} = 600 nA. The fundamental mode at ~2 kHz can be extremely sharp.

The breakdown signature of sample L-4 is also important because it shows that V_{ac} can exhibit extremely periodic oscillations. Fig. 10.18b shows two rms voltage spectra of V_{ac} over a narrow frequency range at I_{dc} = 600 nA. Both traces were obtained at that fixed current about five minutes apart from one another. Amazingly, the blue trace contains a noise mode around 1900 kHz that is narrower than the 1.5 Hz point spacing of the FFT measurement. This corresponds to a Q-factor greater than 1000! Such high-Q modes are only transient, however. In the red trace, the frequency has shifted slightly upward, and its Q is a more typical value of ~100.

10.3.3 Temperature and Field Dependence

Like the breakdown phenomenon itself, the presence of noise in V_{ac} at high I_{dc} only occurs under conditions where the RIQHE forms. In Fig. 10.19a, the average noise level $\langle V_{rms} \rangle$ in the filling factor range $4 < \nu < 5$ is overlaid on the longitudinal resistance data shown in Fig. 10.16a. The quantity $\langle V_{rms} \rangle$ represents the rms noise voltage in a bandwidth of 1 to 25 kHz and averaged over 200 values of I_{dc} from 0 to 3 μA. It was calculated at each filling factor from a spectral fingerprint like that shown in Fig. 10.17a by integrating in quadrature the noise voltage densities from 1 to 25 kHz. Qualitatively, $\langle V_{rms} \rangle$ is a measure of the averaged intensity of such a noise fingerprint. The baseline of $\langle V_{rms} \rangle$ in Fig. 10.19a, about 1.4 μV, is equal to the background noise signal in the 1-25 kHz bandwidth at $I_{dc} = 0$. Clearly, excess noise above this baseline is absent over most of the range $4 < \nu < 5$. In particular, no excess noise is observed in the integer QHE regions at $\nu = 4$ and $\nu = 5$, nor in the region of anisotropic transport around $\nu = 9/2$. (This is true regardless of the direction of the current flow.) In contrast, a strong peak in $\langle V_{rms} \rangle$ is observed in the RIQHE region around $\nu = 4.25$, and a lesser but still noticeable peak is present in the RIQHE near $\nu = 4.75$.

The substantial differences in the noise power exhibited by these two RIQHE states is consistent with other instances where the experimental features of the RIQHE at $\nu \approx 4.25$ are "stronger" than those at $\nu \approx 4.75$. For example, Fig. 4.6 in Chapter 4 showed that the high-field RIQHE of $\nu = 9/2$ possesses larger activation energies than its low-field counterpart. Also, Fig. 10.2 showed that the breakdown of the $\nu \approx 4.25$ RIQHE is more prominent than the one at 3/4 partial filling. Spin effects and/or LL mixing may play a role in breaking this particle/hole asymmetry. The inset to Fig. 10.19a shows that the excess noise observed in the RIQHE is strongly temperature dependent. Just like the sharp threshold to conduction in the RIQHE, and indeed for all other signatures of the collective phenomena in high LLs, the noise vanishes by about 100 mK.

The bottom panels of Fig. 10.19 show nine spectral fingerprints used in the calculation of $\langle V_{rms} \rangle$. The corresponding filling factors of these images are indicated by

the filled-in markers in the $\langle V_{rms} \rangle$ data. At $\nu = 4.27$ where $\langle V_{rms} \rangle$ is largest (nearly 8 μV), a strong response in V_{ac} begins immediately after the breakdown point where V_{dc} exhibits a discontinuous jump. At each of the next two points, $\nu = 4.29$ and 4.30, the details of the spectral fingerprints change significantly even though the magnetic field difference between the adjacent points is only 13 mT. At $\nu = 4.39$, at the very edge of the anisotropic regime, the V_{dc} versus I_{dc} curve shows barely any nonlinearity and there is no sign of any noise in V_{ac}. Very close to the half-filling point, at $\nu = 4.51$, the *I*-*V* curve is virtually flat, and again the spectral fingerprint is blank. Indeed, no noise occurs throughout the anisotropic region of $\nu = 9/2$ (or any other high LL). By $\nu = 4.69$, the $\nu \approx$ 4.75 RIQHE state is just beginning to form, and the dc *I*-*V* curve shows a substantial nonlinear response with a distinct threshold current where dissipation sets in. However, no noise is detectable in V_{ac} at this filling factor. Even at currents above ~1 μA, where V_{dc} shows some small kinks and jumps, the spectrum remains featureless. This set of data is important because it helps rule out the possibility that sharp features in the dc *I*-*V* curves are sufficient for noise generation. Finally, the last three spectral images at $\nu =$ 4.72, 4.74, and 4.76 show that while much weaker, the spectral fingerprints in the $\nu \approx$ 4.75 RIQHE regime share essentially the same characteristics—increasing frequencies with I_{dc}, a mix of narrow- and broad-band noise, etc.—as those around $\nu \approx 4.25$.

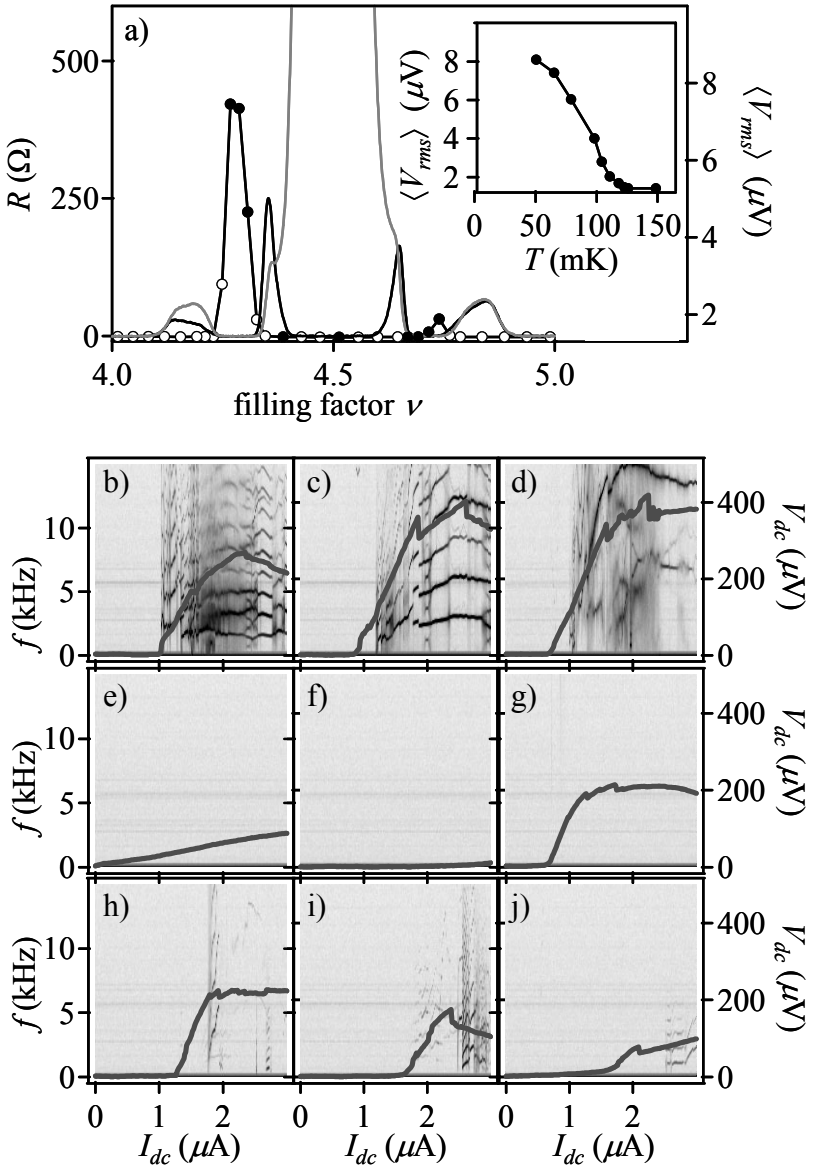

Figure 10.19: a) Main panel: comparison of longitudinal resistance (R_{xx}: gray; R_{yy}: black) and average noise voltage $\langle V_{rms} \rangle$ (circles) for $4 < \nu < 5$ at 50 mK in sample H-1. Inset: Temperature dependence of $\langle V_{rms} \rangle$ at $\nu = 4.28$. b) through j): Spectral fingerprints and dc *I-V* curves at the filling factors denoted by the filled circles in a): $\nu = 4.27$, 4.29, 4.30, 4.39, 4.51, 4.69, 4.72, 4.74, and 4.76. Excess noise is only observed in the RIQHE states.

10.3.4 Higher LLs and In-Plane Fields

While Fig. 10.19 illustrates the ac response of the RIQHE states to a dc current, all the data were obtained from the $\nu = 9/2$ region only. To show that the noise phenomenon is not restricted to that LL, Fig. 10.20 displays two spectral fingerprints and dc *I-V* curves from the RIQHE states at $\nu \approx 5.25$ and $\nu \approx 6.25$. Each shows its own particular noise pattern, but again they share the same general features as before: the onset of noise after the breakdown event; distinct noise modes with frequencies that initially increase with I_{dc}; and regions of narrow- and broad-band signals. Interestingly, even though the $\nu \approx 5.25$ state shows a very gradual onset to conduction, substantial noise is still present at high I_{dc}. Therefore, in this case the presence of oscillations in V_{ac} at high I_{dc} is a better indicator than a sharp dc *I-V* curve is of new physics in the RIQHE regime.

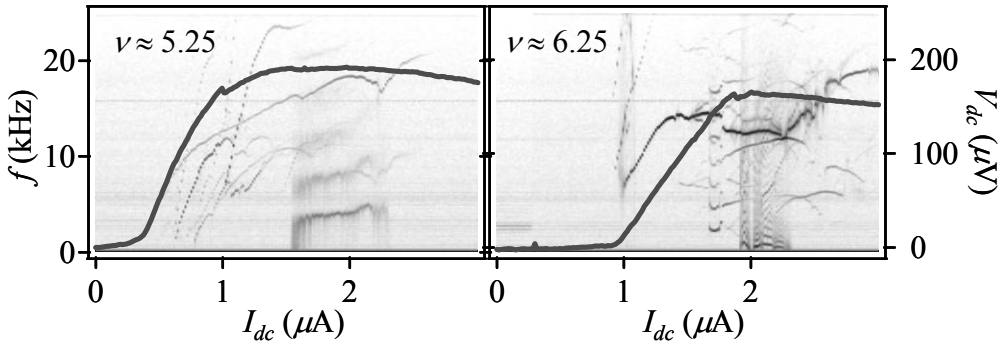

Figure 10.20: 50 mK spectral fingerprints and dc *I-V* curves from sample H-1 in the higher LL RIQHE states $\nu \approx 5.25$ (left) and $\nu \approx 6.25$ (right).

Although not studied thoroughly, the effect of an in-plane field on the response of V_{ac} to high current biases was measured a single time in sample K-1, and the results are shown in Fig. 10.21. Fig. 10.21a contains longitudinal resistance transport data versus $B_\perp$ through the $\nu \approx 4.25$ RIQHE at four angles from 0° to 34°. For each angle, the dc *I-V* curves and the spectral fingerprints taken near the center of the RIQHE are shown in Fig. 10.21b through e. The corresponding in-plane magnetic fields for the four plots are $B_{||}$ = 0.0, 0.53, 1.2, and 2.0 T. As $B_{||}$ increases, the dc *I-V* curves become steadily smoother until by $B_{||}$ = 2.0 T the onset to conduction shows no evidence of a sharp threshold

current. Similarly, the noise level is also gradually reduced until it is gone by $B_{||}$ = 2.0 T as well. However, despite these indications that the physics of the RIQHE state has become significantly different, the longitudinal resistance data of Fig. 10.21a shows that the RIQHE remains broad and insulating all the way up to $B_{||}$ = 2.0 T. In other words, $B_{||}$ apparently can destroy the suddenness of the RIQHE breakdown and the oscillations in V_{ac} *without* substantially affecting the sample's transport properties in the linear response regime.

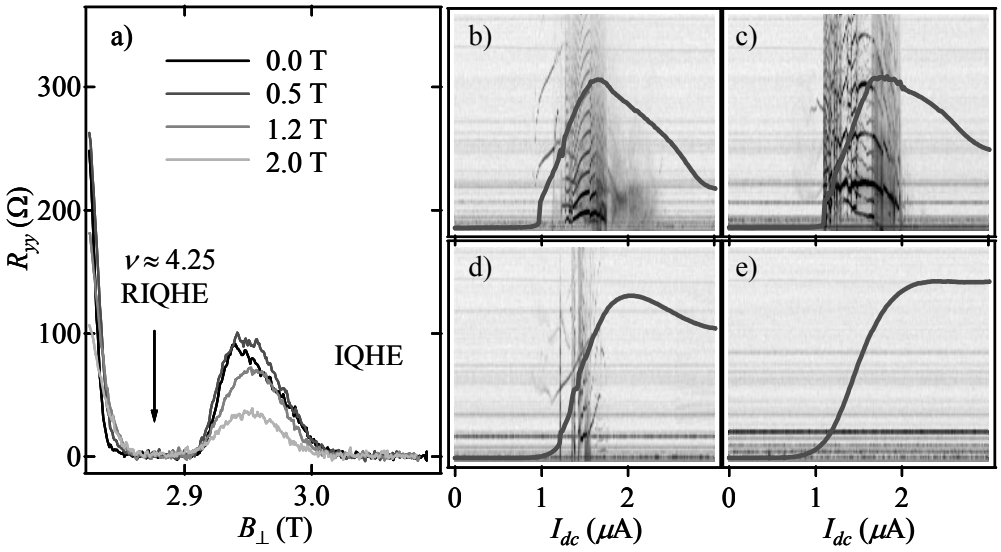

Figure 10.21: a) 50 mK Longitudinal resistance R_{yy} around the $\nu \approx 4.25$ RIQHE of sample K-1 at four in-plane fields with $B_{||}$ along $[110]$. b) through e): Corresponding spectral fingerprints and dc *I-V* curves for $B_{||}$ = 0.0, 0.5, 1.2, and 2.0 T. The vertical axes are the same as in Fig. 10.19. By $B_{||}$ = 2.0 T, the excess noise features are gone even though the RIQHE is still robust in the R_{yy} data.

10.4 Possible Mechanisms of Noise Generation

The mechanism responsible for noise generation at high dc current bias in the RIQHE states is not known. This is not surprising, considering that these unexpected results were only obtained in the last two years and that not even the origin of the RIQHE breakdown is understood (see Section 10.2). Plus, these experiments represent the *first time* narrow-band noise has ever been observed in a quantum Hall system. In this section, several

possible models for the noise generation will be evaluated, with an emphasis on the washboard noise mechanism.

10.4.1 Washboard Noise

Because the breakdown of the RIQHE may reflect the depinning of an electron bubble lattice, it is logical to compare the observed narrow-band noise with the washboard noise encountered in conventional 1D CDWs and vortex lattices (see Section 10.1). Because the temporal periodicity of washboard noise comes from the spatial periodicity of the depinned CDW as it slides across the sample, the noise frequency should be proportional to the current carried by the CDW. In the present case of a 2DES in the RIQHE regime, the generally increasing frequency of the narrow-band noise immediately above the breakdown point is suggestive of a similar mechanism. Of course, the narrow-band noise modes reported here are not as simple as those seen in conventional CDW systems like $NbSe_3$ [1,10]. The frequencies often have a more complicated nonlinear dependence on I_{dc}. There are also occasionally multiple modes oscillating at incommensurate frequencies, and the oscillations sporadically deteriorate into incoherent broad-band noise.

A more serious problem in reconciling the data with a washboard noise model is that the frequencies of the narrow-band noise observed above the RIQHE breakdown are so low. For example, according to the washboard model, the frequency of oscillation is given by $f = v/a$, where v is the velocity of the sliding CDW and a is its lattice constant. For the case of a bubble CDW in the RIQHE, a is on the order of the cyclotron radius, which is approximately 100 nm (see Section 5.2). The velocity, meanwhile, is related to the current carried by the CDW as

$$v = \frac{J_{CDW}}{en_{CDW}} \approx \frac{I_{CDW}}{Wen_{CDW}},$$

where I_{CDW} is the current carried by the bubble CDW in the valence LL, $n_{CDW} \approx 2/a^2$ (for two electrons per bubble), and W is the width of the sample. Here, the approximation is

made that the CDW current is uniform across the sample width. These relationships yield the frequency:

$$f = \frac{I_{CDW} a}{2eW}.$$

For a typical 5 mm wide sample, this equation yields a frequency of ~60 kHz per nA of current carried by the bubble CDW.

Unfortunately, for reasonable agreement with the experimental frequencies of ~5 kHz, this model predicts that the current carried by the CDW needs to be a miniscule ~100 pA! This number is orders of magnitude smaller than any simple estimate of the current carried by the bubble CDW above breakdown. For example, consider the breakdown *I-V* curve and noise data in Fig. 10.17. Just below breakdown, the entire 1 μA of current is carried by the $N = 0$ and $N = 1$ LLs that are submerged below the bulk Fermi level. Therefore above breakdown, an estimate of the *maximum* current that the CDW electrons in the valence LL carry is the difference between the total I_{dc} and 1 μA. For example, at $I_{dc} = 2$ μA the estimated $I_{CDW} = 1$ μA is four orders of magnitude larger than the 100 pA predicted by the sliding CDW model. (More realistically, this excess current will be divided in some way between the electrons in all the LLs.)

This gap of four orders of magnitude between the theory and experiment may be partially bridged by a more accurate estimate of the current carried by the CDW electrons above breakdown. One way of making this estimate is to examine how the Hall voltage responds to I_{dc}. Fig. 10.22a shows the dc *I-V* curve of V_{xy} versus I_{dc} in sample H-1 at $\nu =$ 4.29. Fig. 10.22b contains a spectral fingerprint of the ac component of V_{xy}; note that it, too, shows the usual noise signatures that are present in the longitudinal voltage above the threshold current. The thick trace in Fig. 10.22b is the estimated current carried by the CDW using the following method.

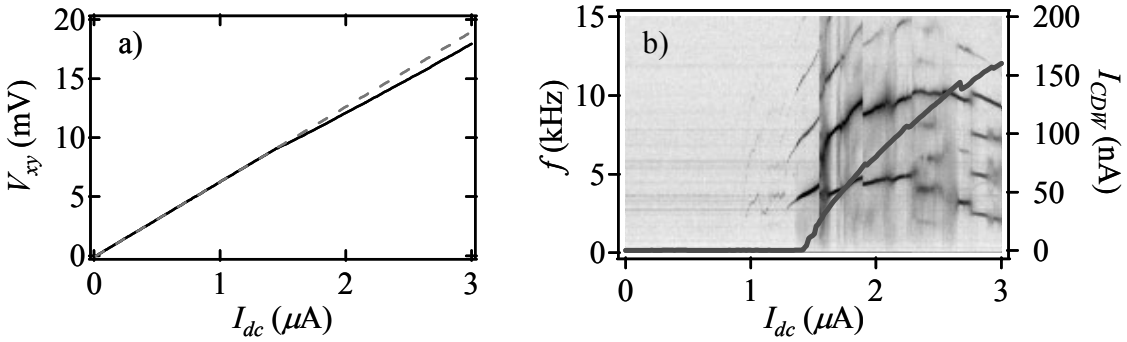

Figure 10.22: a) The dc component of V_{xy} versus I_{dc} in the $\nu \approx 4.25$ RIQHE of sample H-1 at 50 mK. b) Spectral fingerprint of the ac component of V_{xy}. The thick line corresponds to the estimated CDW current using the approximations discussed in the text. For $f \sim 5$ kHz, the estimate yields $I_{CDW} \sim 100$ nA.

In Fig. 10.22a, the straight dashed line has been fit to the low-current region of V_{xy}. Above about 1.4 μA, V_{xy} begins to fall below that line. The initial slope of V_{xy} is simply the quantized Hall resistance of the $\nu \approx 4.25$ RIQHE, i.e., $h/4e^2$. The deviation of the resistance above 1.4 μA comes about as the electrons in the valence LL (presumably part of the bubble CDW) begin to conduct current in parallel with the filled lower LLs. In a simplified model of this process, the total current $I_{tot} = I_{dc}$ passing through the sample is distributed between the lower LLs and the valence LL in such a way that

$$V_{xy} = I_{LLL}\frac{h}{4e^2} = (I_{tot} - I_{CDW})\frac{h}{4e^2},$$

where I_{LLL} is the current carried by the lower LLs. This approximation holds true at least in the two limits of low and high temperatures. For example, at low temperatures where R_{xy} is quantized at $h/4e^2$, I_{CDW} vanishes so that $V_{xy} = I_{tot}h/4e^2$. At high temperatures where R_{xy} is given by the classical value $B/ne = h/\nu e^2$, the current is partitioned into the valence and the lower LLs so that $I_{CDW} = I_{tot}(\nu - 4)/\nu$, and the approximation is satisfied as well. What happens between these two limits is highly model-dependent, but using the approximation anyway implies that the magnitude of the deviation of V_{xy} above breakdown from its linear value of $I_{tot}h/4e^2$ is simply $I_{CDW}h/4e^2$.

Using this formula with the data of Fig. 10.22a, I_{CDW} versus I_{dc} is derived and plotted as the thick trace of Fig. 10.22b. Interestingly, I_{CDW} becomes nonzero around 1.4 μA, about 40% higher than the threshold current (~1 μA) as determined by the longitudinal voltage depinning. Note that a small amount of noise in V_{xy} also appears at currents in the range $1 < I_{dc} < 1.4$ μA. In any case, the values of I_{CDW} estimated using this method are on the order of 100 nA at currents around 1 μA above breakdown. Although this is a factor of 10 reduction in the estimated I_{CDW} compared to the previous estimate, it is still far larger than the 100 pA currents necessary to account for the low frequencies of the narrow-band noise observed above breakdown.

Aside from constructing some reason for I_{CDW} to be absurdly small (~100 pA) above breakdown, another way of obtaining kHz frequencies from the washboard noise model is to consider more carefully how the bubble CDW might move in two dimensions in a perpendicular magnetic field. In particular, if the major assumption is made that the bubble CDW above breakdown is allowed to flow through the two-dimensional sample unimpeded, then its velocity can be derived simply from the characteristic drift velocity in crossed electric and magnetic fields: $v = E/B$. While the magnetic field is the ~3 T quantizing perpendicular field, the appropriate electric field comes from a combination of the Hall and the longitudinal voltages. For example, assuming that the current flows along **x**, an electric field will be generated along **y** with strength $E_y \approx V_{xy}/W$ that points in a direction transverse to the total current flow. Above breakdown a longitudinal voltage component V_{xx} is established, giving rise to an electric field component along the direction of current flow, $E_x \approx V_{xx}/W$. The resulting drift velocity of the CDW then has two components:

$$v_x = \frac{V_{xy}}{WB} \text{ and } v_y = \frac{V_{xx}}{WB}.$$

Typical numbers for $I_{dc} \sim 2\mu$A and $B \sim 3$ T are $V_{xy} \sim 10$ mV (see Fig. 10.22) and $V_{xx} \sim$ 300 μV (see Fig. 10.17). The two velocity components then yield two washboard frequencies according to $f = v/a$: $f_x \sim 7$ MHz and $f_y \sim 200$ kHz. It is not clear at all why there might be two frequencies instead of one that simply corresponds to the net velocity.

One reason might be that the voltage oscillations arise from the bubbles of the sliding CDW hitting the sample edges. Then, because there is one edge parallel to **x** and one parallel to **y**, there might be two frequencies generated.

While still larger than the observed frequencies a few kHz, the value for f_y is encouragingly closer to agreeing with the experiment than any other derived washboard frequency. If correct, this model would imply that $f \sim V_{xx}$; such a trend is indeed often, though not always, observed (see Fig. 10.17). The model would also imply that higher MHz-scale voltage oscillations might be present, resulting from f_x. These have not been detected, but our measurement setup has a bandwidth of only ~100 MHz.

10.4.2 Other Noise Mechanisms

The failure of the washboard noise mechanism to account for the low frequencies observed in the RIQHE breakdown suggests that other models of narrow-band noise generation should be considered. One intriguing possibility is that the oscillations in the RIQHE breakdown come from a train of large domains of the bubble CDW moving across the sample. This scenario is similar to the washboard model, except the period of oscillation corresponds to the characteristic time it takes for large domains (or "chunks") of the bubble CDW lattice to move past a given point, rather than for a single bubble to do so. For a domain of size L, the oscillation frequency would be $f = v/L$. Using the drift velocity $v = E/B = V_{xy}/BW$, for example, implies that at $I_{dc} = 2\ \mu$A the necessary size of the domains for a typical 5 kHz signal is $L \sim 200\ \mu$m. This size seems quite large, but the cleanliness of the 2DES and the strong correlations among the electrons may allow large chunks of the CDW to depin and yet remain internally intact.

Interestingly, the amplitude of the ac voltage signal produced by one of these chunks being absorbed into the current drain contact can be crudely estimated and compared to the experiment. The estimate is made by assuming that the voltage fluctuation due to a single chunk is given by $\delta V \sim \delta I h/4e^2$, where δI is the current pulse due to one of the CDW chunks and $h/4e^2$ is the characteristic (Hall) resistance of the quantum Hall system near $\nu = 4$. Then, δI is related to the period between oscillations and the size of one of the chunks by $\delta I \sim \delta Q f \sim e n_{CDW} L^2 f$, where $n_{CDW} \sim 1/a^2 \sim 10^{10}$ cm^{-2}

is the estimated electron density of the CDW. Putting all this together yields $\delta V \sim 20\ \mu$V at a frequency of 5 kHz. Promisingly, this value for the voltage fluctuation in one cycle of the oscillation is very close to what is measured (see Fig. 10.16). Also, the approximate relation $\delta V \sim \delta I h/4e^2$ was confirmed by monitoring the current fluctuations in the breakdown regime using a current preamplifier.

Another potential source of noise in the breakdown of the RIQHE states is the oscillation of current filaments which might form throughout the bubble CDW above breakdown. Recall from Section 10.2 that some of the slow switching properties of the *I-V* curves are reminiscent of those seen in the depinning of vortex lattices and attributed to the formation of filamentary paths of vortex motion across the samples. The filament formation has also been proposed as a breakdown mechanism of the conventional IQHE [21]. Conceivably, current filaments through the bubble CDW lattice might even become dynamic at high dc current biases. If they were to somehow fluctuate periodically, the narrow-band noise might be accounted for. Further theoretical work is needed to determine whether the breakdown fields we observe of ~10 mV/cm are consistent with the formation of such filaments through a bubble CDW.

---

1 For a detailed review of 1D CDW systems, see G. Gruner, Rev. Mod. Phys. **60**, 1129 (1988); for a concise overview, see R.E. Thorne, Physics Today, May 1996, p. 42.

2 C.C. Grimes and G. Adams, Phys. Rev. Lett. **42**, 795 (1979).

3 B. Tanatar and D.M. Ceperley, Phys. Rev. B **39**, 5005 (1989).

4 H.W. Jiang, R.L. Willett, H. Stormer, D.C. Tsui, L.N. Pfeiffer, and K.W. West, Phys. Rev. Lett. **65**, 633 (1990).

5 J.R. Waldram, *Superconductivity of Metals and Cuprates* (Institute of Physics Publishing, Philidelphia 1996).

6 H.-W. Jiang and A.J. Dahm, Phys. Rev. Lett. **62**, 1396 (1989).

7 V.J. Goldman, M. Santos, M. Shayegan, and J.E. Cunningham, Phys. Rev. Lett. **65**, 2189 (1990).

8 F.I.B. Williams, P.A. Wright, R.G. Clark, E.Y. Andrei, G. Deville, D.C. Glattli, O. Probst, B. Etienne, C. Dorin, C.T. Foxon, and J.J. Harris, Phys. Rev. Lett. **66**, 3285 (1991).

9 S. Bhattacharya and M.J. Higgins, Phys. Rev. Lett. **70**, 2617 (1993).

10 R. Fleming and C.C. Grimes, Phys. Rev. Lett. **42**, 1423 (1979).

11 S.G. Lemay, R.E. Thorne, Y. Li, and J.D. Brock, Phys. Rev. Lett. **83**, 2793 (1999).

12 Y.P. Li, T. Sajoto, L.W. Engel, D.C. Tsui, and M. Shayegan, Phys. Rev. Lett. **67**, 1630 (1991).

13 Y.P. Li, D.C. Tsui, L.W. Engel, M.B. Santos, T. Sajoto, and M. Shayegan, Solid State Comm. **96**, 379 (1995).

14 Y. Togawa, R. Abiru, K. Iwaya, H. Kitano, and A. Maeda, Phys. Rev. Lett. **85**, 3716 (2000).

15 A.C. Marley, M.J. Higgins, and S. Bhattacharya, Phys. Rev. Lett. **74**, 3029 (1995).

16 M. Danckwerts, A.R. Goni, and C. Thomsen, Phys. Rev. B **59**, R6624 (1999).

17 N. Gronbech-Jensen, A.R. Bishop, and D. Dominguez, Phys. Rev. Lett. **76**, 2985 (1996).

18 For a review of QHE breakdown, see G. Nachtwei, Physica E (Amsterdam) **4**, 79 (1999).

19 A.M. Martin, K.A. Benedict, and L. Eaves, http://xxx.lanl.gov/abs/cond-mat/0201532.

20 S. Komiyama, T. Takamasa, S. Hiyamizu, and S. Sasa, Solid State Comm. **54**, 479 (1985).

21 V. Tsemekhman, K. Tsemekhman, C. Wexler, J.H. Han, and D.J. Thouless, Phys. Rev. B **55**, R10201 (1997).

Chapter 11:
Future Directions

The experiments described in this thesis have significantly contributed to the understanding of correlated electron physics in the high LL regime, and any comprehensive account of quantum Hall physics would now be incomplete without a discussion of stripes, bubbles, and their impact on electronic transport measurements. However, by no means has the physics of two-dimensional electrons in high LLs been fully explored. This section provides a short list of some important unresolved issues and suggests experiments that could be performed to address them.

2DES mobility and density. Section 3.1 showed that the anisotropic transport phenomenon is observed in samples with mobilities ranging from $\mu = 4$ to 30×10^6 cm^2/Vs and densities from $n = 1.5$ to 2.9×10^6 cm^2/Vs. What happens beyond these limits? The low-mobility boundary is especially intriguing because it raises the question of how disorder precludes the observation of anisotropic transport. Does disorder inhibit the delicate interactions necessary for stripe CDW formation? Or does it merely prevent the formation of a *coherently oriented* stripe CDW? Some evidence in favor of the latter scenario was presented in Section 6.2, where transport in a low-mobility sample was found to be in good agreement with the semicircle law of stripe CDW transport. If orientationally disordered stripes do exist in lower-mobility samples, then the in-plane magnetic field technique of Chapters 8 and 9 might reveal their presence by providing an orientational pinning mechanism strong enough to overcome the sample's disorder. To be sure, the high-mobility limit is always of experimental interest because ever-more delicate correlation physics will certainly be revealed.

Meanwhile, Sections 3.4 and 4.3 indicated that higher-density samples exhibit anisotropic transport and RIQHE states at higher temperatures. A likely reason for this is that interactions between more closely-spaced the electrons raise the energy scale of the collective states. It would be valuable to quantify the relationship between the 2DES

density and the appearance of many-body physics in high LLs by measuring more samples that cover a wide range of density. Better yet, the development of clean samples with *tunable* densities would be ideal. Undoped, gated FET structures [1] show the most promise for achieving this goal, and Zhu et al. [2] have already observed anisotropic transport in one such sample.

High currents through stripes. An aspect of transport through the anisotropic phase that deserves further scrutiny is the resistance nonlinearity at high dc current bias (Section 3.5). Unlike the anisotropy itself at half-filled high LLs, which is widely thought to arise from charge density wave formation, the origin of the resistance nonlinearities is not understood. One explanation for the initial rise in R_{xx} with I_{dc} is that the stripe CDW becomes more oriented with a dc current running along **x**. If that is the case, then R_{xx} should also be measured with a dc current running along **y** instead. Another possible experiment is to determine whether the intriguing particle-hole asymmetry of the nonlinear resistance on either side of $\nu = 9/2$ filling (Fig. 3.21) exists in higher LLs, and whether it is related to the spin-splitting LL asymmetry (Fig. 3.20).

Small samples. All experiments reported here were performed on 2DES samples with typical dimensions of several millimeters, although the Hall bar samples were as little as ~0.5 mm wide. What happens as the sample dimensions are reduced? New transport phenomena might occur if sample sizes can be reduced to the length scale of individual stripe or bubble domains. Also, edge channel conduction is generally more relevant in small samples [3], and experiments in that regime could address the question of how current is divided between the filled lower LLs and the anisotropic phase in the valence LL (see Section 6.1). Transport experiments on the individual stripe length scales can also be envisioned, and a constricted "hourglass" geometry might reveal unusual quantization effects arising from single-stripe conduction.

Lower temperatures. Like increasing the mobility of a 2DES, lowering its temperature is another route to revealing new correlation physics in the quantum Hall regime. In terms of high LL physics, a major open question is what happens to the stripe phase as T

$\rightarrow 0$. Will the system remain conducting, or will the stripes eventually become pinned by disorder and go insulating? Some of the temperature-dependences of the anisotropic transport reported in Section 3.4 hint that the peak in R_{xx} begins to fall again for $T \leq 25$ mK (see Fig. 3.18), but the results are filling factor- and sample-dependent. Much lower temperatures unattainable with our current apparatus are necessary to make any definitive conclusions. Fortunately, a more powerful refrigerator based on Pomeranchuk cooling is currently being acquired by our laboratory, and temperatures of less than 5 mK are anticipated.

Direct detection of charge modulation. Although circumstantial evidence of their existence is strong, an unequivocal demonstration of stripes and bubbles in high LLs will likely require a direct detection of the CDW charge modulation. This might be possible using low-temperature scanning probe microscopy, and the technique has been used to probe 2DESs in the quantum Hall regime [4]. However, a major difficulty with the stripe and bubble problem is that the 2DES is buried beneath the crystal surface by a distance typically equal to or greater than the estimated charge modulation wavelength in high LLs. As a result, the electric field modulation at the sample surface is exponentially diminished and would be very difficult to detect. Samples with the 2DES closer to the crystal surface would be preferable, but these structures typically have much lower mobilities compared to those where stripe and bubble physics is observed. Plus, the experimental hurdles of building a high resolution scanning probe microscope in a dilution refrigerator environment are daunting.

Radiation and high frequency probes. A recent advance in the physics of high LLs was the detection of microwave resonances associated with the RIQHE states by Lewis et al. [5]. Drawing on an analogy to the $\nu << 1$ Wigner crystal, those authors argue that the resonance represents a pinning mode of the bubble CDW phase. These experiments should be reproduced and also reconciled with the RIQHE breakdown phenomena discussed in Chapter 10. For example, do the microwave resonances vanish above the RIQHE threshold currents because the bubble phase is torn loose from its pinning sites? Also, similar microwave absorption experiments should be performed on the stripe CDW

region around half-filling of high LLs. These experiments might serve as tests of various stripe CDW theories that make predictions regarding stripe dynamics, such as the quantum nematic theory of Radzihovsky and Dorsey [6]. Another route to probing the high-frequency conductivity of the anisotropic phase is to measure the propagation of surface acoustic waves across a 2DES in a GaAs/AlGaAs heterostructure [7], and an effort has begun in our laboratory to accomplish that.

Search for orientational symmetry-breakers. Despite the investigations discussed in Chapter 7, the native crystal symmetry-breaking mechanism of the anisotropic phases in high LLs remains a mystery. One informative experiment might be to examine the high LL anisotropy in a series of samples with varying distances between the 2DES and the sample surface. If the reduced symmetry at the GaAs surface is ultimately responsible for the differentiation between the $[1\,\bar{1}0]$ and $[110]$ directions in the 2DES, then one would expect the anisotropy to be affected by the sample's cap thickness. Also, the piezoelectric orienting hypothesis of Fil [8] predicts a 2DES depth-dependence of the pinning strength, which can be measured using the in-plane field technique of Section 8.4.

The theory of a piezoelectric orienting mechanism can also be tested by more thoroughly examining the effect of an in-plane field along directions other than $[1\,\bar{1}0]$ and $[110]$. As discussed in Section 8.5, the double-well anisotropy potential predicted by the piezoelectric theory should be detectable by measuring how difficult it is to reorient the stripes along unfavorable directions with an in-plane magnetic field. The results of Section 8.5, involving $B_{||}$ directed along [010], were inconclusive. A future experiment designed to address this issue would benefit by two additional experimental techniques: First, a redesigned rotator stage that allows $B_{||}$ to be directed in an arbitrary direction without thermally cycling the refrigerator to room temperature would speed up the data acquisition process enormously. Second, a 2DES with a circular boundary containing many equidistant ohmic contacts would allow resistances in several directions to be compared directly in the same sample.

In addition to identifying the native crystal symmetry-breaking mechanism, other external orienting mechanisms can be sought. Aside from an in-plane magnetic field, one

orienting mechanisms might be crystal strain. Strain can be applied either uniformly by bending a thin wafer about some in-plane axis, or periodically by patterning a unidirectionally modulated gate or dielectric on the sample surface. In the latter case, the period could be varied to search for a strengthened response of the 2DES when the modulation is commensurate with the stripe CDW wavelength. This experiment has already been attempted by Endo and Iye [9], but the resulting transport quality was too poor to make any conclusions regarding stripe physics.

Exploring RIQHE breakdown. A top priority of future experiments should be to test possible mechanisms of RIQHE breakdown and noise generation. For example, the breakdown current threshold could be measured as function of the width of the 2DES. Because the power input to the 2DES scales as the square of the current density while the Hall electric field scales linearly with the current density, the results of such an experiment might distinguish between mechanisms based on depinning versus runaway heating effects. Another way to eliminate heating as a possible cause of RIQHE breakdown would be to observe an onset to conduction in a purely voltage-biased configuration. This is possible using a so-called "Corbino" geometry, where the electrical contacts are totally internal to the 2DES, thus eliminating pre-breakdown edge-channel conduction through the lower LLs.

As for the problem of noise generation above the RIQHE breakdown, high-frequency voltage oscillations should be searched for. In the simplest models, the narrow-band washboard noise expected for a sliding bubble CDW is typically on the order of 10 MHz. The main hurdle in detecting such signals has been the problem of carrying high-frequency signals from the sample to room temperature. The development of a low-power cryogenic preamplifier or other impedance-matching device might solve this problem. Another set of potential experiments involve searching for ac-dc interference effects above breakdown. In conventional CDW systems, a variety of mode-locking, mode-mixing, memory, and chaos effects [10] are observed when an oscillating external perturbation interacts with the sliding CDW. Similar phenomena occurring in the RIQHE may be indicative of the bubble CDW phase.

Finally, the noise should be tested for in small sample sizes. Recall that the spectral noise fingerprints of the RIQHE breakdown are often complicated by what appear to be distinct oscillating modes (see, for example, Fig.10.20). If the sources of these oscillations are spatially localized within the 2DES, then small samples might contain only one such oscillator and therefore reveal a much "cleaner" spectral fingerprint. Also, an intriguing model of narrow-band noise generation discussed in Section 10.3 suggests that ~200 μm-sized bubble domains might play a role in noise generation. If true, then the noise characteristics of a sample should change significantly if its dimensions are reduced to the 100-μm scale.

---

1 B.E. Kane, L.N. Pfeiffer, K.W. West, and C.K. Harnett, Appl. Phys. Lett. **63**, 2132 (1993).

2 J. Zhu, W. Pan, H.L. Stormer, L.N. Pfeiffer, and K.W. West, Phys. Rev. Lett. **88**, 116803 (2002).

3 P.L. McEuen, A. Szafer, C.A. Richter, B.W. Alphenaar, J.K. Jain, A.D. Stone, R.G. Wheeler, and R.N. Sacks, Phys. Rev. Lett. **64**, 2062 (1990).

4 S.H. Tessmer, P.I. Glicofridis, R.C. Ashoori, L.S. Levitov, and M.R. Melloch, Nature **392**, 51 (1998); A. Yacoby, H.F. Hess, T.A. Fulton, L.N. Pfeiffer, and K.W. West, Solid State Commun. **111**, 1 (1999).

5 R.M. Lewis, P.D. Ye, L.W. Engel, D.C. Tsui, L.N. Pfeiffer, and K.W. West, Phys. Rev. Lett. **89**, 136804 (2002).

6 L. Radzihovsky and A.T. Dorsey, Phys. Rev. Lett. **88**, 216802 (2002).

7 R.L. Willett, R.R. Ruel, M.A. Paalanen, K.W. West, L.N. Pfeiffer, Phys. Rev. B **47**, 7344 (1993).

8 D.V. Fil, Lo Temp. Phys. **26**, 581 (2000); D.V. Fil, J. Phys. Condensed Matter **13**, 11633 (2001).

9 A. Endo and Y. Iye, Solid State Commun. **117**, 249 (2001).

10 G. Gruner, Rev. Mod. Phys. **60**, 1129 (1988).

Appendix A
Wet Etching of GaAs Heterostructures

A.1 Etching Mesas to Define 2DES Boundary

The following wet-etch recipe was used to define custom 2DES mesa boundaries such as a Hall bar geometry:

1. Clean sample by rubbing it with a cotton swab in acetone, then methanol, and then de-ionized water. Blow dry.
2. Apply a drop of Shipley 1813 photoresist on sample, and then spin it at 5000 rpm for 30 seconds.
3. Bake sample on hotplate at 115° C for 60 seconds.
4. Align sample beneath desired mask, and expose it for 5 seconds. Our laboratory is equipped with a Karl Suss MJB3 mask aligner.
5. Develop the sample in a 1:2 solution of developer:H_2O using Shipley 351 developer. This normally takes between 20 and 30 seconds, and a visual inspection determines when it is completed.
6. Bake sample on hotplate at 135° C for 60 seconds.
7. Etch sample for a duration of 5-10 minutes in a solution of 100:10:1 H_2O:H_3PO_4:H_2O_2 (with typically 50 ml of H_2O). This removes approximately 100 nm of material per minute, and the etch should reach well below the buried 2DES layer of the heterostructure.
8. Soak sample in acetone to remove photoresist. Blow dry.

A.2 Etching Ledge to Determine GaAs Crystal Axes

To determine the GaAs crystal axes using the etch profile method, it is necessary to etch several microns so that the profile can be resolved using optical microscopy. For such a deep etch, the same procedure as above is used, except that the etch solution is 1:1:1 H_2O:H_3PO_4:H_2O_2 (typically 10 ml each) and the etch time is 2 minutes.

Appendix B:
Monte Carlo Calculation for 2D XY Model

B.1 Theory of Monte Carlo Technique

In the Monte Carlo method of statistical mechanics, equilibrium values of thermodynamic quantities are determined by averaging the configurations of large numbers of random ensembles generated by a computer [1]. For example, the problem encountered in Chapter 9 was to determine the equilibrium magnetization M as a function of temperature T and in-plane field h for the 2D XY model with a director order parameter. For a system of 100 × 100 directors, the energy is given by

$$H = -J\sum_{\langle i\neq j\rangle}\cos\left[2\left(\varphi_i-\varphi_j\right)\right]+h\sum_i\cos\left(2\varphi_i\right). \tag{1}$$

Here φ_i is the angle of the *ith* director, J is the interaction energy between nearest neighbors, and h is the magnetizing field. The magnetization is then determined from the Boltzmann distribution through

$$M = \left\langle\cos\left(2\varphi_i\right)\right\rangle = \frac{\sum_{\{\varphi_i\}}\cos\left(2\varphi_i\right)\exp\left(-H/k_BT\right)}{\sum_{\{\varphi_i\}}\exp\left(-H/k_BT\right)}, \tag{2}$$

where the sums are over all possible configurations of the 100 × 100 directors. The most straightforward way of implementing the Monte Carlo technique is to program a computer to generate very many random configurations of $\{\varphi_i\}$ and directly compute the summations of eq. (2). However, there are so many possible configurations that no real computer will ever be able to sample enough of the system's phase space to make a reliable estimate of M.

The Metropolis algorithm [2] avoids this problem by using the technique of importance sampling, where only configurations of $\{\varphi_i\}$ that contribute significantly to the sums in eq. (2) are considered. These special configurations are found using the principle of detailed balance, which states that in equilibrium, the relative probability of a system being in two configurations *A* and *B* is

$$\frac{P(B)}{P(A)} = \exp\left(-\Delta E / k_B T\right), \tag{3}$$

where $\Delta E = E(B) - E(A)$. The Metropolis method then uses the following algorithm:

1. Select a configuration *A*.
2. Find the magnetization and energy of this configuration, *M* and $E(A)$.
3. Select a new configuration *B* by randomly choosing a single director with an angle φ and changing that angle to a random value.
4. Compute the energy of this new configuration $E(B)$.
5. Maintain the system in configuration *B* if $E(B) < E(A)$. If $E(B) > E(A)$, maintain configuration *B* only with the probability $\exp\left(-\Delta E / k_B T\right)$. Otherwise, revert to configuration *A*.
6. Use the resulting configuration as the input in step 2, and repeat the cycle.

By repeating the steps of this algorithm many times, the system eventually reaches a stable sequence of configurations whose values of *M* are close to the equilibrium value.

A rigorous justification showing that the Metropolis algorithm yields an equilibrium *M* will not be given here. However, an intuitive way of understanding the method is to think of each cycle of the algorithm as a small time interval, so that the magnetization *M* is evaluated at a sequence of times t_1, t_2, t_3, etc. Between each time step, the system is "kicked" by an external perturbation that tries to rotate a randomly-chosen director. The perturbation is always successful if it results in a lower energy. Otherwise, the director is rotated to its new value only according to the Boltzmann probability $\exp\left(-\Delta E / k_B T\right)$. Following this rule, the configurations will ultimately obey

the principle of detailed balance of eq. (3), and $M(t_i)$ will behave similarly to the time dependence of the magnetization of an actual system in contact with a heat bath at a temperature T.

B.2 The Monte Carlo Calculation

To compute $M(h,T)$ in Chapter 9, the Metropolis algorithm described above was implemented using the programming language of the Igor Pro software package of Wavemetrics, Inc. A 100 × 100 grid of directors was used, and after every 10^5 loops of the Metropolis algorithm described above, $M(t_i)$ was recorded. Sequences of either 50 or 100 values of M were recorded for a given h and T to ensure that the equilibrium value was reached. In these calculations, the exchange parameter J of equation (1) was fixed to be 73 mK in order to check for consistency with the results of Fradkin et al. [3], who found $M(T)$ for J = 73 mK and h = 3.5 mK.) For example, for J = 73, h = 35, and T = 100, the sequence of 100 values of M is shown in Fig. B.1. After the fourth iteration, corresponding to 4×10^5 total Monte Carlo steps, M has clearly reached its equilibrium value of 68.4.

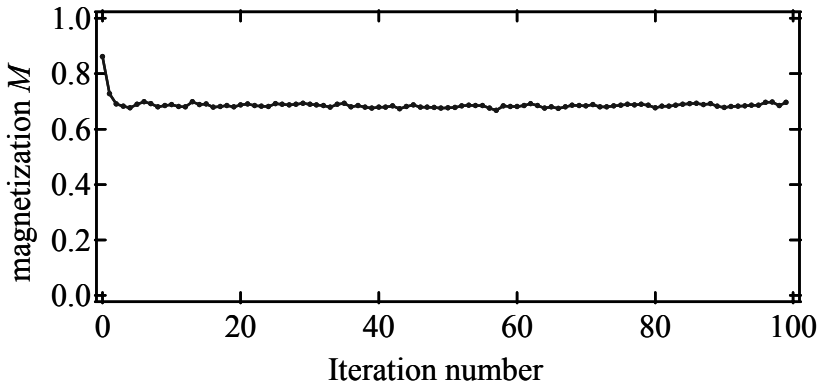

Figure B.1: Sequence of 100 values of the magnetization of a 100 × 100 grid of directors computed using the Metropolis Monte Carlo algorithm. Each point was recorded after 10^5 cycles of the Monte Carlo algorithm; equilibrium is reached after only 4×10^5 cycles in this case. The parameters used in this example were J = 73, h = 35, and T = 100.

The Igor Pro computer code used to make the Monte Carlo calculations is reproduced below.

Monte Carlo Code

```
// This is the main function that yields a set of magnetizations for every 10^5 Monte Carlo
//  cycles.  That set is stored in a wave called "opset".
function mc2dxy(Jcoup,Hcoup,Temp,Num,numrounds)
        variable Jcoup,Hcoup,Temp,Num          // J, h, T, and number of Monte Carlo cycles // per
                                               round.
        variable numrounds                     // number of rounds to record M
        variable currenterror                  // error estimate
        variable i,j,k,m
        variable energy,op                     // "op" is order parameter M
        variable len=100                  // size of grid is 100 x 100
        variable opavg,newspin,denergy
        variable prob,r

        make/o/n=(numrounds) opset             // creates sequence of order params
        make/o/n=(len,len) rgrid

        // If the temperature is high, initialize grid with random directors.
        // Otherwise, initialize grid with all directors pointed the same way.

        if(Temp>(Jcoup+Hcoup))
                randomize(rgrid,len)
        else
                rgrid=0
        endif

        // Determine order parameter of grid

        op = opgrid(rgrid,len)
m=0
do
        k=0
        opavg=0
        do
                // Randomly choose coordinate at (i,j)
                // enoise() is a built-in random number generator
                i=floor((enoise(.5)+.5)*len)
                j=floor((enoise(.5)+.5)*len)
                // Randomly change angle of director at (i,j)
                newspin = (enoise(.5)+.5)*2*pi
                // Calculate change in energy
                denergy = elocal(rgrid,newspin,i,j,len,Jcoup,Hcoup)
                        - elocal(rgrid,rgrid[i][j],i,j,len,Jcoup,Hcoup)
                // Compute Boltzman probability
                if(denergy<0)
                        prob=1
                else
                        prob = exp(-denergy/Temp)
```

```
                endif
                // Update director angle according to detailed balance condition
                r=enoise(.5)+.5
                if(r<prob)
                        op = op + (cos(2* newspin)-cos(2* rgrid[i][j]))/len/len
                        opavg = opavg + op/Num;
                        rgrid[i][j]=newspin;
                else
                        // Compute running average of order parameter
                        opavg = opavg + op/Num;
                endif
                k+=1
        while(k<Num)
// Update order parameter value for this round
opset[m]=opavg
m+=1
while(m<numrounds)
end


// This function randomizes the directions of all the directors in a grid.
function randomize(rgrid,len)
        wave rgrid
        variable len
        variable i,j
        i=0
        j=0
        do
                j=0
                do
                        rgrid[i][j] = (enoise(.5)+.5)*2*pi
                        j+=1
                while(j<len)
                i+=1
        while(i<len)
end


// This function computes the order parameter (i.e. magnetization) of the grid.
function opgrid(rgrid,len)
        wave rgrid
        variable len
        variable i,j
        variable op
        op=0
        i=0
        do
                j=0
                do
                        op = op + cos(2*rgrid[i][j])
                        j+=1
                while(j<len)
                i+=1
        while(i<len)
        return op/len/len
end
```

```
// This function determines the nearest-neighbor energy of a specific director
function elocal(rgrid,angle,i,j,len,Jcoup,Hcoup)
	wave rgrid
	variable angle,i,j,len
	variable Jcoup,Hcoup
	variable ei1,ei2,ej1,ej2
	variable k
	k=0
		if(i>0)
			ei1 = Jcoup*cos(2*(angle-rgrid[i-1][j]));
		else
			ei1 = Jcoup*cos(2*(angle-rgrid[len-1][j]));
		endif
		if(j>0)
			ej1 = Jcoup*cos(2*(angle-rgrid[i][j-1]));
		else
			ej1 = Jcoup*cos(2*(angle-rgrid[i][len-1]));
		endif
		if(i<len-1)
			ei2 = Jcoup*cos(2*(angle-rgrid[i+1][j]));
		else
			ei2 = Jcoup*cos(2*(angle-rgrid[0][j]));
		endif
		if(j<len-1)
			ej2 = Jcoup*cos(2*(angle-rgrid[i][j+1]));
		else
			ej2 = Jcoup*cos(2*(angle-rgrid[i][0]));
		endif
	return -Hcoup*cos(2*angle)-ei1-ei2-ej1-ej2;
end


// This function finds the total energy of a grid
function egrid(Jcoup,Hcoup,rgrid,len)
	variable Jcoup,Hcoup
	wave rgrid
	variable len
	variable i,j
	variable angle,ei1,ei2,ej1,ej2,energy
	energy=0
	i=0
	do
		j=0
		do
			angle = rgrid[i][j]
			if(i>0)
				ei1=Jcoup*cos(2*(angle-rgrid[i-1][j]))
			else
				ei1 = Jcoup*cos(2*(angle-rgrid[len-1][j]))
			endif
			if(j>0)
				ej1 = Jcoup*cos(2*(angle-rgrid[i][j-1]));
			else
				ej1 = Jcoup*cos(2*(angle-rgrid[i][len-1]));
```

```
                        endif
                        if(i<len-1)
                                ei2 = Jcoup*cos(2*(angle-rgrid[i+1][j]));
                        else
                                ei2 = Jcoup*cos(2*(angle-rgrid[0][j]));
                        endif
                        if(j<len-1)
                                ej2 = Jcoup*cos(2*(angle-rgrid[i][j+1]));
                        else
                                ej2 = Jcoup*cos(2*(angle-rgrid[i][0]));
                        endif
                        energy = energy-Hcoup*cos(2*angle)-ei1-ei2-ej1-ej2;
                        j+=1
                while(j<len)
                i+=1
        while(i<len)
        return energy
end
```

---

1 D. Chandler, *Introduction to Modern Statistical Mechanics* (Oxford Univ. Press, New York 1987); also see preprint by K.P.N. Murthy and V. Sridhar at http://xxx.lanl.gov/abs/cond-mat/0104167.

2 N. Metropolis, A.W. Rosenbluth, M.N. Rosenbluth, A. Teller, and E. Teller, J. Chem. Phys. **21**, 1087 (1953).

3 E. Fradkin, S.A. Kivelson, E. Manousakis, and K. Nho, Phys. Rev. Lett. **84**, 1982 (2000).